Photonic Crystal Optical Frequency Combs

Thesis submitted for the degree of Doctor of Philosophy

Department of Electronic and Electrical Engineering

The University of Sheffield

Henry Francis

13 June 2021

Abstract

Nanophotonics, driven by low processing power and high-density integration, is emerging as the next logical step for photonic integrated circuits. Microwave photonics is a diverse research topic that is set to transform traditional microwave electronics. In this thesis, the two topics are combined by investigating the ability for nanophotonic devices to harbour and generate microwave photonic signals.

Generating an optical frequency comb (OFC) plays a vital role in integrated microwave photonics. By investigating the different OFC generation methods as well as the capabilities offered in photonic crystal (PhC) devices, a method to produce an OFC from nanoscale devices is proposed. The proposal is modelled using calculations based on temporal coupled mode theory. Analysis shows that a broadband OFC can be produced using nanoscale devices that favour high-density integration.

The experimental results in this thesis are based around three fundamental areas: PhC device fabrication, optical characterisation and microwave photonic characterisation. Each chapter builds towards the overarching theme of microwave photonic signal processing at telecommunication wavelengths in a nanophotonic device. A new fabrication process for etching PhC structures in nonthermalised InP samples is developed. The developed process has excellent applications in fabrication where the use of thermal grease or a high sample stage temperature is impractical. Optical characterisation of the fabricated samples shows the effects of lithographic and photothermal tuning on the cavity mode frequency. Through this analysis, resonant cavity modes can be designed for a working wavelength within the telecommunication bandwidth. Temporal analysis shows that carrier lifetimes from a QD ensemble that spectrally and spatially overlaps with the PhC cavity are greatly reduced.

Finally, a new measurement set-up is proposed and analysed for the characterisation of microwave photonic signals in nanoscale devices. It is shown that the integration of an ultra-fast laser and a two-arm Mach-Zehnder in-

terferometer can generate a microwave signal within the spectrum of the ultra-fast laser. This signal is integrated into the standard optical characterisation set-up, where it is used to excite PhC optical devices. The results show that the microwave signal present in the ultra-fast laser can be resolved in the emission spectrum of QDs weakly coupled to a PhC cavity.

Acknowledgements

Firstly, I would like to thank the wide range of people from outside the university who have indirectly helped me gain my PhD. My wonderful girlfriend Nina, for putting up with me for the past few years. My mum, for her tremendous support during some difficult times and her invaluable proof reading skills. Finally, the network of friends I have developed over the past 4 years, this has been a constant source of pleasure and strength which I could not have done without.

I am very thankful to Rob Airy, Paul Fry, Ben Royal, Nasser Babazadeh and university cleanroom technicians who provided a plethora of information and advice about the cleanroom facilities at the University of Sheffield. Ian Farrer, Charlotte Ovenden, Aris Tropelis and Max Godsland all gave insightful and constructive conversations throughout my PhD, for which I am grateful.

Finally, I would like to thank my research group. My supervisors, Chaoyuan Jin and Mark Hopkinson, have provided excellent guidance and have given me the opportunity to learn so many invaluable skills. A special thanks to Si Chen for all his help with measurement set-ups and modelling development, it truly was a team effort! Thanks to Xiaodong Zhang and Kaijun Che for their help with modelling and to Yunran Wang for her support.

To my daughter Amélie. This has always been for you.

List of journal publications, conference proceedings and awards

As part of this thesis:

Journal publications

H. Francis, S. Chen, K.-J. Che, M. Hopkinson, and C.-Y. Jin, "Photonic crystal cavity-based intensity modulation for integrated optical frequency comb generation", Crystals, pp. 1–10, 2019
H. Francis, S. Chen, K.-J. Che, M. Hopkinson, and C.-Y. Jin, "Generation of flat optical frequency combs via cascaded intensity and phase photonic crystal modulators" in IEEE J. Sel. Top. Quant. Electron. 27, 2100209 (2021)

Conference proceedings and awards

Proceedings

H. Francis, S. Chen, C. Ho, K.-J. Che, Z.-D. Zhang, M. Hopkinson and C.-Y. Jin "Generating optical frequency combs via nanoscale photonic structures", Proc. SPIE 11274, Physics and Simulation of Optoelectronic Devices XXVIII, 1127412, 2020
H. Francis, S. Chen, C. Ho, K.-J. Che, Y. Wang, M. Hopkinson and C. Jin "Generation of optical frequency combs using a photonic crystal cavity", IET Optoelectronics, vol. 13, no. 1, pp. 23-26, 2 2019.
H. Francis, S. Chen, C. Ho, K.-J. Che, Y. Wang, M. Hopkinson and C. Jin "Modulating photonic crystal structures to generate optical frequency combs", IEEE International Conference on Manipulation, Manufacturing

and Measurement on the Nanoscale (3M-NANO), Hangzhou , pp. 55-59, 2018

Awards

Best Student Paper Award - IEEE International Conference 3M-NANO, Hangzhou, 2018

As part of other research work

Journal publications

L.-F. Wang, Y.-R. Wang, H. Francis, R. Lu, M.-J. Xia, F. Liu, M. Hopkinson, C. Jin "Theoretical modelling of single-mode lasing in microcavity lasers via optical interference injection" Opt. Express 28, 16486-16496, 2020
S. Behera, P. Fry, H. Francis, C. Jin, and M. Hopkinson, "Broadband, wide-angle antireflection in GaAs through surface nano-structuring for solar cell applications" Sci Rep 10, 6269, 2020
S. Behera, P. Fry, H. Francis, I. Farrer, C. Jin, and M. Hopkinson, "Photonic integration of uniform GaAs nanowires in hexagonal and honeycomb lattice towards broadband optical absorption" AIP Advances 10, 105211, 2020

Conference proceedings

S. Chen, H. Francis, C. Ho, K.-J. Che, Y. Wang, M. Hopkinson, S. Zhang, and C. Jin "Control of quality factor in laterally coupled vertical cavities", IET Optoelectronics, vol. 14, no. 3, pp. 100-103, 6 2020.
S. Chen, H. Francis, C. Ho, K.-J. Che, Y. Wang, M. Hopkinson, S. Zhang, and C. Jin "Quality factor control in laterally-coupled vertical cavities", 2018 IEEE International Conference on Manipulation, Manufacturing and Measurement on the Nanoscale (3M-NANO), Hangzhou, pp. 60-64, 2018
Y. Wang, C. Jin, C. Ho, S. Chen, H. Francis, M. Hopkinson, "Thermodynamic processes on a semiconductor surface during in-situ multi-beam laser interference patterning," IET Optoelectronics, vol. 13, no. 1, pp. 7-11, 2 2019

Abbreviations

APD	Avalanche Photo Diode
BE	Band Edge
CAIBE	Chemically Assisted Ion Beam Etching
CCD	Charge Coupled Device
CMOS	Complimentary Metal-Oxide Semiconductor
CW	Continuous Wave
EBL	Electron Beam Lithography
ECR	Electron Cyclotron Resonance
EDFA	Erbium-Doped Fibre Amplifier
EM	Electromagnetic
EO	Electro-Optic
FBT	Fused Biconical Taper
FCA	Free Carrier Absorption
FCD	Free Carrier Dispersion
FEM	Finite Element Method
FPC	Fabry Perot Cavity
FSR	Free Spectral Range
GVD	Group Velocity Dispersion
ICP	Inductively Coupled Plasma
IM	Intensity Modulator
IRF	Instrument Response Function
LIDAR	Light Detection and Ranging
LN	Liquid Nitrogen
MPB	MIT Photonic Bands
MOCVD	Metal-Organic Chemical Vapour Deposition

MWP	Microwave Photonics
MZI	Mach-Zehnder Interferometer
ND	Neutral Density
OFC	Optical Frequency Comb
PECVD	Plasma Enhanced Chemical Vapour Deposition
PIC	Photonic Integrated Circuit
PLC	Planar Lightwave Circuit
PL	Photo-Luminescence
PM	Phase Modulator
Q	Quality
QD	Quantum Dot
RF	Radio Frequency
RIE	Reactive Ion Etching
SAW	Surface Acoustic Wave
SCCM	Standard Cubic Centimetres per Minute
SEM	Scanning Electron Microscope
SK	Stranski–Krastanov
SNR	Signal to Noise Ratio
SNSPD	Superconducting Nanowire Single Photon Detectors
SpE	Spontaneous Emission
TLS	Two Level System
TPA	Two Photon Absorption
V	Mode Volume
WDM	Wavelength Division Multiplexing

Contents

Chapter 1

Introduction

Throughout history, technological advancements have shaped who we are. In the late 19th century, the combustion engine and the use of gas and oil changed factories and our lives for the better. The mid 20th century saw what is now known as the third industrial revolution with the rise of electronics and telecommunications. These technologies transformed the way we process information and led to unprecedented technological advancements. Now we are living in what could arguably be called the fourth industrial revolution: the internet. Since the invention of the world wide web, our thirst for data has increased exponentially year on year. It has been calculated that our band-width requirement grows faster than the predictions made by Moore's law of transistors. One of the driving forces that can enable this band-width growth is light-based telecommunication technology.

Long-distance communication of data has so far been the driving force behind optical technology. However, modern advancements are seeing breakthroughs in chip-scale lasers, modulators and detectors that lead to the integration of photonic devices beyond purely communicative functions. Photonic integrated circuits (PIC) have the potential to transition us from purely electronics-based digital signal processing to highly sophisticated photonic networks on a chip. An emerging technology in PICs is the implementation of high-speed radio frequency signals operating in the optical frequency domain, a technology known as microwave photonics (MWP).

Microwave engineering encompasses electromagnetic waves with a frequency range between 0.3 and 300GHz. The short wavelength dictates that small antennas and low power transmitters can be used for their communication and transmission. This enables both civilian and military applications where device size and weight are a prevalent issue. For example, mobile

phones, Wi-Fi and RADAR all use microwave engineering to operate. The microwave spectrum is a subset of the radio frequency (RF) spectrum, which covers a frequency range from 30KHz up to 300GHz. At lower RF frequencies, standard discrete circuit elements are used, so circuit theory revolves around current and voltage. However, when entering the microwave end of the RF spectrum, circuit elements such as transmission lines and cavity resonators dictate that the circuit theory is better described by electromagnetic fields. In this sense, the theory of photonic and microwave engineering have some similarities that helps towards the convergence of the two.

In the early days of microwave photonics, the rationale was to use optical technologies to overcome some difficulties in electronic microwave engineering, for example, bandwidth limitations and frequency-dependant propagation losses in network links. However, it was also discovered that techniques in microwave electronic engineering could improve photonic communication and system performance. The rise of MWP progressed quickly with impressive demonstrations of various functions, including: the generation of ultra-broadband signals [1], radio-over-fibre [2], programmable filters [3] and photon-enhanced radar systems [4]. These demonstrations, although impressive, were largely based on fibre-optic components; a technology that is relatively bulky and not in a position to compete with standard integrated electronic devices for chip-based applications.

To take advantage of the impressive functionalities promised by microwave photonics, chip-scale implementation is imperative. The convergence of integrated photonic technologies with MWP has led to increased device functionalities with respect to device footprint and reduced power consumption [5]. In much the same way that new functionalities were realised with the combination of microwave and photonic engineering, *integrated* MWP has the ability to produce unique on-chip capabilities. With advanced fabrication techniques and the integration of microscale photonic devices, integrated MWP has experienced fantastic progression. The enhanced non-linear interactions present in small-scale devices has enabled new technologies to come about. These include plasmonic modulators [6], on-chip stimulated Brillouin scattering [7] and on-chip optical frequency comb generators [8].

Continuing on this same trend, on-chip integration of nanophotonic devices will increase optical non-linearity, decrease the device footprint and once again enhance the ever progressing research field of integrated MWP. Nanophotonics offers smaller device footprints that favour high-density integration, low energy consumption and enhanced optical non-linearity [9]. Indeed, cutting edge studies have shown small volume all-optical modulators

[10], low power EO modulators [11] and low threshold topological lasers [12], all implemented using nanoscale photonic devices. To this end, implementing standard MWP components on a nanophotonic platform would open up the area of MWP further. One such component that is yet to be realised in nanophotonics is an optical frequency comb.

This thesis focuses on the generation of an optical frequency comb using nanophotonic technologies. This innovative method combines traditional OFC generation via electro-optic modulation with state-of-the-art nanophotonic technology. In the rest of this chapter, the various OFC generation techniques are introduced as well as the fundamentals of integrated nanophotonics.

1.1 Optical frequency combs

An optical frequency comb (OFC) is a light source with a broad range of equally spaced intensity spikes in the frequency domain. The concept behind the frequency comb relies on the relationship between time and frequency. Initially, OFCs were developed to generate high accuracy clocks based on optical transitions in atoms [13]. However, as technology developed, it became apparent that OFCs had a large number of applications in both research and industry [14]. In the following section, the fundamentals, history and development of OFC generation will be explained. These fundamentals will provide context and background information that is relevant to the reader. To introduce the topic of optical frequency comb generation, the fundamentals of mode locked laser (MLL)-based OFC generation will be detailed. This will ensure relevant context to the terms and concepts used throughout.

1.1.1 Mode locked lasers

John Hall and Theodor Hänsch are the forefathers of OFCs; their pioneering work and visionary innovation led to the first observation of an OFC. They were awarded the Nobel prize in 2006 [15, 16] and OFCs now see more attention than ever. To give an idea of the scope of OFC research, a quick search on *Google Scholar* for exact matches of "optical frequency comb" returns over 17,000 results! As early as the 1980s, phase stabilised MLLs were used for optical metrology. The operation of an MLL is shown in Fig. 1.1, in this figure the time and frequency domain properties of the MLL are shown. It works by introducing many coherent, longitudinal modes in an optical cavity. This forms an ultra-short pulse when all modes constructively interfere with each other; the time between each pulse, T_s is a function of

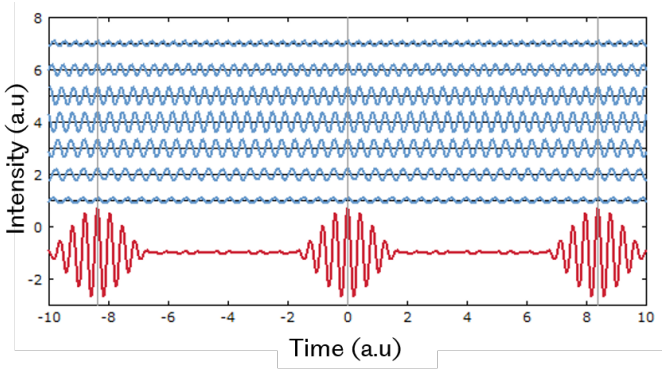

Figure 1.1: A diagram showing the fundamental operation of an MLL, annotated from [17]

the cavity length, such that $T_s{=}2L/\nu_g$, where L is the cavity length and ν_g is the pulse group velocity in the cavity, T_s is typically between 1 and 15ns. To reduce the pulse duration, the amount of frequency components required must be increased. The theoretical limit to the pulse duration in the time domain is dependent on two factors: the number of oscillating modes in the cavity and the frequency separation between them; this makes up the laser bandwidth. The amount of oscillating modes in an MLL can vary from hundreds of thousands to millions and can span over hundreds of nanometers in the frequency domain, covering more than one octave. An octave is a ratio between frequencies, where one octave corresponds to the doubling of an initial frequency. An OFC that spans an octave will mean the highest frequency in the comb will be at least twice the lowest frequency. In terms of spectroscopic measurements, there are obvious advantages to such a broad optical bandwidth with densely packed modes. However, there are two unique properties with regard to the spectrum of an MLL which enhance high precision optical metrology further than simply a broad optical spectrum. These unique properties are: (1) all the modes are perfectly equally spaced in the frequency domain and all the modes are phase coherent, therefore each optical mode in the spectrum is deterministic; (2) the absolute frequency of one can be found from another.

To understand this further, the output from the MLL can be analysed as a periodic, amplitude-modulated light source. The Fourier series can then be used to generate an equation for the frequency components of the light source. In the time domain, the optical field can be described as:

$$E(t) = A(t)e^{i\omega_c t} \tag{1.1}$$

where *A(t)* is a periodic pulse and ω_c is the angular frequency of the light source. Using the Fourier transform each frequency component, or mode, can be calculated as a function of the periodic pulse envelope, to give:

$$E(t) = A(t)e^{i\omega_c t} = \sum_{N=N_i}^{N_{f_r}} A_N e^{iN(\omega_N t)} \tag{1.2}$$

where N is the mode number and the carrier frequency of each mode is represented by f_N=$\omega_N/2\pi$. So ω_c is the angular frequency of the initial carrier light, which means an integer number of f_r will fit into $\omega_c/2\pi$. However, in most cases f_r is not a multiple of f_c. To account for this, the calculated Fourier frequencies are offset and this gives rise to what is commonly known as the comb equation [14]:

$$f_N = Nf_s + f_o \tag{1.3}$$

N is then used to find the frequency of light by multiplying it by the inverse of the time between two pulses from the periodic pulse train, f_s, to within an accuracy of f_0. By using Eq. 1.3, it is then possible to define an optical frequency by attaining only two parts of information about the signal: f_s and f_o. Typically, an MLL will have an f_s of at least 100MHz and can be far into the microwave range, which is another of the OFC's selling points; it can be used to easily convert a microwave signal into the optical domain and vice versa using relatively simple techniques. This brings the application of OFCs into the rich and absorbing field of microwave photonics.

Observing and controlling the frequency offset, f_o, is paramount in the realisation of high-precision optical clocks and metrology. The frequency offset is essentially the phase shift of the optical carrier modes. The realisation of OFCs from MLL was discovered in the 1980s but it was not until 1999 that techniques to detect and control the frequency offset were realised [18, 19]. The technique required an octave-spanning frequency comb so that a frequency component at the bottom end of the comb spectrum could be double and interfered with a frequency component at double the initial comblines frequency. Although relatively straightforward on paper, it proved experimentally difficult to produce a comb of this spectral range. There have been many advances made in this area and it proves to be an engaging and successful research topic. However, the scope of this work does not require detailed knowledge of obtaining and controlling the frequency offset so it will not be discussed further.

The detection and manipulation of the frequency spacing, f_s, in an OFC is of interest to the microwave photonics [5] research community as well as

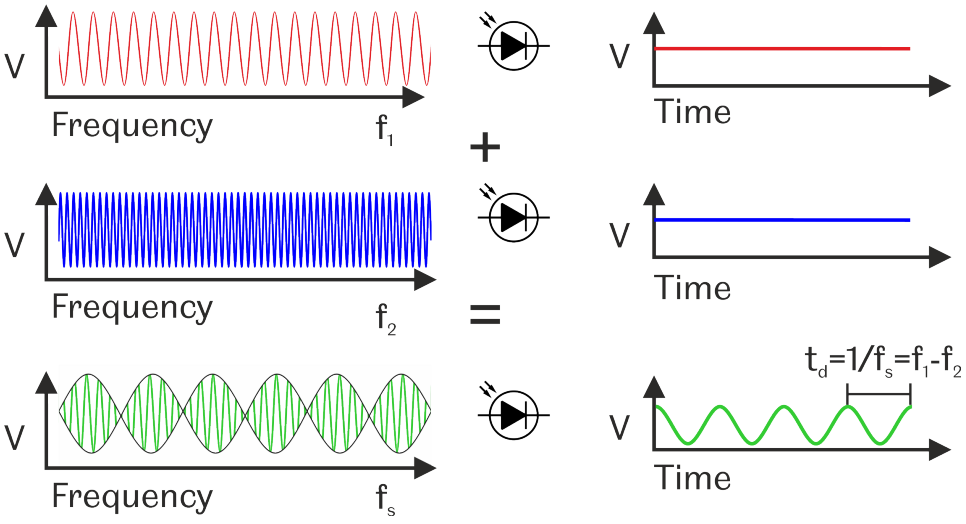

Figure 1.2: Illustrating the key concept behind many microwave photonic schemes

the telecommunications industry [20]. In microwave photonics, the detection of f_s from an OFC results in an electronic pulse train which is made up of coherently related microwave Fourier harmonics. These are a direct relation to the OFC frequency spacing, hence bridging the gap between the microwave and optical domains. In telecommunications, the ability to manipulate f_s leads to the dense integration of many frequency components that can be utilised for WDM.

A simple technique can be used to observe the microwave frequency between two adjacent optical modes, known as the heterodyne optical beat frequency. The two optical modes are interfered with each other and produce an optical signal which has an amplitude modulation frequency equal to their frequency difference. This optical signal is incident on a photodetector, where the signal is converted into an electrical signal with the same proportional amplitude modulation speed, as illustrated in Fig. 1.2. This concept lies at the heart of microwave photonics and is discussed in various forms throughout this chapter and the thesis as a whole.

By mixing a range of frequency components, this same concept can then be extrapolated into OFCs which have many modes that are all interfering with each other. In MLL OFC generation, the f_s is determined by the cavity length. However, technology has progressed and OFCs have become more versatile instruments that stretch across different research fields. New

methods of OFC generation have been proposed and explored, these are discussed in the rest of this section.

1.1.2 Micro-combs

Using optical micro-resonators to generate OFCs has been a subject of great interest since the early 2000s [21]. The reason for their popularity in OFC generation is their ability to trap and confine optical fields on a very small scale. This enables highly non-linear optical phenomena to exist using very low powers. Specifically, the Kerr effect can be used to mix four photons, in a process called degenerate four wave mixing (FWM). In this process, two photons of a single carrier frequency, ω_c, are used to generate two photons of differing frequencies, known as the signal, ω_s, and idler, ω_i, frequency. The two distinctive properties of these generated photons are (a) their combined energy is equal to the energy of the two initial carrier photons and (b) the frequency of the signal and idler photon is above and below the carrier frequency, respectively, at an equal distance. These properties are due to the standard law of the conservation of energy that means the photons satisfy this relation:

$$2\omega_c = \omega_i + \omega_s \tag{1.4}$$

Degenerate FWM, as shown in Fig. 1.3, was first demonstrated using a continuous wave laser to resonantly excite a monolithic micro-toroidal cavity from two independent groups in the same year [21, 22]. The pump laser is coupled to the cavity via an optical fibre, the long lifetime of the photons, enabled by the ultra-high quality (Q) factor and large photon density, allows for degenerate FWM where signal and idler photons populate the neighbouring eigenmodes. This produces a comb with a mode spacing equal to the free spectral range (FSR) of the cavity. As shown by Eq. 1.4, the signal and idler photons are produced at the expense of the carrier photons so although this does show parametric frequency conversion, only a minimal amount of sidebands is produced. This was ground-breaking work as it proved the evidence of optical parametric oscillation in micro-toroidal cavities with low threshold gain, but it was not until three years later that the so-called Kerr comb was born [23]. This differed from the original work by producing non-degenerate FWM within the micro-toroidal cavity.

In order to generate multiple sidebands over a broad frequency range, non-degenerate FWM is utilised. In this process, the first order sidebands, generated by FWM, then mix with the carrier photons to produce second order sidebands which populate the next available eigenmode, as illustrated in Fig. 1.4. This process is repeated many times for higher and higher order

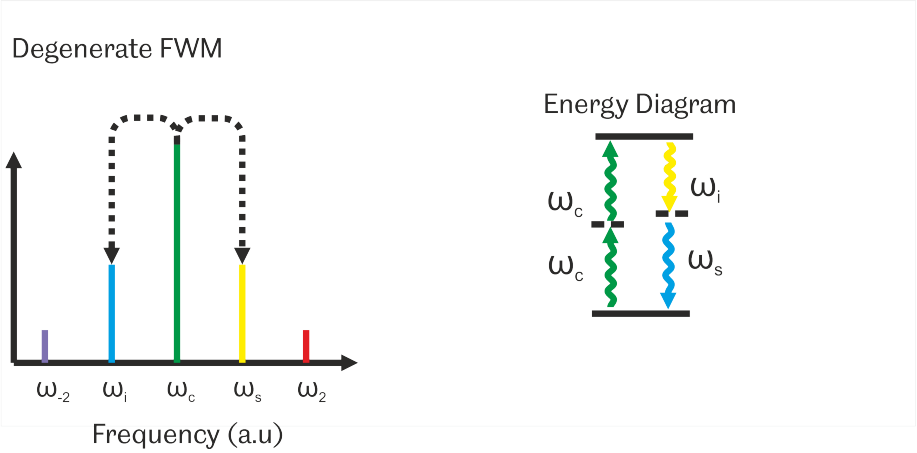

Figure 1.3: Degenerate four wave mixing

sidebands, eventually producing a comb that can spread over a very broad range with many eigenmodes populated.

The mode spacing in a Kerr comb is dependent on the FSR of the cavity therefore the larger the cavity, the smaller the mode spacing. As discussed in the previous section, having a mode spacing that is within the tens of gigahertz range leads to practical application in microwave photonics and telecommunications. For example, light detection and ranging (LIDAR) requires the photonic synthesis of microwave signals that commonly operate at around 15GHz, or in WDM where multi-carrier sources can produce up to 1000 channels with a channel spacing of 7GHz [24]. It also means the detection of the generated frequency spacing can be easily obtained by the observation of the heterodyne beat note. This was first observed using a monolithic, silica-based micro-toroidal cavity with a diameter of 750µm [23]. This led to a frequency spacing of 86GHz, thus producing a simple passive device that has the potential for on-chip integration. The drawback of this type of Kerr comb is the relatively low attainable Q due to the surface roughness of silica. This prohibits silica-based Kerr combs from generating fine-toothed combs because the parametric gain threshold is dramatically increased for larger cavities with lower Q factors [20, 25]. To overcome this, other materials such as fluoride crystals [26, 27] as well as fused quartz [28] can be used, to name but a few examples. In these toroidal structures, the surface roughness is down to the sub-nanometer scale, which induces ultra-high Q factors, up to $3x10^{11}$ [29]. This enables high optical non-linearity for far larger cavities that can generate shorter FSRs. For example, Gru-

dinin *et al.* [30] fabricated a cavity of 4.85mm diameter which produced an FSR of 13.81GHz with an intrinsic Q of $6x10^9$ using an optical input power of 25mW. Despite these impressive figures, the comb efficiency is still very low due to the large effective mode volume; the highest intensity sideband produced was still around 20dB less than the pump laser. So there exists a trade-off between the combline density and parametric gain efficiency; an increased cavity size will increase the combline density but at the cost of parametric gain efficiency. Another important factor in the practical realisation of commercially available chip-based Kerr combs is their fabrication methods and compatibility. To integrate with current CMOS technology and fabrication techniques, silicon-based cavities hold a significant advantage over fluoride or quartz-based cavities.

As discussed in section 1.1, the phase coherence from each mode is imperative for stable operation and industry application. Up until 2011, the phase coherence of the comblines generated from Kerr combs had not been observed. This non-trivial measurement to characterise the coherence of micro-combs was first undertaken by Ferdous *et al.* [31]. Their findings suggested that the chronology of sideband generation through non-degenerate FWM chronology determines their coherence. They outlined two FWM pathways to comb generation and termed them type I and type II, an example of these is given in Fig. 1.5(a) and (b) respectively [31]. In type I, the immediate neighbouring modes are filled, these subsequently mix together and fill their immediate neighbouring mode, the process is cascaded to fill a large number of modes, spaced by one FSR. This leads to good coherence between all the comblines, resulting in temporally invariant pulses. In type II, as the laser comes into resonance with the cavity, initial sidebands that are multiples of the FSR appear first. These sidebands then act as independent optical pumps for the generation of more sidebands, known as secondary combs, as shown in Fig. 1.5. These secondary combs are essentially an array of individual type I combs that have differing offset frequency and hence there is little coherence between these secondary combs. This work provided a method for type I comb generation which is widely used in photonic chip-based frequency combs today [32].

Silicon nitride-based Kerr combs are currently emerging as a strong contender to produce on-chip comb generation on a large scale [33, 34, 35]. The high refractive index, low loss and large Q factors ensure OFC generation is possible. These points, combined with the potential for CMOS compatibility, has meant rapid progress towards a fully integrated on-chip source, as demonstrated by Stern *et al.* in 2018[36]. Mass production of SiN Kerr combs also looks very promising given that current lithography tech-

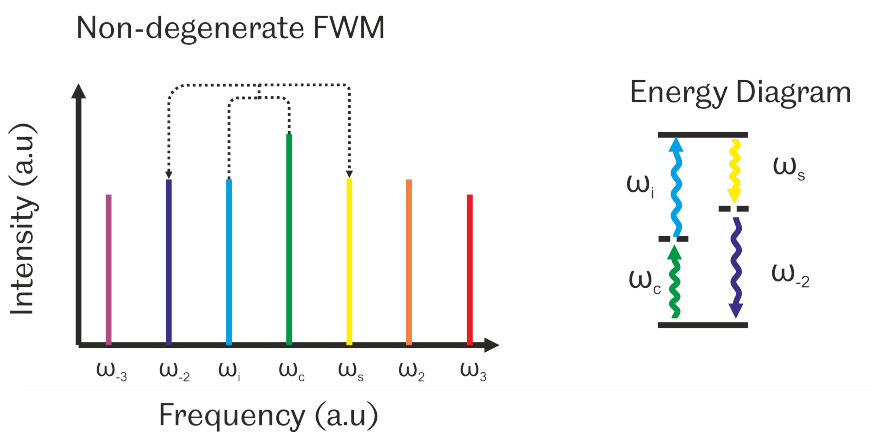

Figure 1.4: Non-degenerate four wave mixing

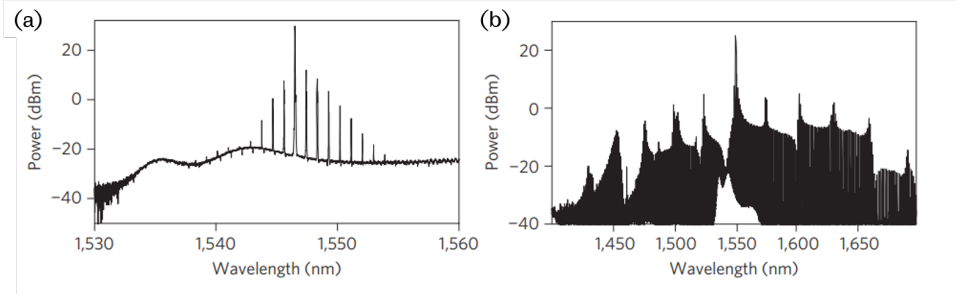

Figure 1.5: An example of (a) type I FWM comb generation and (b) type II comb generation [31]

niques can be adapted from standard silicon-chip based fabrication. Having said this, the current state-of-the-art on-chip Kerr combs have an FSR of around 200GHz, rendering the generated pulses inaccessible using standard electronic devices. Smaller mode spacing, down to 20GHz, have been demonstrated but at the cost of significant power reduction, necessitating external amplification. Hence they are not fully integrative. Much work is now going towards solving these problems in order to realise an on-chip OFC with applicable functionality [32].

Quantum Cascade Laser Frequency Combs

A quantum cascade laser takes advantage of the intersubband transitions in a repeated quantum well stack to generate lasing at an engineered wave-

length [37]. The position of the energy levels within the active region is predominantly dependent on the layer thickness and not on the material properties. This leads to controllable emission wavelengths from a QCL, ranging from 3.5 to 87 µm. Although early in the history of QCLs it was suggested that mode locking could be used to generate ultra-short pulses in far-infra-red [38], thus generating an OFC, the nature of intersubband transition inhibited this. In a standard MLL, the short pulses produced by the round trip frequency of the cavity will have an average power proportional to that of a continuous wave laser. The energy in these two level systems is abruptly released as an optical pulse due to a build-up of energy; this is made possible by the long upper-state lifetimes [39]. Unfortunately, intersubband transitions based on quantum wells exhibit upper state lifetimes on the pico-second scale, far shorter than the round trip time in a millimetre-sized cavity. This meant OFC generation could not be demonstrated using the same techniques that are used in MLLs with ultra-short time domain pulses.

Despite the difficulties in generating ultra-short pulses, QCLs have the ability to generate OFCs via non-degenerate FWM. In fact, the short upper state lifetime that hinders standard mode-locking techniques enables broadband FWM. As with standard two-state systems, third-order optical non-linearity is present. The active quantum well region presents very large, resonant Kerr non-linearity due to the enhanced optical field and the bandwidth of this FMW process is much larger due to the short upper state band lifetime. For this reason, a large number of comblines can be generated over a broad bandwidth at defined frequencies. A fantastic opportunity for applications in sensing therefore exists. In particular, by using a technique known as 'dual comb spectroscopy', which uses heterodyne beatnote detection, very high resolution spectroscopy can be performed in a region known as the molecular fingerprint. This is where the majority of the absorption bands of light molecules can be found, allowing for medical, pharmaceutical and environmental sensing. However, they do not support application in microwave photonics given the comblines' incoherence and relative complexity when compared to other comb generation methods.

1.1.3 Modulation-based comb generation

Given the diversity of OFCs, the required characteristics will inevitably be dependent on the desired application. MLLs are predominantly applied to ultrafast photonics, where short pulses are needed. QCLs are useful in molecular sensing due to their wavelength range and mode spacing. Kerr

combs are emerging as a contender for on-chip integration. In this section, combs generated by electro-optic (EO) modulation will be discussed. Although they do not offer the bandwidth capabilities of MLLs or the chip-scale implementation of Kerr combs, this is the only type of comb generation to offer agile mode spacing and flexibility in the combs' central frequency using a relatively simple and established technology [40]. For this reason, they have undergone somewhat of a renaissance in the past decade as arbitrary waveform generation [41] and microwave photonics [42] have become increasingly popular research topics.

Although the concept of using an electronic microwave signal to modulate an optical signal has been around since 1967 [43], it was not until the year 2000 [44] that it really started to be exploited for generating an OFC. Strong sinusoidal phase modulation of a continuous wave laser leads to the generation of sidebands in the frequency domain. The characteristics of the generated sidebands are dependent on the modulation depth of the electronic signal and its repetition frequency, such that:

$$\Delta\nu = 2f_m\Delta\theta \tag{1.5}$$

where $\Delta\nu$ is the sideband width, f_m is the modulation frequency, typically around 10-20GHz, and $\Delta\theta$ is the modulation index, typically around 100 rad. This phase-modulated light signal can then be fed into an optical group delay dispersion circuit, such as an optical fibre of a specific length or an optical synthesizer. This compresses the chirped light and generates trains of ultra-short pulses with a width inversely proportional to the sideband width and a repetition frequency related to the electronic signal supplied at the modulator. This method has three main advantages: (a) the pulse width can be controlled by the phase modulation index (b) the repetition rate can be controlled by the modulation frequency and (c) the central frequency can be tuned by the input carrier laser.

Although this early work proved innovative in terms of the time domain signal generated and the methods for its control, the intensity of the individual comblines was inhomogeneous. The combline intensity followed a Bessel function and was highly dependent on the wavelength [44]. For many applications a broadband, flat OFC is necessary, so in the work that followed, this was addressed using a variety of different schemes. Initially, intensity and phase modulators were cascaded in series, as shown by Fig. 1.6. In this scheme, the intensity modulator carves pulses into the CW laser to give square-shaped pulses. The phase modulator then provides a chirping mechanism to the signal. This chirping can be set to be as linear as possible

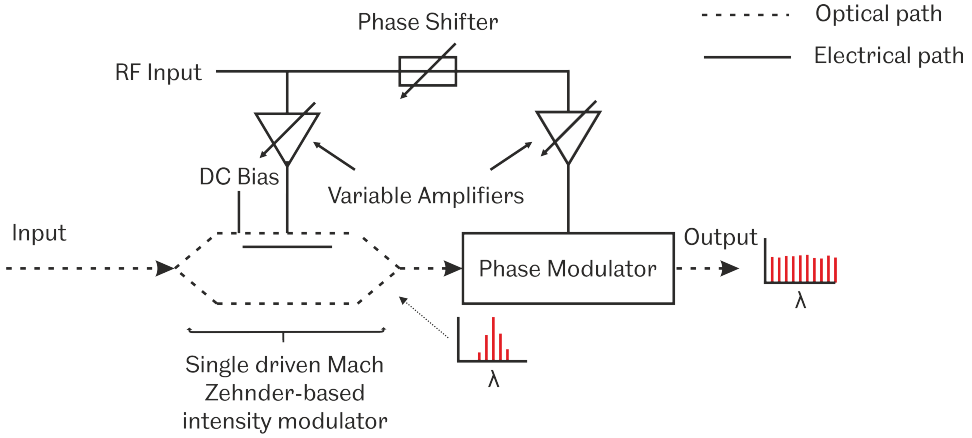

Figure 1.6: Schematic of a standard OFC generation method based on cascaded intensity and phase modulators in series

for the time when the signal is low, thus equalising the spectrum [40]. This can be shown mathematically [45] by representing the electric field of the input light as:

$$E_{in}(t) = e^{i\omega_c t} \tag{1.6}$$

so that the output is expressed as

$$\begin{aligned} E_{out}(t) = exp(i\omega_c t)cos(\frac{\pi}{4}\alpha sin\omega_r ft - \frac{\pi}{2}\gamma) \\ \times exp\{i(\theta\frac{\pi}{4}\alpha + \frac{\pi}{2}\beta)sin\omega_r ft - i\theta\frac{\pi}{2}\gamma\} \end{aligned} \tag{1.7}$$

where $\omega_r f$ is the angular frequency sinusoidal modulating wave, α and β are the electrical voltages, normalised to the half wave drive voltage, of the IM and PM respectively. γ is the DC bias applied to the IM, again normalised to the half wave drive voltage. Careful manipulation of the bias and drive voltages led to a power variation within the comb 5dB over >50% of the bandwidth, shown in Fig. 1.7(a). The drawback of this system was the loss of controllability, which had made modulation-based OFCs so viable. In order to produce this spectral flatness, the authors had to set very stringent parameters, as shown in Fig 1.7(b). This counter plot map, where the Z axis is the combline power deviation, shows that with even a slight change in modulator parameters, the flatness quickly degrades, this produces difficulties in frequency and bandwidth tuning.

Following on from this early work, many schemes have been explored that take advantage of the modulator parameters in order to generate an

OFC. Healy *et al.* [46] used two cascaded intensity modulators, using the theory that each of the generated sidebands will have an amplitude that is based on a Bessel function and a phase that can be controlled by the DC bias of the IMs. With careful control of just these two parameters, it negates the need for a phase modulator. Therefore, precise control of the RF amplitude is not needed, opening up a degree of freedom while maintaining spectral flatness. This operation can be easily understood by describing the operation mathematically. The first line of Eq. 1.7 gives the time domain response of an intensity-modulated light signal. When a sinusoidal modulation wave is used, the frequency domain response is represented as a series of harmonic frequency components, as shown by Eq 1.2. By cascading multiple IMs, the frequency response can be represented by:

$$E_k = \sum_N A_{N,k} cos\{(\omega_c + N \times \omega_{rf})t + \theta_{N,k}\} \tag{1.8}$$

where the amplitudes, $A_{N,k}$ and phase $\theta_{N,k}$ are represented by the following:

$$A_{N,k} = \frac{1}{2} cos\{(\gamma_k + N)\frac{\pi}{2}\} J_N(\frac{\alpha_k \pi}{4}) \tag{1.9}$$

$$\theta_{N,k} = \{1 + N + (-1)^N\}\frac{\pi}{2} + N\theta_k + \theta_{in} \tag{1.10}$$

where α_k, γ_k and θ_k are the drive voltage, DC bias and phase of the k^{th} modulator, respectively, and J_N is Bessel function of the first kind for order N. From Eq 1.9, it can be seen that the RF amplitudes and DC bias of each IM can control the sideband amplitude, similar to the previous case. However, by implementing two identical IMs, it is possible to control the phase shift between the modulators, as shown by Eq. 1.10. The advantage of this can be understood by assuming that each combline from the first modulator is now the carrier frequency for the second modulator. The induced phase difference between the modulators enables the initial modulation parameters to shift onto adjacent comblines, hence amending the combline inhomogeneity due to the Bessel function. This provides a means of controlling the comb by only the DC bias of each modulator and their phase difference. Insusceptibility to RF amplitude fluctuation is shown by the counter map in Fig. 1.8, where the Z axis represents combline power deviation. Releasing the stringent controls of the RF amplitudes opens up the possibility for large bandwidths, above 0.5 THz [46].

This concept was then further developed by Shang *et al.* [47]. They proposed using two cascaded IMs with separate modulation drive frequencies. In this instance, the RF modulation frequency of the second modulator

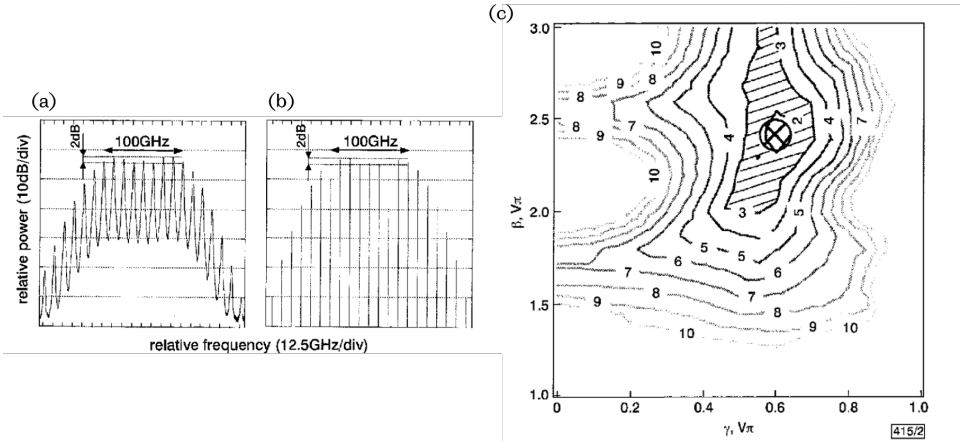

Figure 1.7: The OFC generated using an intensity and phase modulator in series, (a) experimental and (b) simulation. (c) Power deviation counter plot map, where Z is the combline variance for a nine-line OFC [45]. In this paper, they achieved the following key parameters: Comb flatness:2dB, comb FSR: 12.5GHz, bandwidth: 100GHz.

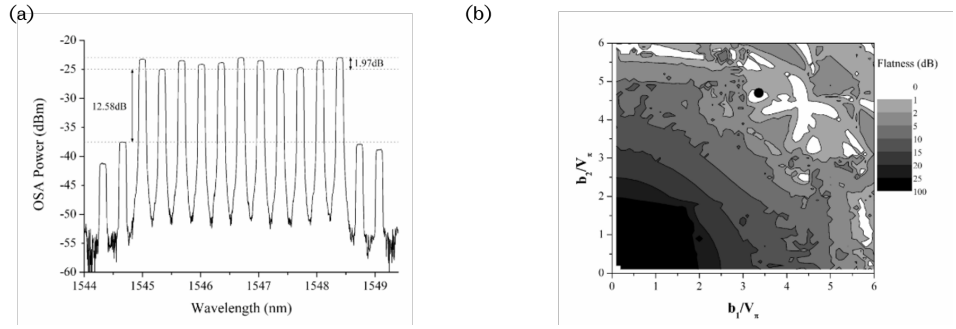

Figure 1.8: (a) The comb generated using two cascaded intensity modulators in series. (b) Power deviation counter plot map, where Z is the combline variance for an eleven-line OFC [46]. In this paper, they achieved the following key parameters: Comb flatness:¡2dB, comb FSR: 42.6GHz, bandwidth: 553GHz.

is one fifth of that of the first. The first modulator, once optimised, gives two comblines either side of the initial carrier frequency within 0.1db over 80GHz, hence producing five frequency components altogether, including the initial carrier. This signal feeds into the second modulator and each combline acts as a carrier. Given the lower modulation frequency, each combline produces two more comblines on each side. These are at an equal distance, hence generating 25 comblines over 80GHz with a variation of only 0.43dB. Simple schematics, using commercially available components, make this a very viable option for OFC generation. Other variations on this same theme have been developed using different types of modulators, for example cascaded polarisation modulators [48] and cascaded phase-only modulators [49].

In 2008, Torres-Company *et al.* [50] proposed a novel way of understanding the spectral flatness achieved by cascaded intensity and phase modulation. They proposed that a pulse in the time domain could be mirrored into the frequency domain via a process known as time to frequency (TTF) mapping [51]. TTF mapping was initially developed as a method to measure ultra-fast optical pulses [52].

A common analogy to understand this is the effects of diffraction and spatial lenses on a beam of light. It is equivalent to the effects of dispersion and time lenses on a pulse of light. A spatial lens causes a spatially varied phase shift and when combined with a diffractive material, it is possible to measure the different frequencies of light by their spatial properties. The same can be done with time. A temporal lens causes a time-varied phase shift and when combined with a dispersive material, the frequency components will be mapped in time and vice versa. This was developed further by Azana *et al.* [53] so that a single quadratic phase modulator could be used to map the time response of an ultra-fast pulse into the frequency domain. This was the idea behind Torres-Company *et al.*'s work [50], they used an electro-optic phase modulator to drive one arm of an MZI using a sinusoidal RF signal. With the proper choice of parameters this can generate a flat-topped pulsed output from a CW input laser, this same RF signal can then be used to induce quadratic phase modulation and produce a flat-topped OFC. So although OFCs from cascaded modulators have already been developed, by satisfying this condition the OFC's bandwidth and the number of comblines generated could be easily controlled, hence loosening up the stringent controls of each modulator.

From this understanding of TTF mapping to induce OFC generation, ensuring quadratic phase modulation for the time that the input pulse has a flat-top is paramount. This can be done by either reducing the temporal

duration of the flat-top [54] or by linearising the chirp of the RF signal at the PM using a tailored modulation waveform [55]. A method that harnessed both these attributes was adopted by Wu *et al.* [56]. They use two IMs to generate a very flat-topped pulse from a cosine RF modulation signal. This feeds into a PM, all with the same radio frequency modulation signal. The resulting comb is flat-topped with a controllable bandwidth. Since then, methods toward generating a flat-topped pulse from an IM using a sinusoidal modulating wave have been explored to increase the flatness and bandwidth of the comb [54, 57, 58].

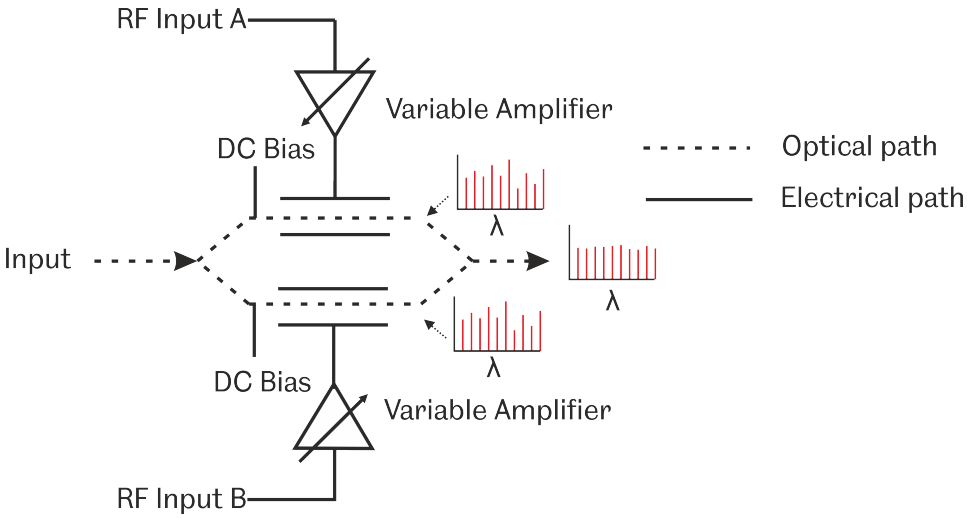

Figure 1.9: Schematic of a standard OFC generation method based on an MZM configuration using phase modulators

In the EO-based combs presented so far, each modulator has been cascaded in series. However, dual-driven Mach Zehnder modulators provide an alternative method to produce flat OFCs [59, 60, 61], which can be assumed to be parallel phase modulators. The overriding concept is that although a single phase modulator will produce an OFC with large power variation, when two are in parallel the spectra complement each other to produce a flat comb, as shown in Fig. 1.9. Using this scheme, similar results to cascaded IM-PM modulators are achieved but with a simpler architecture as only a single device is needed. This does come at a cost of driving power as twice the RF power is needed to achieve the same optical bandwidth [62]. Depending on the application of the OFC, either this method or the one discussed previously can be adopted.

Using intensity and phase modulation to generate an OFC is at the core of many research projects, including this one. This same method can be applied to nanoscale optical devices as will be discussed in section 1.5. By doing this, the concept of a multi-wavelength, on-chip source can be realised through nanoscale OFC generation. This will be discussed in more detail in chapter 3.

Super-continuum OFC generation via highly nonlinear waveguides

For many applications, octave spanning OFCs are imperative. Non-linear optical fibres can shrink the temporal duration of a pulse, thus broadening its spectrum via adiabatic soliton compression. The principle of this operation is that the energy and duration of a fundamental soliton pulse in a fibre is proportional to the group velocity dispersion (GVD) divided by the optical non-linearity. So by increasing non-linearity and decreasing the GVD while maintaining high phase coherence of the input pulse, an octave spanning OFC can be generated [63].

Phase coherence in MLLs is, by design, very high, which meant that early developments of highly engineered low-dispersion optical fibres could be harnessed [64]. These small core fibres confine light via two mechanisms, the first is by a refractive index difference between the core and the cladding. The second uses a photonic bandgap cladding, this enables much stronger light confinement than in standard fibres. The small area into which the light is confined with low loss gives access to optical non-linear phenomena, an example of which is given in Ref. [65]. When a high-intensity pulse is launched into highly non-linear fibres, the intensity is increased due to tight mode confinement and promotes non-linear effects, such as the Kerr effect. The Kerr effect will induce self-phase modulation of the input pulse through modulation of the fibre materials refractive index [66]. This, combined with anomalous dispersion in the fibre, causes spectral broadening via adiabatic soliton compression [19].

This same method cannot be used for modulation-based combs due to inherent modulation instability. Although modern EO modulators exhibit very low instability, it is nevertheless amplified exponentially when operating in the anomalous dispersion regime [68]. As stated earlier, the two factors contributing to continuum generation of a laser pulse are the optical non-linearity and the GVD. In this instance, the GVD must be kept in the normal regime to avoid amplified instability arising from modulation-based combs. Therefore, to generate sufficient broadening, very high power pulses are necessary to induce high optical non-linearity within the propagation

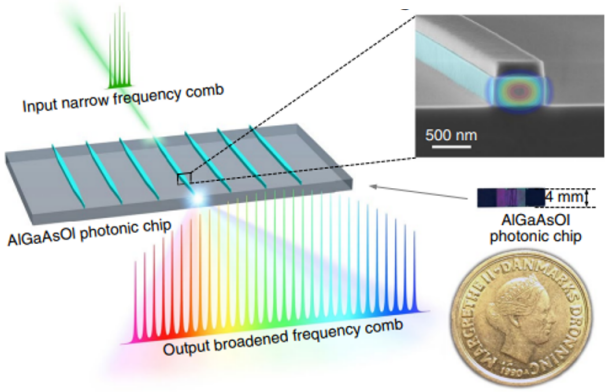

Figure 1.10: A narrow band frequency comb is broadened via self phase modulation by passing through a nano-waveguide. The inset shows a scanning electron microscope image with an artificially added fundamental TE mode [67]

medium. Although many examples of these were realised using optical fibre [69, 70], the real breakthroughs were made with photonic waveguides [71, 72]. The concept of waveguide-based supercontinuum generation is depicted in Fig 1.10. These had the advantage of not only confining light into an even smaller area, hence increasing the light/matter interactions, but also the added advantage of high versatility compared to optical fibres. Lithographic fabrication techniques mean that a high order of controllability can be realised. Tailored waveguides, specific to wavelength and application, mean that they are rapidly gaining popularity.

The low optical powers necessary to induce optical non-linearities are why modulation-based combs benefitted so much. Combs from MLLs have far greater power than EO or Kerr combs, which means they can easily reach high enough powers that optical non-linearity can take place in an optical fibre. For the other cases, an optical amplifier is needed to achieve high enough power. This is where photonic waveguides and nanowires are very beneficial [73]. By using waveguides, the amount of optical energy needed to generate optical non-linearity can be less than 200pJ [73]. Another attractive element is the scope for on-chip integration of such sources. This has led to developments in both silicon [74] and silicon nitride [72] in recent years, which gives a degree of CMOS compatibility. While an OFC cannot

be produced solely from a single nanophotonic waveguide, their ability to broaden an OFC over multiple octaves with very small device footprints makes them a very attractive area for future photonic networks [32].

1.1.4 Comparison of OFC generation types

Throughout this section, different OFC generation schemes have been outlined. Although slight variations and progressions have been made which enhance device performance, for example through supercontinuum generation, the three main generation types outlined here are MLLs, micro-combs and modulators. Table 1.1 shows some general OFC characteristics that can be used for comparison between these types. The parameters listed for each type give very general values and there are always exceptions to each type. The ubiquitous nature of OFCs means that different generation types will lend themselves better to certain specific applications. A number of typical applications are given in the table; however, each generation type is not limited to the applications given.

MLLs were one of the original methods to generate an OFC. The key mechanism of locking a large number of modes together enables perfect phase stabilisation and the generation of ultra-short pulses. They find application in optical atomic clocks and metrology. Kerr frequency combs based on micro-toroidal cavities offer unprecedented on-chip integration capabilities given their small device size and relatively simple operation. They are often used in the generation of microwave photonic signals and in spectroscopy. OFC generation based on the modulation of a carrier light is the only type where the FSR of the generated OFC is tunable. Again, their relatively simple operation means that OFCs can be generated using standard optical table components. Applications of modulation-based OFCs are commonly found in optical communications and microwave photonic signal processing.

1.2 Modulation-based OFC applications

1.2.1 Microwave photonics

A strong argument for the implementation of modulator-based combs, for example EO combs, is their use in microwave photonics. Microwave photonics is an emerging research field that uses photonic devices to generate, manipulate and communicate microwave signals in the optical frequency domain [5]. By upconverting microwave signal into the optical domain, the available processing bandwidth becomes almost abundant; microwave signalling

Table 1.1: Typical OFC characteristics for MLL, Kerr combs and modulation-based comb generation

	MLL	**Kerr comb**	**Modulation-based**	**Proposed nano-comb**
FSR	100s MHz [15]	100s GHz [8]	10s GHz [58]	10s GHz [75]
Number of Comb-lines	10,000s [76]	100s [77]	10s [46]	10s
λ	NIR-IR	NIR	NIR [48]	NIR
Applic.	Optical clocks and metrology [13]	Microwave generation and spectroscopy [32]	AWG, optical communications, RF signal processing [40]	Nanoscale RF signal processing, WDM and chip scale optical interconnects [78]
Adv.	Femtosecond pulse generation	On-chip integration	Tunable mode spacing	Dense on-chip integration and tunable mode spacing
Disadv.	Large size	Difficult to obtain small FSR	Limited number of comblines	Low-yield fabrication techniques required
Material	Ti:sapphire	SiN	LiNbO	InP

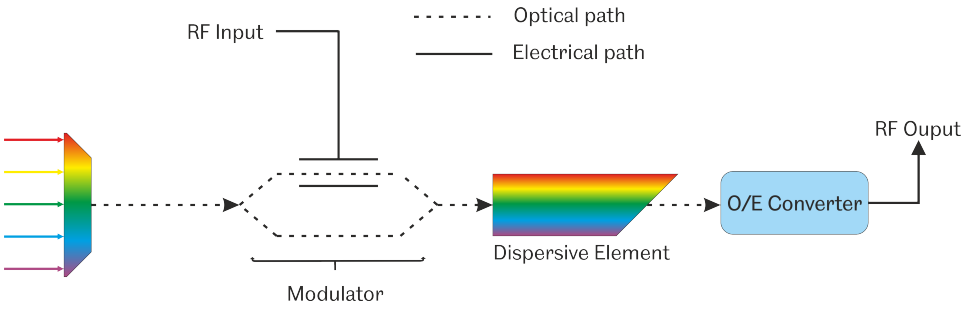

Figure 1.11: A schematic example for how a microwave photonic filter can work

stretches across 300GHz whereas the optical domain can stretch across multiple terahertz. The delivery of microwave photonic systems, which offer multitudes of fast communication capabilities [79], requires the dense integration of coherent light sources [80]. One potential solution is to use multi-wavelength sources, such as optical frequency combs (OFCs). In microwave photonics, OFCs are used in a variety of other ways as well. For example, generating microwave signals through the heterodyne beat note, filtering via optical delay lines [81] and photonic downsampling [82].

By sending microwave signals down optical fibres, instead of coaxial cables, the attenuation and weight benefits are astounding. In a typical fibre optic cable the weight and attenuation per kilometre is around 1.7kg and 0.5dB respectively, compared to 567kg and 360dB for a coaxial cable! The application of optical fibre has the potential to revolutionise wireless communication technology as well as military radar systems and radio astronomy. These applications require a microwave photonic link that can preserve linearity across the spectrum and minimise the noise introduced when attaining and processing the signal, this is no easy task and has been the subject of many research efforts. The operation of a microwave photonic link requires the transfer the RF signal onto the sideband of an optical carrier via an electro-optical converter. The signal can then either be transmitted over long distances or undergo a variety of optical processing techniques. It is here that microwave engineering really benefits from OFC generation. OFCs provide the capability to generate a programmable microwave filter with bandwidths that can span over several gigahertz.

An OFC-based microwave photonic filter is based on the theory of frequency dispersion in an optical waveguide or fibre. Figure 1.11 shows the generalised operation of this type of filter. An OFC acts as a multi-carrier

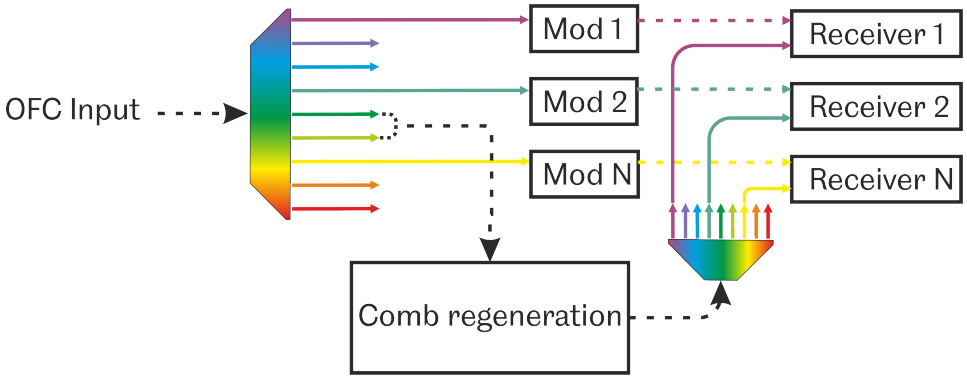

Figure 1.12: A schematic example for how comb regeneration can be used to demodulate a WDM signal. Similar schemes can be found in [84].

source which is then modulated by the RF source to be filtered. This is sent through a dispersive element, such as a waveguide or fibre, and detected by an ultra-fast photodiode. Light at each frequency will travel at different speeds through the dispersive medium. The current generated by the photodiode will be the summation of each optical carrier and its sideband combined, as long as the difference between two consecutive optical carriers is larger than the photodiode's bandwidth. The summation of these dispersed signals produces a finite impulse response type filter [83]. This approach offers a large amount of control over the filter characteristics because these are determined by the OFC and dispersion parameters.

1.2.2 Telecommunications

As stated earlier, modulation-based comb generation has the capability to generate a broad range of coherent, homogeneous combines with a reconfigurable line spacing. This has major advantages for telecommunication, where wavelength division multiplexing (WDM) can be used to encode data onto each combline [84]. WDM was originally implemented using an array of lasers with different frequencies. Data is encoded onto each laser, thus generating parallel data transmission through a single fibre. This system could essentially be crowned as the backbone of the modern internet. Current state-of-the-art systems consist of hundreds of wavelengths down a single core fibre, requiring large stacks of laser sources [85].

Two figures of merit for an OFC as a WDM source are important, the first is the linewidth of the combines and the second is the signal to

noise ratio of the comb and the attainable noise floor. For this application, modulation-based OFC generation supersedes MLLs and micro-combs. In order to be utilised in WDM, a comb source with mode spacing of between 10 and 100GHz is needed. As has been discussed earlier, micro-combs struggle to produce efficient comb generation with an FSR in the tens of gigahertz due to the parametric gain threshold growing exponentially with cavity size. MLLs suffer a similar fate in that the round trip gain for an MLL at such high pulse frequencies would be difficult to maintain. Modulation-based OFCs offer a flat spectral envelope, narrow optical linewidths ($<$ 100KHz), controllable spacing ($<$ 100GHz) and compatibility with fibre optic components. Another attractive feature is the ease at which carriers can be locked to an absolute frequency via control of the absolute carrier frequency and the repetition frequency of the optical pump pulse. Given the large number of comblines needed, continuum generation via highly non-linear fibres is used in conjunction with modulation-based combs. This can generate over 1000 carrier-locked comblines that can be encoded individually for WDM [24].

In terms of receiving the signal from a WDM system, we refer back once again to detection of the heterodyne beatnote using a photodiode. In a coherent WDM system, the RF signal can be detected by the beatnote between the original signal and the modulated signal. Although this can be done using a single local oscillator laser acting as the reference, it is limited by the bandwidth of the photodetectors and the analogue to digital converters [85]. An alternative is to regenerate the transmitter comb and use it at the receiver side. Two unmodulated comblines are sent to the receiver end of the system; from these two lines the phase and frequency information can be extracted and extrapolated. This information can be used to regenerate the same OFC with identical parameters to the one used as the WDM source, as shown in fig. 1.12.

1.3 Photonic Crystals

1.3.1 Fundamentals

A common analogy to describe the operation of photonic crystals is the theory of electron bandgaps in semiconductor materials. Electrons propagate as waves so when a material has a periodic potential, specific waves cannot propagate through the material. This means that electrons with certain energies cannot propagate in certain directions. With a strong enough lattice potential, energy cannot propagate in certain directions through the

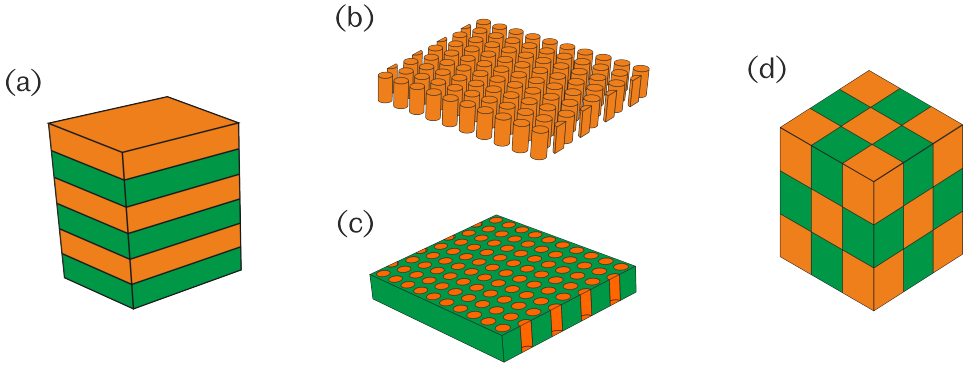

Figure 1.13: Examples of photonic crystals with photonic bandgaps in (a) one dimension (b-c) two dimensions and (d) three dimensions. The examples show here are commonly found in the literature, similar schemes can be found in [88].

material, hence creating a complete bandgap. This is engineered in semiconductor materials, providing a complete bandgap between the valence and conduction band. Photons propagate as waves with a far greater wavelength than electrons. This means that the periodicity of the potential of the semiconducting material will not affect the propagation of a light wave. However, the same theory can be adapted by periodically modulating the dielectric constant of a material through which light propagates. When the dielectric constants of the structure are sufficiently different, and absorption of light in the material is minimal, photons can be prevented from propagating in specific directions, hence creating a *photonic* bandgap. This concept, developed independently by two research groups in 1987 [86, 87], led to the entirely new and vastly investigated research field of photonic crystals.

The periodic structure can be extended in one, two or three directions, as shown in Fig 1.13. A one-dimensional periodic structure will stop the propagation of light in a specific direction at a specific wavelength, illustrated by Fig, 1.13(a). This concept has been around for many years and forms the basis for Bragg reflectors, which are commonly used in many aspects of laser engineering. These 1D PhCs have many uses, however any deviation of the light from normal or near normal incidence and the photonic bandgap properties are lost.

Three-dimensional periodic structures, Fig. 1.13(d), can generate a truly complete photonic bandgap, giving a frequency range in which no electromagnetic states can propagate in any direction [89]. Although these do

provide an unprecedented capability to localise light through a defect in the periodicity, they prove difficult to fabricate. Different approaches have been investigated thoroughly including drilling [89], woodpiling [90] and self-assembly [91]. These processes are complex and costly to develop when compared to the fabrication of two dimensional PhC structures. This has hindered research into 3D PhCs for photonic integration.

Two dimensional PhC structures have hitherto prevailed as the most useful structures for photonic integrated circuits [92]. Their planar operation means various devices can be integrated together and the light can couple in and out of the circuit. There are two typical structures, one is made up of holes in a membrane material where refractive index contrast between the membrane and the holes is high, as shown in Fig. 1.13(c). The other is made of up high refractive index material pillars surrounded by air, shown in Fig. 1.13(b). In both cases, modes with frequencies inside the photonic bandgap cannot exist. The number of modes per unit frequency and unit volume, known as the *density of states*, is zero.

The photonic bandgap exists in the x-y plane but light can propagate in the z direction. To stop propagation in the Z direction, the PhC structure is surrounded by a lower refractive index material. Throughout this work, the focus will be on 2D PhC membrane structures where the structure is surrounded by air. This will not create any photonic bandgap in the z direction but the refractive index contrast will keep losses to a minimum in the z direction.

The 2D PhCs are mirror-symmetric in every perpendicular plane. This leads to electromagnetic waves that either polarise in-plane to the electric field, known as transverse electric (TE), or out-of-plane to the electric field, transverse magnetic (TM). Hole-based PhCs lend themselves to stronger TE-like bandgaps and pillars to TM-like bandgaps due to the continuity of electric field lines in holes-based structures [88]. Furthermore, triangular lattices give larger bandgaps for TE modes than square lattices [88], so this work will solely focus on triangular lattice-based membrane PhCs, as shown in Fig. 1.14(a) to ensure large bandgaps for TE polarised modes.

Figure 1.14(a) shows the dimensional parameters of the triangular lattice as well as the two main symmetry directions in real space ΓK and ΓM. Figure 1.14(b) shows the hexagonal Brillouin zone in reciprocal space with the two symmetry directions represented by the dotted line. Within this triangle is the irreducible Brillouin zone, it is only 1 twelfth of the total zone due to the six-fold rotational symmetry. By calculating a set of wave vectors along the path ΓMKΓ, the edge of the irreducible Brillouin zone, the photonic band structure of the crystal can be found. By using the MPB open-source

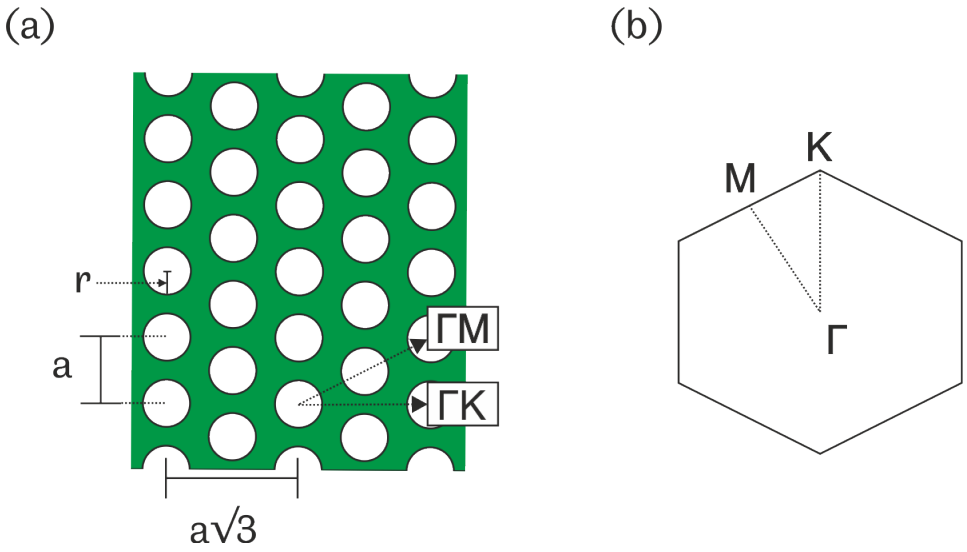

Figure 1.14: A two-dimensional photonic crystal triangular lattice in (a) real and (b) reciprocal space. ΓM and ΓK are the two main lines of symmetry, a and r are the crystal parameters. The irreducible Brillouin zone is within the dotted lines, between M and K.

software package for electromagnetic simulation, the wave vectors for the first four eigenfrequencies are calculated and shown in Fig. 1.15. In this example, the lattice constant, a, is set to 480 nm, the ratio of r/a is 0.3 and the refractive index of the membrane material is set to 3.25. The shaded region represents the photonic bandgap of the crystal. In this region no TE polarised EM modes are available. To quantify the different bands, they are named the dielectric band, which lies just below the bandgap, and the air band, which lies just above. They signify where the electric field is localised: either mainly in the dielectric material or the air holes. In chapter 4, further analysis of these bandgaps will be undertaken along with experimental realisation.

The ratio of hole radius, r, to lattice constant, a and the index contrast between the holes and the membrane can be tuned to increase the photonic bandgap. A very low r/a will produce a thin bandgap which increases linearly with the r/a ratio. However, as r increases, the structure induces higher loss rates due to the reduction in guiding material. Also, with large hole sizes come difficulties in fabrication as the features between holes become very small. A trade-off therefore exists between the bandgap

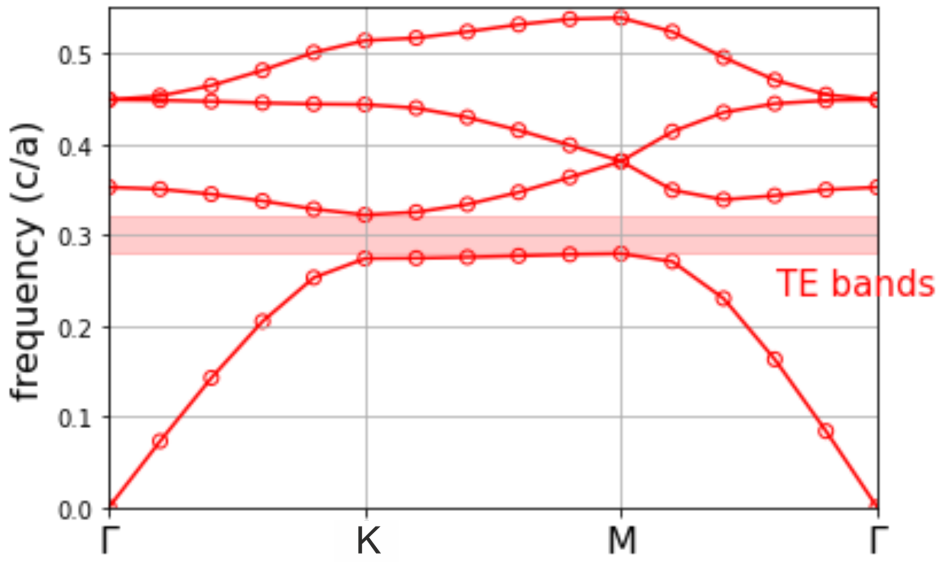

Figure 1.15: Using the MPB open-source software package for electromagnetic simulation, the wave vectors for the first four eigenfrequencies are calculated and shown for TE polarised light.

size and practical limitations. The frequency of the bandgap is dependent on the effective refractive index of the structure as a whole. By increasing the amount of air in the structure, i.e. increasing r/a, the central bandgap frequency will increase. Therefore, the size and location of the bandgap is dependent on the hole size, r, the lattice constant, a, and the refractive index of the material when considering a purely 2D structure.

By removing a single hole, a point defect is created and given that the translational symmetry is broken, the photonic band structure will no longer exist in this region. There will be a peak in the crystal's density of states at a certain frequency which is confined to this region. When this peak lies within the photonic bandgap of the surrounding PhC lattice, the mode will be completely confined to this area. This creates a photonic cavity that is effectively surrounded by mirrors in the x-y plane. Many cavity configurations exist, as shown in Fig. 1.16(a)-(c). Important qualities to any optical cavity are the mode volume, V, and Q factor Q, a measure of the number of oscillations of a mode within a cavity before it dissipates. A high ratio of Q/V will strengthen the light-matter interaction and enable a variety of non-linear optical properties. The smallest type of cavity can be obtained by slightly adjusting two of the holes in the lattice, named an H0, Fig. 1.16(a). The ultra-small volume means that very high optical non-linearities can be generated [93], however achieving high Q is difficult. They also benefit from fast free carrier diffusion, which will be discussed in detail in the next section. Single and multiple point defects, as shown in Fig. 1.16(b) and (c) respectively, also generate photonic cavities. Using multi-point defects and displacing the holes either side of the cavity results in ultra-high Q cavities [94], various different structures have been shown to produce ultra-high Q factors. Another famous example was proposed by Kuramochi *et. al* [95]. In this case, the cavity is formed as part of a waveguide, where holes either side of a specific point in the waveguide are displaced. This causes a local width modulation of the line defect and thus the confinement of light at this point.

This same technique of removing holes from a PhC membrane can be employed to generate a photonic waveguide, as shown in Fig. 1.16(d). Light that falls within the photonic bandgap of the PhC will then propagate along its transverse axis of the waveguide. PhC waveguides and cavities have seen tremendous research activity that has generated splitters, filters, switches and many more devices with overall sizes on the micron scale.

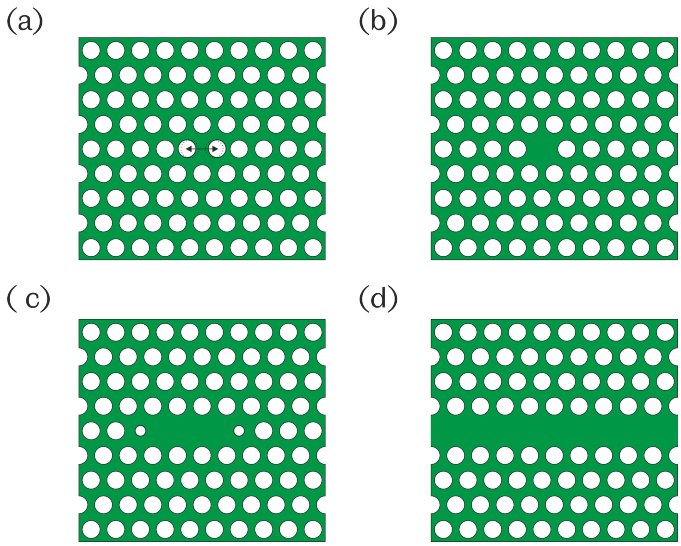

Figure 1.16: Examples of cavities and waveguides in 2D PhCs. (a) H0 cavity [96], (b)H1 cavity [97], (c) L3 cavity [94] and (d) W1 waveguide [98].

1.3.2 All-optical modulation in PhCs

With the fundamental principles behind photonic crystal waveguides and cavities explained, further analysis of how they are used for all-optical modulation can be detailed. The general structure for a cavity-waveguide based modulator is given by Fig. 1.17. It consists of an input waveguide coupled to a cavity which has the ability to trap a discrete set of eigenmodes that oscillate at specific eigenfrequencies. The energy in these modes will decay via various channels, namely scattering into radiative modes, material absorption and coupling into the adjacent waveguides. In this simplified structure, the decay rate from *waveguide 1* into the cavity and from the cavity into *waveguide 2* is denoted by γ_c and all other loss channels are denoted by γ_{loss}.

Light that enters through *waveguide 1* can couple into the cavity when the frequency of the input light matches an eigenfrequency of the cavity. By assuming that there is no coupling between the two waveguides directly, $u = 0$, light will only be able to pass through into *waveguide 2* at the eigenfrequency of the cavity. In this sense, the overall device can be thought of as a bandpass optical filter. The wavelength and bandwidth of this filter are defined by the optical properties of the cavity. By altering these properties, it is possible to shift the frequency of the eigenmodes. This generates a mod-

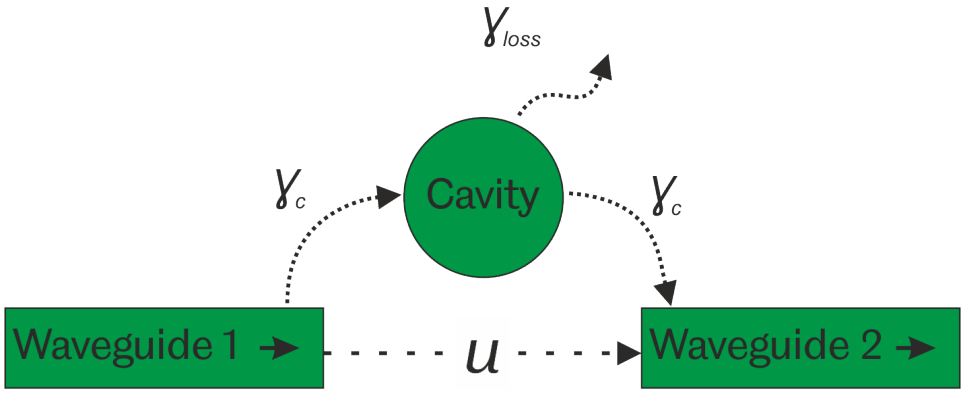

Figure 1.17: Generic scheme for a cavity-waveguide structure, γ_c is the coupling between the waveguide and the cavity, γ_{loss} overall loss coefficient and u is the scattering directly between waveguides.

ulation mechanism where the transmission of light at a specific wavelength can be controlled via the cavity's optical properties. There are various ways of controlling this medium including thermal [99], electrical [100] and optical [10].

Throughout this project the method to control the eigenfrequencies of the cavity is through optical pumping of the cavity itself. Light with sufficient power will induce non-linear optical properties within the cavity. This results in a refractive index shift of the cavity material and thus its eigenfrequencies. The type of non-linear refractive index phenomena used to alter the properties of the cavity can be varied depending on the application.

A standard scheme for all-optical modulators based on optical non-linearities in PhC cavities is shown in Fig. 1.18. Enhanced thermo-optical non-linearity can be utilised to realise all-optical switching in PhCs [99]. However, the relatively long timescale (on the order of micro-seconds) over which the refractive index changes due to the thermal relaxation times restricts modulation speeds. To increase modulation speeds, the Kerr effect and carrier induced non-linearities can be used to change the refractive index of the material. There are several ways in which the generation of free carriers in the cavity causes a change in the refractive index [101]. Free carrier absorption, otherwise known as the *plasma effect*, is common for PhC-based all-optical switches [93, 102, 103]. In this method, free carriers absorb a photon and move to a higher energy state within a band. This changes the absorption characteristics of the material and hence the refractive index [101]. Therefore, an increase free carrier density will lead to a decrease in

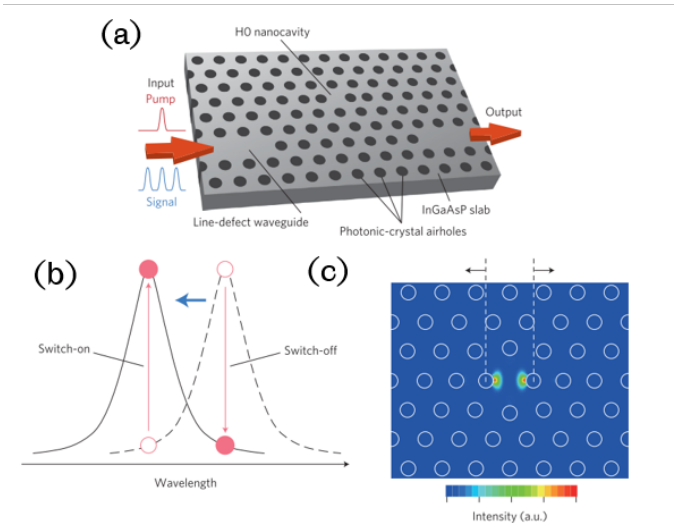

Figure 1.18: Schematic showing the general operation of a PhC-based all-optical switch. (a) A schematic of two waveguides coupled to a H0 cavity. (b) The principle operation, a pumped cavity causes a carrier induced resonant wavelength shift. (c) Electric field of an isolated H0 cavity. Annotated from [104].

the effective refractive index of the cavity, hence blue shifting the cavity resonance. This plasma effect is directly proportional to the concentration of free carriers and the square of the wavelength.

Another technique to generate ultra-low switching powers in PhC switches is to use carrier induced *bandfilling*. Bandfilling generates interesting optical properties due to the fact that the electrons must occupy a range of energies within the conduction band. If parabolic bands are assumed, then the bandgap will vary as the density of states in the conduction band are filled. This results in strong absorption near the band edge but weakening as the excitation wavelength increases. For this reason, the cavity resonance must be close to the band edge of the cavity material. Therefore, with careful design of the material and cavity, ultra-low switching energies can be realised.

The switching speed of any carrier-induced refractive index modulation is dependent on the carrier lifetime. This is relatively large for bulk semiconductor materials. However, this is dramatically reduced in PhC cavities because photon-generated carriers diffuse quickly from the cavity itself.

In the examples so far, carrier induced non-linearity has been exploited.

Another method is to use the Kerr effect. The Optical Kerr effect is a non-linear response that instantaneously changes the refractive index of a material through the electric field of a light wave, such that:

$$\Delta n = n_2 E^2 \lambda \tag{1.11}$$

where n is the refractive index, n_2 is the non-linear index, or *Kerr* constant and E is the intensity of the electric field. The refractive index change occurs on a much faster time scale than carrier-based modulation and creates a red shift of the cavity resonance.

The benefit of Kerr-based refractive index changes is that they do not depend on carrier recombination so the switching speeds can be down to the femtosecond range. The shift generated is the opposite to carrier-based schemes which means the cavity resonance experiences a red shift. The disadvantage of using the optical Kerr effect is that far higher optical powers are needed to induce a refractive index change comparable with carrier-induced effects. The power needed in Kerr-based modulation is far greater than carrier-based modulation. The frequency of the excitation light must therefore be less than half the band gap to ensure it is the dominant process. If the frequency of the light is between 0.5 and 0.69 of the bandgap energy [105] then two photon absorption will cause the generation of free carriers. The blue shift from the carriers will cancel out the red shift from the Kerr effect by a large amount.

The first studies to generate all-optical 2D photonic crystal switches in waveguide-cavity type schemes were based on silicon [103]. This report showed low power consumption at less than 10fJ per bit. This was attributed to the large ratio of Q/V of the PhC cavity. They also reported switching speeds of down to between 50 and 300ps which indicated the speed was not limited by the carrier recombination time of bulk silicon. Prompted by this work, many groups went on to report all-optical switching in both silicon and III/V materials. To reduce the switching times further, ion-implanted silicon was used to introduce non-radiative recombination centres. Switching speeds decreased from 110ps to 50ps [106].

In 2009, H0 cavities in both GaAs and InGaAsP [107] produced low energy switching due to the small cavity size and strong optical non-linearity in III-V materials compared to silicon. A year later, with careful choice of cavity and material properties, sub femtojoule switching powers were realised [10]. In this case, band filling was utilised, as discussed earlier. An InGaAsP composite with a bandedge wavelength of 1470nm and a cavity resonant wavelength at 1550nm ensured very low switching powers. Efforts

to understand the non-linear switching dynamics of an InP-based all-optical switch followed [108, 109, 110]. By understanding how the energy of the pump light affects the switching dynamics, the system can be optimised.

However, there exists a point where the drawbacks of carrier lifetime reduction out-weigh the benefits of ultra-short pulse switching. The refractive index shift Δn is due to the effective carrier population N_{eff} in the cavity. The carrier population builds up by this simple rate equation:

$$N_{eff} = \frac{-N_{eff}}{\tau_{carr} + G(t)} \tag{1.12}$$

where *G(t)* is the duration of the excitation pulse, when τ_{carr} is smaller than *G(t)* the modulation of the cavity becomes weak, leading to poor modulation depth [93, 111]. So a trade-off exists between switching speed and modulation depth. Tailored carrier dynamics could therefore lead to optimised all-optical switches [111, 112].

1.3.3 Integration of PhC cavities and waveguides

With the realisation of all-optical PhC switches, efforts have advanced in the area of large scale integration of photonic crystal devices. By doing this, sophisticated photonic networks can be fully integrated onto a photonic crystal chip [92, 113]. Photonic networks require a variety of functions that must be integrated together, these include wavelength division multiplexers, switches, routers and many more. To this end, PhC devices offer unique capabilities in terms of the high Q/V ratio which induce enhanced light/matter interactions [114].

Wavelength addressable integrated optical memories via PhC cavities and waveguides have been demonstrated using the scheme shown in Fig. 1.19[92]. In this scheme, each L3 cavity has a different resonance, as depicted by the highlighting colour. The cavities are coupled to a common 'bus' waveguide comprised of a line defect. In this configuration each memory bit, spaced in the frequency domain, can be independently modulated by its coupling to a specific cavity. This has been demonstrated using both silicon [115] and InP [92]. There have also been many theoretical studies on cavity-waveguide configurations for complex circuit designs [116, 117, 118]. PhC cavity-waveguide structures have also seen developments in microwave photonics. As has been discussed, PhC cavities offer very narrow linewidths and when coupled to a cavity they can act as a filter for the cavity resonant wavelength.

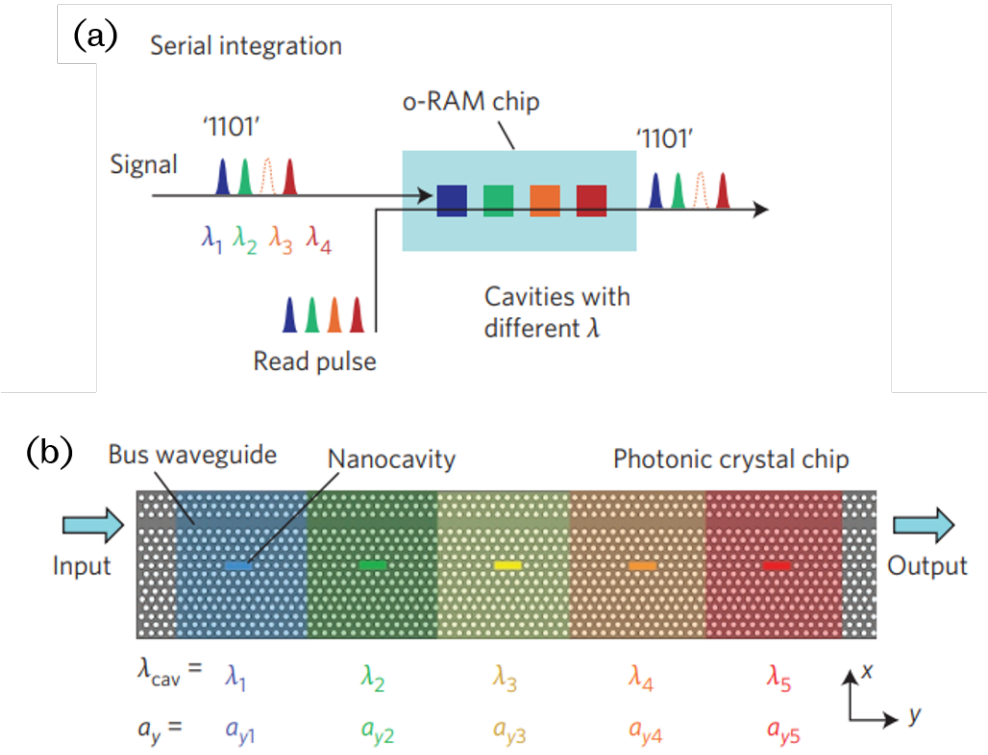

Figure 1.19: Design of integrated optical memory arrays (a) Serial integration example (b) Proposed design based on PhC waveguides and cavities. Annotated from [92]

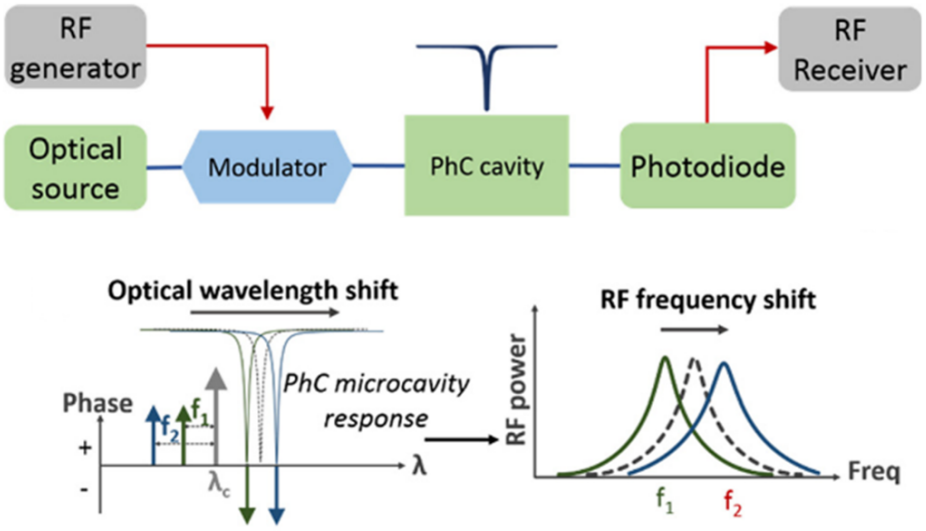

Figure 1.20: Scheme for integrating a microwave photonic filter using a PhC cavity-waveguide system. Annotated from [119].

In microwave photonics, an electric microwave signal can be upconverted into the optical domain via phase modulation. This will generate sidebands in the optical carrier spectrum which are out of phase. As a consequence, when the signal is directly detected by a photodiode, the RF signal cannot be obtained due the phase mismatch of the two sidebands. To overcome this, a bandpass notch filter can be used to cancel out one of the two sidebands meaning that the carrier and one sideband can generate the microwave signal. Although a common scheme in microwave photonics, it was not realised in a PhC cavity-waveguide scheme until recently [119, 120]. Figure 1.20 shows the scheme demonstrated by Long *et al.* [119], the resonance of the cavity is red-shifted away from the carrier wavelength. It shifts further with higher optical input power due to non-linear processes, as discussed earlier in the text. Therefore, the wavelength of the sideband to be attenuated can be tuned by the input power. The narrow linewidth of the cavity means that even low modulation frequencies, down to 4.5 GHz, can be attenuated without degrading the carrier signal. The benefits here are the potential integration possibilities and the tunability of the cavity's resonance with optical input power.

In section 1.2, a popular method for filtering a microwave photonic signals was discussed. Delayed replicas of the microwave photonic signal with

differing intensities are combined to give a finite impulse response type filter [83]. This same method was achieved using PhC waveguides as the delay line and a multi-wavelength modulation source [81]. The delay in PhC waveguides is due to the highly dispersive nature of light confined by a photonic bandgap [121]. A slight change in the effective refractive index of the waveguide modifies the group velocity dispersion (GVD). Therefore the delay can be tuned by controlling the refractive index of the waveguide, this has been demonstrated using both thermo-optic effects in silicon [122] and by lithographic tuning of the holes either side of the waveguide [81]. This structure offers very large operating bandwidths, low power consumption and the potential for on-chip integration with very low device dimensions.

In 2017, Yu *et al.* [123] integrated a cavity and waveguide structure to demonstrate a self pulsing PhC nanolaser. They use Fano interference between a continuum of waveguide modes and the discrete resonance of a nanocavity to act as a mirror within an ultra-small laser. In this system, the laser cavity is made up of a PhC waveguide which has a broadband mirror at one end of the waveguide and a narrow band mirror at the other. The narrow band mirror consists of a side-coupled cavity where the interference between the waveguide and the cavity causes high reflectivity at resonance. With high power CW optical pumping, the interference between the cavity and the waveguide cause a train of self-sustained optical pulses at the output of the device.

1.4 Quantum dots in photonic devices

A quantum dot (QD) is a physically confined semiconductor material with dimensions on the same order as the de Broglie wavelength. The energy of the dot is confined by a surrounding semiconductor material with a wider bandgap. These spatial and energetic confinements lead to complete quantisation of the energy spectrum of a confined carrier. This is illustrated in Fig. 1.21, which shows the band structure for InAs QDs embedded in InP. The bandgap of the InAs QDs is lower than the InP, meaning that the emission wavelength will be longer than the surrounding InP. This increased isolation of electrons/holes from its surrounding environment is the most widely exploited property of the QD. QDs have enhanced many research fields including solar cells, QD displays, telecommunications and quantum information, to name just a few! The bandgap of the QD can be controlled by the material used, the size of the dot, the material it is grown on and the doping levels [124].

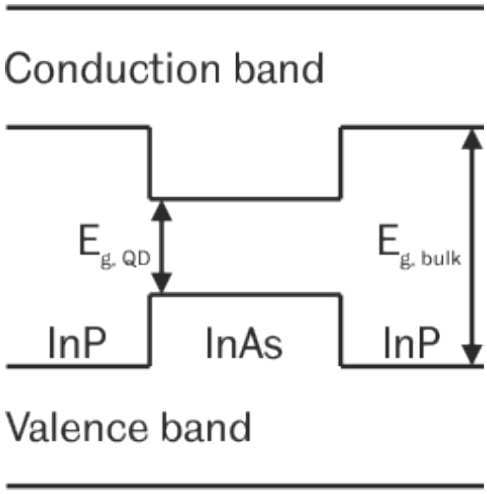

Figure 1.21: Band diagram for InP with an embedded InAs QD

1.4.1 Quantum dots in photonic crystals

Various semiconductor light sources can be embedded into PhC devices including quantum wells (QWs) and dots (QDs). Although QWs have seen a vast amount of applications in PhC devices [125, 126, 127], QDs offer smaller absorption and reduced surface recombination which leads to higher attainable Q factors. In this section, the use of QDs in PhCs is discussed to give the reader relevant information regarding chapters 4 and 5.

Embedded QDs can be used as active emitters in photonic crystal cavities [128, 129]. High density QDs can exhibit broad spectral emission due to inhomogeneous broadening during growth. They also are highly efficient in the capture of photo-excited carriers and exhibit negligible re-absorption [130]. These properties led to the realisation of photonic crystal nanolasers where QDs acted as the gain material [131, 132, 129]. In the experimental part of this thesis, QDs are embedded in the PhC membrane and used as active emitters to characterise the mode structures of the cavities and realise the generation of optical sidebands through fast modulation.

1.4.2 All-optical switching devices based on QDs

Photonic devices which utilise QDs to enable all-optical switching are posed to play an integral role in the future of PIC technology [9]. Various optical nonlinearities have been harnessed to induce switching. A common concept is to use the absorption characteristics of QDs. This was demonstrated

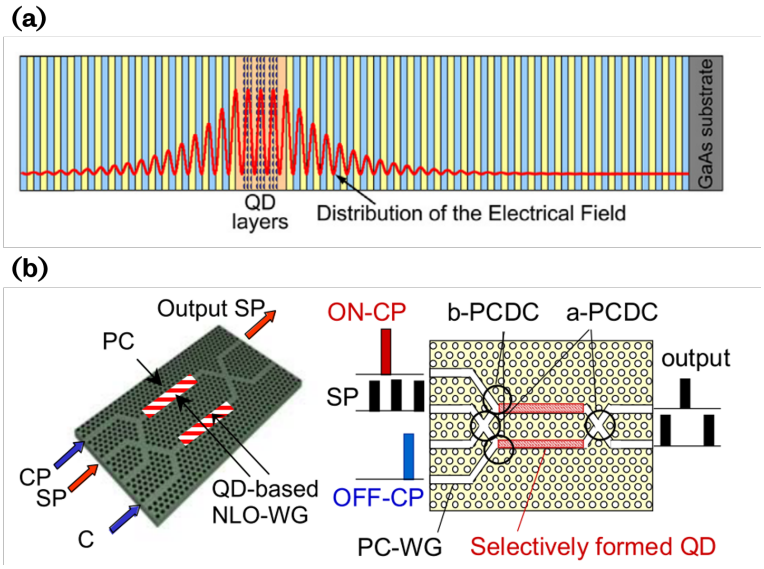

Figure 1.22: QD switch based on QD absorption in (a) a vertical cavity [9] (b) a photonic crystal waveguide [135]

in [9] with a reflection-type optical switch using QDs in a vertical cavity. Strong optical pumping at cavity resonance causes the QDs in the cavity to saturate, an example structure is shown in Fig. 1.22(a). In doing so, the zero reflectivity condition is violated and a switching mechanism based on reflectivity of the laser at cavity resonance is induced. Using this method a switching time of 20ps and a saturation power of 2.5fJ cm^{-2} has been demonstrated.

The saturation of a single QD has also been demonstrated to realise all-optical switching. In one example of this scheme, the coupling between the absorbed single photon in the cavity and the single QD causes a split in the atomic transition. This blocks photons being absorbed at that same energy level. The *blocking* of a photon has been used as a representative of single photon nonlinearities in semiconductor nanostructures by many researchers using a range of devices including vertical pillars [133] and PhCs [134].

Another common method to utilise QDs in an all-optical switch is to take advantage of the phase shift induced with the change in absorption characteristics of the QDs. Although initially proposed in a ridge waveguide structure [136], the high field enhancement and slow light effect in PhC waveguides quickly superseded ridge waveguides for this operation. In the

scheme based on PhC waveguides [135], a MZI-type structure is employed, as shown in Fig. 1.22(b). A control pulse induces saturable absorption of the assembled QDs within one arm of the MZI. This absorption is directly related to a change in the refractive index of the waveguide through the Kramers-Kronig relation. A signal pulse, which is detuned from the control pulse, then experiences the corresponding refractive index change, hence changing its phase through one arm of the MZI. When the signal pulse from each arm is interleaved, the interference will cause the signal pulse to 'switch' on and off. A similar concept has been demonstrated in a vertical cavity-type structure [137]. In this work, the QD absorption is changed by a control light to a value still within the broadened absorption spectra of the QD ensemble. A signal light, detuned from the control light, will experience an appreciable refractive index change in the QD layer. This will shift the phase of the signal light when it transmits through the device.

1.5 Fast modulation of optical nanostructures

In section 1.1 methods for generating OFCs have been discussed with particular emphasis on modulation-based schemes. The ability to modulate light through photonic crystal structures was discussed in section 1.3. In this section, an overview of research that relates to the combination of these subjects will be reviewed. Specific research on OFC generation from PhCs is very limited so it will also include modulation of nanostructures to generate sidebands, which is a very closely related field.

In 2014 Li *et al.* [139] developed a model for the generation of high-order sidebands through the strong coupling of a QD to PhC cavity. In their model they assume a single QD is strongly coupled to a cavity which in turn couples to a waveguide. In this scheme, a bichromatic driving field propagates through the waveguide. The field is made up of two lasers of differing frequencies. The field will couple to the cavity from the waveguide and, as there is strong coupling to the QD, this field will excite the QD. As shown by Fig. 1.2, when two frequencies are combined, field amplitude fluctuation exists at a rate inversely proportional to the frequency difference. Therefore, the QD is amplitude modulated by the bichromatic field. At low field intensities, the QD does not exhibit non-linear properties and follows normal optical behaviour. This leads a to standard amplitude modulated frequency response that follows a Bessel function. However, when the power is increased, optical non-linearity is enhanced by the QDs and many high-order sidebands are generated, hence producing an OFC. Li *et al.* have

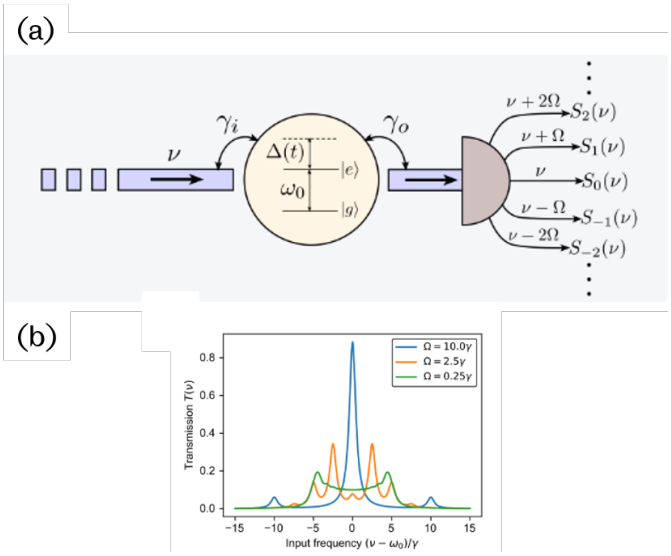

Figure 1.23: The scheme used to generate sidebands from a single quantum emitter using fast modulation techniques. Annotated from [138]

extended this model for similar single atom systems [140, 141]. Other groups have proposed similar concepts of fast modulation of a two level quantum emitter which is confined to a bandgap environment, such as a PhC. They showed that the emission spectrum varied with modulation speed, generating control over the radiative processes from a single quantum emitter [142, 143].

Only very recently has a paper been published that proves these concepts experimentally [138]. In this paper, the spectral control of single photon emission is achieved by rapidly modulating an optical two level system (TLS). The general schematic of single photon scattering from a modulated TLS is given in Fig 1.23(a). Modulation of the TLS is achieved via the Stark effect, where the presence of an electric field shifts the emission wavelength of an atom. Using a radio frequency electric field to modulate the TLS, sidebands can be generated in the frequency domain, as shown by Fig. 1.23(b). In some ways it can be thought of as a higher level form of optical modulation. Instead of manipulating the refractive index or electromagnetic field strength of a cavity to modulate a CW emitter, the emitter itself is modulated.

1.6 Thesis overview

As discussed at the beginning of this chapter, nanophotonic devices pave the way for future PICs. Already applications of nanophotonics are contributing towards integrated PICs. Therefore, developing a method for nanoscale OFC generation creates another building block for all-optical circuitry. This thesis endeavours to achieve this goal both theoretically and practically. Each of the following chapters will build upon the preceding to describe a novel method to generate OFCs using PhC devices.

Chapter 2 will describe the methodology for generating OFCs both experimentally and theoretically. It will briefly describe the fabrication processes, measurement facilities and modelling programs used. This will lay the ground work for the following chapters.

Chapter 3 builds a computational model to simulate photonic crystal cavities and waveguides. In this chapter, ultra-fast all-optical modulation of PhC devices is utilised to generate OFCs. This framework proves that nanoscale optical frequency generation is possible using PhC devices.

Chapter 4 describes the fabrication of PhC devices. In this chapter, a new recipe for fabricating PhC devices in nonthermalised InP is developed. It also describes the mechanisms developed to ensure vertical sidewalls during pattern transfer from photoresist to hard mask to InP.

Chapter 5 shows the optical characterisation of the fabricated devices. The effect the laser excitation power has on wavelength and Q factors is described. Time resolved measurements are also undertaken that show a decreased carrier lifetime for QDs coupled to the PhC devices.

Chapter 6 measures L3 cavities using a high repetition rate laser. In this chapter, sidebands are observed from the cavity when the correct repetition rate is used. The observation of the sidebands shows the potential for OFC generation and microwave photonic signal processing in nanoscale PhC devices.

Chapter 7 will conclude the work. It will look at various ways in which the findings of the project could be applied to PICs and integrated microwave photonics. Future work and the prospects of PhCs in microwave photonics are discussed.

Chapter 2

Methods and Materials

2.1 Materials

The application of the chip-based devices in this thesis is broadly aimed to be used in conjunction with other standardised telecommunication equipment, for example fibre optics. For this reason, the working wavelength of the devices will be at the fibre attenuation minima of 1550nm. At this wavelength the absorption characteristics of light in glass is lowest so attenuation in fibres is kept to a minimum. In many standard telecommunications devices, such as lasers and photo-detectors, InGaAsP is used. InGaAsP is a quaternary compound semiconductor material which is an alloy of group III and group V atoms. It is used because the mole ratios between the group III elements and group V elements can be tuned to tailor the bandgap. InGaAsP is commonly used in InP-based PICs because the lattice match allows single-crystal epitaxial growth of InGaAsP onto InP.

The samples used in this thesis are made up of an InGaAsP membrane with QDs embedded in the membrane, as shown by Fig. 2.1. As discussed in section 1.4.1, localised QD emission is achieved by surrounding with a larger bandgap semiconductor. In this case, InGaAsP is the larger bandgap material, where the alloy composition generates a bandgap of 1200nm. When the sample shown in Fig. 2.1 is excited by an above bandgap laser, spontaneous emission from both the InGaAsP layer and the QDs is observed in the samples' photoluminescent (PL) spectrum, as shown by Fig. 2.2.

The self-assembled QDs are grown using the Stranski-Krastanov (SK) mode. This produces a layer of QDs with a random size distribution which leads to a broadband emission wavelength from the QD layer. The samples are epitaxially grown using metal-organic chemical vapour deposition

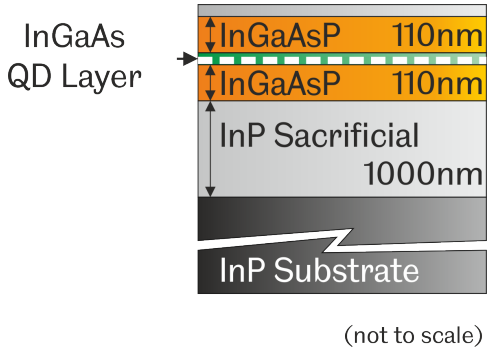

Figure 2.1: Wafer heterostructure for the PhC membrane

(MOCVD) onto an InP wafer. MOCVD is a common method to deposit thin films of single crystal layers onto a wafer and is widely used in III-V compound semiconductor manufacturing. In the MOCVD process, reactant gases combine at high temperatures and deposit on the surface of a wafer. For example, at high temperature $In(CH_3)_3$ and PH_3 will undergo pyrolysis and the resulting subspecies will react and deposit on the wafer, producing a InP layer.

The samples grown here are illustrated in Fig. 2.1, an InP sacrificial layer is grown on an InP substrate, this layer will be grown at a different temperature to the substrate so will react differently to isotropic chemical etching, as discussed in section 2.3. An InGaAsP quaternary layer is grown on top with a thickness around 110nm, then via the SK mode QDs are deposited. Another InGaAsP layer of 110nm is grown on top to cap the QD layer. Finally a thin layer of InP, around 50 nm, is deposited on top. This terminates the growth and protects the membrane's top surface from pollutants during fabrication. The emission wavelength of QDs is determined by their size. In this case, the dot density is around $3 \times 10^{10} cm^{-2}$ and the fluctuation in size produces broadband emission with a peak wavelength around 1600nm. Fig. 2.2 shows the PL spectrum of the wafer without any processing. From this figure, the PL from the different materials can be seen. At around 1200nm, PL from the InGaAsP layer can be seen, then broadband emission is observed which starts around 1250nm and indicates the emission from the QDs. The peak of the QD layer is not shown due to the limited detection wavelength range of the detector. Figure 2.1 shows the cross section of the wafer, PhC structures fabricated are patterned into the wafer vertically. Using both isotropic and anisotropic etching, as discussed in section 2.3, the resulting PhC structures reside in the InGaAsP

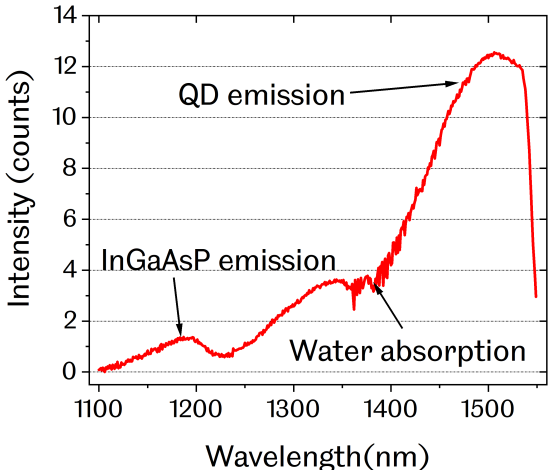

Figure 2.2: PL spectrum of the unprocessed wafer.

layer which is suspended in air.

2.2 Simulations

Various simulation tools have been used throughout this project. To calculate the EM field strength in PhC cavities and waveguides, Comsol Multiphysics has been used. Calculating the photonic band structure to find the correct lattice constant and fill factor was undertaken using MIT Photonic Bands (MPB). Finally, Matlab was used to build a theoretical model based on coupled mode theory (CMT) to describe the non-linear switching mechanism in a PhC cavity-waveguide system. The CMT model was built and developed as part of this project using models and equations from the relevant literature [108, 88, 144].

2.2.1 Commercial software

MPB

MPB, which is an acronym for MIT Photonic Bands, is a free and open-source software package that is designed for computing the band structures and EM modes of periodic dielectric structures. It computes the harmonic modes of Maxwell's equations in periodic structures using fully vectorial and three dimensional methods. The advantage of this software is that it uses

a targeted eigensolver, meaning that modes closest to a specific frequency can be computed instead of starting with the lowest frequency. Thereby reducing the number of bands that need to be computed in resonant mode calculations. In this thesis, MPB has been used to calculate the photonic bandgap generated when holes are etched into a InGaAsP membrane. In doing so, it is possible to find the frequencies at which light will propagate within an optical cavity consisting of defects in a PhC membrane.

Comsol Multiphysics

Comsol Multiphysics is a finite element method (FEM) analysis tool with a simple, user friendly interface. It can be used to design and simulate a wide range of devices and processes. In this case, a 2D PhC design can be modelled to study the propagation of EM waves. To do this, the structure is defined in terms of various parameters including boundary conditions and material properties. The structure is then broken down into a mesh of small elements. Each element in the mesh is then described by linear equations to give an approximate solution for that part of the structure. The sum of these elemental solutions makes up the total structure. The smaller the individual elements of the mesh, the smaller the approximations so the more accurate the simulation. The size of the elements in the mesh is dependant on the size of the components in the structure. Smaller components will need a finer mesh to be accurately simulated. The mesh size will also have a large influence on the time it takes to simulate the device.

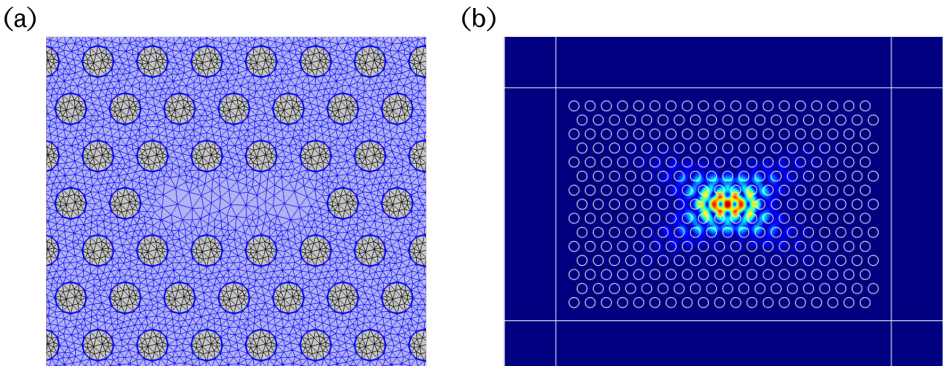

Figure 2.3: (a) The mesh geometry for an L3 PhC cavity, finer mesh structure are drawn around high-density areas. (b) Field distribution of the eigenfrequency of the L3 cavity

An example of a L3 cavity simulation is shown in Fig. 2.3. In this model, the eigenfrequency of the cavity is studied. The materials are defined by the refractive index, in this case the holes are air and the rest of the material is InGaAsP with a wavelength dependant refractive index. The structure is surrounded by a *perfectly matched layer* which acts as an absorbing boundary with the same properties as the material it surrounds. This is to ensure the outer boundary does not influence the wave function by reflection from it. The mesh is then user defined by the minimum and maximum element size and automatically written by Comsol to create a non-uniform mesh, as shown by Fig. 2.3 (a). The non-uniformity allows for increased resolution at the interfaces and objects of interest, hence decreasing overall complexity without losing accuracy.

A set of EM eigenfrequencies is found for a standing wave inside the cavity. As discussed in section 1.3 a triangular lattice of low refractive index material holes surrounded by a higher refractive index material will result in strong confinement of TE polarised modes. Comsol will solve both the TE and TM fields for the x, y, and z plane and return a discrete set of eigenmodes. Figure 2.3 (b) shows the first order eigenmode for TE polarised light. The lattice constant is 480nm and the filling factor is 0.3, this leads to a eigenfrequency of 1552nm.

Using Comsol, an electric field can be applied in the form of a point or line source. By doing this, the propagation of light through a waveguide or standing wave in a cavity can be analysed for a range of frequencies. In chapter 4 this is used to simulate a PhC cavity-waveguide device acting as a photonic filter. It is this filtering device that forms the basis of the all-optical switch.

2.2.2 Temporal coupled mode theory

Coupled mode theory (CMT) is a generalised framework for describing a set of idealised components, for example cavities and waveguides, that are coupled or perturbed in some way [88]. CMT takes many forms, often used to provide a numerical result for specific geometries. In this case, temporal CMT is utilised, this incorporates a description of direct transmission through a cavity-waveguide device [145]. It is commonly used to describe Fano resonance [146], ring resonator optical filters [147], optical bistability [148] and all-optical switching [108]. This section will build up the model for an all-optical switch based on optical nonlinearity in PhC devices. This model is the basis for the majority of the work undertaken in chapter 3.

Without taking into consideration any PhC-based structures, the general

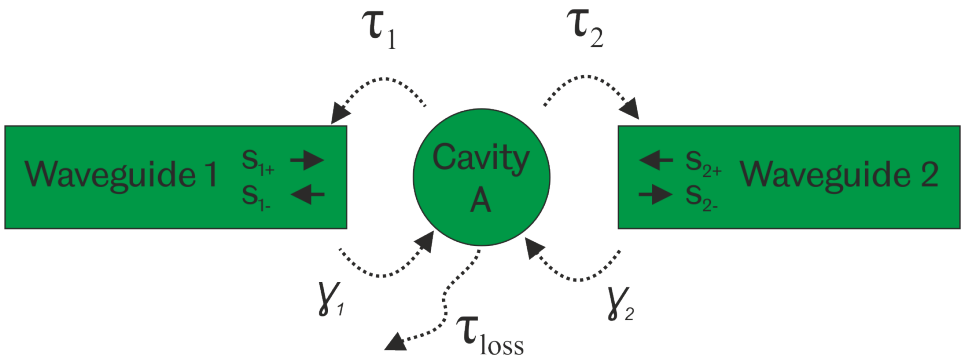

Figure 2.4: Generic illustration of the cavity-waveguide structures considered in this thesis.

principle of the model used is shown in Fig. 2.4. The building blocks are simple propagating modes in the waveguides, $s_{1\pm}$ and $s_{2\pm}$, and localised modes in the cavity, A. The units of A can be chosen arbitrarily as it is just a variable that is proportional to the standing wave, in this case $|A|^2$ is the EM energy in the cavity. $s_{1,2+}$ is the amplitude of the wave going towards the cavity and $s_{1,2-}$ going away from the cavity for waveguides 1 and 2. The units of $s_{1,2\pm}$ are also arbitrary but it is chosen to make $|s_{1,2\pm}|^2$ the power of the propagating modes. It is assumed that weak coupling exists between the cavity and the waveguides and the conservation of energy is always maintained.

If energy in the cavity has two loss mechanisms with decay constants of τ_1 and τ_2 then there will be a total lifetime of $1/\tau_d = 1/\tau_1 + 1/\tau_2$. The rate of energy loss is proportional to the energy inside the cavity, $|A|^2$, hence the decay rate, τ_d is exponential. With no energy source, the amplitude A will satisfy the differential equation:

$$\frac{dA}{dt} = -i\omega_0 A - \frac{A}{\tau_d} \tag{2.1}$$

which has the solution $A(t) = A(0)e^{-i\omega_0 - t/\tau_d}$. With an equation for A, the waveguides can be added to the model. The waveguides will act both as a source through which energy is input into the cavity and as a drain where the energy will dissipate. Energy from the two waveguides will couple into the cavity, acting as a source, via a coupling coefficient denoted by γ_1 and γ_2 in Fig. 2.4. The propagating light in the waveguides will either couple into the cavity or reflect at the cavity-waveguide interface. Light that is reflected will form part of the $s_{1,2-}$ amplitude and light that couples in the

cavity will form part of the cavity amplitude. Adding this into Eq 2.1, gives

$$\frac{dA}{dt} = -i\omega_0 A - \frac{A}{\tau_1} - \frac{A}{\tau_2} + \gamma_1 s_{1+} + \gamma_2 s_{2+} \tag{2.2}$$

$$s_{1,2-} = -s_{1,2+} + \gamma_{1,2} A \tag{2.3}$$

In order to eliminate as many unknowns as possible, $\gamma_{1,2}$ can be written in terms of τ_2, to do this the outgoing wave from the cavity is analysed. Assuming there is no light being input to the cavity and the cavity is completely decoupled from waveguide 2 and the cavity energy will decay exponentially into waveguide 1, with the energy from the cavity, $|A|^2$, solely going into the power of waveguide 1, $|s_{1-}|^2$, therefore:

$$\frac{d|A|^2}{dt} = |s_{1-}|^2 = |\gamma_1|^2 |A|^2 = \frac{2}{\tau_1}|A|^2 \tag{2.4}$$

given that the phase of the outgoing light in this case is arbitrary, $\gamma_1 = \sqrt{\frac{2}{\tau_1}}$. The same can be said for the situation where all the energy from the cavity is dissipating into the power of waveguide 2. In this case, no light will couple into waveguide 1, so $\gamma_1 \to \infty$, and $\gamma_2 = \sqrt{\frac{2}{\tau_2}}$. This shows how, in terms of $\tau_{1,2}$, the power dissipates into each waveguide but does not show how it builds up within the cavity. By assuming time reversal symmetry, how the power builds in the cavity can be understood. The energy exponentially grows so a solution to Eq. 2.2 in the form of $A(t) = A(0)e^{-i\omega_0 + t/\tau_d}$ can be found. Assume that there is no energy in the cavity and the input field into waveguide 1 is $s_{1+} = \sqrt{2/\tau_1}A$. Again, by making the cavity decoupled from waveguide 2 and plugging $A(t)$ into Eq. 2.2, it is seen that $\gamma_1\sqrt{2/\tau_1}A = 2A/\tau_1$. The same applies for the situation where waveguide 1 is decoupled and the input field in waveguide 2 is $s_{2+} = \sqrt{2/\tau_2}A$. By understanding this, Eq. 2.2 and 2.3 are given in terms of just three factors, ω_0, τ_1 and τ_2. In Fig. 2.4, there is a loss function due to radiative losses given by γ_{loss}, this includes coupling to other modes in the cavity and out of plane losses. This can be easily incorporated into Eq. 2.2, given the weak coupling between the cavity and the waveguides, the radiative losses will not affect the waveguide fields, only the cavity field, including this into Eq. 2.2 gives:

$$\frac{dA}{dt} = -i\omega_0 A - \frac{A}{\tau_1} - \frac{A}{\tau_2} - \frac{A}{\tau_{loss}} + \sqrt{\frac{2}{\tau_1}} s_{1+} + \sqrt{\frac{2}{\tau_2}} s_{2+} \tag{2.5}$$

As discussed in section 1.3.2, the scheme shown in Fig. 2.4 is acting as a transmission filter, where only light of a specific wavelength can transmit

from waveguide 1 to waveguide 2. It is assumed that power will only transmit through the device in one direction, so $s_{2+} = 0$. When the input wave has a fixed frequency, ω, then the field in the waveguide will oscillate as $e^{-i\omega t}$ thus, $dA/dt = -i\omega A$. With this in mind, Eqs. 2.5 and 2.3 give:

$$-i\omega A = -i\omega_0 A - \frac{A}{\tau_1} - \frac{A}{\tau_2} - \frac{A}{\tau_{loss}} + \sqrt{\frac{2}{\tau_1}} s_{1+} \tag{2.6}$$

$$s_{2-} = \sqrt{\frac{2}{\tau_1}} A \tag{2.7}$$

The transmission is the amount of input power compared to the amount of output power as a function of frequency, such that $T(\omega) = |s_{2-}|^2/|s_{1+}|^2$. So to find the transmission over a given spectrum, Eq. 2.7 can be divided by s_{1+} to give Eq. 2.6 in terms of A/s_{1+}, this gives:

$$T(\omega) = \frac{\frac{2}{\tau_2}|A|^2}{|s_{1+|^2}} = \frac{\frac{4}{\tau_1\tau_2}}{(\omega - \omega_0)^2 + (\frac{1}{\tau_1} + \frac{1}{\tau_2})^2} \tag{2.8}$$

This equation shows how a cavity coupled to two waveguides acts as a narrow band photonic filter. A common way to simplify the modelling of light propagation in PhC devices [108] is to use the slowly varying envelope approximation (SVEA). In this approximation, it is assumed that the phase and amplitude of the propagating light vary at a much slower rate than the electro-magnetic field. Using SVEA to define the fields $a(t)$ and $s(t)$ gives the relations:

$$A(t) = a(t)e^{-i\omega t} \text{ and } s(t) = s(t)e^{-i\omega t} \tag{2.9}$$

From these equations a dynamical model for the energy inside the cavity and waveguides can be built:

$$\frac{da(t)}{dt} = (-(\omega - \omega_0) - \frac{1}{\tau_d} - \frac{1}{\tau_{loss}})a(t) + \sqrt{\frac{2}{\tau_1}} s_{1+}(t) \tag{2.10}$$

$$s_{2-} = \sqrt{\frac{2}{\tau_1}} a(t) \tag{2.11}$$

These equations form the basis of an all-optical switch and are used repeatedly throughout chapter 3.

2.2.3 Perturbation Theory

Hitherto the cavity resonance has not been subject to dynamical change and the model built is linear. In order to realise all-optical switching, a nonlinear interaction that will cause the carrier light signal to be influenced by the pump light is required. To this end, it is commonly stated [144, 108, 102] that the complex refractive index of the device material can be included in temporal CMT as perturbations of the real and imaginary part of the cavity eigenfrequency. In this section, treatment of the perturbation theory is outlined. Two kinds of effects that change the refractive index of the material are used throughout chapter 3, these are the Kerr effect and effects from free carrier generation.

Third-Order Nonlinear Optical Susceptibility

A material's susceptibility to third-order nonlinear processes is complex, such that $\chi^{(3)} = \chi_R^{(3)} + i\chi_I^{(3)}$. Here, the third order susceptibility of a standard III-V material without quantum confinement through a QD or QW region is derived. The real part is denoted as the Kerr effect and the imaginary part relates to TPA. The perturbation of the cavity resonant wavelength can be written as:

$$\omega_1(t) = (-K_{kerr} - iK_{TPA})|a(t)|^2 \tag{2.12}$$

where

$$K_{kerr} = \frac{\omega_0 c n_2}{n_{eff}^2 V_{kerr}} \tag{2.13}$$

and

$$K_{TPA} = \frac{\omega_0 c \beta_{TPA}}{n_{eff}^2 V_{kerr}} \tag{2.14}$$

where $\omega^{(0)}$ is the cavity resonance, $n_2 = (3/2n^2\epsilon_0 c)\chi_R^{(3)}$ is the nonlinear refractive index, n_{eff} is the refractive index of the material, V_{kerr} is the Kerr nonlinear volume used to characterise the average saturable absorption rate in the cavity and c is the speed of light. These can then be included into Eq 2.10, to give:

$$\begin{aligned}\frac{da(t)}{dt} = -i[(\omega - \omega_0) - K_{kerr}|a(t)|^2]a(t) - [\frac{1}{\tau_d} + \frac{1}{\tau_{loss}} \\ +K_{TPA}|a(t)|^2]a(t) + \sqrt{\frac{2}{\tau_1}}s_{1+}(t)\end{aligned} \tag{2.15}$$

From this equation, it is simple to interpret the function of both parts of the third-order nonlinear susceptibility. The resonance change due to the change in the real part of the refractive index is contained in K_{kerr}. This change in the real part is accompanied by a change in the absorption properties of the cavity which perturbs the decay rate proportionally to K_{TPA}.

Carrier-based nonlinearity

The effects of carrier-based nonlinearity were discussed in section 1.3.2. These effects are included in the model to give a complete understanding of the PhC all-optical switching mechanisms. In simplified terms, the refractive index of a semiconductor material will be affected by the excitation of electrons from the valence band to the conduction band [101]. The changes in the real and imaginary part of the refractive index are related by the Kramers-Kronig relation. To describe the change in cavity resonance through carrier density-based nonlinearity, equations that express carrier density need to be coupled to Eq. 2.10. The change in resonance frequency is directly related to the change in the dielectric function. So, by relating the change in carrier density to the change in dielectric function, the resonance shift can be calculated. These are related by:

$$\Delta\epsilon_R = \frac{d\epsilon_R}{dN}\Delta N \tag{2.16}$$

$$\Delta\epsilon_I = \frac{d\epsilon_I}{dN}\Delta N \tag{2.17}$$

where $\Delta N = N - N_0$ and N_0 is the unperturbed carrier density. ϵ_R and ϵ_I represent the real and imaginary parts of the dielectric function. The temporal dependence on the carrier density is given by:

$$\frac{dN(t)}{dt} = -\frac{N(t)}{\tau_{fc}} + G(t) \tag{2.18}$$

where τ_{fc} is the effective free carrier lifetime and $G(t)$ is the source that generates free carriers. In the simulations carried out in this thesis, on resonant excitation of the cavities at 1550nm dictates that carrier generation through linear absorption of the InGaAsP membrane will not occur due to below band excitation. In this case, TPA will dominate the carrier generation process, meaning:

$$G(t) = \frac{\beta_{TPA}|a(t)|^2}{2\hbar\omega V_{car}}|a(t)|^2 \tag{2.19}$$

V_{car} is the volume over which carriers spread and recombine [144]. In this approximation, the carriers are assumed to spread and distribute homogeneously within V_{car}, which corresponds to the membrane region, delimited by the holes in the membrane that surround the cavity. Although this approximation is not very precise, it is a reasonable choice for the device simulated here. From Eq.s 2.16 and 2.17, changes in the eigenfrequency due to carrier density fluctuation can be written as:

$$\omega_1(t) = -\omega_0[K_{FCD} + iK_{FCA}]N(t) \tag{2.20}$$

where the K_{FCD} and K_{FCA} are the coefficients that represent free carrier dispersion (FCD) and free carrier absorption (FCA), respectively, and are given by

$$K_{FCD} = -Re\{\omega_0\}\frac{d\epsilon_R}{dN} = \frac{e^2}{2n^2\omega_0\epsilon_0 m_0} \tag{2.21}$$

$$K_{FCA} = Im\{\omega_0\}\frac{d\epsilon_I}{dN} = \frac{\sigma c}{n} \tag{2.22}$$

where e is the elementary electric charge, n is the refractive index of the material, ϵ_0 is the vacuum permittivity, m_0 is the effective mass of carriers and σ is the absorption cross section for the carrier density $N_c(t)$. So by substituting Eq. 2.20 into Eq. 2.15, an equation for the cavity field including all nonlinear terms can be written as:

$$\begin{aligned}\frac{da(t)}{dt} &= -i[(\omega - \omega_0) + K_{FCD}N(t) - K_{kerr}|a(t)|^2]a(t) - \\ [\frac{1}{\tau_d} + \frac{1}{\tau_{loss}} &+ K_{FCA}N(t) + K_{TPA}|a(t)|^2]a(t) + \sqrt{\frac{2}{\tau_1}}s_{1+}(t)\end{aligned} \tag{2.23}$$

2.2.4 Absorption enhancement through QD layer

The equations stated above are standard building blocks for PhC cavity-waveguide all-optical switches. In the devices simulated here, there is an active QD layer within the membrane structure. Switches that incorporate QDs often require lower switching energies because the state filling effect in a single QD only uses one photon to alter the optical spectrum from absorption to transparency. However, the magnitude of optical nonlinearity is generally low in self-assembled QDs due to the extremely small effective cross section and interaction length. To enhance the interaction between light and the QD layer, a high Q cavity with a low effective volume is needed. In this case, this is present via the PhC cavity which greatly enhances the third-order nonlinearity of QDs. For a 1D PhC vertical cavity structure, the

third-order nonlinear susceptibility, $\chi^{(3)}$, has shown an enhancement of 60 times [9]. This will greatly affect the nonlinear refractive index, n_2, as given in Eq. 2.13. In this work, this enhancement third-order susceptibility has been included so that the effects from the QD layer are accounted for.

The carrier lifetime in the QDs will contribute towards limiting the modulation frequency of the cavity-waveguide device. A longer QD lifetime will cause the switching time to increase because the carriers will take longer to relax back to their non-excited state. QD interband transitions are not intrinsically faster than, for example, QWs. However, discrete energy states within the QDs can be utilised to increase the modulation bandwidth. Fast switching speeds, down to 20ps, have been demonstrated in a 1D PhC cavity [137]. This high speed is due to both interband carrier relaxation transitions between QD high energy states and ground states and the carrier escape time from the excited state to the QD barrier.

With the TCMT equations outlined here, it is possible to use an optical RF input to develop a platform for simulating PhC devices with an embedded QD layer that are operating in the microwave photonic domain. This is the basis for the work carried out in chapter 3.

2.2.5 Fourier transform

The Fourier transform is a mathematical transformation that is used to describe a function in terms of its constituent frequencies. Although it is not limited to time domain studies, in this case, it is used purely to transform a time domain signal into the frequency domain. The Fourier transform can be calculated using computational methods if the signal is both discrete and periodic. In the case of simulating time domain measurements, the signal will inherently be discrete. To ensure periodicity, the simulated time domain signal can be thought of as a sample which is infinitely repeating in time. Calculating the Fourier transform in this way is known as the discrete Fourier transform (DFT). DFT can be calculated in a number of ways, most commonly used is the fast Fourier transform (FFT) method. A simple example of displaying a signal in terms of its frequency components, calculated using the FFT method, is shown in Fig. 2.5. The signal on the bottom row of Fig. 2.5(a) (black line) is made up of the three signals above it.

When the top three lines in Fig. 2.5(a) are added together, it creates a square wave, which is shown by the bottom line. Using Matlab, the black line is transformed into the frequency domain through the FFT. The resulting frequency domain spectrum is then given in Fig. 2.5(b). The

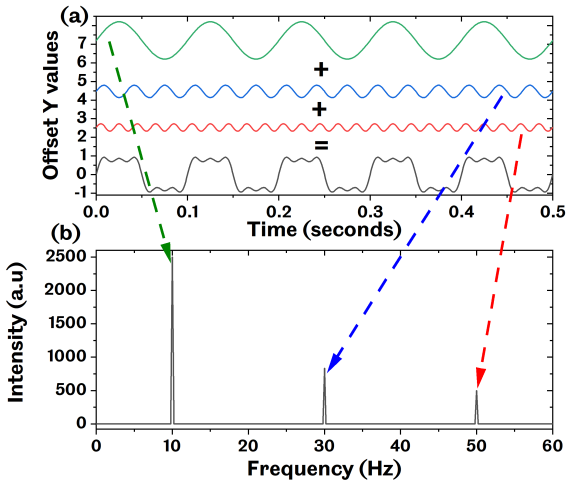

Figure 2.5: (a) The time domain response where a square wave (black line) has been generated by three sinusiodal wave functions (green, red and blue lines). (b) the FFT of the black line in (a)

relative intensity and position of each peak relates to the amplitude and frequency of its corresponding wave in the time domain, respectively, as denoted by the arrows. Initially, the frequency domain signal is given in terms of frequency bins, which are a product of the sampling rate in the time domain. In order to convert this into Hertz, the Fourier transform is multiplied by the sampling rate divided by the total length of the signal. This same FFT concept is used throughout chapter 3 to transform the time domain response of the PhC modulators into the frequency domain. In this way, it is possible to observe the generation of OFCs.

2.3 Fabrication

The general fabrication method is described below and illustrated in Fig. 2.6. Initially the sample is cleaned by a three stage process to remove any unwanted particles from the surface. The sample is submerged in heated n-butyl then transferred into acetone and finally into isopropyl. This removes any loose particles on the surface, further removal of any particles is undertaken by ashing the sample. After ashing, the sample is submerged in diluted orthophosphoric acid to de-oxidise the surface and help to promote the deposition of silicon nitride during plasma enhanced chemical vapour

deposition (PECVD). A silicon nitride layer is deposited via PECVD onto the sample. An electron beam resist layer is deposited onto the silicon nitride via spin coating, Fig. 2.6(a). Electron beam lithography (EBL) is then used to pattern photonic crystal devices in the resist layer and the sample is developed using a solvent to remove the exposed parts of the electron beam resist, Fig. 2.6(b). The sample is then plasma ashed for a short time to remove any *cupping* of the nanoscale holes, Fig. 2.6(c). The pattern is then transferred into the silicon nitride hard mask by reactive ion etching (RIE) using fluoroform (CHF_3), Fig. 2.6(d). The remaining parts of the electron beam resist are then removed via a combination of plasma ashing and submerging in solvent. The sample is then etched using chlorine and hydrogen gases with an inductively coupled plasma (ICP) RIE process. The ICP etch penetrates to the bottom of the sacrificial layer, Fig. 2.6(e). The remaining silicon nitride is then removed using hydrofluoric acid. A selective wet etching process consisting of low temperature hydrogen chloride is used to remove the InP above and beneath the InGaAsP, leaving a membrane structure, Fig. 2.6(f).

The following subsections detail each process to give context to chapters 4 and 5. These chapters describe the development of a unique fabrication recipe which allows for room-temperature etching of nanoscale devices in InP and the optical characterisation of such devices. This unique ICP fabrication process for PhCs in nonthermalised InP had not been studied previously and the process was entirely developed as part of this project.

2.3.1 PECVD

PECVD is typically used in nano-fabrication techniques for depositing thin films onto samples or wafers. A plasma is used to provide energy to the deposition reaction that takes place during chemical vapour deposition. In this method, reactant gases flow into the chamber from the top, in an equally distributed formation. A plasma is generated through an RF bias which ionises the reactant gases. This ionisation generates a large number of chemically reactant radicals which form a thin film on the top of the sample. The key advantage here is the low temperature at which thin films can be deposited given that plasma is used to generate radicals instead of heat.

Various parameters affect the thin film properties. In this case, high etching ratios between the silicon nitride hard mask and InP are needed in order to generate deep etching. The gases used in PECVD are SiH_4, NH_4 and N_2 at flow rates of 100sccm, 5sccm and 900sccm, respectively. N_2 is acting as an inert carrier gas for SiH_4. SiH_4 and NH_4 react to produce

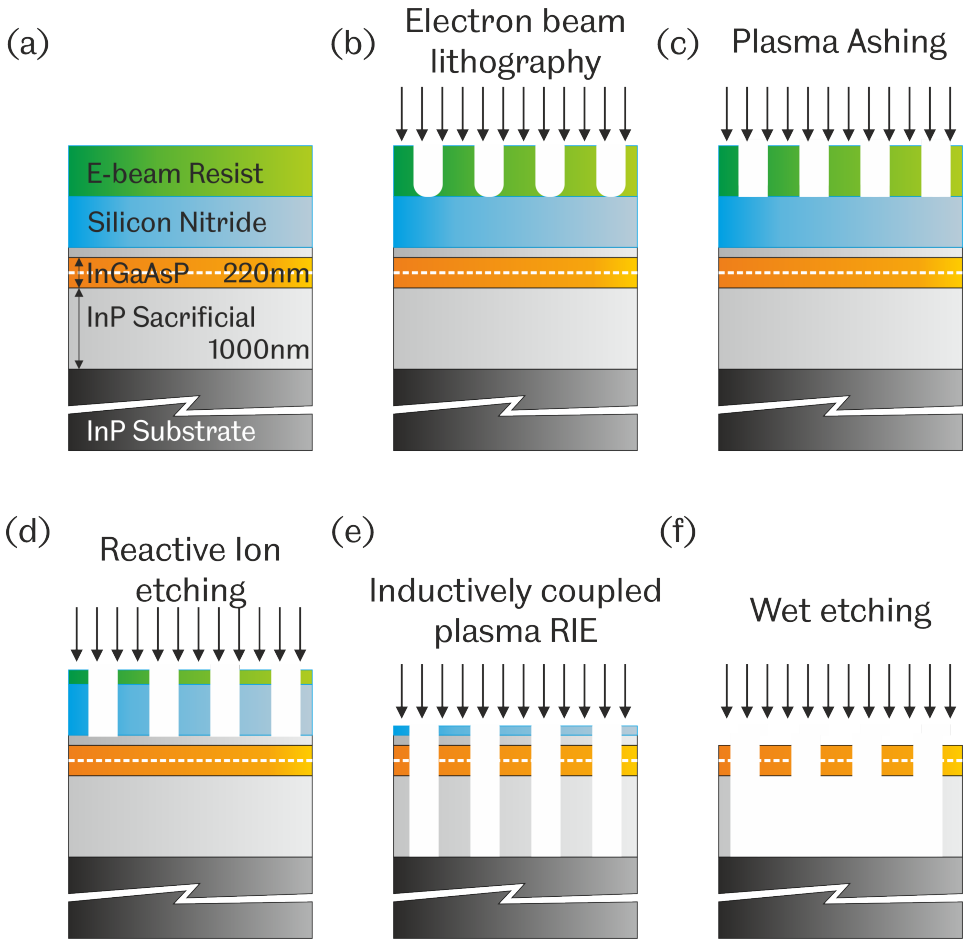

Figure 2.6: The sample at different steps in the fabrication process (a) Si_3N_4 is deposited on the sample via PECVD and CSAR is spin coated onto the sample. (b) EBL creates a pattern in the CSAR layer and plasma ashing (c) is employed to remove any hole cupping. (d) The pattern is etched into the Si_3N_4 via RIE. (e) The pattern is transferred from the Si_3N_4 to the sample via ICP etching. (f) Undercut etching using HCl is employed to create a membrane structure.

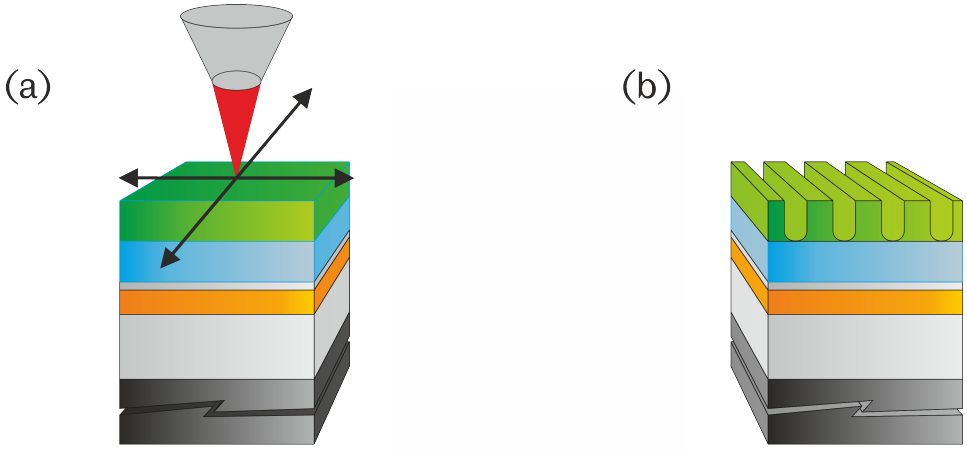

Figure 2.7: (a) The electron beam is focused onto the sample to change the solubility of the CSAR (b) The pattern is developed using Xylene, leaving the unpatterned CSAR on the sample.

SiN_4 and H_2. The pressure is set to 900mTor and the temperature of the sample table set to 300°C. The RF power is set to 25W, a trade off exists between deposition rate and uniformity, using this recipe the rate is around 12 nm/minute. In the following processing steps, deep etching into InP is realised through ICP etching. For this reason a thick hard mask is needed, a 400nm thick SiN_4 layer is deposited onto the sample which ensures holes with a radius down to 150nm can be produced and the hard mask thickness is sufficient for deep etching into InP.

2.3.2 Electron beam lithography

A focused beam of electrons incident on a electron-sensitive film, such as CSAR-65 [149], can change its solubility, enabling selective removal of either the exposed or non-exposed areas. Using a nanometer resolution mechanical stage, the EBL system scans the sample across the beam of focused electrons, as shown in Fig. 2.7. With this technique, custom patterns of a resolution down to less than 10nm can be drawn. In this work, a 'Raith Voyager' system is used to define the PhC patterns in the resist. The patterns are drawn using standard CAD software, provided by Raith. A Matlab program has been built to generate large matrices of PhC patterns. Unlike photolithography, a

mask is not needed to produce the pattern, which opens up the possibility for research and development in semiconductor devices with enhanced flexibility and optimisation capabilities.

The pattern resolution is dependent on the molecular weight, structure and thickness of the resist. Typically, minimum patterning sizes can be down to around one third of the resist thickness. In this thesis, a photonic bandgap that centralises around 1550nm is specified and it is calculated that a hole radius of around 144nm is needed. Given the thickness of the hard mask, a resist layer thickness of 400nm is necessary to ensure the resist does not etch away before the hard mask. This is achieved by spin coating undiluted CSAR-65 for 30 seconds at 4000rpm. The *dose* of electrons delivered has the units $\mu C/cm^2$ and is used to specify the number of electrons in the beam. This value is critical for accurate patterning of the PhC devices. A high dose will lead to over exposure and holes that are larger than specified. A low dose will under expose the resist, meaning it cannot be removed by the solvent.

The proximity effect is an overriding issue in EBL, it is the occurrence of over exposed patterns that are within close proximity to each other. There are two processes that cause the proximity effect: forward and backward scattering. Forward scattering occurs when a propagating electron from the beam interacts with another electron, causing it to change direction slightly, thereby increasing the beam size. The second is backscattering; this is where the electron penetrates all the way through the resist and into the substrate. When the electron comes into contact with a heavy particle, for example the substrate nucleus, it will reflect back and lead to scattering at a wide angle. Depending on the material involved and the acceleration voltage of the beam, the electrons can scatter up to tens of microns. If there is a single patterned object with no surrounding pattern then the effect of scattering is negligible, however with the dense integration of many objects, it becomes a serious issue. Built into the Raith software is a proximity correction tool. By setting stringent parameters, good hole diameter uniformity can be achieved.

For the patterning of PhC devices in CSAR-65, the electron beam was set to 75 $\mu C/cm^2$. Within the software a dose factor can be used to vary the dose incrementally. When developing the EBL process for PhC devices in a CSAR resist on InP, the dose was varied from 70% to 130% of the initial $75\mu C/cm^2$ dose. It is then possible to know the specific dose needed for accurate device patterning. The column mode is set to give a voltage of 50kV with low current and a beam aperture of 40µm. The low current and small aperture give higher resolution at the cost of patterning speed. In this case, resolution is more important than speed of patterning because

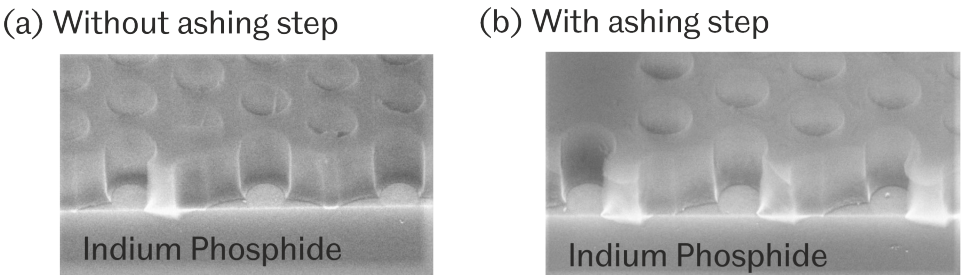

Figure 2.8: (a) Holes in the Si_3N_4 layer show prominent cupping at the bottom without the ashing step (b) The cupping is reduced with the use of an ashing step.

the patterning area is relatively small.

Once the sample has been exposed, it is submerged in Xylene for 60 seconds at 23°C. Xylene is an organic solvent that removes the low-molecular-weight exposed resist and leaves the cross-linked, high-molecular-weight, unexposed resist. Once the sample has been developed, slight cupping is present at the bottom of the holes. When transferring the pattern into the hard mask, this cupping shape will also transfer. To overcome this, the sample is plasma ashed using oxygen. This removes these small remaining parts of the CSAR that are present at the bottom of the holes before etching the hard mask. Figure 2.8 is an SEM image of the side profile of the device after RIE etching. The transferred cupped shape is present in the hard mask in Fig. 2.8(a), however by including an ashing step the cupped shape is removed, as shown in Fig. 2.8(b). Although this cupping issue can be resolved by correcting the EBL parameters further, slight changes in the local environment for each run through make this difficult. Therefore, the ashing step is a preferred method in this process.

2.3.3 Plasma etching

Following the patterning in the EBL resist, two dry etching processes transfer the device structure, initially into the hard mask and subsequently into the InP. First RIE is used to transfer the pattern into the hard mask. RIE uses chemically reactive plasma to remove material from a sample. The etchant gas is released into the RIE chamber. A plasma is initiated by an RF electromagnetic field between a cathode and anode on the top and bottom of the RIE chamber respectively. The stripped electrons accelerate up and down the chamber, hitting both the sample and the chamber upper wall.

Through this process, electrons are deposited onto the sample and cause a large negative charge build up. At the same time, the plasma has a positive voltage due to the ratio of ions to free electrons. The voltage difference between the plasma and sample cause the ions to drift towards the sample. As the plasma reaches the sample, two etching effects are present: chemical and physical. The reactive gas in the plasma reacts chemically with the sample, causing the sample to break down. Heavy ions in the plasma also have a kinetic energy which causes ion bombardment. The bombardment is a directional etching process, so anisotropic etching can be achieved, generating vertical sidewalls in the hard mask material.

To etch into silicon nitride, CHF_3 is used as the etchant with a gas flow rate of 40sccm. Low pressure inside the chamber ensures a high resolution, which is imperative for nanoscale devices, but also decreases the etching ratio of CSAR-65 and Si_3N_4. Given the relatively thick CSAR layer, a low chamber pressure of 25mTorr is adopted. The RF power is set to 80W, this gives an acceptable etching ratio.

ICP RIE has a similar operation to RIE, the key difference is the use of a second RF source, known as the ICP RF. The ICP RF source creates a magnetic field above and perpendicular to the etching direction which controls the ion flux. Given the field direction, it will not contribute towards sample charging. It is a mechanism to separate the density of ions in the plasma and the energy used to etch the sample. To control the plasma flow onto the sample, a standard RIE type scheme is utilised. This decoupling of the ion density and energy gives way to very high etch rates, process flexibility and etch profile control. After RIE etching all the CSAR is removed through oxygen ashing for 5 minutes. In this process, the oxygen combines with the photoresist to form an ash which is removed with a vacuum pump. The sample is then submerged in 'Microposit^{TM} Remover 1165', this is a commercially available mixture of pure organic solvents, specifically formulated for the removal of photoresist. The sample is then ready for the next dry etching stage: ICP RIE.

Chapter 4 details the development of ICP etching parameters for nanoscale devices in nonthermalised InP samples. The etching gases used are Cl_2 and H_2 using ICP and RF powers of 125W and 1000W respectively and a chamber pressure of 2 mTorr. This enables deep etching in InP, up to 800nm with straight sidewalls and low surface roughness.

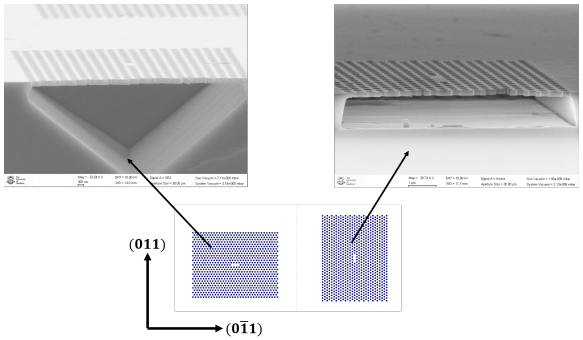

Figure 2.9: The SEM images show the difference in undercut etching when the PhC Γ-K direction is shifted 90°relative to the crystalline plane.

2.3.4 Wet etching

The final stages in the process consist of a two-stage wet etch process. After ICP etching, a thin film of silicon nitride still exists on the surface of the sample. To remove this, the sample is submerged in 40% hydrofluoric acid for 90 seconds. Once the hard mask has been fully removed, the sacrificial InP above and below the membrane must be isotropically etched to leave the InGaAsP membrane structure. This is done using a low temperature HCl-H_2O mixture.

Depending on the orientation of the triangular PhC lattice, the etching profile of the InP will change. This is because the crystalline structure of the InP has an absence of a centre of symmetry and this means that different etching directions can have different chemical etching properties. Figure 2.9 shows the cleaved side profile of two PhC devices where the orientation of the Γ-K plane is perpendicular to the (011) plane and perpendicular to the (0$\bar{1}$1) plane. In the perpendicular case, lateral etching is promoted by a change in the growth temperature of the InP. This leads to an etch-stop point and a flattened etch profile beneath the membrane, as shown in Fig. 2.9. Through SEM analysis of the structure from above, the undercut profile can be analysed. Using this analysis as well as the optical characterisation results, it was found that a Γ-K plane orientated at 45°from the (0$\bar{1}$1) plane produced the most consistent results. Further analysis into the wet etching process is given in chapter 4.

2.4 Measurements

2.4.1 Micro-Photoluminescence

Micro-photoluminescence allows for the optical characterisation of microscale and nanoscale devices. In this section, each part of the micro-PL set-up is discussed, including confocal microscopy, spectroscopy and InGaAs photodiodes. The design and construction of the optical lab was undertaken as part of this project.

Confocal microscopy

Using confocal microscopy, the samples are optically probed. Confocal microscopy allows optical probing at a specific place on the sample. The sample is excited and its emission is collected through the same objective which is situated above the sample. A diagram of the measurement light paths is given in Fig. 2.10. The point source laser beam is collimated and sent into the objective where the light is focused onto the sample. Emission from the sample acts as a point source which is partly collected by the objective. The emission is collimated and then focused into the spectrometer. A slit at the input of the spectrometer ensures no background light enters the spectrometer and increases the measurement resolution. A broadband light source and CMOS camera is also incorporated into the measurement set-up to illuminate the sample and observe the position of the excitation spot relative to the sample.

Spectroscopic measurements

Optical emission from the sample is spectrally analysed using a grating spectrometer. Using this instrument, the energy of the light can be spatially separated. A slit is placed at the output of the spectrometer so that only light of a specific wavelength leaves the spectrometer. By spatially rotating the grating, the wavelength of light leaving the spectrometer is shifted. This enables the intensity at a specific wavelength to be measured using a single pixel detector when the spectrometer and grating parameters are known. The spectrometer used throughout this thesis is the Horiba Scientific FHR1000, the 1m focal length dictates a specified spectral resolution of 0.01nm when the input and output slits are at 10µm. The spectrometer has two output ports; to make full use of this, the front exit is used for frequency domain measurements and the side is used for time domain measurements, as shown in Fig. 2.11. A single pixel, solid state photoemissive InGaAs

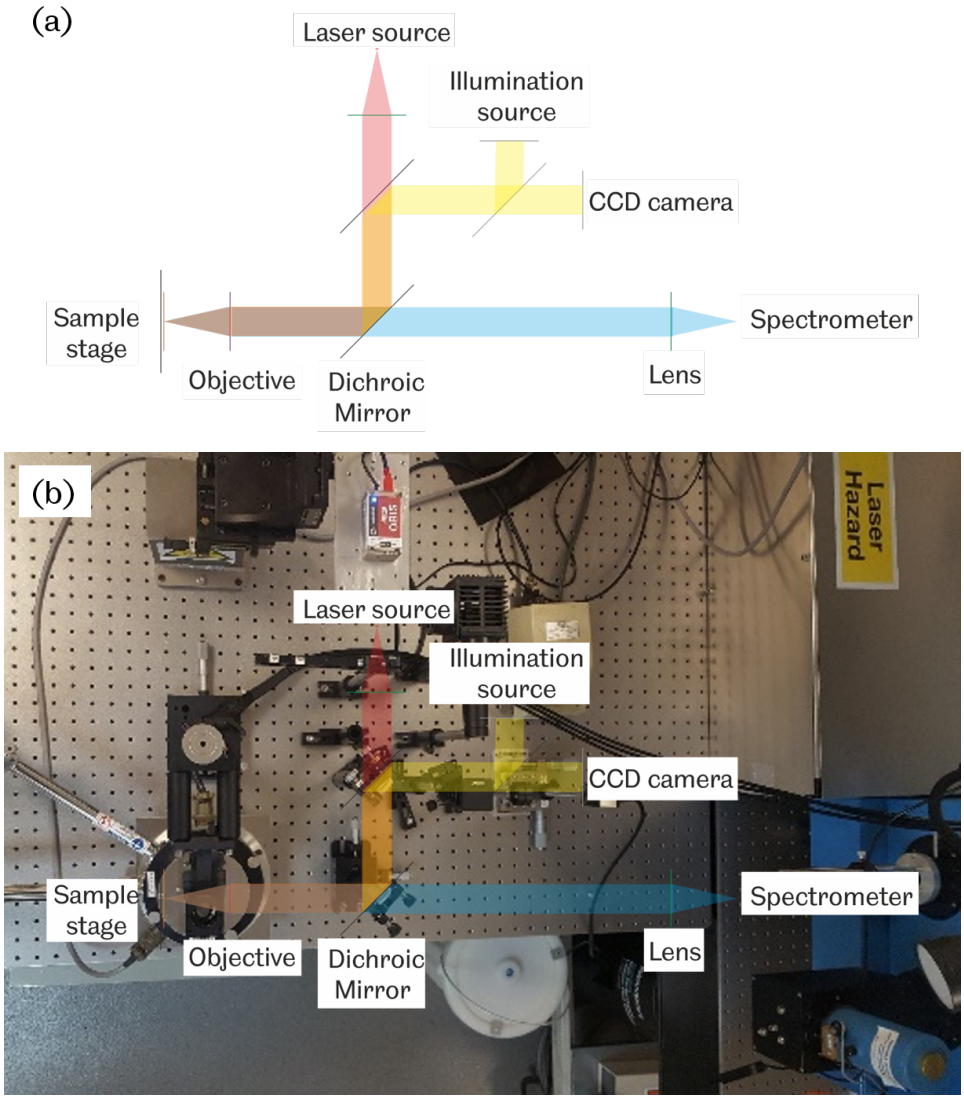

Figure 2.10: Diagram of the confocal set-up used for µPL and TCSPC measurements

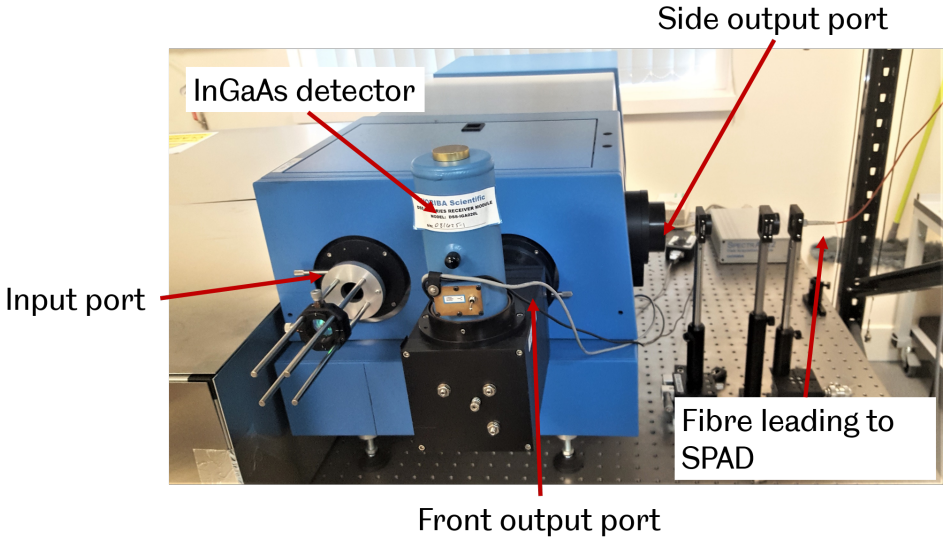

Figure 2.11: A photo of the FHR1000, showing the output ports for both time and frequency measurements

detector is placed at the output of the spectrometer. The detector is LN cooled to reduce the dark current, hence increasing the signal to noise ratio.

2.4.2 Time correlated single photon counting

In this thesis, time correlated single photon counting (TCSPC) is used to measure the lifetime of the QDs in the sample. TCSPC works by correlating the arrival time of a photon to a reference point in time. By correlating many single photon arrival times, a histogram is built up that will show the time response of the QD emission. Figure 2.12 shows a diagram of the TCSPC set-up used throughout this thesis. In the TCSPC set-up there are three key elements: the ultra-fast excitation laser, the single photon detector and the timer. In this section, the three are briefly discussed. Explanation of this state-of-the-art system set-up, testing and trouble shooting is outlined in the appendix.

Ultra-fast laser

To generate femto-second pulses, an MLL is used; the operation of this has been described in section 1.1. The laser used is the Spectra-Physics HighQ-

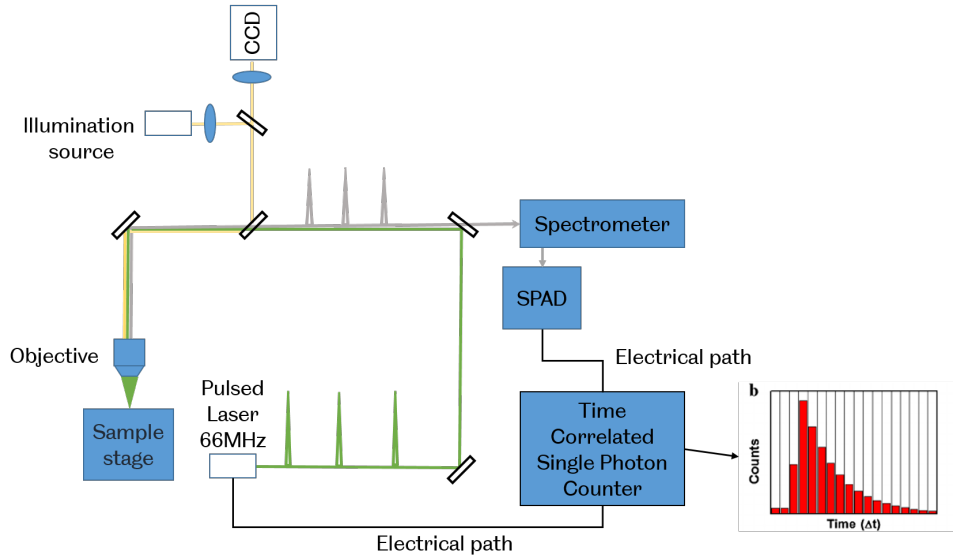

Figure 2.12: The TCSPC set-up used in this thesis. SPAD - Single photon avalanche diode, CCD - charged coupled device.

2, it emits a < 250fs pulse every $1/(66 \times 10^6)$ seconds. The wavelength is fixed at 1044nm and the output beam has a Gaussian spatial profile. It is used to excite the sample and the emitted light is then incident on the single photon detector, as discussed below.

Single photon avalanche diode

Single photon detection can be achieved using a variety of different techniques including photomultiplier tubes, superconducting nanowires (SNSPDs) and single photon avalanche diodes (SPADs). SPADs offer unique capabilities given their small device size, low power consumption and controllable detection range. The underlying principle of SPAD technology resides in the operation of a standard avalanche photodiode (APD). By inducing a large reverse bias across a photodiode, the generated carriers can accelerate and gain energy from the electric field. The high-energy carriers impact atoms in the semiconductor lattice, causing the atoms to ionise in a process named impact ionisation. The carriers generated through impact ionisation also gain energy through the high electric field and the process repeats, causing an avalanche of carriers. In this process, the internal gain can be very high, meaning very low light signals can be detected without the need for external

amplification, this is what is known as an APD.

Extending this practice even further and increasing the bias voltage above what is known as the breakdown voltage, single photon detection becomes possible. The breakdown voltage is a threshold above which the photodiode readily conducts current. When operating above the breakdown voltage, a single carrier causes an avalanche that generates constant current flow across the photodiode. To stop the current flow, the bias voltage must be dropped below breakdown voltage. The key resulting difference is that the current across an APD increases and decreases proportionally with input light intensity. In a SPAD, a flow of current represents the presence of a photon, at which point it must be reset before it can detect another photon. The time it takes for the detector to reset is known as the deadtime. During this time, the detector is effectively blind to incoming photons. Each time a single photon is detected, it sends an electrical pulse to the single photon correlator, as discussed below. Throughout this thesis, the IDQ-230 infrared single photon detector is used which has a timing resolution of around 0.1ns. It is possible to run this detector in both gated and free running mode. In gated mode, when a photon is absorbed by the detector but the gate is closed, it will not trigger, meaning no associated deadtime. This means that as soon as the gate is open, the detector is guaranteed to be 'on'. This is very useful for running several detectors at the same time, for example in coincidence detection. It is also useful when unwanted light impinges the SPAD operation. The gated mode will reduce the level of noise and afterpulsing effects. For the measurements undertaken here, only a single detector is used so it is kept in free running mode to reduce complexity. The deadtime can be altered in this detector, a shorter deadtime leads to higher afterpulsing but more counts per unit time. In all experiments carried out in this project, it is kept at 10µs.

Single photon correlator

A single photon correlator measures the time between the reference pulse from the laser and the photon arrival pulse from the SPAD. The module used in this work is a Becker-Hickl SPC-130. The electrical reference pulse triggers a rising voltage, this is stopped by a second electrical pulse from the SPAD. Therefore, the amount that the voltage rises directly relates to the time between the two consecutive pulses. By repeating this measurement many times, a histogram of arrival times builds up. This produces a time domain measurement of the excited sample. The TCSPC set-up is used in conjunction with the spectrometer so that time domain measurements of a

specific wavelength can be performed.

2.4.3 Cryogenics

In chapter 6, measurements at 70K are performed. To do this, an open cycle continuous flow cryostat is used. A pressurised liquid nitrogen (LN) container enables the flow of LN through a coil in the bottom of the cryostat. This cools a stage at the top of the cryostat. The stage has piezoelectric-based nanodrivers that control the position in X, Y and Z of the sample during measurements. The temperature of the stage is measured at both the top and bottom. A temperature difference of around 20K exists between the top and bottom due to poor thermal conduction in the Piezo stack. A heater is installed in the stage to specifically control the stage temperature. The sample is thermally coupled to the stage using vacuum grease. The actual temperature of the sample can also be measured using the bandgap of the sample substrate as this is directly proportional to temperature. The stage used here is an Attocube ANP Nanopositioner and the cryostat is the Janis ST-100 Optical Cryostat.

Chapter 3

Optical frequency comb generation via cascaded photonic crystal modulators

3.1 Abstract

In this chapter, OFC generation based on all-optical modulation of light in nanophotonic structures is proposed. A theoretical model based on temporal coupled mode theory is developed to describe cascaded all-optical PhC intensity and phase modulators. Using a pump light with a sinusoidal waveform, a carrier light is modulated to generate an OFC. Various PhC cavity-waveguide integration schemes are analysed in terms of their OFC generation capability. By manipulating the modulation power and device dimensions, a flat OFC that spans over 600GHz is delivered. The proposed system offers OFC generation with tunable combline spacing using nanoscale devices with high-density integration capabilities.

3.2 Introduction

Microwave photonics (MWP) research has enhanced the optical communication industry and is expected to play an essential role in the future of PICs [5]. The applications behind PICs have facets in both analogue and digital signal processing. Modern PICs are transforming into sophisticated on-chip photonic networks. With this transformation, the need for integrated devices that can generate and process microwave photonic signals becomes apparent. The delivery of integrated MWP systems [79] requires

the dense integration of coherent light sources [80]. One approach is to use multi-wavelength sources, such as optical frequency combs (OFCs). In recent years OFC generation has become an indispensable building block that has taken many forms [32], in this chapter a new method to generate nanoscale OFCs is proposed.

Among the available OFC generation technologies, optical parametric oscillation based on micro-resonators has hitherto prevailed as a simple and elegant solution towards on-chip OFCs [77]. With careful consideration of the dispersion characteristics, optical nonlinearity and fine tuning of the pump laser, chip-scale coherent OFC generators have been realised [32]. However, the pump-to-comb efficiency can be very low, often less than 1% for the bright soliton case [150]. Furthermore, micro-resonator based combs produce a fixed FSR between comblines which is dependent on the resonator size.

Defects in the PhC lattice produce cavities and waveguides that have the ability to modulate the intensity and phase of an input carrier light [151, 136]. The high Q/V ratio in PhC cavities leads to highly nonlinear optical processes which facilitate low power all-optical intensity modulation (IM). Switching energies of less than 1 femto-joule per bit [10] have been demonstrated for PhC cavity-based IM and a range of material platforms have been studied to tailor the operation wavelength and modulation bandwidth [108, 144, 99]. Embedded quantum dots (QDs) in a PhC waveguide enhance third order nonlinear susceptibility which causes cross phase modulation through saturable absorption of the QD layer [152, 153, 135]. A pulsed pump light can therefore modulate the phase of an input carrier light via a PhC waveguide.

This chapter is split into two sections; the first models cascaded PhC cavity-based intensity modulators (IM) in both series and parallel. The second models PhC cavity-based IMs followed by PhC waveguide-based phase modulators (PM). In both instances, the potential for OFC generation using nanoscale optical devices is analysed. In generating an OFC through optical modulation of PhC cavities and waveguides, this work looks towards improving spectral homogeneity, reducing the device volume and exploring the potential for nanoscale photonic integration of OFCs.

The rest of this chapter is organised in the following way: first, an overview of EO modulation-based OFC generation is given. This will give an understanding of the mechanisms used to produce an OFC via the modulation of the carrier light characteristics. Then the equations used to simulate both PhC-based IM and PM are derived. Following from this, the output from a PhC IM is analysed in terms of its time and frequency response. Us-

ing this information various integration schemes, whereby IMs are cascaded in series and parallel, are analysed. The OFCs generated through this mechanism are then analysed in terms of their spectral broadness and combline homogeneity. In the next section, a cascaded IM PM scheme is analysed. The effect of PhC waveguide length on the generated OFC is studied as well as the power of the modulating control light. Finally, the two schemes are compared in terms of their simplicity, OFC generation capability and experimental realisation potential.

3.2.1 Modulation-based OFC generation overview

A common method of OFC generation is the use of cascaded EO $LiNbO_3$ intensity modulators (IM) [47]. Using a single IM, the light is modulated with a sinusoidal electrical signal. This generates sidebands in the frequency response of the modulated light. The position of these sidebands relative to the carrier light is dependent on the frequency of the modulating electrical signal, such that $\omega_{sb}(n) = \omega_c \pm n\omega_{rf}$. Where ω_{sb} is the angular frequency of the n^{th} sideband and n is the number of sidebands away from the initial carrier frequency, ω_c. ω_{rf} is the frequency of the sinusoidal electrical signal. The amplitude of the sidebands is determined by the modulation depth and phase shift of the modulator which is governed by the voltage of the electric signal and the DC bias, respectively. By fine control of these parameters, an intensity modulator can generate multiple sidebands in the frequency response of the modulated light which have homogeneous power distribution [46]. The use of a second IM which leads from the output of the first IM results in an increase in the number of available comblines, a diagram representing this configuration is given in Fig. 3.1(a). In this instance, the voltage of the RF and DC bias is kept the same but the modulation frequency is a fraction of the first IM. Each of the initial comblines from the first IM then becomes a seed for the second IM and comblines are generated with a smaller FSR, which generates a large number of comblines in the modulated light spectrum. This technique provides a simple solution to generating a multiple wavelength source.

By cascading an intensity and phase modulator together in series, as shown in Fig. 3.1(b), it is also possible to generate an OFC based on time to frequency mapping. The carrier light is intensity modulated to generate a flat-topped pulse in the time domain. This flat-topped pulse is then focused into a very short pulse by ensuring a time varying quadratic phase shift is incident on the intensity modulated signal via a PM. In doing so, the shape of the intensity modulated signal is mapped into the frequency

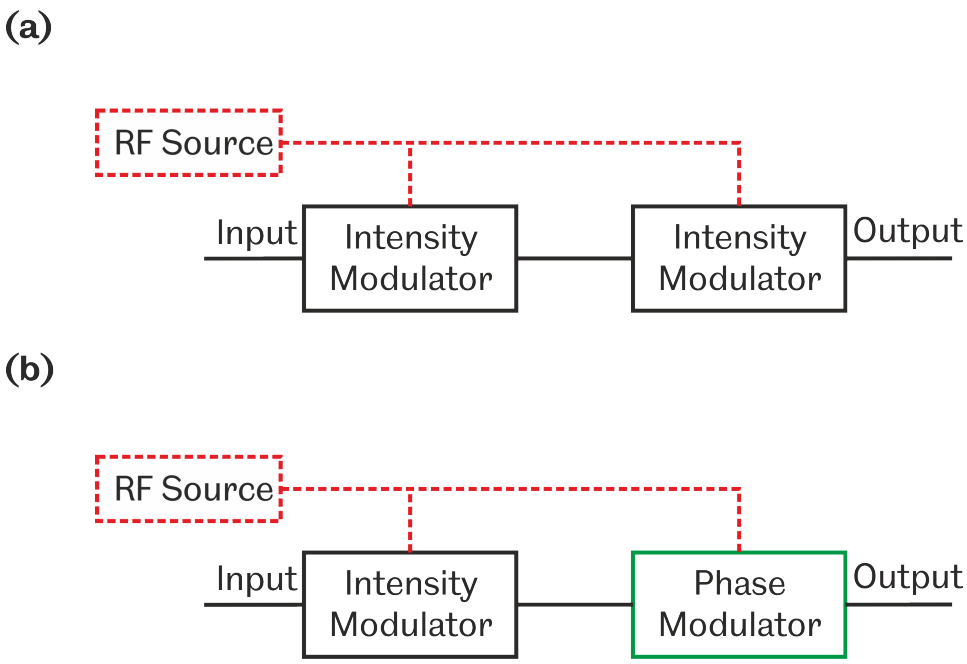

Figure 3.1: Diagram of modulation schemes used to generate an OFC (a) Cascaded IMs (b) Cascaded IM/PM

domain. The spectral shape of this pulse then matches the temporal shape of the pulse at the output of the IM. This leads to a flat-topped OFC being produced from a simple device made up of an intensity and phase modulator. Time to frequency mapping was originally used for characterising ultra-short optical pulses [52] but has been adapted for the generation of OFCs [56]. This method of OFC generation is a common technique that has seen many advances in terms of electro-optical modulation-based OFC generators [40]. However, implementing this method using chip-scale components causes difficulties due to the relatively large waveguides necessary to achieve deep enough modulation. In the work presented here, the operating principles outlined above are adapted and built upon for the implementation in PhC waveguides and cavities.

3.3 Methods

The device structure comprises of InAs QDs, with broadband emission which peaks at around 1600nm, embedded in a 220nm thick InGaAsP membrane. Holes are etched into the membrane in a triangular lattice in order to produce a photonic bandgap. A lattice constant of 480nm and fill factor of 0.29 ensure a fundamental mode wavelength at 1551nm when three holes are removed to produce an L3 cavity. A side profile SEM image of an L3 device, fabricated as part of this project, is shown in Fig. 3.3(a). The fundamental mode of an L3 cavity with these dimensions has been simulated using Comsol and shown in Fig. 3.3(b). In chapter 5, the L3 cavities are experimentally characterised. To create a waveguide through which light within the photonic bandgap can propagate, a line of holes are removed from the structure, as depicted in Fig. 3.2(a) and 3.2(b). This section outlines the equations used to model both cavity-based IM and waveguide-based PM.

3.3.1 Implementing intensity modulation via PhC cavities

Two schemes that are commonly used to implement an IM using PhC cavities and waveguides have been studied here, they are side-coupled and direct-coupled cavity-waveguide structures, as shown in Fig. 3.2(a) and 3.2(b), respectively. Figure 3.4(a) shows the transmission characteristics for both the side and direct-coupled scheme. In the direct-coupled scheme, when the frequency of the propagating wave and the cavity resonance are equal, the light can transmit to the output waveguide. At all other frequencies, the light reflects at the waveguide-cavity interface. Conversely, for the side-coupled

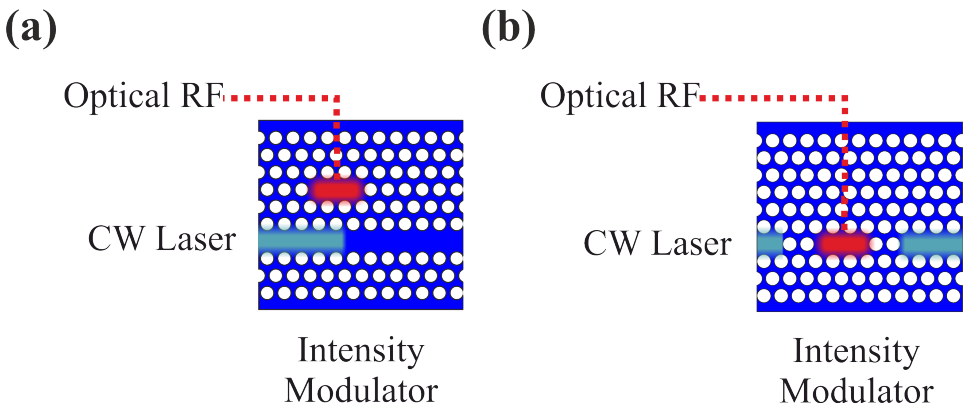

Figure 3.2: (a) side-coupled cavity modulation scheme (b) direct-coupled cavity modulation scheme

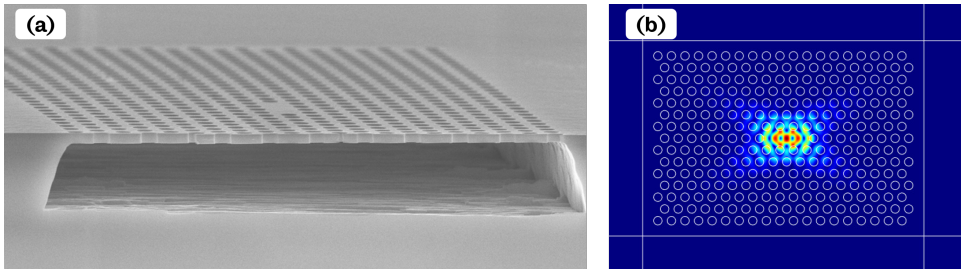

Figure 3.3: (a) An SEM image of a photonic crystal membrane with an L3 cavity in the centre (b) FEM calculation of the fundamental mode at 1551 nm.

scheme the interference between the energy in the cavity and the propagating wave through the waveguide causes a drop in the transmission at the cavity resonance. However, at all other frequencies, the wave can transmit through the device. To generate an all-optical switch, the cavity resonance can be perturbed via optically induced nonlinear interactions. Fig. 3.4(b) is a 3D map which shows the perturbation of the cavity resonance with the presence of a pump pulse. The white lines in Fig. 3.4(b) show the cavity mode spectrum. It gives an illuminating example that shows how a so-called cavity switch works when a very short pulse of 1.5 ps excites the nanophotonic cavity [10, 108]. The cavity mode goes from 1551 nm and increases to 1552 nm when the pump pulse is incident. When the direct-coupled scheme is used, the carrier light wavelength is set to 1552 nm. The pump light will cause the cavity to come into resonance with the carrier light, hence generating transmission of the carrier light. For the side-coupled scheme, the carrier light is set to the initial cold cavity resonance at 1551 nm, meaning that no light can transmit through the device. The pump light causes the cavity to come out of resonance with the carrier light, hence allowing transmission.

This method of all-optical modulation-based on PhC structures is a well-established technique [10, 154, 102] in which various optical nonlinearities are utilised. Since optical nonlinear effects are the basis for realising a cavity resonance shift, it's necessary to analyse the nonlinear process in the target situation. In principle, any type of nonlinearity can be utilised for shifting the cavity resonance and in this study, both carrier and intensity-based nonlinearities are considered. By exciting a PhC cavity with an increasing pump energy, the refractive index of the cavity material will decrease due free carrier dispersion [101] through carriers excited by two photon absorption (TPA), this term is calculated using Eq 3.5. Bandfilling is another common phenomenon used in all-optical switching where the material absorption changes as the conduction bands are filled. However, this can only be utilised when the cavity resonance is close to the material band edge. Therefore this effect can be neglected due to the use of an InP-based membrane structure. In addition to this, absorption of the QD layer within the membrane leads to an enhanced third order nonlinear susceptibility [9, 155] which will change the refractive index of a material, as defined through the Kerr coefficient in Eq. 3.3. Cavity resonance shifts due to thermal effects occur over a relatively long time [11] and the band-filling effect is negligible due to low pump photon energy, so these are not included in the model.

A model based on temporal coupled mode theory (CMT) [108, 88] is used to numerically analyse the optical modulation characteristics of the

Table 3.1: Parameters used for CMT calculations

Symbol	Parameter	Value
Q_{int}	Intrinsic Q factor	variable
Q_c	Coupling Q factor	variable
γ_{QD}	Decay rate of carriers in QDs	1.25×10^{10}s^{-1} [157]
σ_{FCA}	FCA cross section	4.5×10^{21} m^2 [108]
β	TPA coefficient	2.4×10^{-10} m/W [108]
V_{TPA}	TPA volume	$3.13(\lambda/\mathrm{n})^3$ [102]
n_2	Enhanced Kerr coefficient	1.24×10^{-15} m^2/w [136]
n	Refractive index	3.17 [108]
V_{car}	Free carrier cavity volume	$4.62(\lambda/\mathrm{n})^3$ [102]
τ_{fc}	Free carrier lifetime	50ps [108]
α	Scattering loss of PhC waveguide	230 m^{-1} [158]
n_g	Group index	40 [152]

two schemes shown in Fig. 3.2(a) and 3.2(b). The equations used in this chapter are derived from common CMT techniques for the modelling of PhC all-optical switches [108, 156, 109, 144]. The simulations are carried out using a standard routine for solving ordinary differential equations. The dynamic variables in the model are the field amplitude and the free carrier density inside the cavity. The physical parameters used are shown in Table 3.1. The material system is made up of a InP membrane with InAs quantum dots embedded within the membrane.

The devices shown in 3.2(a) and 3.2(b) are driven by an input field from the left waveguide, the field amplitude in the waveguide is given by $s_{in}^{p,c}$, where p and c represent the pump and carrier light respectively. The amplitude of the cavity field is given in the form $a_{p,c}$. The energy of the field in the cavity is $|a_{p,c}(t)|^2$ and the power of the field in the waveguides is equal to $|s_{p,c}(t)|^2$. Using the slowly varying envelope approximation to define the field amplitude in the cavity gives the relation:

$$\frac{da_{p,c}(t)}{dt} = (-i(\omega_0 + \Delta\omega_p(t) - \omega_{p,c}) - \gamma_{total}/2)a_{p,c}(t) + us_{p,c}^{in}(t) \tag{3.1}$$

It is assumed that $a_p(t) >> a_c(t)$, so only $a_p(t)$ will have an effect on the change in cavity resonance, denoted by $\Delta\omega_p$. In Eq. 3.1, ω_0 is the angular frequency of the cold cavity resonance, $\omega_{p,c}$ is the angular frequency of the

input light, for either the pump or carrier light. The total energy decay rate in the cavity is represented by $\gamma_{total} = \gamma_{int} + 2\gamma_c + \gamma_{QD} + \gamma_{FCD} + \gamma_{TPA}$ The intrinsic loss rate γ_{int} is dependent on the vertical Q factor of the cavity, such that $\gamma_{int} = \omega_0/Q_{int}$. $\gamma_c = \omega_0/Q_c$ represents the coupling strength between the cavity and the waveguides. γ_{QD} represents QD absorption recovery time. $\gamma_{TPA} = K_{TPA}|a(t)|^2$ and $\gamma_{FCA} = K_{FCA}N_c(t)$ represent the losses due to optical absorption via TPA and FCA, respectively. The coupling coefficient is defined as $u^2 = 2\gamma_c$[88]. The shift in cavity resonance is dependent on the energy inside the cavity and the density of generated free carriers, given by:

$$\Delta\omega_p(t) = -(K_{kerr}|a_p(t)|^2 - K_{FCD}N_c(t)) \tag{3.2}$$

K_{FCD} represents the contribution from free carrier dispersion in the InGaAsP membrane which blueshifts the resonance frequency [108]. K_{Kerr} represents a simplified value for the third order nonlinear dynamical process [10, 102] which redshifts the cavity resonance. The expansion coefficients K_{Kerr}, K_{TPA}, K_{FCD} and K_{FCA} are given by:

$$K_{kerr} = \frac{\omega_0 c n_2}{n_{eff}^2 V_{kerr}} \tag{3.3}$$

$$K_{TPA} = \frac{\omega_0 c \beta_{TPA}}{n_{eff}^2 V_{kerr}} \tag{3.4}$$

$$K_{FCD} = \frac{e^2}{2n^2\omega_0\epsilon_0 m^*} \tag{3.5}$$

$$K_{FCA} = \frac{\sigma c}{n} \tag{3.6}$$

where e is the elementary electric charge, n is the refractive index of InGaAsP, ϵ_0 is the vacuum permittivity, σ is the absorption cross section for the carrier density $N_c(t)$. m^* is the effective electron mass of InGaAsP, $0.06m_0$, c is the speed of light in vacuum, n_2 is the enhanced Kerr coefficient and V_{Kerr} is the Kerr nonlinear volume used to characterise the average saturable absorption rate in the cavity. $N_c(t)$ gives the carrier generation term due to TPA in the device [108, 144], this is given by:

$$N_c(t) = -\frac{N_c(t)}{\tau_{fc}} + \frac{\beta_{TPA}|a(t)|^2}{2\hbar\omega V_{car}}|a(t)|^2 \tag{3.7}$$

where $\hbar$ is Planck's constant, τ_{fc} is the free carrier lifetime and V_{cav} is the cavity volume for free carriers [102].

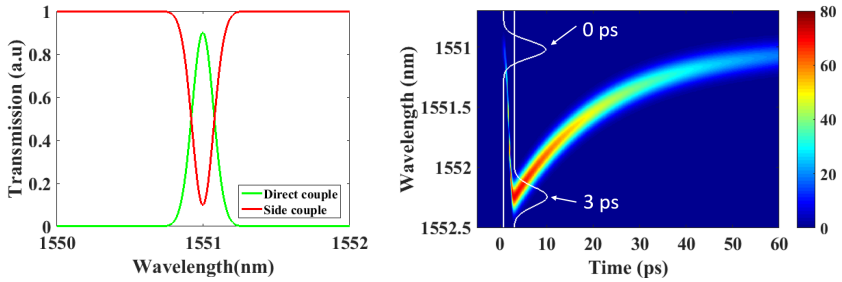

Figure 3.4: Modelling results of devices shown in Fig. 3.2, parameters given in Tab. 3.1. (a) Frequency domain transmission characteristics for both the side and direct-coupled cavity scheme. (b) A 3D plot, showing how the resonant cavity mode shifts when a pump light is incident on the device, the white lines represent the mode spectrum at 0 ps and 3 ps.

In the side-coupled scheme, shown in Fig.3.2(a), the output of the device will be dependent on the energy inside the cavity, the coupling factor and the energy from the input directly. This gives rise to:

$$s_c^{out}(t) = u\frac{a_c(t)}{2} + s_c^{in}(t) \tag{3.8}$$

s_{out}^c is the field amplitude in the output waveguide. Conversely, in the direct-coupled scheme, shown in Fig.3.2(b), the output energy will only depend on the energy coupled into the waveguide from the cavity. This gives rise to equation 3.9:

$$s_c^{out}(t) = u\frac{a_c(t)}{2} \tag{3.9}$$

3.3.2 Implementing phase modulation via PhC waveguides

The output from the IMs, given in Eq. 3.8 and 3.9, is fed into an all-optical phase modulator implemented via a PhC waveguide. In this scheme, a pump light is used to induce saturable absorption of QDs in the waveguide, which leads to a refractive index change in the waveguide material via Kramers-Kronig relation [136]. The carrier light experiences a corresponding refractive index change, resulting in a phase shift of the carrier light. This phase shift is therefore proportional to the intensity profile of the pump light [152, 136]. In this study, a single optical pump light is used for both the intensity and phase modulator, this ensures coherence between

the two modulators. The induced phase shift is calculated using standard equations for PM:

$$E^{out}(t) = |s_c^{out}(t)|^2 exp(i\Delta\theta - \alpha L_{wg}) \tag{3.10}$$

$s_{out}^c$is the output from either the side or direct-coupled scheme. α is the scattering loss within the waveguide. The propagating signal will deplete due to both scattering losses and TPA induced attenuation. The induced scattering loss will be far greater than the TPA-induced loss to the extent that the TPA term can be neglected [158, 159]. $\Delta\theta$ is the phase modulation index (PMI) in a PhC-waveguide PM [159], given by:

$$\Delta\theta(t) = k_0 L_{wg} \frac{n_g}{n_0} n_2 \frac{|s_p^{in}(t)|^2}{A} \tag{3.11}$$

where k_0 is the wavenumber in vacuum, L_{wg} is the waveguide length, n_g is the group index and A is the cross section of the waveguide mode. The nonlinear refractive index coefficient in the waveguide, n_2, is derived from the literature, where similar schemes have been realised [152, 136]. This is estimated to be $1.24 \times 10^{-15} m^2/W$. The PMI is therefore dependent on two key parameters, the length of the waveguide and the power of the pump light.

3.4 Cascading PhC intensity modulators to generate an OFC

In this section, IMs based on a PhC cavity side-coupled to a waveguide are cascaded in both series and parallel, as shown by Fig. 3.5(a) and 3.5(b), respectively. An optical RF signal with a 10GHz sinusoidal intensity profile is used to pump the cavities and control the transmission of the carrier light. Initially, a single cavity coupled to a waveguide is analysed to understand the intensity profile of the carrier light at the output of both the side and direct-coupled cavity.

Fig. 3.6(a) shows one pulse of the sinusoidal waveform at 10GHz, given by the dashed line and the intensity modulated carrier light at the output of the side-coupled cavity-based IM, given by the solid black line. The output from this side-coupled scheme shows a broad, asymmetric pulse. This shape is due to the carrier light transmitting through the device as soon as its frequency is shifted from the cavity resonance. A sharp increase in the transmission is observed since the carrier light travels directly through

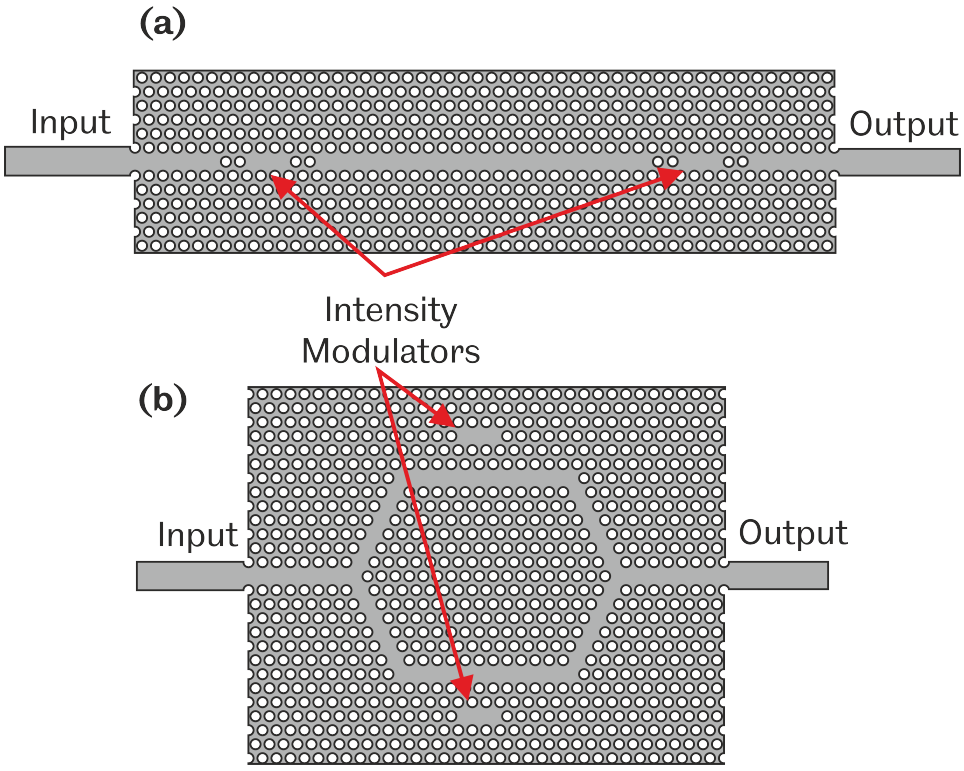

Figure 3.5: Schematics for the proposed photonic crystal (PhC) all-optical optical frequency combs (OFC) generators. (a) Two direct-coupled cavity modulators in series. (b) Two side-coupled cavity modulators in parallel.

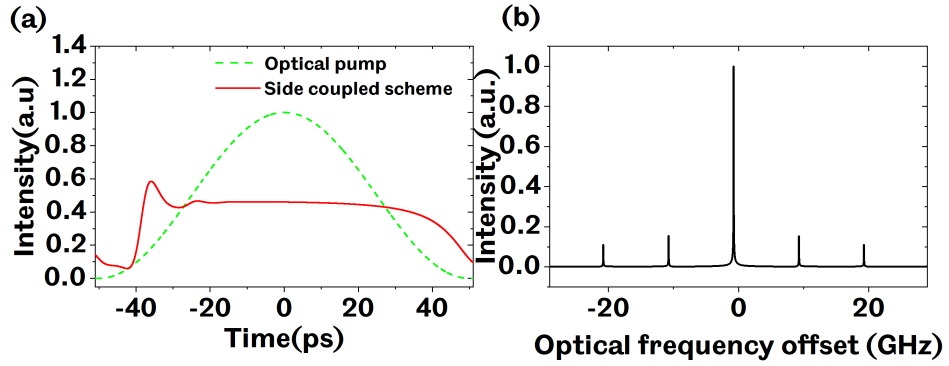

Figure 3.6: Modelling results of side-coupled cavity scheme, shown in Fig. 3.2(a), parameters given in Tab. 3.1. (a) The time domain response of the modulated carrier (solid black line) and the RF pump (green dashed line) light. (b) The frequency domain response of the intensity modulated carrier light.

the waveguide to the output of the device. The frequency response of the carrier light is given in Fig. 3.6(b). The broad pulse size dictates that the sidebands produced through sinusoidal modulation are suppressed, giving a power disparity of 9.5dB between the initial carrier light and the generated sidebands. Their position relative to the carrier light frequency, denoted as 0 on Fig. 3.6(b) is a direct relation to the modulation frequency at 10 GHz.

The temporal response of the carrier light through a direct cavity modulator matches the pump light more closely than the side coupled modulation scheme. As the cavity resonance goes towards the carrier light frequency, more energy can transfer to the output waveguide, therefore matching the modulation light closely, as shown in Fig. 3.7(a). The frequency response at the output of the direct coupling IM scheme is given by Fig 3.7(b). More prominent sidebands are present for the direct-coupled scheme, giving a power disparity of only 5.1dB because the signal has a more sinusoidal profile.

The schemes described in section 3.2.1 [47, 46] can then be adapted so that two cavity-based IMs are cascaded in series. In this scheme, two separate modulation frequencies are needed so that sidebands can be produced at two spacings. Prevalent sidebands produced from each of the IMs will generate a flatter comb. Comparing the side and direct-coupled schemes, the direct-coupled scheme generates higher intensity sidebands. It is therefore suited to this type of OFC generation based on cascaded IMs in series.

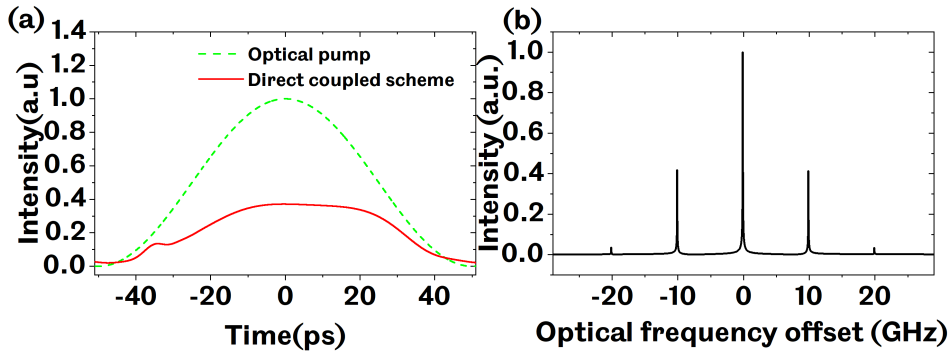

Figure 3.7: Modelling results of direct-coupled cavity scheme, shown in Fig. 3.2(a), parameters given in Tab. 3.1. (a) The time domain response of the modulated carrier (solid red line) and the RF pump (green dashed line) light. (b) The frequency domain response of the intensity modulated carrier light.

When two direct-coupled cavities are in series with each other, as shown in Fig. 3.5(a), the output from the first IM will be the input for the second. The system is assumed to consist of two separate PhC IMs where the output of the first IM, $s_c^{out}(t)$ given by Equation 3.9, is used as the input for the second IM. The equation for the carrier light energy inside the second cavity (a_{c2}) is given by:

$$\frac{da_{c2}}{dt} = (-i(\omega_0 + \Delta\omega_{p2}(t) - \omega_c) - \gamma_{total})a_{c2}(t) + \sqrt{2\gamma_c}s_c^{out}(t) \tag{3.12}$$

where $\Delta\omega_{p2}$ is the change in cavity resonance due to the secondary pump light which has a sinusoidal intensity profile with a frequency of 3.3GHz. The output from the second IM is then given by:

$$s_{c2}^{out}(t) = u\frac{a_{c2}(t)}{2} \tag{3.13}$$

Figure 3.8 shows the frequency response at the output of the second IM. The pump light that is perturbing the second IM has a modulation frequency one third that of the first, meaning that the generated sidebands will have an FSR one third that of the original FSR. Two extra comblines are generated on each side of the carrier frequency; they are the sum of the generated sidebands from both the initial carrier light and the sidebands generated from a single IM. This scheme then generates 7 comblines that are 3.3GHz apart.

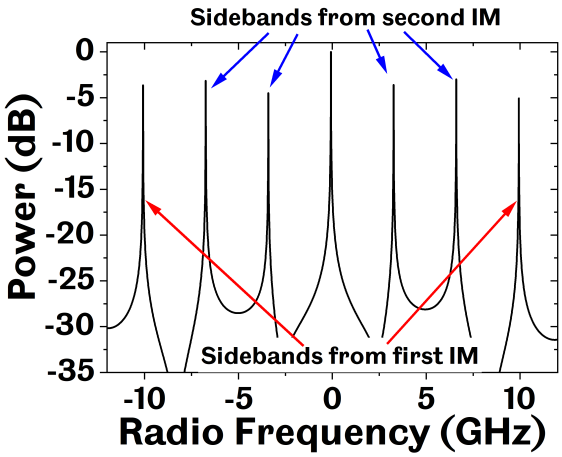

Figure 3.8: Modelling results showing the generated OFC from two all-optical PhC direct-coupled modulators in series, as depicted in Fig. 3.5. Modelling parameters given in Tab. 3.1.

Although adopting such a scheme using optical modulators is theoretically possible, it would prove cumbersome in terms of experimental realisation. Difficulties would arise in coupling two separate modulating light sources into the device for each cavity. One option might be to couple the pump light from the top, rather than the side, however this would reduce the overall efficiency of the device. A more viable option is to cascade the cavities in parallel, as in Fig. 3.5(b).

Using the parallel scheme, side-coupled cavities are used instead of direct-coupled cavities to generate an OFC because the generated pulse has a quick rise time and higher extinction ratio. These attributes mean that short, high-intensity pulses are produced. The PhC device design, outlined in Fig. 3.5(a), consists of a waveguide leading into a Y junction symmetric splitter [160, 161], where the pump and carrier light split evenly into each arm. An L3 cavity is coupled to each arm of the device to induce intensity modulation of the split carrier light. The two intensity modulated carrier lights then interleave via a Y junction to produce a dual modulated carrier signal. This technique of waveguide splitting and recombining in PhC waveguides is common when implementing PhC-based Mach-Zehnder interferometers [162, 135]. The interleaved pulses at the output of the devices are given by:

$$s_c^{out}(t) = (u\frac{a_{c1}(t)}{2} + s_{c1}^{in}(t)) - (u\frac{a_{c2}(t)}{2} + s_{c2}^{in}(t)) \tag{3.14}$$

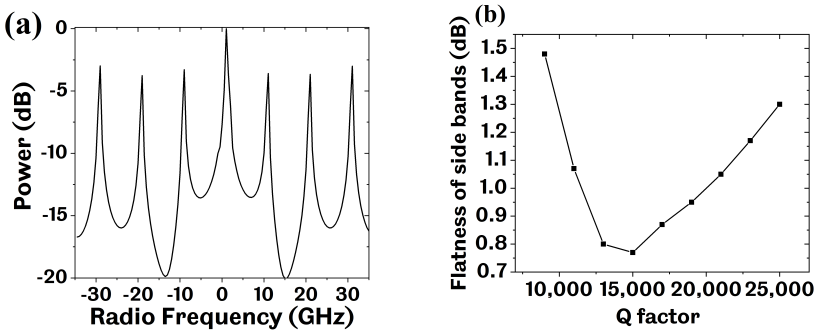

Figure 3.9: Modelling results of device shown in Fig. 3.5(b), parameters given in Tab. 3.1. (a) The generated OFC from two all-optical PhC side-coupled modulators in parallel. (b) Homogeneity between the sidebands against the cavity Q factor.

where $s_{c1}^{in}(t)$ and $s_{c2}^{in}(t)$ represent the input to the bottom and top cavity respectively. $a_{c1}(t)$ and $a_{c2}(t)$ represent the amplitude of the carrier signal in the bottom and top cavity, respectively. Using this process, the shape of the carrier light will be determined by a number of parameters unique to this type of modulation, these include the phase difference of the pump light in each arm, the coupling efficiency of the light into the cavity and the Q factor of the cavity.

This method of modulation generates 3 comblines with a maximum intensity difference of 1dB on each side of the central carrier frequency, hence 7 comblines all together as shown in Fig. 3.9(a). Additional comblines exist at much weaker intensities further away from the initial carrier frequency. As can be seen, the power disparity between the initial carrier light and the sidebands is around 5dB. Nevertheless, the homogeneity in intensity between the sidebands remains very uniform, at around 1dB. The homogeneity of these sidebands is dependent on the parameters stated above and can therefore be optimised to generate a very flat comb, as shown in Fig. 3.9(a).

Figure 3.9(b) shows the effect the intrinsic cavity Q factor has on the uniformity with an optimum Q factor of 15,000. This is due to the shape of the carrier light through each arm when it recombines to generate the intensity-modulated signal. Cavity Q factors in PhC L3 cavities can be greatly enhanced by altering the position of the holes surrounding the L3 cavity [163]. It is therefore possible to design the L3 cavity with the desired Q factor via fine tuning of the hole positions. The 7 comblines observed

have a maximum fluctuation in intensity of less than 1 dB if the carrier frequency is not taken into consideration. In the literature, the intensity of the initial carrier frequency has also posed a problem in modulation-based combs [164] and micro-cavity-based combs, due to the high energy needed to induce nonlinearity within the micro-cavity [8]. A method to overcome this is to include a cavity-based notch filter. To obtain the required suppression of the carrier signal, the coupling coefficient, size and loss coefficient of the filtering cavity can be optimised. The filter will induce an overall loss to the carrier wave signal of around 5 dB, but the flatness of the 7-line OFC will be greatly enhanced.

During experimental implementation of the proposed scheme, there will be disparity between the optimised parameters given here and the fabricated device. Although this will have an effect on the OFC quality, it is expected that a 7-line OFC can be observed for a broad range of parameter values. Figure 3.9(b) shows that for cavity intrinsic Q factors between 10,000 and 25,000 the sideband intensity fluctuates to a maximum of 1.5 dB. This shows that a wide range of Q factor values will still achieve a 7-line OFC. The coupling coefficient will also affect the output signal through the obtainable extinction ratio. This will have an effect on the intensity of the generated comblines relative to the intensity of the central carrier frequency. However, 3 sidebands on either side of the initial carrier frequency can still be generated for a broad range of realistic coupling coefficients.

3.5 Cascading PhC intensity and phase modulators to generate an OFC

When cascading a PhC-based IM and PM, both the side and direct-coupled scheme can be used to generate an OFC. This is because the mechanism behind the OFC generation is fundamentally different to cascading IMs. As outlined in section 3.2.1, a quadratic phase shift which is incident on a intensity modulated pulse will lead to time to frequency mapping of the intensity profile. One pump light is used to induce both intensity and phase modulation. This ensures coherence between the two modulators and enables realistic experimental conditions. A schematic of the device is given in Fig. 3.10. The pump light has a sinusoidal intensity profile with a frequency of 10GHz. The sinusoidal shape of the pump light will induce a quadratic phase shift for the duration of the carrier pulse. The output response in the frequency domain from the PM is calculated via the Fourier transform.

An important variable when analysing the functionality of an OFC gen-

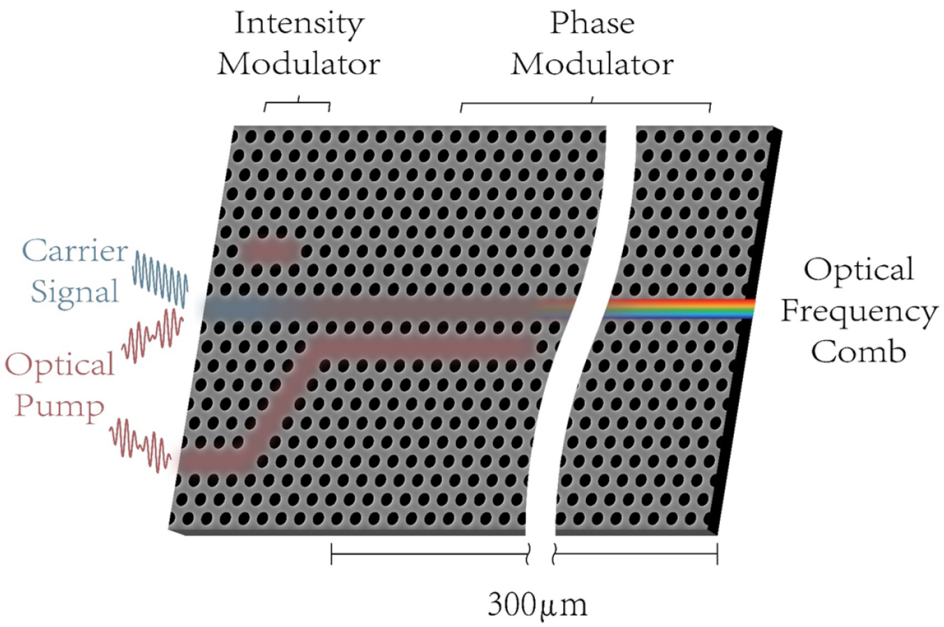

Figure 3.10: An artistic drawing of the proposed scheme, showing the implementation of 3.1(b) using PhC structures.

erator is the amount of input power needed to generate the resulting comb. In all calculations, the pump power is split between the IM and PM with a total pump power of 50mW. The very high light confinement obtainable in the L3 cavity dictates that the amount of power needed from the pump light to induce sufficient switching of the carrier light is less than the waveguide-based PM. It is found that a pump light power of 10mW causes sufficient intensity modulation. However a pump light power of 40mW is needed to induce sufficient PM of the carrier light. This higher power needed for the PM when compared to the IM is due to scattering of light in the waveguide and its larger size. These input powers are assumed throughout this chapter with exception of section 3.5.1, where the pump power is scaled equally for both the IM and PM.

Without a proceeding IM, an OFC is produced, this is shown in Fig, 3.11(a). The benefit of a cascading IM-PM scheme can seen from the comparison of Fig, 3.11(a) to Fig. 3.11(b) and 3.11(c). The resulting comb from the PM only scheme shows a nonflat spectrum, where the maximum combline difference has been calculated to provide a figure of merit concerning the comb flatness. In the case of PM without a preceding IM, the

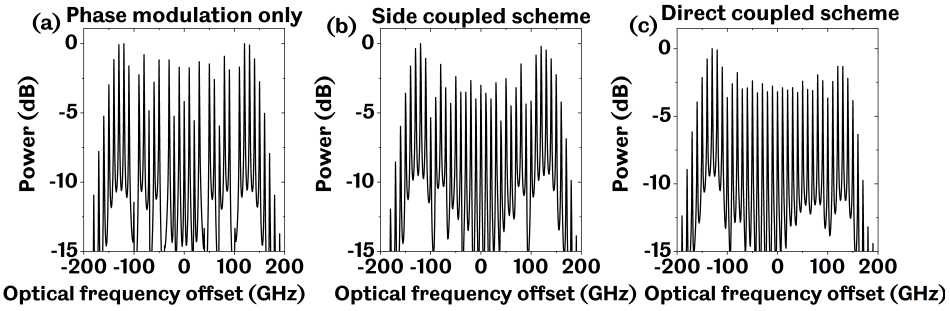

Figure 3.11: Modelling results which show the generated OFCs at the output of the device. Parameters given in Tab. 3.1. (a) shows the output without a PhC IM used, (b) shows the OFC using the side coupled cavity scheme, show in Fig, 3.10 and (c) shows the OFC from the direct coupled cavity scheme.

difference is 13.3dB. This is improved to 5.6dB for the direct coupled scheme and down to 3.6dB for the side-coupled scheme. Figure 3.6(a) shows the output from the IM when the side-coupled scheme is used. In this IM scheme, output pulse is slightly broader than the sinusoidal pump pulse used for modulation, as shown in Fig. 3.6(a). This means that at the beginning and end of each carrier pulse the induced phase shift will be very small, resulting in points where the instantaneous frequency function dwells and a drop in combline power is observed. This can be seen in the resulting OFC, given in 3.11(b), where the combline power drops at around -100 GHz and 100 GHz.

Conversely, the direct-coupled cavity-waveguide scheme follows the shape of the sinusoidal input more closely, as shown in Fig.3.7(a). The field amplitude in the output waveguide reaches its high output value when the pump light is close to the top of the sinusoidal curve. This results in a more parabolic phase shift being incident on the carrier pulse. This gives rise to more accurate mirroring of the signal and therefore a flatter comb, as shown in Fig. 3.11(c). There are exaggerated comblines around the OFC minima and maxima at -150 GHz and 150 GHz respectively. The slightly asymmetric shape of the output carrier light from the IM and the phase mismatch between the peak of the sinusoidal wave and the peak of the output wave, as depicted in Fig. 3.7(a), cause these exaggerated comblines.

This phenomenon has previously only been reported using electro-optic modulators [40]. In this case all-optical, nanoscale devices have been used to realise modulation-based OFC generation. Using a waveguide length of 300 µm, an OFC can be produced using both the side and direct cavity-

waveguide scheme as well as without a preceding IM as shown by Fig, 3.11. Although the use of a waveguide-based PM increases the overall device geometry, a waveguide length within the hundreds of microns shows a significant reduction in size when compared to EO waveguide-based PMs. To further scale down the size of PM devices, PhC cavities can be considered which will generate a scalable phase change by increasing the cavity Q factors [137].

3.5.1 System Optimisation

In the previous section, two cavity-waveguide IM configurations have been compared. It has been found that a direct cavity-waveguide configuration leads to a flatter OFC. In this section, the characteristics of the pump light used to modulate the carrier light are analysed for the direct-coupled scheme. Manipulation of the pump light modulation speed and power leads to a change in the resulting OFC characteristics. It is therefore possible to tune the OFC and increase the application versatility of the proposed device.

Using modulation-based OFC generation, the FSR between the comblines can be tuned by the modulation frequency, this leads to a number of varied applications. For example, tightly confined frequency components are needed for optical frequency synthesis of microwave signals [165], this can be achieved by decreasing the modulation frequency. However, for wavelength division multiplexing, a broader comb can prove beneficial as it spans a larger frequency band [46]. By increasing the modulation frequency, the FSR between the comblines is increased, hence broadening the comb. The maximum modulation speed of the PhC-based IM is a product of the cavity resonance switching time. To find the maximum modulation speed, a pump pulse with a pulse duration of 1.5 ps is incident on the cavity. Fig. 3.4(b) shows the dynamical change of the cavity resonance using a 1.5 ps pump pulse. The cavity switching time calculated here is less than 20 ps. Therefore, the maximum FSR between comblines is limited to 50 GHz. However, increasing the modulation speed above 50 GHz causes significant reduction in the extinction ratio attainable from the PhC IM. The FSR can also be tuned to produce very close comblines in the OFC spectrum by decreasing the modulation speed

It is possible to increase the number of comblines in the OFC at the output of the devices through manipulation of the waveguide length. As shown in Eq. 3.11, the PMI depends on the power of the pump light and the length of the PhC waveguide. A longer waveguide will enhance the PMI and therefore increase the spectral width of the OFC. In this study, the modulation speed is set to 10 GHz, which leads to an FSR of 10 GHz

between the comblines, the length of the waveguide is then increased from 200 µm up to 600 µm. Fig. 3.12(a) shows a waveguide length of 300 µm, the resulting OFC spans over 200 GHz, Fig. 3.12(b-c) shows waveguide lengths of 450 µm and 600 µm, respectively. Although the number of comblines and therefore the spectral width of the OFC is increasing, it comes at the cost of combline intensity homogeneity. By calculating the power for each of the generated comblines, an average combline power can be found which correlates to the overall flatness of the comb. As the waveguide length increases, the average combline power steadily decreases, as shown in Fig. 3.12(d). This is because the area over which the quadratic phase shift is induced on the pulses is increasing. As the area increases, the pump light that is incident on the carrier pulse causes dwelling of the frequency function on the outer edges of the OFC, inducing greater combline power disparity.

The number of comblines and therefore the spectral broadness of an OFC can also be optimised by manipulating the power of the pump light used. An increase in the power of the pump light will lead to a larger phase shift of the carrier light when propagating through the waveguide, thus increasing the spectral broadness of the resulting OFC. However, by increasing the power of the pump light going to the IM, a larger cavity resonance change takes place. This has a detrimental effect on the shape of the carrier light at the IM output because the cavity resonance shifts away from the carrier light wavelength at the peak pump power.

The red curve in Fig. 3.13(a) represents the output after the IM when a higher pump power is used but the carrier light frequency remains unchanged. A large dip in intensity is present when the pump light is at its maximum, at time 0. This is due to the wavelength mismatch between the carrier light and cavity resonance at this point. When this signal undergoes quadratic phase modulation via the PhC waveguide, this shape is mirrored in the frequency domain where a large dip is present in the OFC output spectrum, shown in Fig. 3.13(b). Although the power disparity of the comblines in Fig. 3.13(b) is large, the OFC spectral range has been improved to span over 600 GHz, this is due to the increased power in the PhC waveguide.

To generate a flatter comb, a pulse with a flat top is needed from the IM. To obtain this, the carrier light frequency can be tuned so that it matches the cavity resonance when the pump light is at its peak value. The blue curve in Fig. 3.13(a) shows the output of the IM using a 0.5 nm red shifted carrier light. A flatter OFC is observed in the frequency domain at the output of the device, as shown by Fig. 3.13(c). To increase the combline power homogeneity again, the carrier light can be shifted further, the green curve shows a 1.3 nm shifted carrier light. By shifting the carrier light

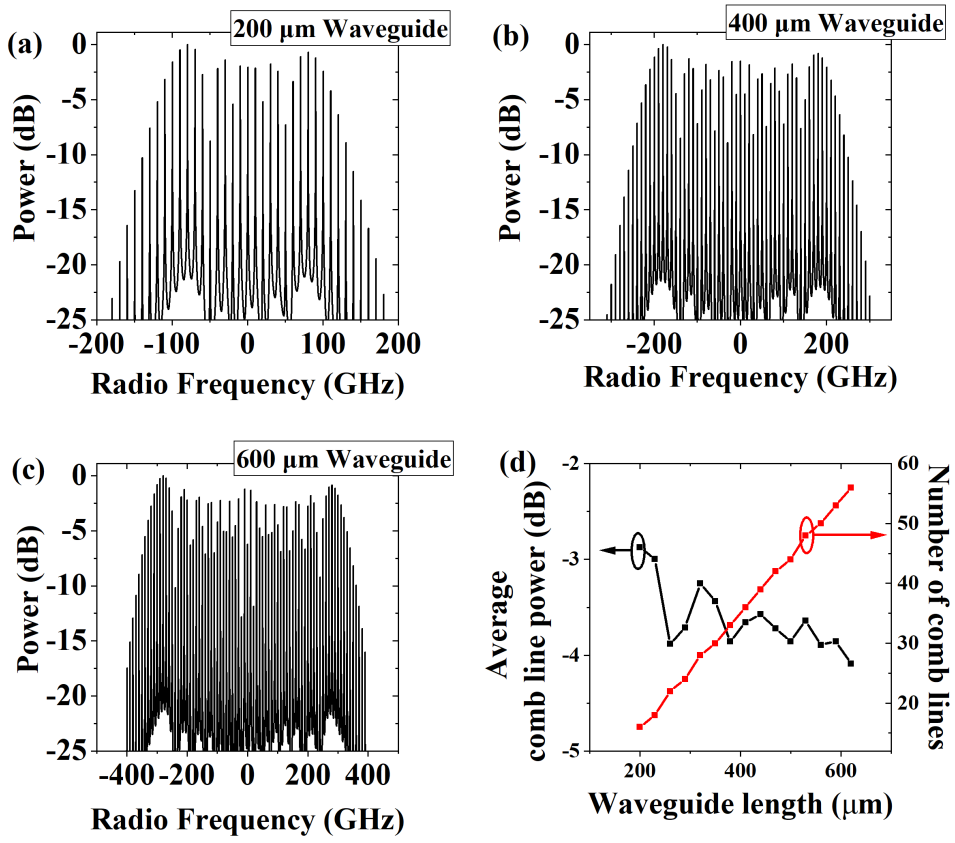

Figure 3.12: Modelling results, showing the effect on OFC generation by increasing the waveguide length (a) 300 µm waveguide, (b) 450 µm waveguide (c) 600 µm waveguide (d) shows the flatness and number of generated comblines against waveguide length. Modelling parameters given in Tab. 3.1.

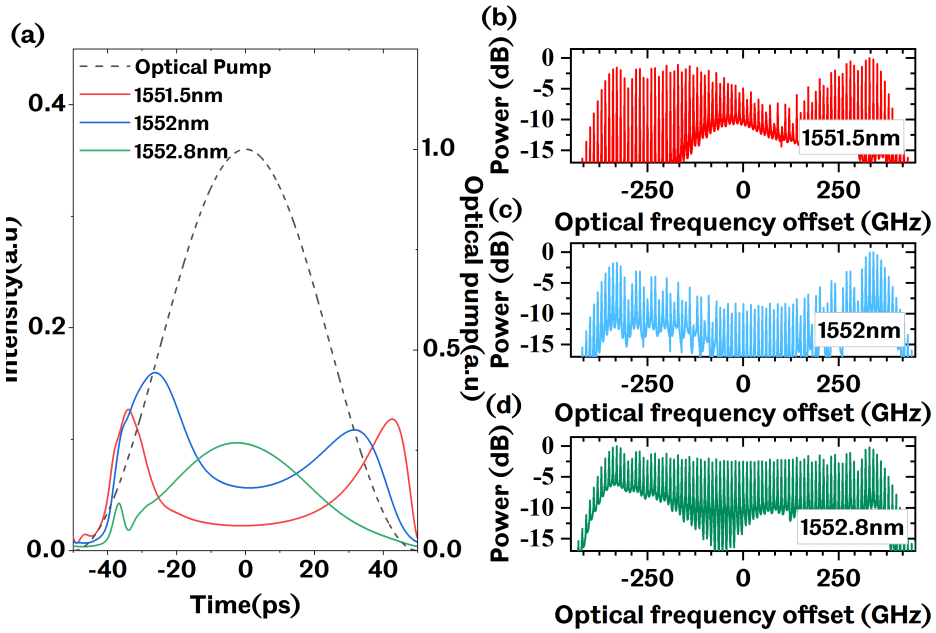

Figure 3.13: (a) Increased RF pump light (dashed line) with output of IM with no wavelength change (red), 1 nm wavelength change (blue) and 1.5 nm wavelength change (green). (b) The frequency response after PM for 0 nm shift, (c) 1 nm shift, (d) 1.5 nm shift. Modelling results, parameters given in Tab. 3.1.

by 1.3 nm, a flat-topped pulse is produced in the time domain. The corresponding time to frequency converted spectrum, Fig. 3.13(d), shows that by increasing the pump light power and shifting the carrier frequency the spectrum is increased to span over 600GHz and its homogeneity has improved dramatically.

3.6 Summary and conclusion

To summarise, a novel approach to generating nanoscale OFCs is proposed and theoretically verified. A theoretical study, developed using temporal CMT has provided validation to the realisation of OFCs on this scale. The model consists of all-optical PhC modulators that are driven by optical waveforms at a repetition frequency in the RF range. This method of OFC generation provides new insights into the scalability of microwave photonic techniques using state-of-the-art nanoscale optical devices. The work in this chapter has been split into two main parts: the cascading of two IMs and the cascading of an IM and a PM.

In the cascaded IMs scheme, analysis of the cavity coupling scheme as well as their integration in series and parallel was undertaken. It was found that both the series and parallel integration schemes were able to produce up to 7 comblines over 5dB. However, the experimental realisation of the series integration scheme proved to be unrealistic. Using side-coupled cavities in a parallel scheme is experimentally feasible and therefore the preferred method of implementation when using cascaded IMs.

By cascading a PhC waveguide-based PM with a PhC cavity-based IM, the number of generated sidebands is greatly increased when compared to cascaded IM-based schemes. Both the side and direct-coupled cavity-waveguide schemes are analysed for the implementation of the IM. The results indicate that a direct-coupled cavity modulator will achieve a flatter comb and hence be preferred for integrated OFCs. Furthermore, manipulation and optimisation of the pump light characteristics and devices parameters resulted in a comb that spans over 600GHz. This is the first instance of PhC devices being implemented as OFC generators based on their modulation capabilities. The structures have excellent potential for applications in photonic integrated circuits and optical signal processing.

Chapter 4

Development of nonthermalised ICP etching for PhC nanostructures

4.1 Abstract

Inductively coupled plasma (ICP) etching is studied for a range of plasma chemistries to etch PhC devices into InP. The ICP process is developed for nonthermalised samples, where thermal grease on the back side of the sample is not used. It is therefore suitable for industrial implementation or when subsequent step requirements dictate high purity levels, for example epitaxial regrowth. The process yields a sidewall angle of $< 1\%$ and exhibits very little surface roughness while producing up to 800nm hole depth. A selective wet etching process, consisting of an HCl:H_2O composition, is then developed to quasi-isotropically etch the sacrificial InP while leaving the suspended InGaAsP membrane. Development of this process shows that high selectivity between InP and InGaAsP can be achieved using an etching temperature of 2 °C and a HCl:H_2O of 4:1.

4.2 Introduction

Various techniques can be employed for etching PhC devices in InP samples. Chemically assisted ion beam etching (CAIBE) [166] has been commonly used with Cl_2-based chemistry. However, using an ion beam for etching requires a relatively high chamber vacuum which exhibits difficult operation when using corrosive gases such as Cl_2. Electron cyclotron resonance

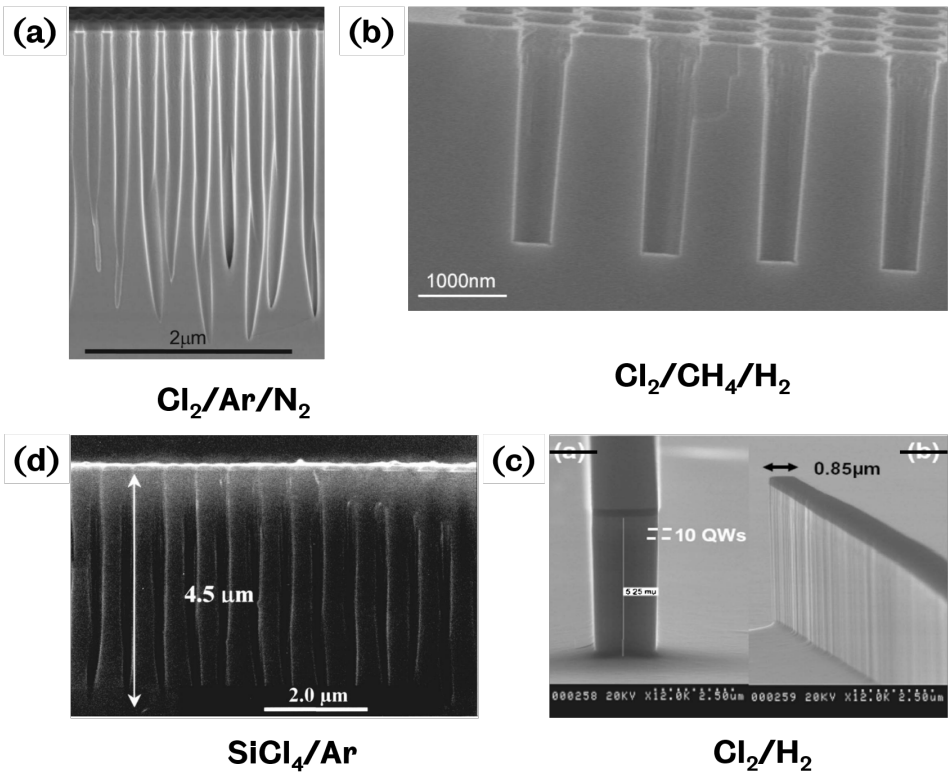

Figure 4.1: Examples of photonic devices etched into InP, all images are taken from the journal papers referenced (a)$Cl_2/Ar/N_2$ [168] (b)$Cl_2/H_2/CH_4$ [169] (c)$SiCl_4/Ar$ [170] (d)Cl_2/H_2 [171].

(ECR) has also been demonstrated as an etching technique for InP-based photonic devices [167]. However, the plasma in ECR etching is known to become unstable due to 'mode hoping' so has been generally replaced by ICP etching. ICP etching is a versatile and robust technique that is used in many applications where high aspect ratio etching is necessary.

In standard ICP etching of InP to produce high ratio etching with small devices features ($<$ 300nm), the sample is thermally coupled to the stage via thermal grease [168, 172, 173]. The sample temperature can then be controlled by the stage and etching is performed at elevated sample temperatures, above 200 °C. The volatility of the sample elements will change dramatically with temperature which influences the chemical etching component. Therefore, control of the substrate temperature will have a marked

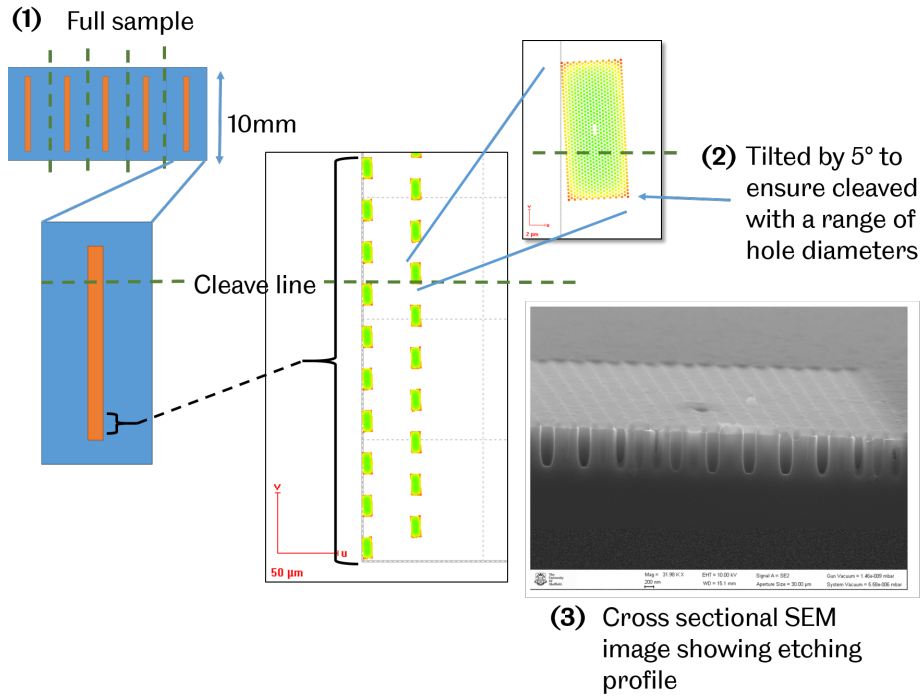

Figure 4.2: Development process pattern design. Many line-sets of devices are fabricated on one sample, point (1). The devices are tilted away from the cleaving place by 5°, point (2). A cross sectional SEM imaging is used to analyse the etching profile, point (3).

effect on the etch rate, selectivity and surface roughness. Examples of photonic crystal structures etched into InP using different chemical etching compositions at high stage temperatures are shown in Figs. 4.1(a)-(c). In the study undertaken in this chapter, therml grease is not used. Under these conditions, referred to as *nonthermalised*, the temperature of the sample is dictated by the plasma conditions. In some facilities, including those at the University of Sheffield, stage temperatures cannot be elevated above a certain temperature. In that case, processes that exhibit a high ratio etching under nonthermalised conditions are necessary. In addition, the use of thermal grease can hinder subsequent steps where high purity is needed and it is not commonly used within an industrial setting.

In this chapter, an new etching process is developed for the etching of photonic crystal devices using nonthermalised samples. Initially a short lit-

erature review is given to show the standard chemical compositions used for etching photonic structures into InP. A selection of these already standardised processes is then adapted to explore their compatibility with nonthermalised samples. The etching characteristics from $SiCl_4$/Ar, $Cl_2/H_2/CH_4$, $Cl_2/Ar/N_2$, Cl_2/Ar and Cl_2/H_2 are discussed below and then experimentally analysed in section 4.3.

$Cl_2/Ar/N_2$ is commonly used for InP etching [168, 174], an example result, taken from Ref. [168], is shown in Fig. 4.1(a). The Cl_2 acts as the reactive species in this process, causing both chemical and physical etching. The Cl_2 bonds with the In and P to produce $InCl_3$ and PCl_3, respectively. In order to produce smooth sidewalls, it is imperative that In and P are removed at the same rate. PCl_3 is far more volatile at low temperatures so is removed faster than $InCl_3$. Therefore, high temperature etching is needed to increase the volatility of $InCl_3$ and ensure a smooth etching profile. Ar has a heavy ion atomic mass of 40 amu, it therefore is commonly used in ICP etching to achive ion bombardment. The predominant function of N_2 is sidewall passivation; through N-P bond formation, the formation of $InCl_3$ is inhibited. When etching PhC devices, an increased nitrogen content helps increase the etch depth. This is because the passivated sidewalls deflect the bombardment ions towards the bottom of the holes, leading to deep but conical holes. Using this method, a balance must be struck between chemical and physical etching and sidewall passivation.

In $Cl_2/CH_4/H_2$ etching [175], all gases can act as reactive chemicals. As discussed above, Cl_2 produces a low volatility compound with In. To overcome this, CH_4 is used, this produces a high volatility compound when bonded with In. The introduction of CH_4 induces polymer deposition on the sample which has both positive and negative effects. Polymer-induced sidewall passivation generates smoother sidewalls but at the same time significantly reduces the etch rate and deposits polymeric compounds on the sample surface. The addition of H_2 in this process has two effects. The first is to chemically bond with Cl_2, this will decrease the number of available radicals responsible for chemical etching, therefore giving fine control of the chemical etch rate. The second is to act directly as a chemical etchant. In this case, H_2 will generate selective etching depending on the material composition. For example, H_2 will etch InP at a higher rate than InGaAs due to the As concentration. It is therefore possible to optimise the H_2 content depending on the necessary application. An example of the etching results possible from using an optimised $Cl_2/CH_4/H_2$ recipe is shown in Fig. 4.1(b) [169].

$SiCl_4$/Ar has been shown to produce deep etching ratios in InP, as shown

in Fig. 4.1(c) [170]. In this case, both $SiCl_4$ and Ar act to bombard the sample, causing physical etching. Chemical etching is also present via Cl_3, creating $InCl_3$ and PCl_3. Similarly to $Cl_2/Ar/N_2$ etching, high temperatures are necessary for smooth sidewalls. This method has proved effective in producing high etch ratios when high temperatures are used.

In all of the aforementioned schemes, the sample is thermally coupled to the stage via thermal grease. It is therefore possible to control the sample temperature through the stage. Nonthermalised etching of InP structures has been demonstrated using a Cl_2/H_2 chemistry [171, 176]. In this study, photonic devices on the tens of micron scale are etched into InP, these devices are shown in Fig. 4.1(d). The ratio of Cl_2 to H_2 is varied to generate anisotropic etching. It is found that balancing Cl_2 and H_2 generates anisotropic etching with low surface roughness. However, etching of photonic crystal devices, which necessitate very high etching ratios from nanoscale patterning features, has not been demonstrated using nonthermalised etching.

In each of the schemes outlined above, specific device requirements dictate their optimisation process. For the fabrication of PhC devices specific to this project, the following requirements must be fulfilled:

- Very smooth and straight sidewalls are needed in the first 300nm to ensure high-quality optical cavities. The roughness of fabricated sidewalls will contribute towards the overall optical loss in the device. Below the first 300nm of the sample is the sacrificial InP layer which is removed so the verticality and surface morphology of this part is inconsequential.

- An etch depth of at least 800nm is needed. Following the ICP etch, isotropic wet etching is employed to remove the sacrificial InP. The holes must penetrate deep into the sacrificial InP to allow for isotropic etching. Shallower holes will necessitate longer wet etching times to produce the same result which can compromise the membrane structure.

The sample is prepared using the steps outlined in chapter 2. First, 400nm of Si_3N_4 is deposited onto the sample. The sample is then spin coated with 400nm of CSAR and the PhC pattern is defined in the CSAR layer via EBL. This pattern is transferred into the Si_3N_4 via RIE using CHF_3. In each process run, multiple line-sets of devices are patterned, as shown by point (1) in Fig. 4.2. Each line-set contains three lines of devices where the diameter is varied from 200 to 240nm. After RIE, the sample is

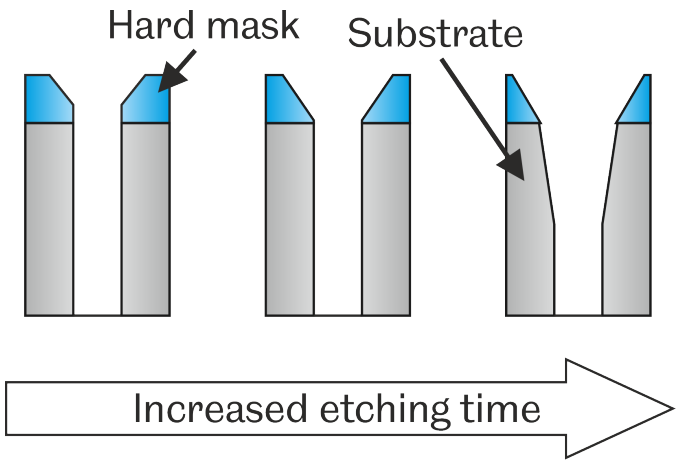

Figure 4.3: Schematic of hard mask erosion. The mask edge is etched faster than the top surface, resulting in tapering. This is transferred into the sample if the etching is not stopped before the tapered hard mask edges reach the sample.

cleaved so that each line-set is separated. This technique means many ICP test runs can be performed where all preceding steps are kept constant and a range of hole sizes are analysed. To analyse the ICP etching results, the sample is cleaved and the cross section is analysed through SEM imaging. The PhC devices are tilted 5°off the cleave plane so that a different part of the cross section is visible for each hole, illustrated in point (2) of Fig. 4.2. On the SEM stage, the samples are vertically tilted by 45° so that the etch profile can be analysed, a cross sectional image is shown by point (3) in Fig. 4.2.

During initial testing many etching runs are necessary, it is therefore practical to use standard InP instead of the QD-based sample. Once there is an optimised process, the process can be shifted to the QD-based sample and slightly adjusted given the difference in material composition between InGaAsP and InP. In this way, it was possible to test a range of different etching processes to find the most appropriate. As stated above, deep etching is beneficial for subsequent processing steps. In all etching tests, the maximal etch depth is reached, this is done by measuring the amount of Si_3N_4 left on the sample. When the hard mask thickness is around 150nm, the etching process is stopped. This is to avoid mask faceting that can occur when the hard mask is etched to a very thin layer, see Fig. 4.3. The hard mask thickness is measured using laser interferometry-based end point de-

tection. A laser is incident on the substrate and the intensity of the reflected light is measured. The interference between the reflections from the Si_3N_4 surface and the InP surface causes differences in the reflected beam intensity depending on the Si_3N_4 thickness. The Si_3N_4 thickness can therefore be measured as a function of the reflected beam intensity, which follows a sinusoidal curve as the thickness decreases.

4.3 ICP etching gases

Given that nonthermalised sample conditions for PhC devices have not been demonstrated before, a vast range of plasma compositions are analysed. There are many configurable parameters for each process, including ICP and RIE RF power, gas flow and ratio and chamber pressure. It is therefore not practical to test all parameters for all plasma compositions. Instead, using the literature and information from the University of Sheffield and Oxford Instruments, the ICP manufacturers, specific parameters are chosen for each process. Using parameters that were suitable elsewhere gives a starting point to find which gases give the most viable option for nonthermalised etching. It is then possible to optimise the parameters of the most favourable chemical composition.

4.3.1 $Cl_2/H_2/CH_4$

Initially, an ICP process based on $Cl_2/H_2/CH_4$ is used, the parameters are given in Tab. 4.1. In this case, physical etching is minimal given the atomic weight of the gases used and their chemical reaction with both In and P. This leads to very isotropic etching and shallow holes, shown in Fig. 4.4. The temperature of the sample will be highly elevated due to the high ICP power at 1500W. This means that $InCl_3$ becomes more volatile and the In and P will be removed at a similar rate. From Fig. 4.4(b), it can be seen that the sidewalls are very smooth due to the high temperature of the sample. Unfortunately, the dominating chemical etch leads to a highly lateral etch, resulting in merging underneath the Si_3N_4 mask. This suggests that although the high temperature does induce smooth sidewalls, physical etching is needed for depth and surface passivation is needed to increase the anisotropy of the etch.

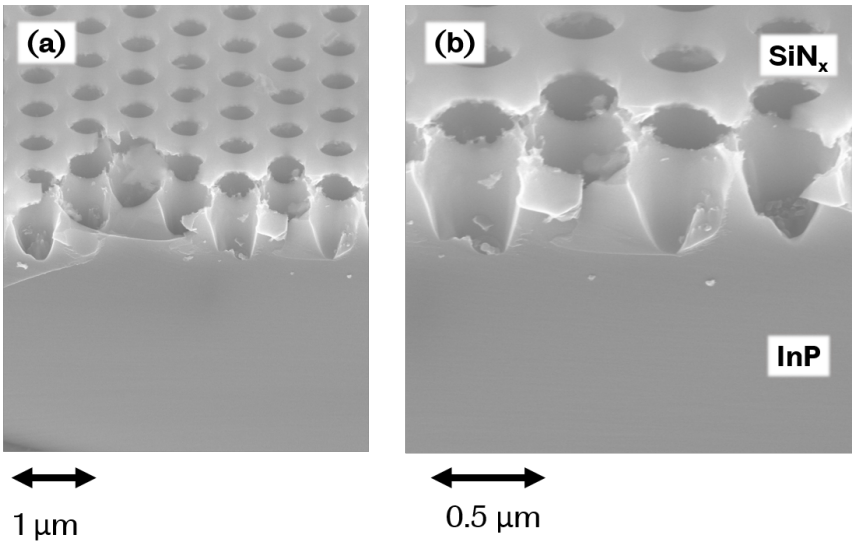

Figure 4.4: Cross sectional images of the $Cl_2/H_2/CH_4$ etching profile. Detailed etching parameters given in Tab. 4.1.

Table 4.1: $Cl_2/H_2/CH_4$ Parameters

Cl_2	15 sccm
H_2	15 sccm
CH_4	12 sccm
ICP Power	1500W
RF Power	150W
Chamber Pressure	4mTorr
Time	180 Seconds

Table 4.2: $SiCl_4$/Ar Parameters

$SiCl_4$	8 sccm
Ar	30 sccm
ICP Power	1000W
RF Power	220W
Chamber Pressure	2mTorr
Time	128 Seconds

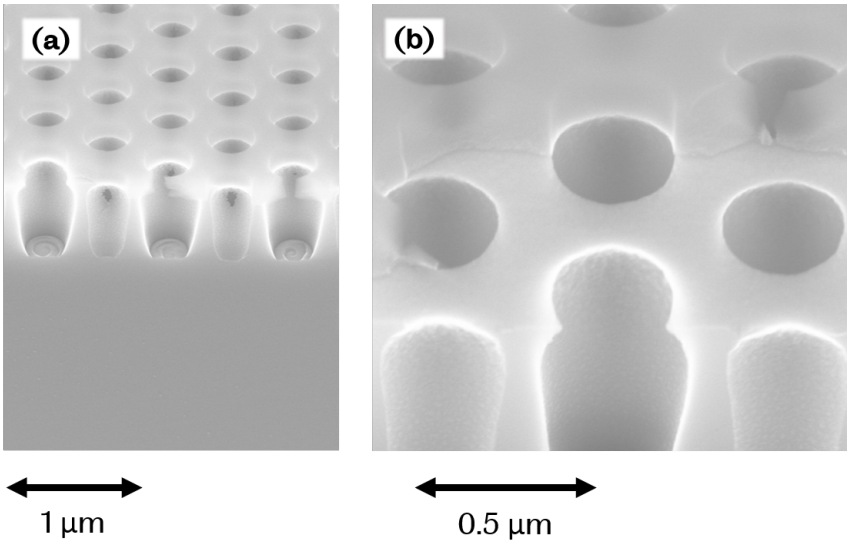

Figure 4.5: Cross sectional images of the $SiCl_4$/Ar etching profile. Detailed etching parameters given in Tab. 4.2.

4.3.2 $SiCl_4$/Ar

Both at the University of Sheffield [177] and elsewhere [170], $SiCl_2$-based ICP etching is used for fabricating photonic structures in InP. The ICP parameters used here are outlined in Tab. 4.2. Ar dominates the gas ratios meaning that etching through physical bombardment should dominate over chemical etching. However, the ICP power is set relatively high at 1000W, resulting in an elevated sample temperature. From Fig. 4.5(a) the depth of the holes can be seen, this has reached a maximum of around 500nm. The bottoms of the holes show a smooth surface with an obvious spiral feature in each hole. This indicates that chemical etching has dominated over bombardment. From the literature, it has been shown that deep holes, up to 3µm with a conical shape can be produced using an $SiCl_4$/Ar recipe, where bombardment dominates over chemical etching. In this case, the dominating chemical etch is due to the nonthermalised sample. Further indication of chemical etching is evidenced in Fig. 4.5(b); isotropic etching results in undercutting just below the sample surface. The surface roughness visible in Fig. 4.5(b) is attributed to a disparity in P removal over In. An ICP power of 1000W means that the volatility of $InCl_3$ is lower than PCl_3 due to sample temperature. Passivation of the sidewalls can help to improve

Table 4.3: $Cl_2/N_2/Ar$ Parameters

Cl_2	10 sccm
N_2	2 sccm
Ar	5 sccm
ICP Power	600W
RF Power	160W
Chamber Pressure	2mTorr
Time	180 Seconds

the surface roughness and a lower sample temperature will ensure physical etching plays a larger role in the etching process, resulting in deeper holes with straighter sidewalls.

4.3.3 $Cl_2/Ar/N_2$

As discussed above, surface passivation is crucial for etching PhCs in InP. To generate surface passivation, a $Cl_2/Ar/N_2$ recipe is used. In this process, Cl_2 induces chemical etching, Ar induces physical etching and N_2 increases the sidewall surface passivation through N-P bonds which inhibit $InCl_3$ bonds. The etching product $InCl_3$ also passivates the sidewall surface when the sample is kept below the $InCl_3$ sublimation temperature of 150 °C [178]. Table 4.3 gives the parameters used and Fig. 4.6 shows the resulting etch profile. The reduced ICP power decreases the chemical etching and allows for more anisotropic etching. The Ar bombardment causes deep etching down to 2µm but the sidewalls show signs of surface roughness caused by the physical etch. Figure 4.6(b) shows vertical streaks that are caused by charged Ar ions as they propel towards the bottom electrode and are deflected from the passivated sidewalls. This deflection causes deep but conical holes due to the majority of Ar ions hitting the central part of the bottom of the holes [168]. The evidence from the study suggests that over passivation has led to the degradation of hole quality. Given that the sample is nonthermalised, the temperature of the sample is unknown. However, this over passivation stems from either the ratio of N_2 being too high or contributions towards passivation are coming from both N_2 and $InCl_3$, meaning the sample temperature is less than 150°C.

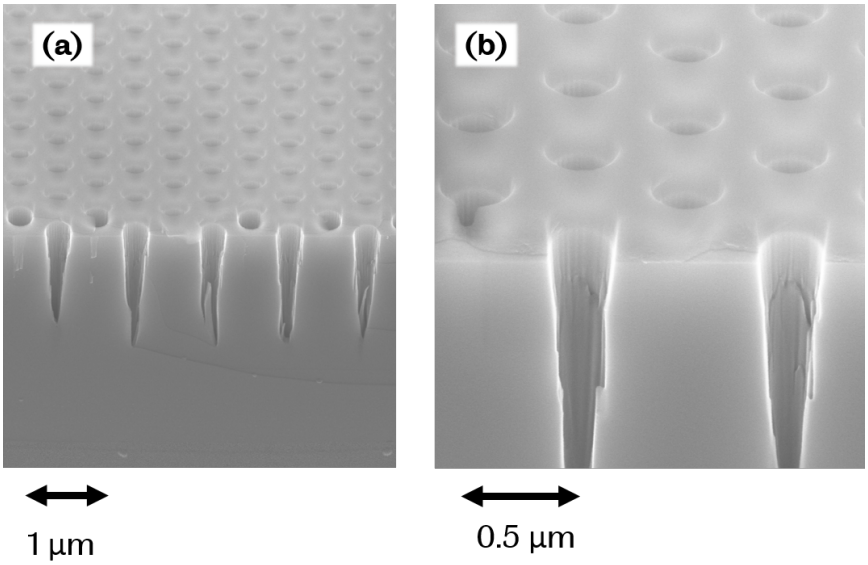

Figure 4.6: Cross sectional images of the $Cl_2/Ar/N_2$ etching profile. Detailed etching parameters given in Tab. 4.3.

4.3.4 Cl_2/Ar

Evidence from the $Cl_2/Ar/N_2$ process suggests that the inclusion of N_2 results in over passivation. To rectify this, the N_2 is removed and all other parameters are kept the same as those given in Tab. 4.3. Figure 4.7 shows the results, improvements have been made in both hole depth, reaching up to 2.5µm, and sidewall roughness. Vertical streaks are still visible but less so than in the previous etching process. This suggests that bombardment is still dominating over chemical etching. However, there are signs of chemical etching where the surface roughness can be attributed to a disparity between the removal of In and P. The shape of the holes gives a conical shape with the ends of the holes tapered; a common feature for deep etching in InP [168, 170]. The angle of the side wall is around 5° in the upper 0.5µm. As discussed in the introduction, straight and smooth sidewalls are more important for this application than deep etching. Reducing the physical etch will result in shallow holes but may improve the anisotropy and sidewall surface roughness.

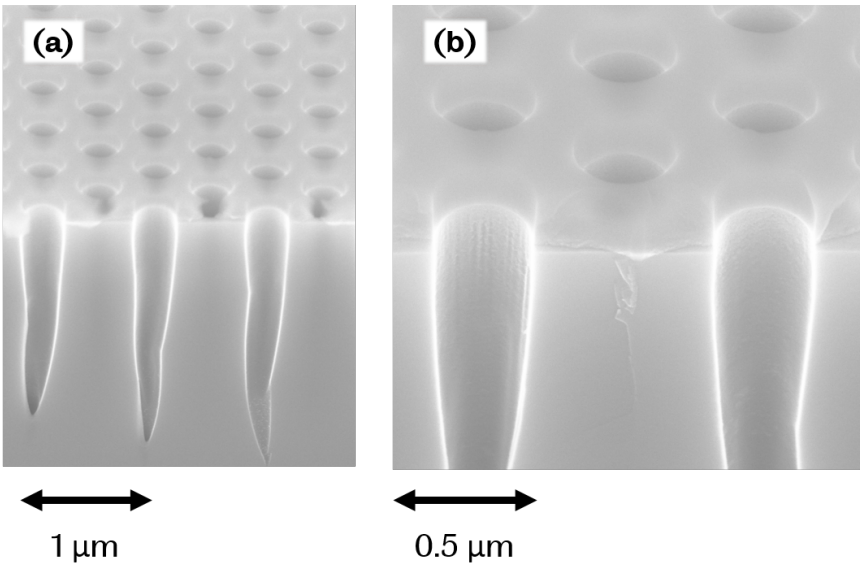

Figure 4.7: Cross sectional images of the Cl_2/Ar etching profile. Detailed etching parameters given in Tab. 4.4.

Table 4.4: Cl_2/Ar Parameters

Cl_2	10 sccm
Ar	5 sccm
ICP Power	600W
RF Power	160W
Chamber Pressure	2mTorr
Time	180 Seconds

4.3.5 Cl_2/H_2

Finally, a Cl_2/H_2 composition is analysed, here the amount of chemical etching will be controlled through the ratio of Cl_2 to H_2 [179]. As has been shown in this chapter thus far, elevated sample temperatures are necessary for chemical etching. However, this can also result in isotropic etching if the sample is too hot or the ratio of the dominating chemical etchant is too high. Studies on the role of H_2 in ICP etching of InP using a $Cl_2/Ar/H_2$ have shown that the ratio of Cl_2 to H_2 will greatly affect the etching profile [179]. They found that a balanced ratio of Cl_2 to H_2 will result in an anisotropic etch which produces smooth sidewalls. At elevated temperatures $InCl_2$ becomes more volatile so is easily removed and H_2 promotes the removal of P, thus producing smooth sidewalls by ensuring a balanced removal of In and P [171]. Also, in this balanced region there is only a small amount of chemically active radicals compared to when Cl_2 is the dominating gas. This reduces the lateral chemical etching potential and ensures anisotropic etching.

Table 4.5 shows the etching parameters used in this process and Fig. 4.8 shows the results. Although the depth is reduced to around 600nm due to the lack of physical etchant, the sidewall angle and surface roughness have been greatly improved. The sidewall angle is less than 1°and the sidewall surface roughness has reduced for two reasons. The first is the lack of physical etching which means the surface is not scarred by heavy ions with kinetic energy. The second is due to the balanced removal of In and P through the introduction of H_2.

It is worth noting that a $Cl_2/H_2/Ar$ process was also performed to increase the etch depth. All parameters given in Tab. 4.5 were kept the same and Ar introduced. Ar flow rates were varied from 3-10sccm, a flow rate of 5sccm gave the best etching results, which are shown in Fig. 4.9. The physical etching generated a slight increase in hole depth, up to 650nm but at the cost of sidewall roughness. The lower part of the holes also suffered from a radius widening, attributed to reflection of the Ar ions at the bottom of the holes.

4.4 ICP parameters

Both the Cl_2/H_2 and Cl_2/Ar processes were observed to be at the limit of what is acceptable for the outlined specification. Deeper etching is achieved at the cost of sidewall quality in a Cl_2/Ar ICP process, whereas shallow etching with high quality sidewalls is achieved for Cl_2/H_2. In this section, both

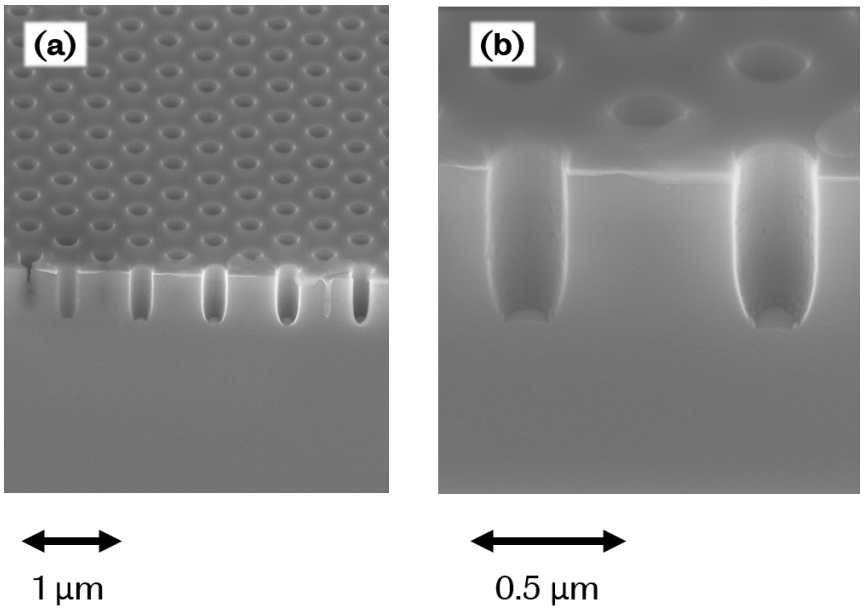

Figure 4.8: Cross sectional images of the Cl_2/H_2 etching profile. Detailed etching parameters given in Tab. 4.5.

Table 4.5: Cl_2/H_2 Parameters

Cl_2	7 sccm
H_2	8 sccm
ICP Power	1200W
RF Power	100W
Chamber Pressure	2mTorr
Time	180 Seconds

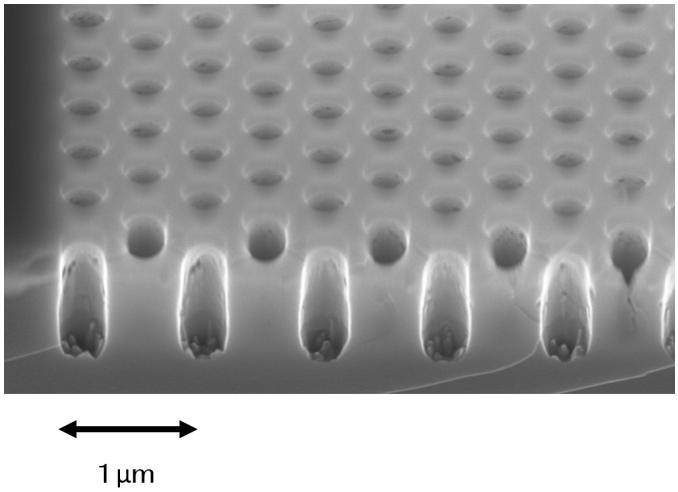

Figure 4.9: Cross sectional image of the $Cl_2/H_2/Ar$ etching profile

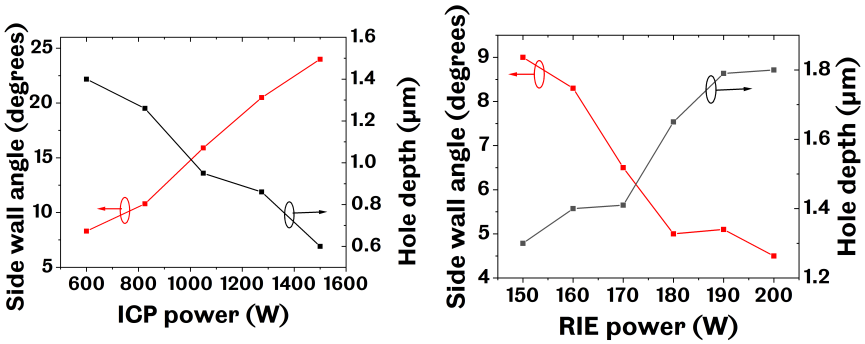

Figure 4.10: Optimising ICP parameters for Cl_2Ar process (a)ICP power against sidewall angle and hole depth (b)RIE power against sidewall angle and hole depth

processes are optimised via tuning of the ICP parameters. The parameters focused on are the ICP and RIE powers and the chamber pressure.

Using the Cl_2/Ar process, the ICP power is varied from 600W to 1500W, Fig. 4.10(a) shows the ICP power against maximum hole depth and sidewall angle in the upper 0.5 µm. An increasing ICP power heats the sample and induces chemical etching from the Cl_2 to dominate. This leads to surface passivation of the sidewalls and causes the etch depth to decrease. On top of this, the dominating Cl_2 etch generates slight undercutting of the sample and therefore increases the sidewall angle. On the other hand, the sidewall roughness is decreased for higher ICP powers so a trade off exists between angle and depth of the holes and sidewall roughness. Figure 4.10(b) shows the influence of the RF power when varied from 150 to 200W. A larger RIE power will lead to higher kinetic energy of the charged Ar ions. When the ions hit the sample with higher kinetic energy, the etching speed is increased, as shown by the black line in Fig. 4.10(b). The increased energy also means that the ions deflect less, causing straighter sidewalls. Above 170W, the influence of the RIE power over the sidewall angle decreases. This suggests that increasing the RIE further will not induce straighter sidewalls, meaning a maximum sidewall angle of 4° is possible through manipulation of the RF power. The sidewall roughness for a changing RIE power shows similar characteristics to that shown in Fig. 4.7. After optimisation of the chamber parameters, it can be said that Cl_2/Ar etching of nonthermalised samples cannot be used for PhC device fabrication to the specification needed in this project.

Using Cl2/H2, similar experiments were performed to optimise the etching process. The ICP power was varied from 1000W to 1500W and the RIE power was varied from 100 to 200W. An increased ICP power produced elevated sample temperatures and an increased $InCl_2$ volatility. Consequently, the surface roughness increased to an unacceptable level due to In being removed at a different rate to P. It was also found that undercutting beneath the sample surface increased with higher ICP powers, this is largely due to increased lateral chemical etching. Changing the ratio of Cl_2 to H_2 might improve both of these parameters but does not provide any extra benefits compared to the process given in Tab. 4.5 so is not considered here. Decreasing the ICP power caused an increase in vertical etch rate, producing holes up to around 750nm for an ICP power of 1000W. An increased RIE power generated a slightly increased hole depth but also caused an increase in hole radius in the lower part of the holes, giving a slightly degraded sidewall angle. A trade off between hole depth and sidewall angle meant that an optimised RIE power of 125W was realised.

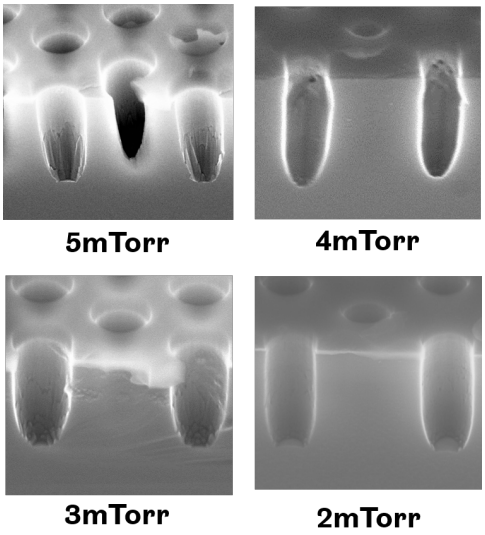

Figure 4.11: Cross sectional images showing the effect of chamber pressure on sidewall roughness

Finally, the chamber pressure was optimised; previous studies [171, 180], have shown that a lower pressure will induce higher etch rates. The problem with lower pressure (< 2mTorr) is the difficulties in plasma striking. At low pressures the ICP plasma cannot strike, to overcome this the pressure must start higher to induce striking and then be lowered to the desired pressure. This then causes changes in etch profile as the pressure is lowered and causes difficulties in maintaining the plasma. It was found that pressures below 2mTorr were unstable so could not be used. Increasing the pressure meant less time to reach the desired pressure from the initial strike pressure of 8mTorr. Increasing the pressure from 2mTorr to 8mTorr did not have a marked effect on the etching depth, but did increase the sidewall roughness, as shown in Fig. 4.11. This is due to a change in ion density as the pressure is increased.

With all of the above taken into consideration, an optimised ICP process has been found which generates holes with smooth and straight sidewalls that are around 800nm deep. Using this etching process, given in Tab. 4.6, low-loss PhC devices can be fabricated in the QD sample which is outlined in chapter 2. After ICP etching, the remaining Si_3N_4 is removed from the sample via submergence in HF for 90 seconds. The final critical stage for PhC processing is to remove the sacrificial InP layers.

Table 4.6: Optimised Cl_2/H_2 Parameters

Cl_2	7 sccm
H_2	8 sccm
ICP Power	1000W
RF Power	125W
Chamber Pressure	2mTorr
Time	180 Seconds

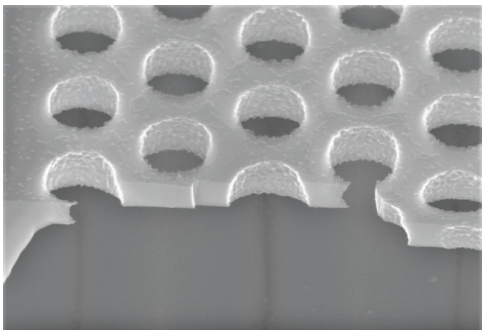

Figure 4.12: Room temperature wet etch showing degraded surface morphology

4.5 Wet etching

The isotropic wet etching of the sacrificial InP layers is crucial to successful fabrication of PhC membrane structures. A high etch selectivity is needed between InP and InGaAsP to ensure the membrane is not significantly etched. Initially, room temperature HCl/H_2O etching is used with a ratio of 1:2 $HCl:H_2O$ for 4 minutes. It was found that the $HCl:H_2O$ etched the membrane layer, causing degraded surface morphology on both the sidewalls and top surface, as shown in Fig. 4.12. The ratio of $HCl:H_2O$ and the etchant temperature will heavily influence the sample etching rates and selectivity. Figure 4.13 shows the results from etching at 2°C when the ratio of $HCl:H_2O$ is varied from 2:1 to 6:1 and the etch time is kept constant at 15 minutes. Using a ratio of 2:1, the HCl content is not enough to fully etch the InP. The v-grooves present in Fig. 4.13(a) form due to the different etch speeds in different crystallographic directions. The transition point between the sacrificial InP layer and the InP substrate can be seen by the horizontal line beneath the v-grooves. This is achieved by a change in temperature dur-

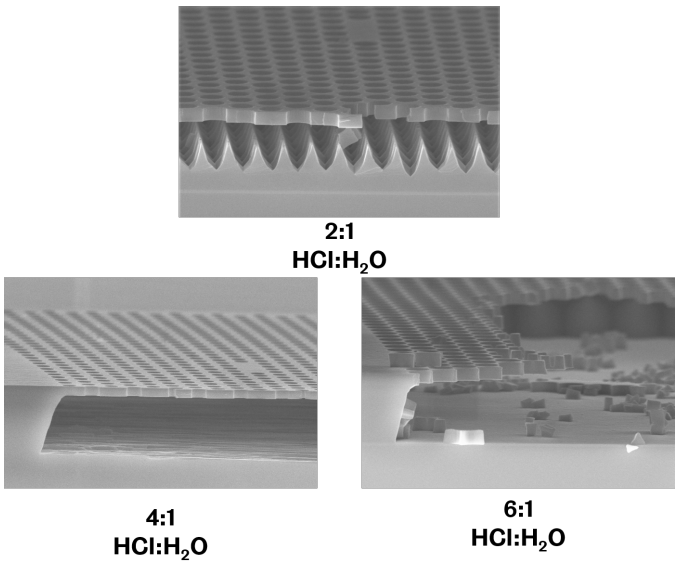

Figure 4.13: Cross sectional images which show the effect of HCl concentration on etch rate and selectivity

ing sample growth and it promotes lateral etching over longitudinal etching. In Fig. 4.13(b) and (c), vertical etching is inhibited below the InP substrate layer. The implementation of this promoted lateral etching is dependent on the Γ-K PhC direction relative to the crystallographic direction. By tilting the Γ-K PhC direction 90° to the crystalline direction, a singular v-groove will be etched that goes deep into the substrate. This undercut etching profile will not affect the optical characteristics of the sample but helps to identify the depth of the undercutting, as discussed in the next chapter.

An etch ratio of 4:1 provides enough undercut etching to remove all the sacrificial InP without degrading the membrane material, as shown in Fig. 4.13(b). When the HCl content is increased further, the membrane structure degrades. This is evidenced in Fig. 4.13(c), the membrane collapses due to the thinned spacing between the holes. The centre of the device degrades first due to the higher density of holes in the centre and greater tensile strain.

The acid is cooled using an ice bath method; the beaker containing the acid is placed inside a large beaker which contains ice and water. The acid is left to cool for 5 minutes before the sample is added. During testing of the ice bath method, the acid temperature was monitored directly, it was found that 5 minutes provided enough time to cool the acid while maintaining temperature of 2 degrees was possible for over 20 minutes. During device

etching, the acid temperature is monitored by measurements of the ice bath temperature, measuring the acid directly can cause contamination of the acid so is avoided. Once the sample has been removed the acid temperature is measured to ensure continuity between fabrication runs.

4.6 Summary and conclusion

In this chapter, various etching chemistries and parameters were analysed for nonthermalised etching of InP nanostructures. The ICP power is shown to greatly affect the sample temperature and thus influence the dominating etching process. At low ICP powers, the etching is dominated by physical etching through heavy ions, such as Ar ions. The resulting etch profile shows deep etching but high surface roughness. This roughness is due to the physical etch, which causes vertical streaks in the sidewalls, and the disparity in chemical etching rates of In and P. Increasing the ICP to over 1000W elevates sample temperatures and chemical etching becomes prevalent. The sidewall roughness in this case is improved but undercutting beneath the Si_3N_4 layer becomes prevalent due to lateral chemical etching.

Of the etching chemistries analysed, it was found that Cl_2/H_2 process gave the smallest sidewall angle (<1°) and lowest surface roughness. In this process, the Cl_2:H_2 ratio is 7:8 and the ICP power is set to 1000W. The high power promotes the etching of In through Cl_2 and H_2 ensures P is removed at a similar rate, thus producing smooth sidewalls. H_2 also enables fine control over the reactive radicals present in the plasma which helps to slow lateral etching. Control of the ion density through the chamber pressure showed that a decreased pressure helps reduce the surface roughness.

After ICP etching, the sample is isotropically etched to remove the sacrificial InP above and below the InGaAsP membrane. A study was undertaken that analysed the effects of temperature and concentration of HCl:H_2O on the etching rate and selectivity of the sample. It was found that room temperature etching leads to degraded surface morphology on both the sidewall and top surface. An optimised concentration revealed high selectivity and etch rate using HCl:H_2O 4:1 at 2°.

In this chapter, a new etching process for the fabrication of PhC devices in InP has been developed. It has been shown that even without the use of thermal stabilisation through the stage temperature, straight sidewalls with low surface roughness can be achieved. This process is perfect for membrane-based PhCs but could not be used for slab-based PhCs where a very deep etch is needed. Research into PhC device fabrication in InP is a developed

subject area. However, development of a nonthermalised process specifically for PhC membrane structures has not been undertaken and was necessary for this project. The benefit of nonthermalisation is that it negates the use of thermal grease, thus opening this fabrication up to industrial areas or where critical further steps, for example epitaxial regrowth, are required. Also, at facilities where high temperature stage control is not available, this process can be used.

Chapter 5

Photonic crystal nanocavities

5.1 Abstract

In this chapter, air holes in a hexagonal lattice etched into a InGaAsP membrane with embedded InAs QDs as active emitters are investigated. The structures generate photonic bandgap materials where removal of a number of holes will produce an optical cavity. In the region where no holes exist, the local density of optical states increases due to the omission of the photonic band gap. When the emission wavelength of the QDs overlaps with the optical states in the cavity, the QD emission will channel into these modes. Room temperature micro-photoluminescence measurements are undertaken in both the time and frequency domain to characterise these modes. Through lithographic control, the lattice constant and fill factor are tuned over a wide range. The results show that the resonance can be controlled across the InAs QD emission spectrum. To understand the effects of thermo-optic induced resonance shifting, the cavities are excited using a laser power which ranges from 10nW up to 350nW. The results show that a 5nm reversible wavelength shift is induced. Finally, time resolved measurements are undertaken to show the interaction between the cavity and emission from the QDs. This interaction causes an enhancement of the spontaneous emission rate.

5.2 Introduction

The control of the cavity resonance of nanoscale photonic devices plays an important role in next generation PICs [181]. Various tuning methods have been demonstrated which include geometric alteration [182] and changing

the refractive index of the device material [108]. Dynamic tuning of the cavity resonance can be obtained through free carrier generation, the Kerr effect and thermal tuning. In free carrier generation based tuning, the influx of free carriers in the membrane structure will cause a blue shift in the cavity resonance. Tuning speeds via free carrier generation are limited by the free carrier lifetime. It is therefore strongly dependent on the material used and device geometry. The Kerr effect causes a red shift in the cavity resonance and is in principle capable of terahertz modulation. Enabling the Kerr effect to dominate over the free carrier effect can be problematic as free carriers are generated via two photon absorption when pumping the cavity. One method to overcome this is using a pump photon energy below half the bandgap [105]. Using this method, very high powers are needed to generate third-order optical non-linearity. Thermal effects occur on a relatively slow time scale but have the ability to tune over a far greater bandwidth. Thermal effects cause an expansion of the semiconductor lattice and an increased phonon population, this results in a change in the bandgap and hence a cavity resonance change. The free carrier and Kerr effect have been discussed in chapter 3, in this chapter thermal effects via photothermal irradiation are discussed.

The effects discussed above are based on dynamic change in the refractive index of the material, however a static change is also possible through lithographic tuning. Geometric flexibilities in the PhC structure will inherently offer full control over the spectral properties of the cavities during fabrication. Different optical modes with various spectral characteristics can be generated through geometrical change. Along with spectral controllability, the Q factor of the cavities can also be manipulated to suit the application. This offers a method to engineer the defect mode characteristics both in terms of their spectral position and cavity Q.

Many studies have been undertaken that consider QD emission within a PhC device. Investigations into the effect on QD spontaneous emission (SpE) rate in the presence of a PhC lattice where no defects exist found suppression of the SpE rate [183]. This suppression is due to the lack of in-plane emission channels for the QD emission. By removing a set of holes and creating a defect, the local density of optical states will be increased. The QD emission can then be enhanced by coupling the emission to the localised modes. In this chapter, the cavities are made to spectrally overlap with the QD emission at telecommunication wavelengths through lithographic tuning. The mode structure of the cavity is visible above the QD background because the emission rate and collection efficiency is increased by the cavity. The SpE rate of the QDs is shown to greatly increase when the emission spectrum

is manipulated by the presence of a PhC cavity [184]. The excited carriers recombines faster due to a number of factors including the Purcell effect, surface recombination and carrier diffusion. The Purcell effect is a quantum phenomenon that describes the manipulating of a system's emission rate by altering its environment [185], in this case, QD active emitters in a PhC cavity. Surface recombination within the cavity will be enhanced due to the increased surface area of the fabricated devices. Finally, carrier diffusion will decrease the carrier lifetime because in an ultra-small cavity, the photon-generated carriers will diffuse quickly from the cavity. These phenomena are studied by collecting resonant and non-resonant emission from the QDs in a PhC device. A maximised QD emission rate will ensure fast modulation capabilities when using a pulsed excitation laser with a repetition rate in the gigahertz range. It is therefore beneficial to study the QD emission rate in detail in this chapter.

Initially in this chapter, lithographic tuning of L3 cavities will be investigated. The tuning is obtained through changing both the lattice constant and fill factor of the L3 cavities during the EBL patterning process. This leads to precise tuning of the cavity resonance. In this part, the reproducibility of the fabrication process is assessed and a comparison is drawn between the pattern parameters set during a EBL and the realised hole size. During fabrication, anomalies can occur which can reduce the ability for light confinement. It is shown that variation between holes in a single device will cause degradation in the devices spectrum. Following this, the devices are thermally tuned through a change in the excitation laser power. Finally, time dependent micro-PL measurements of the QD emission both with and without cavity enhancement are performed over a range of wavelengths.

5.3 Lithographic tuning of the fundamental mode

In terms of controllability over the resonant wavelength, emission direction and quality factor, photonic crystal devices offer fantastic advantages. By slight variation of the hole size, lattice spacing and membrane thickness will have large effects on the cavity characteristics. To this end, a large number of PhC cavities can be fabricated onto a single chip where the cavity frequency can vary between devices. Multi-channel all-optical switching has also been realised due to lithographic tuning of an array of cavities [92]. In this scheme, multiple cavities are coupled to a single waveguide. The resonance of each cavity is slightly different due to a change in the device geometry thus enabling concurrent switching when each memory bit

is spaced out in the frequency domain. Another application of lithographic tuning can be realised for spectrally encoded PhC cavities for bio-sensing [182].

In chapter 5 of this thesis, specific cavities are pumped using a high repetition rate excitation laser to analyse the validity of nanoscale microwave photonics. In this later study, it is imperative that the operational wavelength falls within the telecommunications bandwidth. Fine control over cavity resonance through device geometry will ensure this is possible.

5.3.1 Mode structure

A continuous wave laser at 976nm is used to excite the PhC cavities for all frequency domain measurements. The full set-up is discussed in chapter 2, all measurements in this chapter were performed at room temperature using a micro-photoluminescence set-up. Figures 5.2(a) and (b) show the mode structure of a standard L3 cavity in experiment and simulation, respectively. Due to the relatively large size of an L3 cavity, multiple modes are confined which fall within the photonic bandgap. In Fig. 5.2, each mode has been labelled for reference and Comsol has been used to find the mode patterns for the three modes, these are represented in Fig. 5.2(c-e). The slight difference between the simulated device and the experimental realisation is due to two dominating effects. The first is the discretisation used for calculation. As discussed in the methods chapter, Comsol breaks down the structure into small sections to enable fast and accurate computational simulation. However, given that the holes of the PhC are circular and the mesh is broken up into triangular shapes, there is always discrepancy between the circular shape of the hole and the triangular mesh. This can be accounted for by increasing the mesh size at the cost of computational memory and calculation time. The second error is due to the fabrication imperfections, this can be minimised by imaging the devices through SEM and using that specific data in simulation but not completely eradicated. In this work, identifying the modes is important to show the effects of a change in geometric conditions. Each mode will act as an emission channel for the QD carrier recombination, by understanding how the emission rate changes in each mode, fast modulation can be achieved.

5.3.2 Fill factor control

The fill factor, f is defined as the hole radius r in relation to the lattice constant a of the hexagonal lattice, such that $f = r/a$. In this study, the

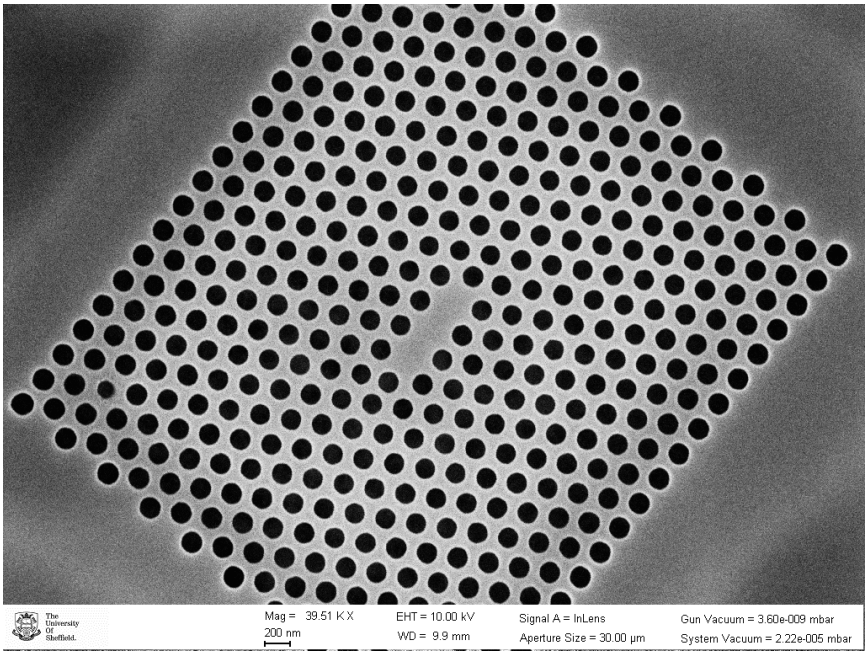

Figure 5.1: An SEM image of the measured L3 cavities.

lattice constant is kept constant and the radius of the holes is varied to change the filling factor of the PhC. Two lattice constants were studied, 464 nm and 488 nm, and the fill factor of the holes was varied from 0.26 up to 0.3. Figure 5.3(a) and (b) show the results for the lattice constants of 464nm and 488nm respectively. In Fig. 5.3(a) the photonic bandgap degrades and the fundamental mode cannot be recognised above f=0.27, this is due to fabrication errors. The devices are patterned in a matrix grid, where the fill factor increases in the X direction and the lattice constant in the Y. Using this method can lead to larger numbers of devices not functioning if an area of the sample degrades in some way. For example, slight deformation in the growth of the sample can lead to small defects that protrude out of the sample surface. Then during spin coating of the EBL resist, this protrusion will cause a change in the resist thickness which will deform the holes in the PhC. Depending on the size of the affected area, many devices can degrade in this way. This is just one example of the fabrication errors that can cause a decreased device yield. In this case, all devices with a fill factor larger than 0.27 have been affected since they are all within a close range of each other. The deformation can have a range of effects, in this case analysis of

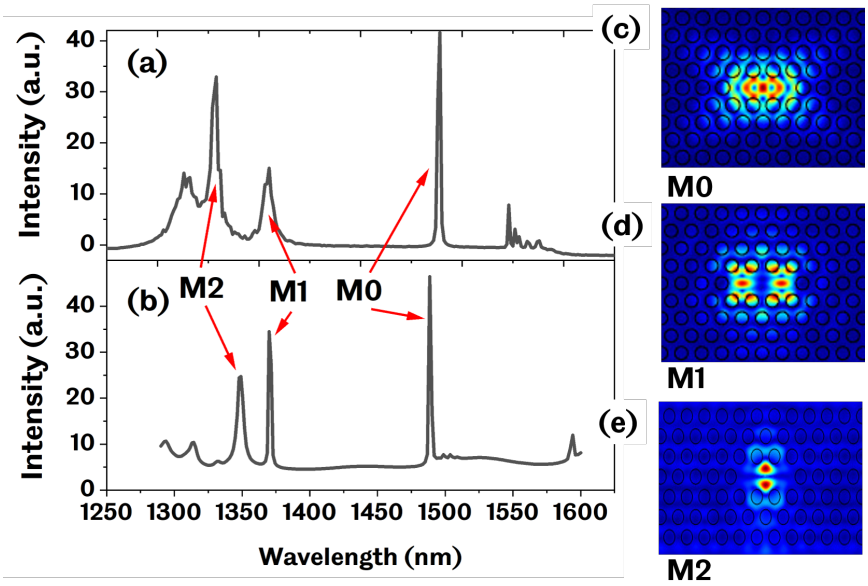

Figure 5.2: (a) Experimental results showing the typical optical spectrum of an L3 cavity (b) shows the COMSOL simulation results when the same devices parameters from (a) are used. (c-e) shows the mode structure, simulated in COMSOL, of the modes labelled in (a) and (b)

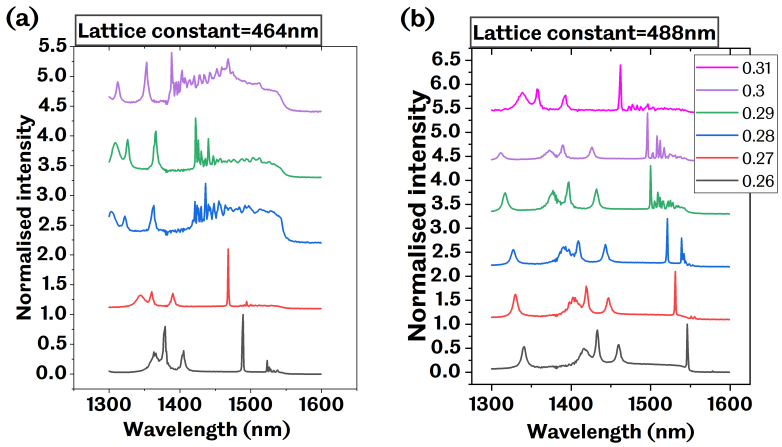

Figure 5.3: Experimental results, (a) shows the spectral change of the cavity modes when the lattice constant is kept constant at 464nm and the fill factor of the PhC is varied from 0.26 to 0.3. Fill factors above 0.27 exhibit a severely degraded mode structure. (b) shows the spectral change using a fixed lattice constant of 488nm and a fill factor variance from 0.26-0.3.

the undercut etching profile provides reasoning behind the decreased mode structure quality.

As discussed in chapter 4, the HCl infiltrates the substrate through the PhC holes. Isotropic etching then results in a membrane device structure. However, if some holes are slightly deformed then the HCl is less likely to etch the sacrificial substrate to a sufficient degree. In this case, the sacrificial layer around the centre of the device will etch but the outer edges will not. Figure 5.4(a) and (c) show the side profile for isotropically etched devices where HCl has partially etched and fully etched, respectively. This can also be seen from the top view of a device; Fig. 5.4(b) shows a partially etched device and Fig. 5.4(d) shows a fully etched device. Orange lines have been superimposed on top of Figs. 5.4(c) and (d), to show the etching profile of the HCl. SEM analysis of the devices above f=0.27 in Fig. 5.3(a) shows that the devices have slight deformation and undercut etching has not been fully realised. Therefore, the photonic bandgap of the L3 devices has been compromised and has degraded the light confinement capabilities.

Figure 5.3(b) shows that an increase in the fill factor blue shifts the fundamental cavity mode, M0, by 80 nm with a fill factor change of 0.05. As the fill factor increases, the cavity size will decrease, hence shrinking the effective cavity length. The decreased cavity length will impede longer

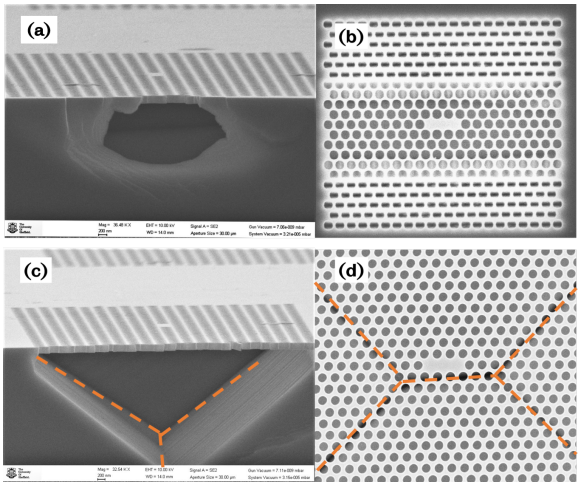

Figure 5.4: (a) the side profile of an under etched device due to fabrication anomalies, (b) is the top profile of an under etched device. (c) shows the side profile of a fully etched device and (d) the corresponding top profile. The orange lines superimposed on top of (c) and (d) show the etch profile of the HCl undercut etching.

wavelengths from resonating in the cavity, hence changing fundamental cavity resonance. The effect of the fill factor on the cavity mode wavelength will change depending the mode. As the fill factor increases, the gap between the fundamental mode, M0, and the second order mode, M2, decreases in size. However, the gap between M2 and M1 increases, this difference in the shift magnitude of the first order mode, as depicted in Fig. 5.5, shows how each mode reacts differently to geometrical changes. The fundamental mode is very sensitive to change given the mode profile whereas higher order modes are less dependent on the geometric structure.

5.3.3 Lattice constant control

In order to investigate the tuning effect of a change in lattice constant, the fill factor is kept arbitrarily constant at 0.28 and the lattice constant is varied from 440nm to 500nm in increments of 12 nm. In this way, the modes can be tuned throughout the emission of the range of the embedded QDs. Figure 5.6 shows the shift of mode wavelengths as the lattice constant is increased. The fundamental mode shifts from 1410nm to 1546 nm; a larger shift is possible to observe using a lattice constant of 500nm, however the

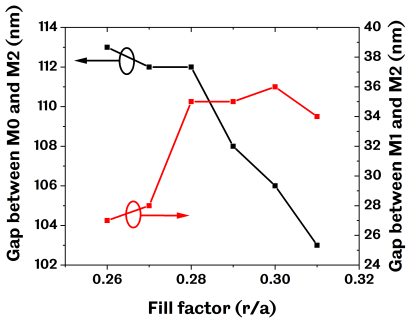

Figure 5.5: Experimental results, the black line shows how the gap between M0 and M2 closes with an increased fill factor. In contrast, the red line shows how the gap between M1 and M2 opens with an increased fill factor.

measurement is limited by the detector bandwidth. This shift is enabled by the changing of the effective cavity length. The extracted peak wavelengths for modes M0-M2 are plotted in Fig. 5.6. The modes all shift in a similar way to higher wavelengths for an increased lattice constant. As discussed, the PhC structure creates a photonic bandgap in which frequencies within this band cannot propagate. In Fig. 5.6(a), the lower band edge is observed, labelled as BE. Modes with frequencies below this band edge are weakly confined to the cavity. As can be seen, many indeterminate modes are present due to the physical confinements of the holes surrounding the cavity, their weak relative power indicates a longitudinal loss within the structure. Although the band edge also experiences a redshift, the distance between the band edge and the fundamental mode increases with increasing lattice constant. This suggests that the photonic bandgap and the mode structure can be tuned independently. Using this knowledge, breakthroughs in multi-cavity devices have been made [115]. Tailoring the fundamental mode is imperative for this work when fine tuning the working wavelength of the device for telecommunication applications.

5.4 Photo-thermal tuning of the fundamental mode

Photo-thermal tuning of a cavity through laser irradiation is a mechanism used to obtain the desired operation wavelength from an optical nanocavity. Using above band excitation results in free carrier generation and heating, where effects due to heating will dominate over the free carrier effects, causing a red shift in the cavity wavelength. The predominant effect of the

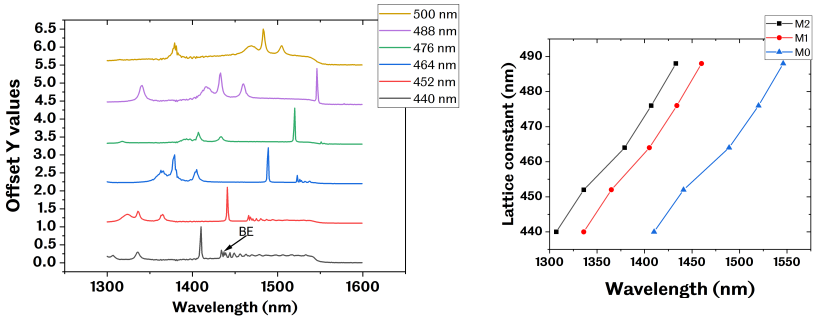

Figure 5.6: Experimental results, (a) shows the cavity spectrum with a fixed fill factor and a varied lattice constant. (b) is the extracted peak wavelengths for modes M0-M2.

increased temperature will be the change in dielectric constant of the material. Higher temperatures cause a semiconductor lattice expansion and an increased phonon population which change the band gap of the material and hence its dielectric constant. There may be added effects of thermal tuning due to physical expansion of the devices due to heating but given that the linear thermal expansion coefficient of InGaAsP sits at around $4.6\text{x}10^{-6}/°\text{C}$ this would be a minimal amount.

Figure 5.7(a) and (b) show the effects of photo-thermal tuning on the fundamental mode wavelength. A linear line of best fit is used to analyse the difference in thermal influence at high and low powers. Using a laser power between 0.01 and 0.09mW the influence on the cavity resonance is relatively low with an increase of 0.6nm, this gives rise to a linear fitting slope gradient of 8.6 as shown in Fig. 5.7(a). However, when higher powers are used, the gradient increases to 12, as shown in Fig. 5.7(b). This implies that thermal effects on the cavity mode wavelength are greater when high powers are used.

Figure 5.7 (c) and (d) show the cavity spectrum for the fundamental cavity mode at various laser powers. Initially, an increase in laser power increases the cavity emission intensity, as shown in Fig. 5.7(c). However, as the laser power goes above 0.3mW, the cavity emission intensity decreases, as shown in Fig. 5.7(d). This is due to the higher temperatures causing increased non-radiative recombination from the QDs. Thermal effects will also influence the linewidth of the cavity mode, hence altering the cavity Q factor. In Fig. 5.7(d) this spectral broadening of the cavity linewidth is clearly visible. Figures 5.7(e) and (f) show the obtained Q factor against laser

power. At low powers, the Q factor varies slightly but centres around 1400. As the laser power increases from 0.1mW to 0.15, the Q factor increases to 1570 due to saturated absorption in the QDs. The obtained Q then drops steadily with laser powers above 0.2mW, this is caused by phonon-assisted transitions.

5.5 Observation of fast spontaneous emission decay in a PhC cavity

Measuring the QD SpE rates and understanding what affects this rate will ensure an increased modulation depth when exciting the cavity using a pulsed, high repetition rate laser. As stated above, broadband emission of the inhomogeneous QD layer dictates that part of the emission spectrum will couple to the cavity fundamental mode wavelength. The rate at which the carriers recombine is affected by the cavity due to three dominant phenomena: the Purcell effect, surface recombination and carrier diffusion. In this section, firstly the theory behind the Purcell enhancement is outlined to show how the cavity Q/V ratio effects SpE rates. Then a comparison between the QD SpE rate for the bulk membrane and QD SpE rate coupled to the cavity fundamental mode is made. Although this does show an enhancement, it does not give clear indication of the dominating fast carrier recombination effect. To study this, both on and off resonant emission from the cavity is collected and analysed.

Weakly coupled cavity QED system - the Purcell regime

When QD emission couples to a cavity, the Eigenfrequencies of the QD-cavity coupled system [186] can be written as:

$$\frac{E_{\pm}}{\hbar} = \omega_{\pm} = \frac{\omega_0 + \omega_{QD}}{2} - i\frac{(\kappa+\gamma)}{2} \pm \sqrt{(\frac{\delta - i(\kappa-\gamma)}{2})^2 + |g|^2} \qquad (5.1)$$

where ω_0 and ω_{QD} are the angular frequencies of the fundamental cavity mode wavelength and QD emission respectively. $\kappa = \omega/2Q$ represents the losses in the system due to cavity imperfections and γ represents the losses of the QD emission into other modes and non-radiative decay. κ and γ are the half width half maximum of the cavity and emitter respectively. δ represents the detuning between the cavity resonance and emitter and $\hbar$ is Planck's constant. Assuming the emitter is spatially aligned with the cavity,

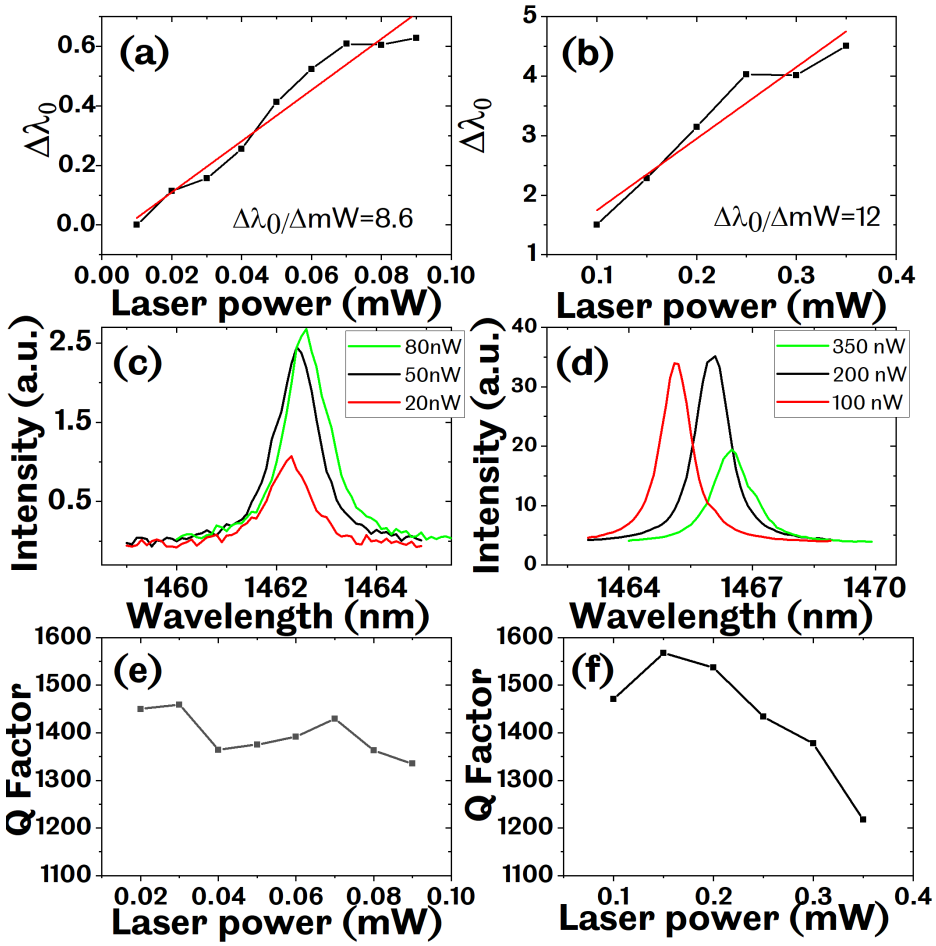

Figure 5.7: Experimental results, (a) and (b) show the change in fundamental cavity mode wavelength with a changing excitation laser power. (c) and (d) show the spectrum of the fundamental cavity mode at different excitation powers. (e) and (f) is the measured Q factor with respect to the excitation laser power.

the coupling strength can be written as:

$$g = \frac{\mu}{\hbar}\sqrt{\frac{\hbar\omega}{2\epsilon V}} \tag{5.2}$$

where ϵ is the dielectric constant in the cavity and μ is the periodic part of the Bloch state. The real part of Eq. 5.1 gives the eigenfrequency of the coupled system and the imaginary part gives the losses. In the weak coupling regime the coupling strength, g, will be far less than half of the cavity mode linewidth, κ, ($g << \kappa/2$). Therefore the losses in the cavity will dominate over the coupling between the cavity and emitter and the expression under the square root in Eq. 5.1 becomes negative. In the case considered here δ is zero so the two eigenstates exist with the same frequency but different loss mechanisms. The loss mechanisms, given by the imaginary part of Eq. 5.1, of each state are given by:

$$\frac{\kappa}{2}\mp\sqrt{\frac{\kappa^2}{4}-|g|^2} = \frac{\kappa}{2}\left(1\mp\sqrt{1-\frac{4|g|^2}{\kappa^2}}\right) \approx \frac{\kappa}{2}\left(1\mp\left(1-\frac{1}{2}\frac{4|g|^2}{\kappa^2}\right)\right) \approx \begin{cases} |g|^2/\kappa \\ \kappa \end{cases} \tag{5.3}$$

This regime is known as the Purcell regime, where the SpE rate of the emitter will be effected by the presence of a cavity. In this regime, two eigenstates exist: the cavity mode and the emitter. The energy decay rate of the cavity mode is 2κ, defined by the cavity Q. The energy decay rate of the emitter eigenstate, at the same frequency as the cavity mode eigenstate, is modified due to its coupling to the cavity mode to equal $2|g|^2/\kappa$. This is very different to the energy decay rate of the emitter in a bulk material, which is given by $\Gamma_n = n\Gamma_0$, where $\Gamma_0 = \frac{\mu_{eg}^2\nu^3}{3\pi\epsilon_0\hbar c^3}$ is the Einstein A coefficient. The ratio between the SpE with and without the presence of a cavity is known as the Purcell factor:

$$F = \frac{2|g|^2/\kappa}{n\Gamma_0} \tag{5.4}$$

Eq. 5.2 can be plugged into Eq. 5.4 as well as expressions for κ and Γ_0 to find the maximum Purcell factor:

$$F = \frac{3}{4\pi^2}\left(\frac{\pi}{n}\right)\frac{Q}{V} \tag{5.5}$$

From this equation, it can be seen that a high Q and low V will lead to an enhancement of the Purcell factor. PhC cavities have a high Q factor, as shown in section 5.3, and a small mode volume which enables an enhancement of the quantum dot emission via the cavity mode.

5.5.1 Time-domain micro-photoluminescence

In the experiments carried out, the PhC L3 cavity is excited using a pulsed laser at 66MHz. The excitation wavelength is fixed at 1044nm and the pulse width of the laser is less than 250fs. Time correlated single photon counting (TCSPC) is used to measure the SpE from the QDs. The overall timing precision of the TCSPC system is summarised in the instrument response function (IRF). The IRF is measured using a reflective mirror under the objective. The laser light is attenuated down to nanowatt levels of power before being sent into the objective. The reflected laser light is then detected using the single photon detector and the IRF is measured to be around 0.1ns, as shown by the green line in Fig. 5.8.

Figure 5.8 shows the QD SpE for the bulk membrane material, given by the red line with an exponential curve fitted. The carrier lifetime is measured to be 0.8ns, this is a common value for InAs QDs [184]. The QD emission that is coupled to the fundamental mode of an L3 cavity is measured as a comparison to the bulk material. This is shown by the blue line in Fig. 5.8 and an exponential curve is fitted on top. The SpE rate has been enhanced, giving a decay rate of 0.2ns. The enhancement factor, E_n, is defined as:

$$E_n = \frac{\tau_{cav}}{\tau_{bulk}} \tag{5.6}$$

An enhancement factor of 4 gives clear indication of QD emission coupling to the fundamental mode of the cavity. However, it is not clear whether this enhancement is due to surface recombination, carrier diffusion or the Purcell effect. The spot size of the excitation laser is greater than the cavity, meaning that carriers are generated in and around the cavity. However, there will be a greater concentration of carriers in the cavity compared to the surrounding areas due to the air holes in the membrane. This greater concentration of carriers will then diffuse quickly out of the cavity area given its small size. However, according to the literature [187, 188, 189], the presence of a PhC cavity has little effect on carrier diffusion rate. On the other hand, surface recombination will greatly increase the speed that the carrier recombine in a cavity. This is because of the enhanced surface area compared to a membrane without any fabricated devices. This holds true for both QD emission that overlaps with the cavity and QD emission at other wavelengths. Measuring the off resonant cavity emission, it is found that an enhancement of the QD SpE is still present. This strongly suggests that surface recombination is playing a major role in determining the QD carrier lifetime.

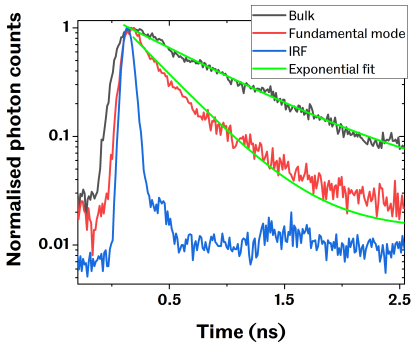

Figure 5.8: QD time resolved emission measurements. The black and red line represent the SpE of the bulk and cavity coupled QDs, respectively. The blue line gives the IRF.

When the QD emission is spectrally detuned from the cavity mode, the QD SpE rate due to the Purcell effect will follow a Lorentzian shape. This is due to the local density of optical states in the cavity [186]. To further analyse the effect of QD emission coupled to the cavity fundamental mode, a resonance sweep across the M0 mode spectrum is taken. Time domain measurements are taken every 0.5nm for 6nm that overlap with the cavity mode. Figure 5.9(a) shows the QD carrier decay time across a wavelength range, given by the black boxes and a Lorentzian distribution curve is fitted to the data, given by the green line. The fundamental mode is given by the red line which shows that at resonance, the decay time is at a minimum. Figure 5.9(b) gives an example in the time domain of the decay rate at the fundamental mode wavelength and 1 nm away from it. Although the emission is still enhanced by the presence of the PhC device through surface recombination, it is greatly decreased at cavity resonance, indicating Purcell enhancement.

5.5.2 Effect of Q factor on Purcell enhancement

As shown by Eq. 5.5, an increased Q factor will generate greater Purcell enhancement and therefore decrease the QD carrier lifetime. Therefore, to further show that the Purcell effect is dominating the QD emission, a study is performed on the cavity Q factor. The Q of a cavity will be affected by a range of parameters including the surface passivation during fabrication, hole size homogeneity, the number of holes surrounding the cavity and the cavity geometry. A range of devices has been measured to find their Q

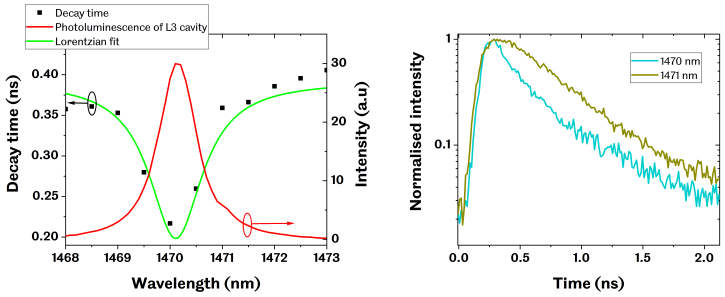

Figure 5.9: Experimental results, (a) shows how the SpE rate increases when the collected emission is on resonance and deceases when collection is off resonance. (b) gives an example in the time domain of the SpE rates both on (blue line) and off (green line) resonance.

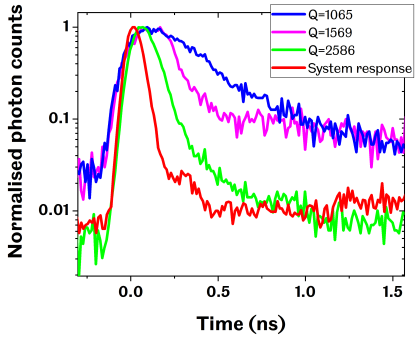

Figure 5.10: Examples of the Q factor dependence on the SpE rate from experimental measurements

factors and this has been compared to their QD carrier lifetime. It has been found that a lower Q factor will have a detrimental effect on the SpE rate, as shown in Fig 5.10. This final measurement indicates that the SpE rate is enhanced due to the Purcell effect at cavity resonance and is not related to other possibilities including surface recombination. When the Q is above 2500, the SpE rate is similar to the IRF, this can obscure the measurement and cause false data. It is therefore difficult to tell what the realistic SpE rate is for cavities in this sample with a Q above 2500 using this set-up. However, this result implies the cavities have potential for light emitting nanoscale devices based on cavity QED effects.

5.6 Summary and conclusion

In this chapter, foundations have been built for ultra-fast excitation of a PhC cavity operating at the telecommunications wavelength. It has been shown that the fundamental mode of a PhC cavity can be tuned using a number of different methods. Lithographic tuning offers a huge tuning range which spans the emission spectrum of the InAs QDs. On a single sample, various cavity operational wavelengths can therefore be realised through lithographic tuning.

Photothermal effects on the fundamental cavity mode have been studied. It was found that an expansion of the semiconductor lattice and increased photon population cause a change in the PhC material band gap and hence the dielectric constant of the material. An ultra-fine tuning range was exhibited when using very low power excitation. At higher powers, the tuning range is larger but the cavity suffers increased absorption losses, leading to a decreased Q. Although thermal effects on the cavity resonance have been demonstrated previously [190], in this work it has been shown that the tuning ratio when using photothermal effects changes depending on laser power. The linear tuning ratio from 0.01 to 0.1mW is 8.6 whereas between 0.1 and 0.4mW the ratio increases to 12. This shows that at low excitation laser power very high accuracy control can be obtained for the cavity resonance. This accuracy proves beneficial in applications such as all-optical, cavity-based switching; a slight change in the cavity resonance will cause significant changes to the switching characteristics.

Finally, time domain measurements were undertaken to analyse SpE enhancement factor of QDs coupled to a nanocavity. Previous studies have shown Purcell enhancement of QD emission in a PhC cavity [188, 191]. However, in this work the QD carrier lifetime at highly specific wavelengths was measured. By taking a time resolved measurement every 0.5nm over the cavity resonant mode, it was found that the carrier lifetime decreased significantly at the cavity resonance. The carrier lifetime followed a Lorentzian distribution curve as the collection wavelength shifted away from cavity resonance, suggesting Purcell enhancement. This method of highly specific wavelength dependent time domain measurements over a fine tuning range provides an alternative method to separate effects of Purcell enhancement from other effects such as surface recombination. The results also show that an increased cavity Q will generate faster carrier dynamics given that the Purcell factor depends on Q/V.

The information gained from these experiments provides evidence that fast excitation of QDs coupled to PhC cavities can deliver an optical source

at a specified wavelength with high repetition rates. The measurements indicate that the devices have excellent potential as either light emitters based on cavity QED effects or coupled to a waveguide as part of an all-optical PhC switch.

Chapter 6

The generation and characterisation of optical sidebands

6.1 Abstract

Generating low-noise microwave photonic signals requires high-specification equipment and a large level of complexity. In this work, the combination of an ultra-fast laser and a two-arm MZI provides a simple method to generate a microwave signal within the ultra-fast laser spectrum. In doing so, a microwave photonic signal is generated using commercially available, low-cost optical components. This creates a low-noise microwave photonic signal that does not suffer from delay line length sensitivity or large, system-wide losses, negating the need for signal amplification. This chapter shows that an OFC with a 66MHz FSR can be easily manipulated to produce an OFC with an FSR ranging from 1GHz to 40GHz. Integration of this scheme into the micro-PL measurement set-up enables the excitation of PhC cavities using a microwave photonic signal. Spectral analysis shows that the microwave signal is resolved in the emission spectrum of the QDs coupled to the PhC cavity. This novel and relatively simple microwave photonic measurement set-up and its usage in the characterisation of nanoscale devices provides evidence of nanoscale microwave photonics.

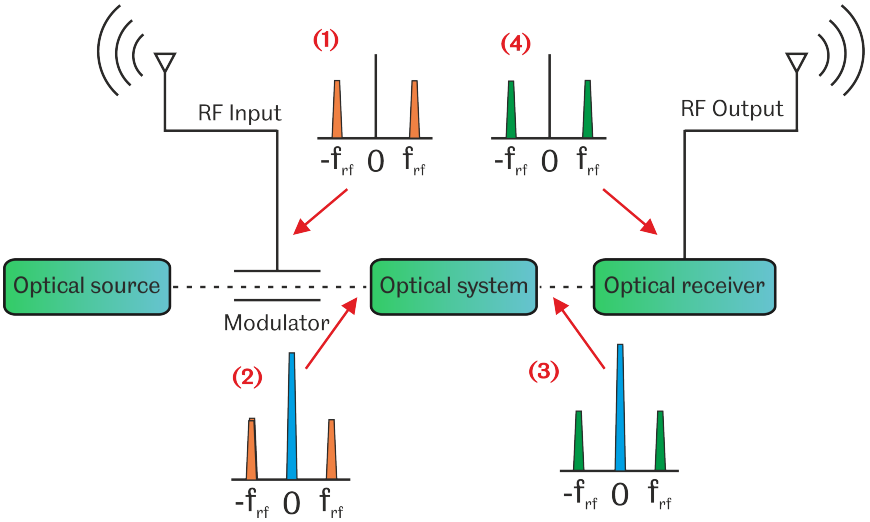

Figure 6.1: A basic schematic of a microwave photonic system.

6.2 Introduction

MWP allows the processing and transmission of microwave signals with a new level of capability compared to traditional microwave technologies [5]. A key driver behind upconverting signals from the RF domain into the optical domain is the bandwidth capabilities. The entire RF and millimetre wave spectrum only constitute a very small part of the optical carrier wave frequency. Therefore, frequency-dependent losses and dispersion when using optical devices are minimal. Another strong advantage to MWP waves is the immunity to electromagnetic interference which inhibits various microwave applications [192]. These two advantages, along with the fast tunability and reconfigurability, have meant a plethora of research and applications has been realised [193, 80, 194].

The basic concept of a microwave photonic system is shown in Fig. 6.1. At its starting point, an optical source is modulated via an electrical RF input. The RF source will have frequency components centred at frequencies $\pm f_{rf}$, indicated by point (1). This signal is upconverted into the optical frequency domain via a modulator so that the sidebands are now centred around $\nu \pm f_{rf}$, where ν is the centre frequency of the optical source, shown by point (2). This signal is then processed by a system composed of several optical devices. The operation of the system is to modify the spectral characteristics of the optical signal and thus the sidebands that represent the

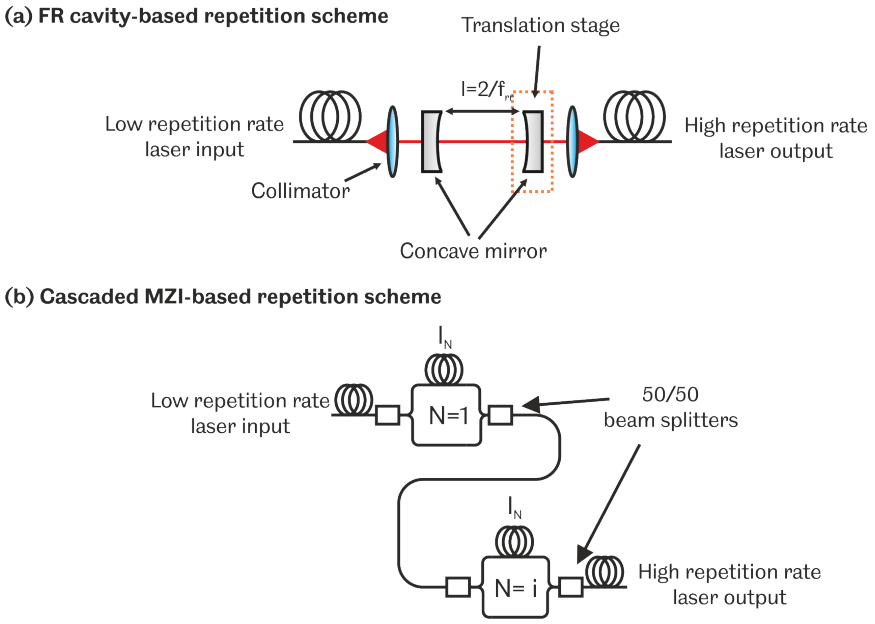

Figure 6.2: Optical bit rate multiplying via (a) a Fabry-Perot cavity and (b) interleaved pulse trains.

RF signal, point (3). Finally, beating between the carrier and the sidebands onto a detector recovers the RF signal and downconverts it back into the electronic domain, point (4).

As shown in Fig. 6.1 the generation of sidebands in the optical frequency domain is a core concept which fundamentally drives the research field. In order for nanophotonic devices to be realised as a viable option for future integrated MWP, sidebands in the spectrum of a nanophotonic cavity must be realised. The modulation of nanophotonic cavities to produce optical sidebands has been theoretically demonstrated by various research groups. Li *et al.* [139] developed a model to generate a high number of sidebands using QDs strongly coupled to a cavity. They proposed a two CW laser pump system where the FSR between the generated sidebands in the cavity is equal to the spectral difference between the laser frequencies. Calajo *et al.* [142] proposed a scheme where a two-level quantum emitter, such as a QD, in a photonic bandgap environment is externally modulated. In this case, the quantum emitter is weakly coupled to the bandgap environment and it is shown that peaks will appear in the quantum emitter's spectrum at points equal to the modulation frequency.

The generation of sidebands in a QD spectrum has also been realised using single QD coupled to a vertical geometry cavity, in other words a 1D PhC cavity. In this work, modulation of a QD was performed by applying a periodic strain on the material via a surface acoustic wave (SAW). A SAW enables tunable strain components near a semiconductor surface at high frequencies. The QD is excited using an above band laser and then modulated using a SAW with a repetition rate at 1GHz, the resulting spectra shows clear indication of sidebands produced through periodic perturbation of the QD strain. Recently, another approach has been taken to modulate the emission characteristics from a two-level system acting as a single photon source [138]. By shifting the emission wavelength of the TLS via the Stark effect, they enable temporal modulation of the emitted photons. The resulting spectrum from the two-level system shows sideband generation at points equal to the temporal modulation speed which is varied from 1GHz to above 10GHz. Using a PhC cavity-waveguide system, Yu *et al.* [123] demonstrated a self-pulsing laser where one of the mirrors is based on the Fano resonance between a waveguide continuum and the discrete resonance in a nanocavity. The mirror acts as a passive saturable absorber which leads to the generation of discrete pulses from a CW laser excitation source. The generated pulse rates are a product of the laser power. By increasing the power, pulse trains up to 8GHz have been experimentally achieved. In the spectra at the output of the device, a frequency comb is generated where the comb line spacing increases with increasing power.

In all of the aforementioned schemes, the overriding concept is the excitation and modulation of a system using high repetition rates which fall within the RF bandwidth. Throughout this thesis, optical excitation has been the overriding method used to characterise nanophotonic devices. In this chapter, methods to generate sidebands from the nanophotonic cavity are realised through optical excitation using a laser with high repetition rates in the RF range. Here, cavity excitation is achieved using an ultra-fast laser with a fixed wavelength at 1044nm, a pulsewidth of less than 250fs and an initial repetition rate of 66MHz. By increasing the repetition rate of the laser, sidebands are visible in the laser spectrum at a distance equal to the repetition rate. This signal can then be encoded onto the cavity and hence generate sidebands in the mode spectrum of the cavity.

Generating microwave photonic signals from a MLL using standard optical table components has been a topic of research over the past decade [195, 196, 76, 197, 198]. The focus in these works is to reduce the amount of noise inherent in the photodetection process when generating microwaves using optical signals. Two common methods to increase the repetition rate

are shown in Fig. 6.2. The method shown in Fig. 6.2(a) is based on an FPC (Fabry-Perot cavity) composed of two concave mirrors with a 97% reflectivity, giving a finesse of around 100. The pulse enters the cavity and when it hits the mirror, 3% of the pulse is emitted out of the cavity and 97% is reflected. The reflected pulse then travels a distance of twice the FPC length before emitting another 3%, thus forming consecutive pulses with a delay equal to twice the FPC length. The spectrum of the input MLL is a frequency comb with the FSR a product of the laser cavity length. Fine adjustment of the FPC length can enable matching between a harmonic of the laser cavity and the FPC. The output of the FPC produces a thinned frequency comb with a combline spacing that is a product of the FPC length. Therefore, the FPC can essentially be thought of as a cavity mode filter. For example, if the input repetition frequency is 250MHz and the output is 5GHz, then 1 out of every 20 modes is passing through the system and the other modes are reflected. The advantage in this system is the phase alignment for each pulse, this will always be perfectly aligned for each harmonic. It also has the capability to dynamically alter the mode filter by adjusting the FPC length. On the other hand, this arrangement set-up is fairly complicated and losses through the system are very high, typically around 20dB. The signal to noise ratio then needs to be increased with the use of a erbium doped fibre amplifier (EDFA) which inherently limits the system capabilities to the EDFA specification and increases system complexity. Another method, based on cascaded Mach-Zehnder interferometers (MZI) is shown in Fig. 6.2(b). This scheme proves to exhibit far less loss and is the basis for measurements undertaken throughout this chapter. This is discussed in detail in the next section. A third way to generate a microwave signal from an MLL is through harmonic mode locking. In this case, multiple ultra-short pulses are circulating within the laser resonator with equal temporal spacing. In active MLLs, this can be achieved by driving the modulators with a harmonic of the round trip frequency. In passive devices, this technique becomes more complicated and pulses can appear in bunches rather than equally spaced. Various techniques have been employed to overcome these difficulties, for example resonant sub-cavities. Detailed analysis of harmonic MLLs is beyond the scope of this project so is not discussed in detail.

6.3 Optical pulse interleaving for bit rate multiplication

The approach used to increase the repetition rate of the laser is shown in Fig. 6.2(b). It is based on cascaded MZIs which act to split the pulse train and temporally delay one arm of the MZI through spatial manipulation. The two pulse trains are then temporally interleaved to double the number of pulses in the laser pulse train. The pulses are made to be equally spaced in the time domain by ensuring the delay line length in each MZI follows:

$$l_N = \frac{1}{f_{rr} \times 2^N} \times \nu \tag{6.1}$$

where N is the number of cascaded MZIs, f_{rr} is the repetition rate of the laser and $\nu = c/n$ is the speed of light in the fibre, where n is the refractive index of the fibre material and c is the speed of light. By cascading multiple MZIs the laser pulse repetition rate can be increased by $f_{rr} \times 2^N$.

The laser is coupled into a single-mode fibre with a core of 9µm and cladding of 125µm. Each MZI consists of two fibre-based beam splitters; the first splits the pulse train into two and the second interleaves the two pulse trains. There are two commercially available types of fibre beam splitters: fused bionical taper (FBT) and planar lightwave circuits (PLC). FBTs are commonly used due to their simplicity, it is essentially two fibres that are fused together by twisting, melting and then tapering. PLCs are lithographically etched circuits which have increased flexibility and control over the propagating light. Therefore, they have the advantage over FBTs because number of arms and splitting ratio can be user-specified. However, they are a lot more expensive and less widely available commercially.

FBTs are employed in the initial testing of this OBRM system due to their simplicity and reduced cost. The fibre delay lines are fabricated by splicing two fibres together. Fibre splicing was carried out in the lab using a cut and splice machine. Repetition rates into the tens of gigahertz is needed for experimental implementation which means up to eight two-arm MZI schemes are needed. To measure the output from each MZI, TCSPC is employed giving a timing accuracy down to 0.1ns. This is limited by the IRF, as discussed in the previous chapter. Figure 6.3 shows the output from the first seven MZIs and table 6.3 gives the real and ideal cases for each arm for all eight MZIs. The timing of each arm for the eighth MZI is measured individually to find their difference. However, when the two arms are interleaved at this speed (16GHz) they cannot be individually recognised because the delay is less than the IRF.

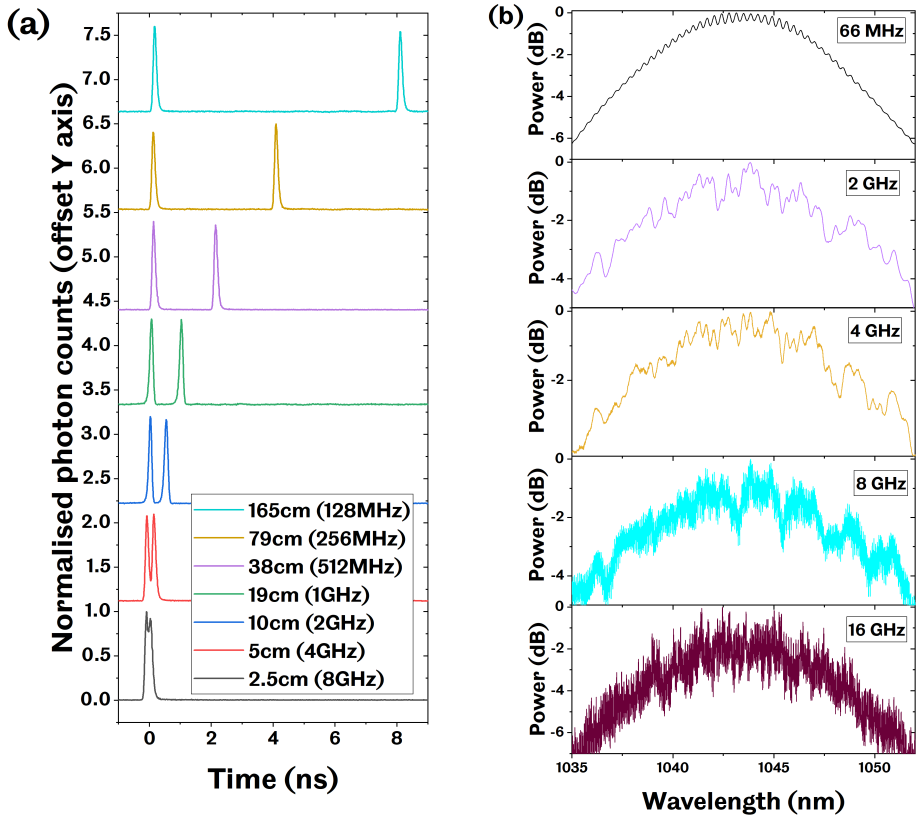

Figure 6.3: Experimental results, (a) the time domain response of each individual MZI scheme. (b) the frequency domain response of an increasing number cascaded MZI schemes

MZI	Rep. rate (GHz)	Ideal delay (ns)	Real delay(ns)	Error(ns)
1	0.132	7.94	7.937	0.003
2	0.264	3.97	3.969	0.002
3	0.528	2.004	1.984	0.02
4	1.056	0.965	0.992	0.027
5	2.112	0.513	0.496	0.017
6	4.224	0.232	0.248	0.016
7	8.448	0.122	0.124	0.002
8	16.896	0.073	0.062	0.011

It is found that with precise splicing of the fibre, a maximum error of 0.027ns has been achieved. This relates to maximum difference in arm length of 5mm between the real and ideal case. The error resides in the fibre cleaving; a clean break must be made to ensure good end-to-end connection between the two fibres. If the fibre is not cut perfectly then high losses will be endured at the fusion point. Ensuring right-first-time cleaving on two fibre ends proves to be very challenging. In some cases, a second cleave was needed, thus shortening the length of the fibre and creating a larger error.

Using all eight MZIs in series, laser pulses at 16GHz is achieved, by cascading fewer MZIs, laser pulses at a range of repetition rates can be achieved. Using a fibre-coupled optical spectrum analyser (OSA) the spectrum of the laser can be analysed, this is shown in Fig. 6.3(b). The OSA used is a Yokogawa AQ6370D Telecom OSA, the wavelength range is between 600nm and 1700nm and provides a wavelength resolution and accuracy of 0.02nm and $\pm$0.01nm, respectively. At 66MHz, the spectrum shows a Gaussian curve with slight aberrations in its peak. At 2GHz, the spectrum is altered by the time domain changes in the pulse train. The laser generates pulses via a passive mode-locking mechanism. Each mode in the system is separated by 66MHz in the frequency domain, this separation is determined by the length of the laser cavity. At 66MHz, it is not possible to resolve each frequency component individually as this would require ultra-high resolution spectroscopy. From Eq. 6.2 it is found that at 1044nm, a 66MHz pulse train generates frequency components that are around 0.2pm apart.

$$\lambda_{spac} = \frac{c}{f_0} - \frac{c}{f_0 + f_{rr}} \tag{6.2}$$

where f_0 is the peak laser frequency, λ_{spac} is the wavelength spacing between frequency components. As the repetition frequency is increased, the spectrum will separate out into frequency components that match the repetition frequency. Using Eq. 6.2, the minimum calculated repetition rate that can

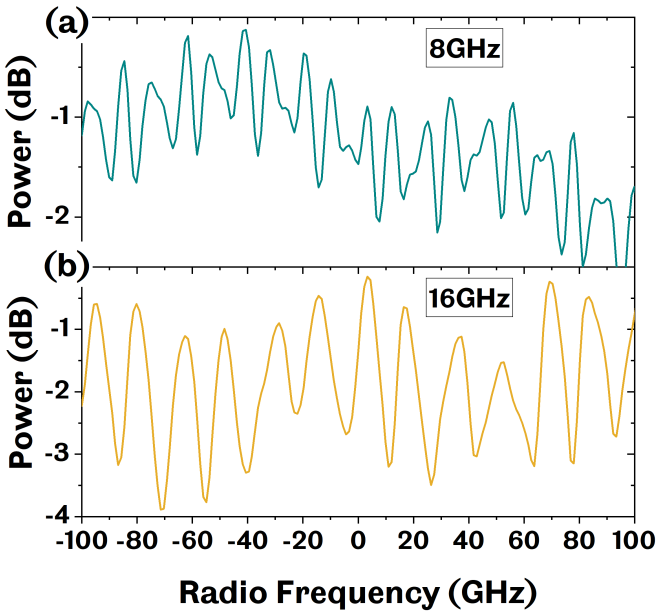

Figure 6.4: The spectrum of the laser when (a) seven MZIs are cascaded and (b) eight MZIs are cascaded. Experimental results

be distinguished using the OSA is found to be around 10GHz, giving frequency components that are 0.04nm apart. In Fig. 6.3(b), at 2GHz and 4GHz, the frequency components cannot be resolved but there is alteration in the spectrum. As 8GHz is reached, the individual frequency components can be seen in the spectrum. Figure 6.4(a) and (b) give a high resolution plot of the laser spectrum when the repetition frequency is increased to 8GHz and 16GHz, respectively. The signal-to-noise ratio (SNR) is given by the ratio between the peak and the trough of the frequency components. At 8GHz, this is relatively low with a maximum of 1.3dB. The sampling rate of the OSA is very close to its limit so the components are still very difficult to distinguish. When the repetition rate is doubled again using the eighth MZI, the frequency components are drawn further apart. They therefore become more distinguishable in the laser spectrum and the SNR improves to a maximum 3.1dB, as shown in Fig. 6.4(b).

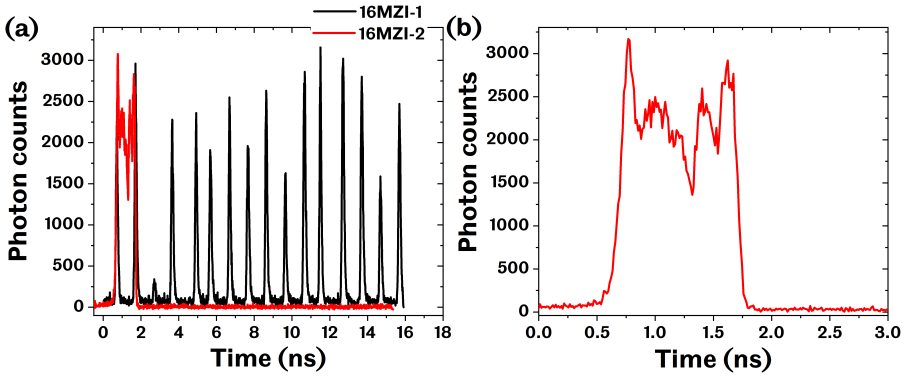

Figure 6.5: The time domain response of the 16MZI-1 in black and the 16MZI-2 in red. (a) shows the entire 16ns response from both devices (b) shows only the 16MZI-2 over a time period of 3ns. Experimental results.

6.4 Effect of timing accuracy on generated frequency components

In an ideal case, when the laser repetition rate is increased to 16GHz, the spectrum would exhibit comblines with equal width, a large SNR and individual combline intensity that equals the Gaussian shape of the laser spectrum. However, the comblines shown in Fig. 6.4(b) are inhomogeneous in both their width and their intensity. As discussed above, there is error in the timing between the pulses which is due to two main functions. The first is the time domain detection method which is only accurate to 0.1ns, this causes errors when measuring the timing between pulses. The second is due to the difficulties in fibre splicing which directly causes a difference in the timing between consecutive pulses. The frequency components are a summation of the time between consecutive pulses. A large variation in the time between two consecutive pulses will cause the frequency components to become wider and thus hard to resolve [196]. When generating a microwave signal from an optical signal, it has been found that an error of 9ps between pulses will greatly degrade the generated microwave signal [198].

To overcome this issue, fibre splicing has been outsourced to an external company. A company that specialises in PLC technology was able to produce 16-arm MZIs with user-specified delays. Using PLC fibre beam splitters, the laser pulse train can be split into 16. Each of the 16 arms is coupled to a fibre and spatially delayed before being interleaved to give a pulses repetition rate at $f_{rr} \times 16^N$, where N is the number of 16-arm MZIs. Two

16-arm MZI devices were designed as part of this project and constructed by an external company, one to generate a 1GHz pulse train from a 66MHz pulse train, which will be denoted as 16MZI-1 and the other to generate 16GHz from 1GHz, which will be denoted as 16MZI-2. By cascading the two, a 16GHz pulse train is produced from a 66MHz pulse train. In this scheme the average power loss through the entire system is 20dB. Although this is still very high, it is greatly reduced compared to the two-arm MZI scheme. In using cascaded two-arm MZIs, the loss through each MZI was 6dB so eight cascaded devices led to very low power at the output. The time domain measurements using the TCSPC for both 16MZI-1 and 16MZI-2 are shown in Fig. 6.5 by the black and red line, respectively. Each arm in the 16MZI-1 needs to differ in length by $\nu \times 1/f_{rr}$ metres. Unfortunately, when measured using the TCSPC, the timing between the pulses has a maximum error of 0.26ns, relating to a length disparity of 5cm. For the 16MZI-2, the required distance between each pulse is 0.062ns, which cannot be resolved using this TCSPC method. However, as can be seen in Fig. 6.5(b), all pulses are compressed into 1.1ns, suggesting that the distance between pulses is 1.1/16ns. The spectrum from cascading both the 16MZI-1 and 16MZI-2 together and 16MZI-2 on its own has been measured using the OSA and is shown in Fig. 6.6(a) and (b), respectively. As can be seen in Fig. 6.6(a), the spectrum shows frequency components with a maximum SNR of 2.1dB and some frequency components that are indistinguishable and not matching the 16GHz FSR. Comparing this with the two-arm MZI scheme, with a timing error of 0.027ns, the effect of timing accuracy on the laser spectrum can be seen.

Figure 6.6(b) shows the spectrum when only 16MZI-2 is used. The spectrum shows similar characteristics to the cascaded 16-arm MZI scheme: a maximum SNR of 2dB and an inconsistent FSR. However, individual frequency components are still visible with an FSR around 16GHz. The 16MZI-2 scheme delivers a pulse train of 16 pulses with a separation of around 1.1/16GHz every 1/66MHz. The timing accuracy of 16MZI-2 is assumed to be low given that the timing accuracy of the 16MZI-1 is low. Regardless of this fact, frequency components are clearly visible without the need to deliver 16GHz pulses. This suggests that the laser pulse train does not need to repeat at 16GHz but needs to deliver pulses that have a 1/16GHz delay between them.

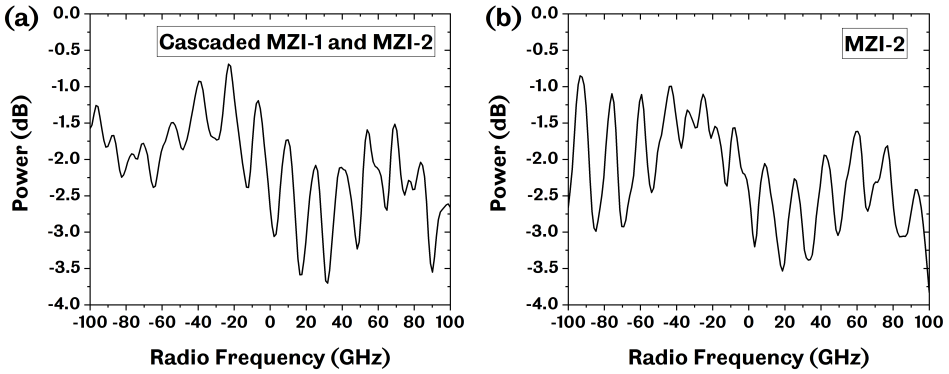

Figure 6.6: Experimental results of (a) frequency response of cascaded 16MZI-1 and 16MZI-2. (b) frequency response of 16MZI-2

6.5 Double-pulsing method

The challenge thus far in both the work undertaken here and in the literature [198, 76] resides in key two points. Either the phase between the pulses can be perfect using the FPC method but with very low signal strength so an EDFA is necessary. Or the signal strength can be increased but the phase between pulses is inherently limited by splicing accuracy and cannot match that of the FPC scheme. To overcome both of these issues, a single two arm MZI is employed where the delay is equal to the inverse of the desired microwave frequency. In this case, frequency components at two spacings will exist in the laser spectrum at $f_{rf} = 1/\tau_{rf}$ and $f_d = 1/\tau_d$, where τ_{rf} is the spacing between two pulses in the time domain equal to a specified RF signal and $\tau_d = -\tau_{rf} + 1/f_{rr}$. Assuming $1/f_{rr} >> \tau_d$, then only f_{rf} will be visible in the frequency domain. In this scheme, the timing between two consecutive pulses will always be equal which eradicates fundamental error when cascading multiple MZIs. The loss through the system, which hinders the FPC microwave generation method, is greatly reduced. In this case, a total loss of 6dB is achieved, however, this could be further reduced with higher quality fibre beam splitters.

To show this new method functioning, various MZIs have been fabricated where the arm length is varied, the data is shown in Fig. 6.7. Even down to 4GHz, Fig. 6.7(a), the frequency components can be distinguished which suggests a very high level of pulse phase accuracy and a potential low-noise floor. As the spatial length of the delay arm decreases, the distance between the frequency components increases. An increase in the FSR means

higher resolution of the frequency components, which gives a large SNR. The SNR of the individual frequency components increases up to a maximum of around 8dB when the time between two pulses is $0.046ns = 1/22^9$, as shown in Fig. 6.7(e). This new method to generate microwave photonic signals has shown to decrease losses in the system compared to FPC systems and increase the pulse phase accuracy compared to the cascaded MZI systems.

This double-pulse scheme can then be exploited for the excitation of PhC nanocavities to analyse their functionality in microwave photonics. Although many research facilities have ultra-fast lasers to analyse the time domain response of micro and nano scale devices, no system utilises ultra-fast lasers in this way. In doing so, the gap can be bridged between standard optical characterisation of nano scale devices and microwave photonics, using fibre optic components that are commercially available.

6.6 Exciting PhC cavities using interleaved double-pulses

In this section, PhC devices are characterised using the double-pulsing method. The micro-PL set-up is used in conjunction with the ultra-fast increased repetition rate laser with central wavelength at 1044nm. A range of PhC L3 cavity devices with an active QD layer and lithographically tuned fundamental mode wavelengths is excited. In this section, the challenges faced in this type of new measurement are discussed as well as potential future applications.

6.6.1 Resolving frequency components with low FSR

As outlined in the previous section, resolving sidebands at microwave frequencies using optical spectroscopy requires very high-resolution measurements. In the micro-PL set-up, a Horiba FHR1000 spectrometer is used which has a company-specified spectral resolution of 0.01nm when 10µm slits are used at the entrance and exit of the spectrometer. A spectrometer works by converting components in the frequency domain into the spatial domain via a diffraction grating. Therefore, by ensuring the diameter of the light beam being input into the spectrometer and output onto the detector is as small as possible, the resolution can be increased. In the previous section, it was found that spectral components that are separated by as little as 0.015nm (4GHz spacing at 1044nm) could be resolved using the OSA, this is far lower than the company specification. To test the actual resolution

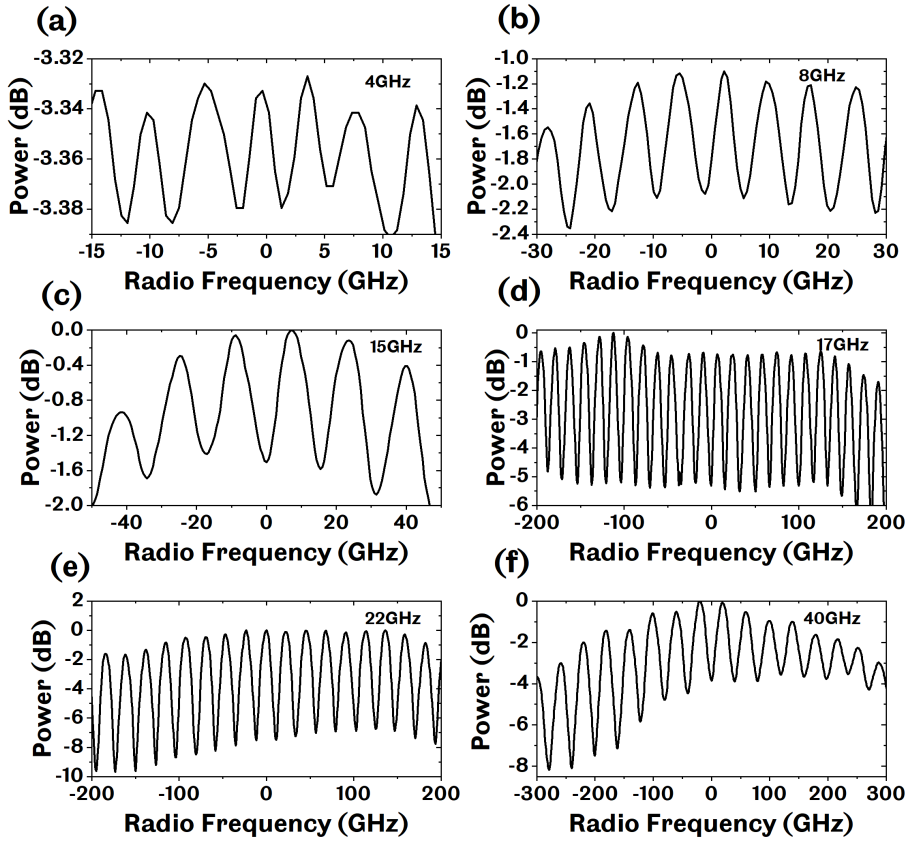

Figure 6.7: Experimental frequency response at the output of a single two-arm MZI where the arm difference is varied.

of the FHR1000 spectrometer, rather than the given specification, the output from the two cascaded 16MZIs is measured. By reducing the slit size, the spectral resolution is increased and individual frequency components are distinguished, as shown by Fig. C.4(a). The time domain pulse train for the 16MZI-2 device is given in Fig. 6.5(b). There is an increase in intensity at the beginning and end of the pulse train, suggesting that there is a pulse of higher intensity at these points. The distance between them is 1.1ns, which relates to a τ_{rf} of 0.91GHz. Therefore, in the pulse train there are two prevalent beatnotes, at 0.91GHz and 16GHz. With the slits at 100µm, neither beatnote can be identified, as shown in Fig. C.4(a). Reducing the slit size, the peaks from the 16GHz signal can be distinguished at around 50µm. At a slit size of 10µm, aberrations appear within the 16GHz frequency components. Figure C.4(b) shows a detailed spectrum of the laser when a 10µm slit is used. The secondary peaks that only appear in the spectrum at low slit sizes are 0.91GHz apart, suggesting the beatnote from the pulses at the beginning and end of the 16MZI-2 pulse train is resolved using the FHR1000.

It is worth noting that Horiba cannot guarantee slit size accuracy below 100µm, so although it has been set to less than this value, there is room for error here. As a test of this error, a measurement was taken with a slit size of 20µm, then the slits were increased to 2000µm and decreased back to 20µm and another measurement was taken. The results found that the resolution changed between measurements, indicating a disparity between slit sizes at this level.

From Fig. C.4, it can be said that a slit size of less than 50µm is needed to resolve low frequency microwave photonic signals. By decreasing the slit size, less of the emitted light will reach the detector. The radius of the emission beam at the point where it enters the spectrometer is limited by the diffraction limited spot size, which is given by the following equation:

$$\emptyset_{spot} = \frac{4\lambda l_f}{\pi D} \tag{6.3}$$

where l_f is the focal length of the coupling lens specified by Horiba to be 100mm and D is the beam diameter of the collimated emission beam which is dictated by the objective aperture. For the 100x Mitutoyo objective used, this is 2mm. Hence a minimum beam diameter of around 100µm can be realised, assuming a central wavelength at 1.55µm. This is greater than the necessary slit size, meaning a significant loss in sensitivity at this resolution.

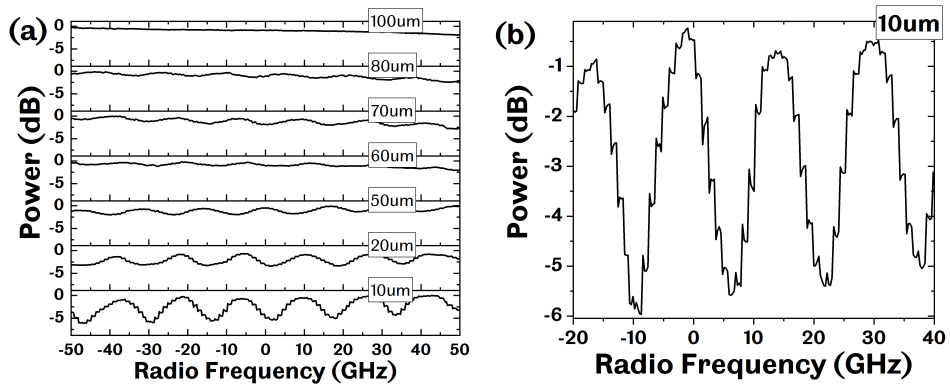

Figure 6.8: Frequency response of cascaded 16MZI-1 and 16MZI-2 using a high resolution spectrometer

6.6.2 Device measurement

When measuring the L3 PhC at room temperature with a slit size within the tens of microns, the signal was not strong enough to be detected above the noise floor inherent in the system. By cooling the sample down to 77k, the emission from the QD layer becomes far brighter due to the reduction of non-radiative recombination. By scanning over a wide range of devices, QD emission which is coupled to the cavity resonance will emit light with stronger intensity and therefore can be detected when the slit size is less than 50µm.

PhC cavities are excited with the double-pulsed laser, where a two-arm MZI is used and the arm length difference is set to $\tau_{rf} = 1/4GHz$. The fundamental mode of an L3 PhC cavity is shown in Fig. 6.9(a). At cryogenic temperatures the linewidth of the mode is greatly decreased and the central wavelength will blue shift compared to room temperature characterisation. The mode shows signs of aberrations in its peak, this is a result of double-pulse excitation, where τ_{rf} is set to 1/4GHz. The peak of the mode is shown in Fig. 6.9(b), where the x axis is given in terms of the relative RF away from the central fundamental mode wavelength at 1376nm. The Y axis in Fig. 6.9(b) has been given in relative power so that the SNR can be analysed and comparisons to the laser spectra can be made. The QD emission spectra shows clear signs of breaking down into frequency components that are 4GHz apart with a maximum SNR of 1.2dB. This is the first indication that PhC L3 cavities are capable of handling microwave photonic signals. As outlined in the introduction, an integrated microwave photonic

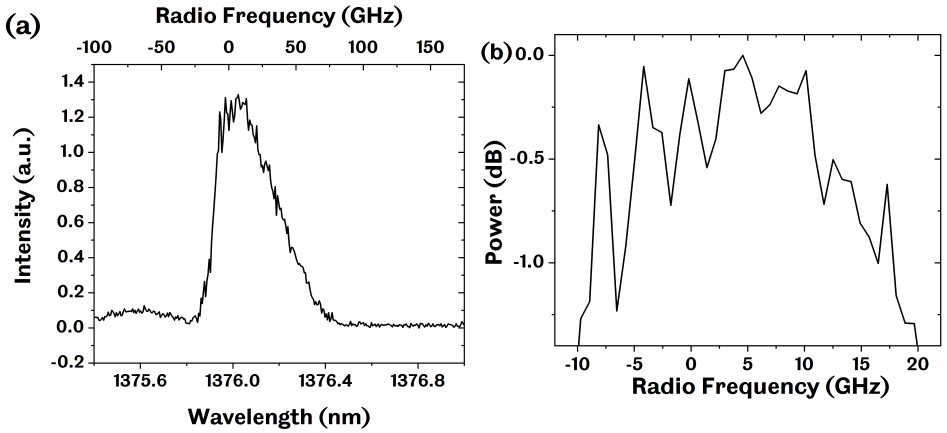

Figure 6.9: Experimental realisation, (a) the spectrum of the PhC L3 cavity when pumped using the double-pulse method at 4GHz (b) a high resolution graph showing the individual frequency components at 4GHz separation.

system is composed of various functionalities where RF signals are present in the sidebands of an optical device. Here these sidebands are present in the emission spectrum of the QDs coupled to a PhC cavity. It is also the first step in generating OFCs using PhC L3 cavities. As discussed in chapter 3, cascading a PhC cavity-waveguide based intensity modulator with a waveguide based phase modulator will produce a broadband OFC. In this case, an L3 cavity has been excited using an optical RF signal without the presence of a waveguide. The result shows the presence of individual comblines. By coupling this cavity to a PhC waveguide, the number comblines could be increased through phase modulation and generate a wide band OFC.

Unfortunately, the SNR in this case is very low, at 1.2dB, meaning that the frequency components are hard to distinguish. The small SNR is due to the carrier lifetime of the QDs. When measuring the laser pulses, sidebands at 4GHz are easily distinguishable, as shown in Fig. 6.7(a). As discussed in section 6.5, this is partly due to accurate pulse timing from the double-pulse system but also due to the laser pulses having a very narrow linewidth in the time domain. This means that there is clear distinction between each pulse. However, by using emission from the QDs coupled to a PhC L3 cavity, the pulsewidth is greatly increased in the time domain. As discussed in chapter 5, the carrier recombination time is around 0.1-0.2ns. Therefore, the two pulses from the QD emission will overlap slightly. To understand the effects this will have on the spectra, the double-pulse excitation method

can be thought of as an intensity modulation scheme. The modulator is the excitation laser and the carrier light is the emission from the QDs. The double-pulsing from the laser can be encoded onto the QD emission via excitation. In this case, the modulation depth of the device at 4GHz is low given the QD carrier lifetime. This results in a low SNR between the generated 4GHz frequency components in the QD emission spectra. Any decrease in τ_{rf} results in the FSR becoming indistinguishable due to the carrier lifetime of the QDs in the cavity. An increase in τ_{rf} causes difficulties in resolving the spectra while maintaining high enough PL when the slit size is reduced. Another limiting factor is the cavity mode linewidth; a linewidth equal to or less than the generated sideband position, at 4GHz from the initial cavity resonance, would produce more prominent sidebands that are easily distinguishable from the cavity mode.

Having said this, the results shown have important significance for the research field. The concept of breaking up the cavity mode field by temporal amplitude fluctuation is relatively abstract. As outlined in the introduction, there are some groups with a similar concept in mind: generating optical sidebands in the emission spectrum of a TLS via temporal modulation either though optical transitions [138] or by SAW [143], to give two examples. This work has used optical modulation to move towards achieving sideband generation from QDs coupled to an optical nanocavity so although the modulating scheme is different, the concept is the same. There has also been some theoretical work that has specifically dealt with QD emission in a photonic bandgap environment, such as a PhC. In these cases, a single QD has been simulated with either weak [142] or strong [139] coupling to the PhC cavity environment. The case studied experimentally here is different to these cases given the QD ensemble in the cavity but the general concept goes towards achieving the same goal. This work is significant due to its experimental realisation; it has proved that the emission spectrum of a QD ensemble weakly coupled to a PhC cavity can be manipulated by temporal modulation. With this in mind, progress in this area can be pushed forward with more confidence. For example, by showing manipulation of the QD ensemble emission spectrum though temporal modulation provides an argument for single QD emission manipulation through temporal modulation.

6.7 Summary and conclusion

This chapter has revolved around two parts. The first demonstrated a novel method to generate and characterise microwave photonics signals. Using

commercially available optical components and a mode-locked laser, pulse trains that harbour two time domain spacings with perfect phase alignment are produced. The interleaved double-pulsing method builds upon methods undertaken by other research groups where cascaded pulse interleaving is used. However, this method simplifies the operation and reduces noise induced by delay line length disparity.

In this double-pulsed scheme, the spacing between the comblines in the MLL are separated by the inverse of the two time domain spacings: $1/\tau_{rf}$ and $1/\tau_d$. The spacing is controlled by the MZI arm length difference in a two-arm MZI scheme, hence generating tunable optical RF signals. During these experiments, optical RF signals were produced from 1GHz up to 40GHz. This method has the potential to characterise microwave photonic signalling in nanoscale devices using components that are common to any ultra-fast photonics lab.

The second part of this chapter utilised the interleaved double-pulsing method to excite PhC nanocavities. Using the double-pulsing method, individual frequency components spaced at 4GHz in QD emission that is weakly coupled to the PhC cavity are observed. The realisation of microwave signal in the optical spectrum of a PhC cavity provides evidence of microwave photonic signal processing using next generation PIC technology.

Chapter 7

Summary and future work

The ambition of this project was to study microwave photonic phenomena, such as the generation of optical sidebands, within a nanophotonic system. To realise this goal, nanoscale all-optical modulators based on PhC structures operating in the microwave frequency range were simulated. Following this, a unique measurement set-up for the characterisation of MWP signals incident on nanophotonic devices was developed. In doing so, knowledge was gained in the inherent challenges and potential benefits of nanoscale MWP. Through a literature review, simulation, fabrication and measurement, each chapter of this thesis contributes to the overarching theme of nanoscale MWP. In this final chapter, the work from each of the previous chapters is summarised and the scope and future direction of this new research field are discussed.

7.1 Summary

Chapter 1 introduces the basic concepts of OFC generation and its position within MWP. The prevalence and ubiquitous nature of OFCs in modern research, and notably in MWP, is presented. This provides an argument for the necessary realisation of nanoscale OFC generators. Research into all-opitcal modulators based on nanoscale devices is then outlined to provide a methodology to this realisation. Chapter 2 details the methods used to obtain the results presented in chapters 3 to 6. These include the TCMT model built for simulations, the fabrication techniques used to create the devices and the measurement procedures used to characterise the devices.

With the realisation of PhC-based optical sources, filters and modulators, these structures have shown strong potential for future photonic

on-chip networks. Chapter 3 provides another building block for the PhC repertoire which shows the potential for an on-chip OFC generator. In this chapter, a model based on TCMT is built to simulate all-optical modulators based on PhC devices. Initially two cavity-based IM schemes are analysed: side and direct coupling to the waveguide. With the same sinusoidal input, each scheme produced very different output dynamics. The output from each scheme provided unique capabilities for OFC generation when multiple modulators are integrated. The two integration schemes analysed are the cascading of two IMs and an IM followed by a PM. It was found that the direct coupled IM scheme when integrated with a waveguide based PM produced a broadband OFC with low combline power disparity.

Following the simulation of PhC structures, in chapter 4 a process is developed for their fabrication in nonthermalised InP. This method of nonthermalised fabrication has advantages in industrial processing or for critical subsequent steps where the use of thermal grease is detrimental to the process. It can also be used in facilities where high temperature ICP etching is not possible. A range of gases and ICP chamber parameters were analysed in terms of their capability to produce a straight etching profile with low surface roughness. The optimised etching process produced excellent capabilities for etching PhC structures. Subsequent anisotropic etching steps then produced a free-standing PhC membrane. With this now established process, future studies on PhC structures in InP can be performed at the University of Sheffield. Although research into development processes for PhC structures is a relatively established area, with most research being undertaken 10-15 years ago, the work presented here offers unique capabilities for nonthermalised etching.

Optical characterisation of the devices fabricated in chapter 4 is undertaken in chapter 5. In this chapter, both lithographic and photothermal control of the device cavity resonant wavelengths are demonstrated. Lithographic tuning is obtained by varying the geometric parameters of the PhC during EBL patterning. Photothermal tuning is undertaken by increasing the laser power and observing the frequency shift. Following this, time domain studies on the cavity lifetime are performed both on and off resonance. It was found that Purcell enhancement contributed significantly to decreasing the carrier lifetime in QDs coupled to the cavity resonance. Uncoupled QDs that spatially overlap with the cavity still see a reduction in their carrier lifetime when compared to the emission of QDs in the bulk material. This is due to enhanced carrier diffusion and surface recombination that are inherent to PhC cavity structures. The results from these experiments provide evidence that excitation of QDs in a PhC cavity will generate an optical

source at a specified wavelength which has the potential for fast modulation, only limited by to the QD carrier lifetime.

The final experimental chapter of this thesis develops mechanisms for characterising MWP signals in nanoscale optical devices. The interleaved double pulsing method developed here reduces the complexity of MWP signal generation when compared to standard cascaded pulse interleaving methods and F-P cavity-based schemes. The signal is integrated into the micro-PL set-up and used for nanoscale device characterisation.

This characterisation was undertaken to observe optical sidebands in the mode spectrum of the PhC cavity. In doing so, the emission spectrum of a QD cavity coupled to a PhC cavity is manipulated by its temporal modulation speed. Although the results show only a small SNR, there is still clear indication of frequency components that are separated by a constant microwave frequency. This is the first step in the development of PhC devices with MWP applications.

7.2 Future work

This PhD project has been a success in terms of producing innovative results and laying the foundations for future research revolving around microwave and nanophotonics. With this in mind, it is important to discuss the potential future work that can grow from these foundations.

First and foremost, experimental realisation of the simulated devices outlined in chapter 3 is key to the development of this research area. In this thesis, all the necessary ground work to follow through with this has been laid, this includes the core concept, fabrication processes and optical measurements. With these in place, further optical measurement developments can lead to the pump and carrier signal formation that is outlined in chapter 3. Efforts would be needed in the coupling of light in and out of the device as well as additional light paths added to the measurement set-up. In terms of fabrication, grating couplers have been developed which couple to a PhC waveguide, however no measurements of these devices were carried out. Progression can be made by measuring these devices and coupling an L3 cavity to the waveguide to generate an optical switch.

The model in chapter 3 accurately simulates the output from a cavity-based PhC IM and PM, however improvements could be made. In the model, a single decay rate is used to define the carrier recombination time. This could lead to slight disparity between the real and the simulated parameters where the decay rate is not a single exponential. Depending on the carrier

density, the carrier lifetime will differ due to diffusion characteristics and surface recombination. This was not included in the model here given the small effects it will have on the output pulse shape when a sinusoidal input is used. However, future work could be undertaken in this direction to ensure a higher level of accuracy. Furthermore, the PM scheme uses relatively basic calculations to analyse the output dynamics from the PhC waveguide-based PM. Given that the refractive index change is a direction relation to the pump light energy, this basic treatment seems fair. However, a more sophisticated model could be built to model the modulation dynamics of a PhC waveguide in more detail.

In the last part of chapter 5, the QD carrier lifetime is shown to be a product of the cavity Q factor. To further decrease this lifetime, the cavity could be modified to increase the Q factor beyond the results given here. A common way to do this is to shift the holes adjacent to the cavity. This is one way in which the work in this chapter could be carried forward. A decreased cavity lifetime would mean faster modulation capabilities and generate more prominent sidebands in the emission spectrum of the device. An increased Q would also ensure the FSR between the resonant wavelength and the generated sidebands is greater than the linewidth of the cavity. This could produce sidebands that are outside the cavity mode spectrum. Studying the characteristics of these sidebands in terms of their lifetime and linewidth will provide insight into the mechanisms involved in their generation.

Other interesting work that can stem from these foundations is the use of a PhC based waveguide as a super-continuum OFC generator. In chapter 1, section 1.1, a method to broaden the bandwidth of an OFC via a highly non-linear waveguide is outlined. In this method, a broadened OFC produced is due to the waveguide's decreased GVD and increased non-linearity while maintaining high phase coherence. The measurements of the interleaved double pulsed laser show an OFC that spans 20nm where the FSR is dependent on the delay line of the 2-arm MZI. This OFC has the potential to then be broadened using a highly nonlinear PhC waveguide. Although there is a substantial amount of work needed to understand and realise dispersion control in a PhC waveguide, evidence suggests this is entirely possible. The potential for a broadband OFC produced in this way would have large implications in terms of contributions to both the nanophotonic and OFC research field.

Appendix A

TRPL system set-up, testing and trouble shooting

A.1 Set-up

Figure A.3 shows the block diagram of the TCSPC card. The pulsed electrical signal from the laser (sync) and the detector (trigger) has a positive voltage, however the counting card requires a negative voltage so an inverter is used on both signals. The inverted pulses are initially measured using an oscilloscope and Fig. A.1(a) and (b) show the pulses from the sync and trigger, respectively. The pulses lead into a constant fraction discriminator (CFD) which triggers at a constant fraction of the pulse amplitude. Using a CFD reduces the risk of an amplitude jitter caused by amplitude fluctuation in the incoming pulse. The CFD triggering threshold is set to the lowest possible voltage to help negate amplitude jitter. In this case, the triggering threshold for the laser pulse is set to -40mV and the detector pulse is set to -900mV. The shape of the sync pulse before inversion is a sinusoidal curve so the signal does not change dramatically, as shown in Fig. A.1(a). However for the trigger, before inversion the signal is a square pulse which is 10µs wide. The inverter causes a short pulse at both the rising and falling edge of the pulse, where only the rising edge causes a negative pulse, as shown in Fig. A.1(b). A triggering of the CFD from the sync will start the time to analogue converter (TAC), a triggered CFD from the trigger will stop the TAC. Path lengths both in the optical domain and the electrical domain, will greatly affect the results from the TAC. An example of this is shown in Fig.A.2. A difference in path length can mean that the signal can be cut off, either at the beginning or end. To rectify this, the path lengths can

Figure A.1: Oscilloscope measurements of the (a) sync pulse and (b) trigger pulse

be manipulated; a one nanosecond shift corresponds to 30cm in the optical domain or 20cm in the electrical domain.

The software user interface is shown in Fig. A.4 in emulation mode. The bottom left of the screen shows the rate in photons per second. The green bar and number represents the number of pulses per second from the sync, this is determined by the repetition rate of the laser. The black bar is the number of times the CFD on the detector side is triggered per second. The blue and red bars represent the number of successful TAC and ADC conversions per second. In this instance, the collection time is set to 600 seconds and the software is set to do a single measurement, rather than constantly repeat.

A.2 Testing

Two tests are undertaken to confirm working operation of the TCSPC set-up: measurement of the reflected laser pulse and a reference sample. The overall timing precision of the entire system is summarised in the instrument response function (IRF). By placing a mirror on the sample stage the laser pulse is reflected and collected by the SPAD. The time between the sync

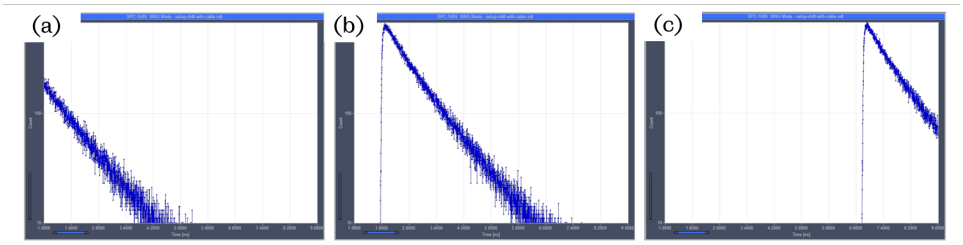

Figure A.2: Altering the sync path length. (a) The path length is too short; the beginning of the pulse is cut off. (b) The path length is correct; all of the pulse falls within the measurement time. (c) The path length is too long; the end of the pulse is cut off.

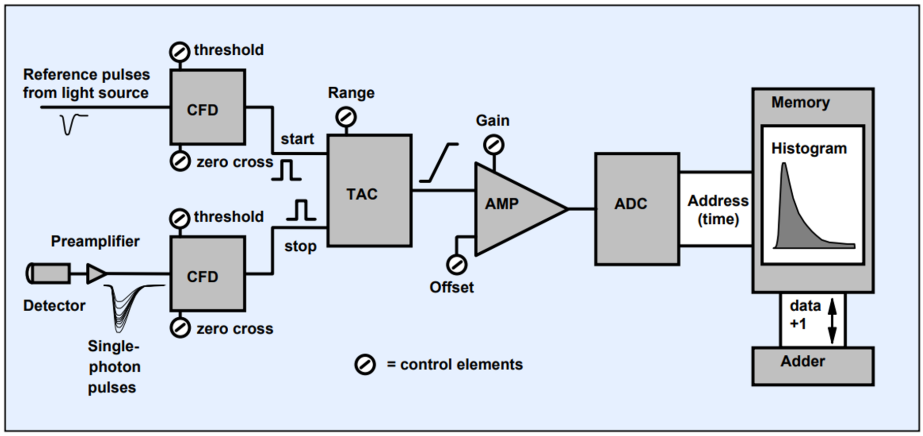

Figure A.3: Block diagram from TCSPC manual

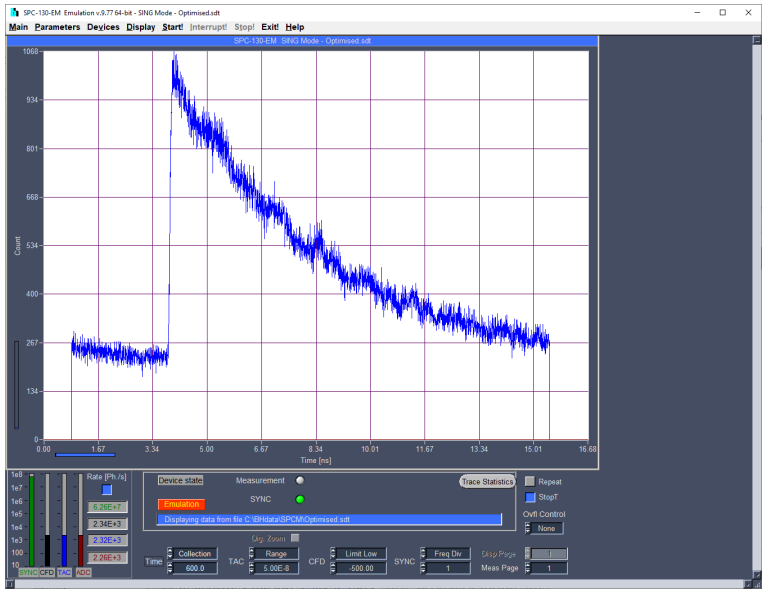

Figure A.4: TCSPC software user interface

pulse sent to the TCSPC card and the trigger from the SPAD, which is measuring the reflected laser light, gives the timing resolution. The limiting factor for the timing resolution is the SPAD. This resolution is defined by the time between when the photon arrives at the SPAD and the electric signal is generated. Before triggering an avalanche, the photon must diffuse from the absorption point to the depletion region. This delay depends on the device structure and the diffusion coefficients of the SPAD material. An increased reverse bias will result in better timing resolution but at the cost of dark counts, which generate noise. The timing resolution is given in the specification for the detector, this simple measurement can therefore determine that no other elements in the set-up are causing interference and changing the expected outcome. Fig. A.5(a) shows the result, a Gaussian pulse has been fitted which shows a FWHM of 0.1ns, as expected.

To further confirm the operation of the set-up, a sample with a known decay time is measured. In this simple measurement, a multi-QW sample consisting of 3 InGaAs QWs in a GaAs substrate is measured. The MQWs have a peak wavelength at 982nm and a linewidth of 17nm. Although exact carrier recombination times are not known for this sample, it is assumed that the carrier lifetime will be on the order of 3 to 5ns. Figure A.5(b) shows the TRPL measured at 982nm, the carrier recombination time is found to be

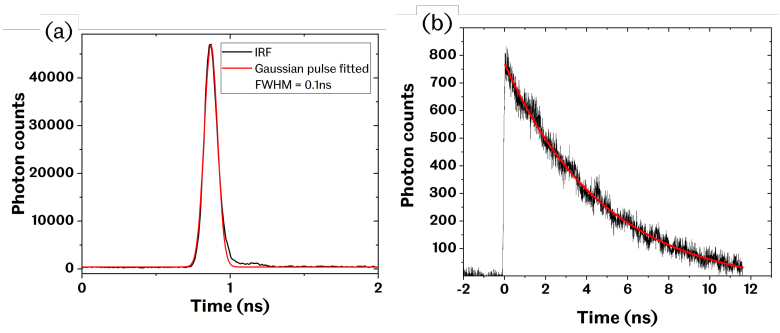

Figure A.5: (a) IRF measurement. (b) TRPL of InGaAs MQW sample.

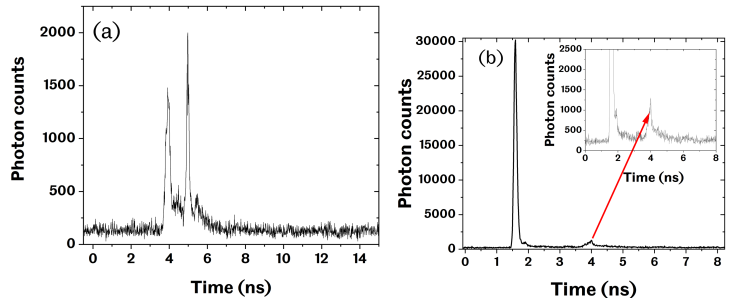

Figure A.6: (a) Unwanted reflections. (b) Time specific noise.

4.5ns, this agrees well with the expected recombination time for this sample.

A.3 Troubleshooting

During initial set-up of TRPL various issues arose that caused significant problems to the measurement. When measuring the IRF, it was common to see a second pulse in the measurement, as shown in Fig.A.6(a). This was caused by laser reflections between specific components, for example a fibre facet and a mirror. To rectify this, the reflected beam path was identified and an extra optical component added to ensure no unwanted reflected light affected the detector. Another common problem was time specific noise, scattered light was picked up by the detector and generated noise at a certain point in time, as shown by Fig. A.6(b). One of the main sources of this was the coupling of laser light into fibre. To reduce this, the laser and the fibre coupler were placed in an optical table containment system. It has two main functions: to stop time specific noise affecting the

TRPL results and to ensure the safety of all users in the lab given the high power of the class 4 laser. The laser has an average power of 1.5W with a <250fs pulse repeating at 63MHz, giving a peak power of above 80kW, therefore scattering and the potential for damage to skin and eyes is very high. Another important issue due to the high power was coupling the light directly into a fibre, some of the scattered light reflected back into the laser cavity, causing an excess gain in the cavity and its automatic shut down. To overcome this, an optical isolator is used, this ensured any reflected light did not scatter back into the laser cavity. It was also found that the use of absorptive neutral density (ND) filters was not suitable because the laser would burn the filter. Instead, reflective filters are utilised, where the filter will not absorb the light.

Appendix B

Supplementary modelling results

B.1 Model comparison

When developing a model, it is imperative that it is verified against either existing experimental or modelling work. The model given in chapter 3 focusses on a red shift in the cavity wavelength due to the Kerr effect. It was built using equations and models outlined in the literature [109, 110]. In these examples, a blue shift is assumed due to carrier-based nonlinear mechanisms. The results given in this section verify the model built in this project by observing a blue shift in the cavity resonance and comparing it to the results in the literature.

In this verification, only the direct coupled cavity-based IM is taken into consideration. The carrier light is blue shifted away from the cavity resonance and the transmission through the IM is modelled using the equations given in chapter 3. The wavelength of the carrier light is varied and the results show a change in the device transmission characteristics. This same observation was found by Yu *et al.* [109]. In the figure, the results from this model are compared to that paper. This was an initial step taken to verify this model against the literature. From Fig. B.1 it can be seen that very similar results are found. One difference between our models is the cavity size, this will affect the volume over which carriers recombine. Another difference resides in the Kerr coefficient, which is higher in this model due to the presence of QDs. This causes a stronger red shift for the time the signal light in present in the cavity.

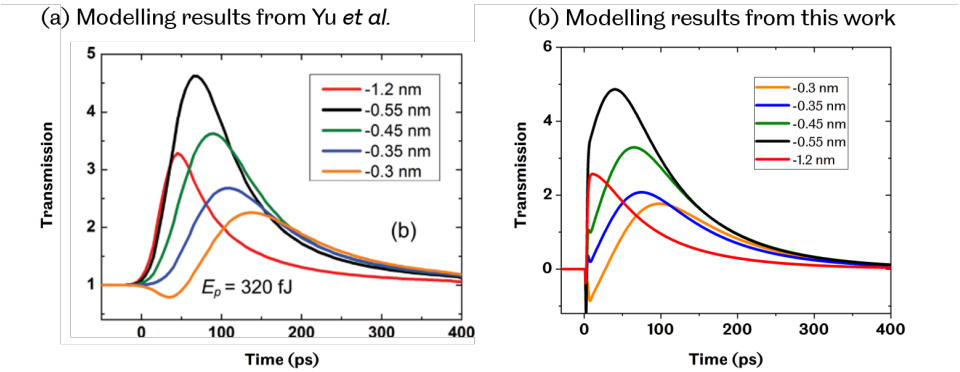

Figure B.1: Modelling results comparing the model built by Yu *et al.* [109] (a) and the model built in this work (b).

B.2 Parameter variation

In the development of a model, there are many variables to take into consideration. One of the critical values in this model is the kerr non-linear susceptibility. This is dependant on the material being modelled and cannot be easily modified. However, the inclusion of quantum dots will mean an enhancement of this value. Although quantitative analysis on the change in susceptibility due to QDs is not undertaken, the effect of change in susceptibility is shown in Fig. B.2. In this model, the integrated IM-PM system is modelled. By increasing the Kerr coefficient to $1.44 \times 10^{-}15m^2/W$ the comb band width is increased. This is due to the affect this has on the phase modulation depth in the waveguide part of the PhC OFC generator. When the Kerr coefficient is decreased to $1.04 \times 10^{-}15m^2/W$, we see the opposite effect. A smaller Kerr effect, caused by less QD absorption, will induce a lower phase modulation depth and a narrower comb. A change of $\pm 0.2 \times 10^{-}15m^2/W$ was taken into consideration because it is within realistic limits of what can be achieved. On top of that, it is possible that with a large increase in the Kerr coefficient, the carrier light intensity would then also cause a shift in the resonance. The output from the intensity modulator would then be very unstable and would lead to incoherence between the transmission through intensity modulator and the modulating light in the phase modulator.

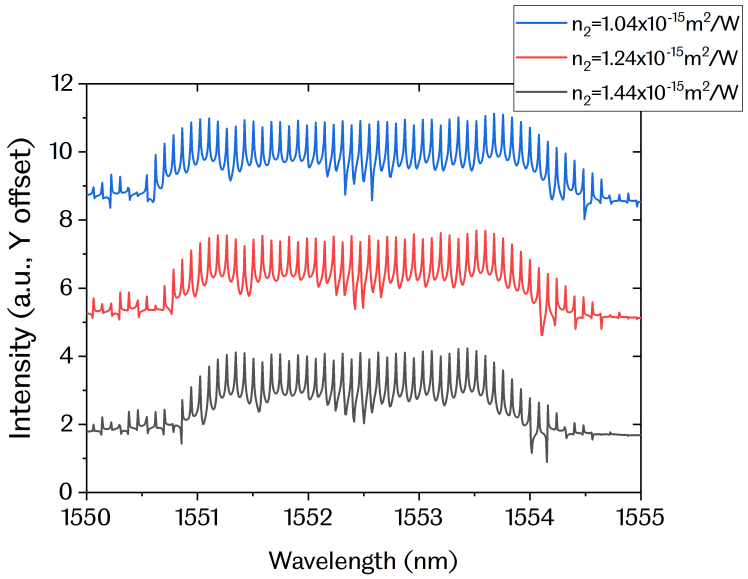

Figure B.2: Modelling results comparing a change the the Kerr coefficient.

B.3 Conclusion

The comparison between the two models helps to give confidence in the accuracy of the model. The slight difference between the two also confirms that the larger cavity and higher Kerr coefficient present in the device affects the output from the intensity modulator. Varying the Kerr coefficient has an affect on the bandwidth of the comb. This helps to confirm that even with a variation in the Kerr coefficient, a comb can still be generated. This variation also confirms the rigidity of the model, when parameters are changed within realistic limits.

Appendix C

Supplementary experimental results

During this project, the set-up and measurement procedure were developed to ensure accurate measurement of photo-luminescence from nanophotonic devices. During this process, many measurements were taken to understand and verify each part of the measurement. This appendix contains some supplementary measurements which were undertaken to consolidate the measurement set-up and functionality.

C.1 Square cavity

For initial verification of the fabrication and measurement set-up, a simple square cavity was fabricated. This was made by defining a strip around the edge of a square via EBL and then following the fabrication steps outlined in chapter 2 and the etching recipe developed i chapter 4. An SEM image of the resulting structure is given in Fig. C.1. A µPL measurement was then performed to see the mode structure of the square cavity. As can be expected, there were multiple modes within the structure, as shown in Fig. C.2(b). Figure C.2(a) shows the spectrum of the bulk material without any processing, for a comparison. This was the first step in validating both the fabrication process and measurement setup.

C.2 Working Distance

An objective lens is used throughout this project to focus the excitation laser spot onto the sample and collect the emission from the sample. This has a

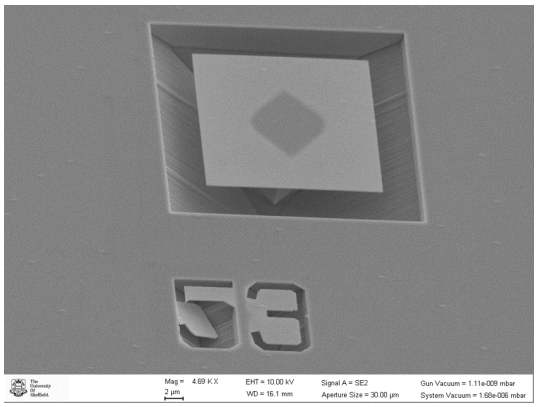

Figure C.1: SEM image of the square cavity.

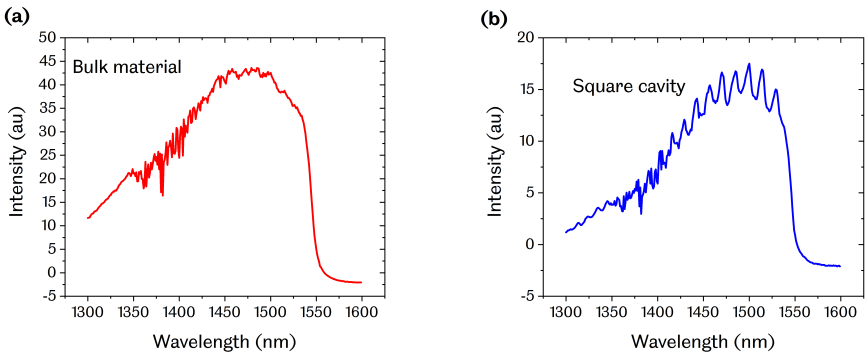

Figure C.2: PL spectrum of (a) the bulk sample and (b) the square cavity.

specific working distance for a given wavelength. To find the right working distance, the sample is put at roughly the right focal distance. Then, a real time measurement is undertaken at a single frequency, using a spectrometer slit size of 900µm. The distance can then be optimised by varying the height between the objective and the sample to find the highest emission intensity.

To understand the tolerance of the working distance, a small study was undertaken. In this study, the height is first optimised and the spectrum is measured, this is given by the black line in Fig. C.3. The distance is then varied by ±10 µm away from the optimised value. A scan is taken for both the near and far working distances, given by the blue and red line, respectively, in Fig. C.3. The Y axis is the real value given by the photo-diode. This shows that with a decreased working distance between the sample and the objective, the noise floor is increased and the intensity of the fundamental mode relative to the noise floor is decreased. In this case, the noise floor in increased because the focussed light is penetrating further into the sample and picking up more background light that is being emitted from the sample.

In the opposite case, when the light is further way from the sample, the noise floor and fundamental mode intensity decreases because the objective is collecting less light and the focussed laser spot is above the sample. A change in the wavelength of the mode can also be seen. The blue shift in cavity resonance as the working distance is decreased can be attributed to a change in the amount of power being focussed onto the cavity.

C.3 Slit size measurements

Two important factors when using a free-space spectrometer are the alignment of the light going into the spectrometer and the size of the slits used at the input and output. A free space spectrometer converts frequency components into the spatial domain via a diffraction grating. Therefore, the resolution can be increased ensuring the aperture at the input and output of the spectrometer are as small as possible. This is controlled by the slits in the spectrometer. To ensure an accurate measurement, it is important to understand which slit size is necessary for the measurements undertaken. To do this, a narrow linewidth L3 PhC cavity is measured with a varying slit size. In the experiment, both the input and output slits are kept equal. The excitation laser used is a 976nm CW laser with a power of around 0.1mW Figure C.4 shows the results. There are two outcomes from varying the slit size. The first is the output power; as the slits are narrowed, less light can

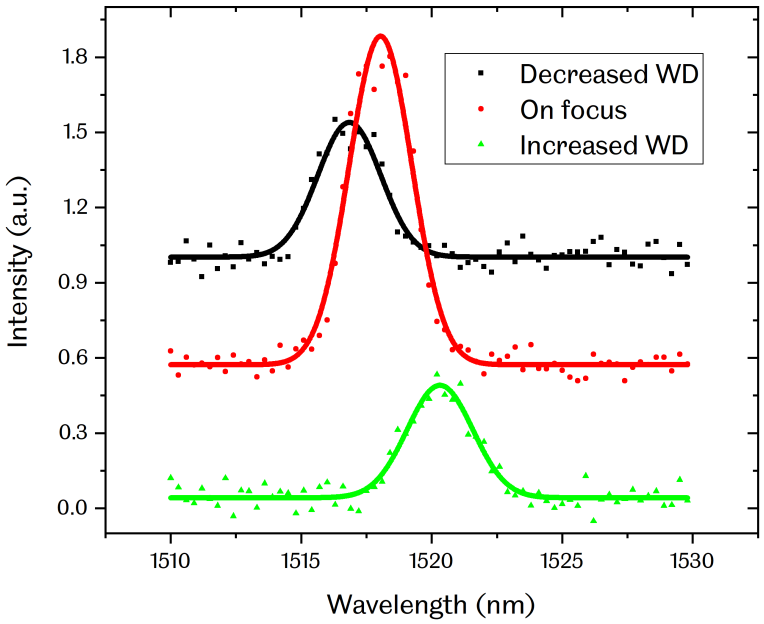

Figure C.3: The affect of the working distance between sample and objective when measuring an L3 cavity. The dots are the measurement values and the line is a Gaussian fit.

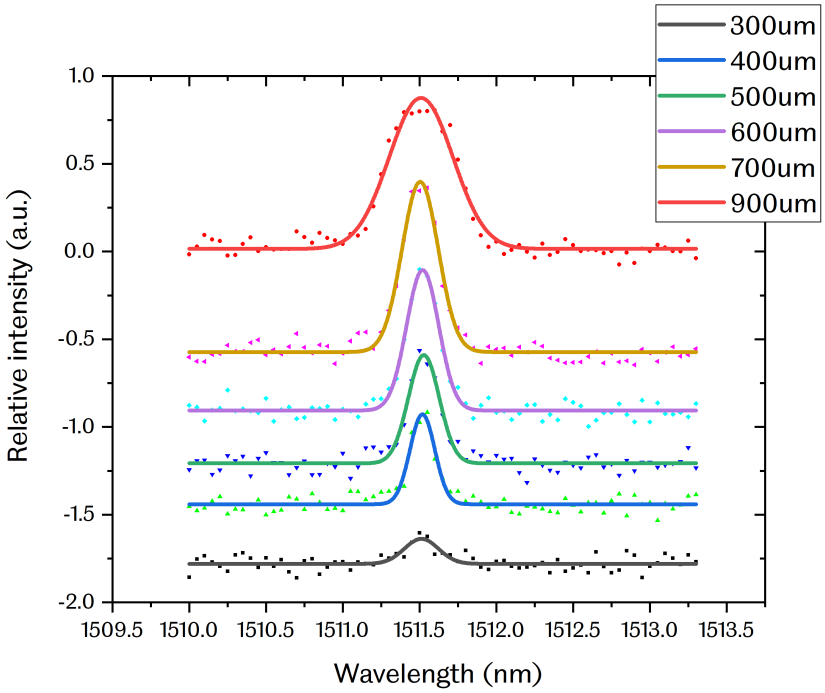

Figure C.4: The affect of spectrometer slit size when measuring an L3 cavity. The dots are the measurement values and the line is a Gaussian fit.

enter and exit the spectrometer meaning that there is less light hitting the photodetector. The second is a narrowing of the cavity linewidth, this indicates a higher resolution. With the slits at 900µm, the linewidth is much larger than with a slit width of 300µm. However, the linewidth difference between 300µm and 400µm is minimal but the power drops significantly. This shows that there is a trade-off between resolution and efficiency that needs to be taken into consideration when undergoing measurements of this type. In this work, when measuring the cavity linewidth using a CW excitation laser, the optimal slit size is 400µm.

C.4 3G vs 66M

The measurement results in chapter 6 show the generation of optical sidebands due to temporal modulation of the PhC cavity using a 4GHz repetition rate laser. In this section of the appendix, results are given to show

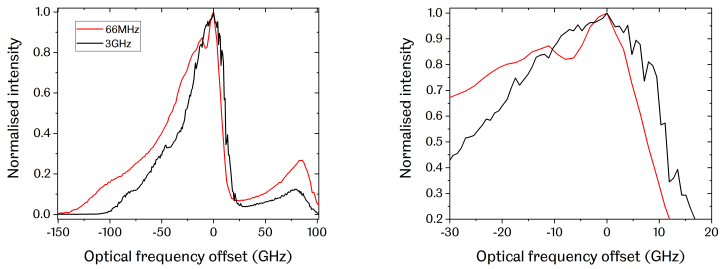

Figure C.5: PL spectrum of PhC laser when excited using different excitation laser repettion rates. (a) full spectrum of cavity linewidth (b) a detail view of the spectrum, covering a smaller frequency range.

the PhC cavity spectrum when excited by a laser with 66MHz repetition rate and 3GHz repetition rate. These results show how the difference in excitation repetition rate affect the PhC emission spectrum.

The measurement set-up and laser used for excitation is the same as given in chapter 6. Figure C.5 (a) shows the entire linewidth spectrum of the cavity. The red line is the cavity spectrum when a 66MHz repetition rate laser is used and the black line when a 3GHz repetition rate laser is used. The red line is a smooth curve, this is due to the relatively slow speed at which the cavity is being excited. The individual frequency components at 66MHz cannot be observed by the spectrometer due to the resolution limits. In the case of gigahertz excitation repetition rate, the individual components start to appear. Figure C.5(b) shows a more detailed view of the cavity linewidth at its peak intensity. In this figure, individual frequency components can be seen at intervals of around 3GHz. The extinction ratio between the frequency component minima and maxima is very small, this is because the spectrometer is at the limit of its resolution. In chapter 6, a repetition rate of 4GHz is used and the components become more visible in the cavity linewidth spectrum.

C.5 Time domain measurements of high repetition rate excitation laser

In chapter 5, the time domain response of the emission from the L3 cavity is measured using TRPL. In the following chapter, the cavity is excited using the same laser but with a higher repetition rate. In this section of the appendix, the time domain response of the emission from the cavity using

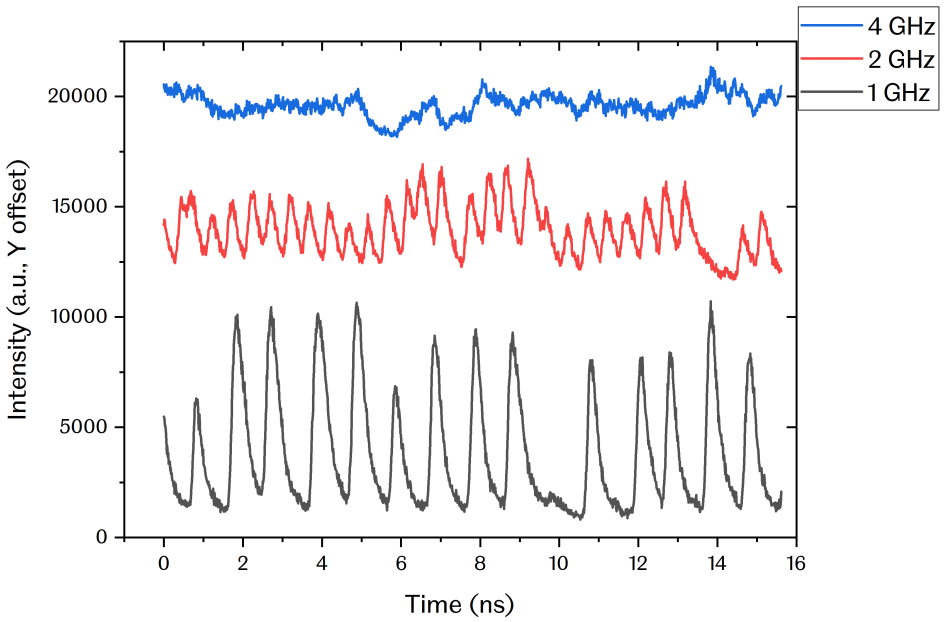

Figure C.6: Time domain response of the emission from PhC cavity when excited using a 1Ghz, 2GHz and 4GHz repetition rate laser.

a high repetition rate laser is given. The laser interleaving method used to increase the repetition rate is outlined in chapter 6; the 66MHz pulse is interleaved 16 times using a 16-arm MZI to get a 1GHz repetition frequency, this is then doubled using a two arm MZI to reach 2GHz and doubled again to make 4GHz.

The black line in Fig C.6 shows the 1GHz response. The individual pulses can be seen with a pulse period of 1ns, corresponding to 1GHz repetition frequency. The width of the pulses is dictated by the cavity Q factor and QD carrier recombination time, as outlined in chapter 5. The red line shows the 2GHz response. In this case, the cavity emission does not fully deplete before the subsequent excitation pulse. The amplitude of the pulse compared to the relative noise floor is therefore much smaller than the 1GHz case. Finally, the blue line represents the 4GHz case, here the peaks cannot be detected against the noise floor. This is limited by both detector IRF and the cavity lifetime. The 4GHz frequency components are observed in the frequency response of this spectrum, suggesting that the limitation here is due to the IRF of the detector.

Appendix D

Comparison of results

Although there are some fundamental differences in the devices simulated in chapter 3 and measured in chapter 6, a comparison can be drawn between the two. The simulation results show how the transmission of a carrier light through a PhC device can be modulated. This enables the generation of sidebands in the optical spectrum of the carrier light and hence an OFC. The measurement results show how the emission from QDs confined to a PhC cavity can be modulated. This enables the generation of sidebands in the optical spectrum of the QD emission.

Table D.1 gives the results from the simulation work in chapter 3 and the experimental results from chapter 6. The first four columns detail the set-up: the device measured/simulated, the result type, the repetition rate of the modulation or excitation laser and the result type, either transmission of the carrier light or the emission from the QDs. The next three columns detail the key performance parameters: the number of sidebands produced, the power of the first sideband relative to the initial carrier frequency and the noise floor between the sideband peaks relative to the carrier frequency. The final two columns give reference to where a schematic diagram and the results can be found in the main body of work.

The repetition rate of the excitation laser in the model is greater than in the measured case. This is because the switching speed of the cavity-based intensity modulator is faster than the carrier recombination time of the QDs in the cavity. The in model, the carrier light is red shifted, hence the switching mechanism is dictated by the Kerr effect. In the experiment, the emission from the QDs is observed, hence the switching speed is dictated by the carrier recombination time. Although the sideband power is higher for the experimental case, a higher noisefloor is present, making the sidebands

Table D.1: Modelling results comparing the model used by

Set up				Key performance parameters			Page no. in thesis	
Device	**Result type**	**Excitation laser rep. rate**	**Output**	**No. of sidebands**	**Sideband power (dB)**	**Noise floor (dB)**	**Schematic**	**Results**
Side coupled cavity modulator	Sim.	10GHz	Trans.	4	-7	-27	74	81
Direct coupled cavity modulator	Sim.	10GHz	Trans.	2	-4	-25	74	82
Integrated side coupled cavity modulators in parallel	Sim.	10GHz	Trans.	6	-3.5	-12	80	84
Integrated direct coupled cavity modulators in series	Sim.	10GHz/ 3.3GHz	Trans.	6	-3	-27	80	83
Integrated side coupled cavity modulator with waveguide-based phase modulator	Sim.	10GHz	Trans.	29	-4.5	-10	86	87
Integrated direct coupled cavity modulator with waveguide-based phase modulator	Sim.	10GHz	Trans.	29	-3	-10	-	87
L3 PhC Cavity	Exp.	66MHz	QD Emis.	0	-	-	118	169
L3 PhC Cavity	Exp.	3GHz	QD Emis.	2-4	-0.2	-0.35	118	169
L3 PhC Cavity	Exp.	4GHz	QD Emis.	6	-0.1	-0.7	118	148

harder to distinguish. Indeed for the 3GHz modulation speed, the noise floor is very close to the sideband power.

Bibliography

[1] J. Yao, S. Member, F. Zeng, and Q. Wang, "Photonic Generation of Ultrawideband Signals," *Journal of Lightwave Technology*, vol. 25, no. 11, pp. 3219–3235, 2007.

[2] C. Lim, A. Nirmalathas, M. Bakaul, P. Gamage, K.-l. Lee, Y. Yang, D. Novak, and R. Waterhouse, "Fiber-Wireless Networks and Subsystem Technologies," *Journal of lig*, vol. 28, no. 4, pp. 390–405, 2010.

[3] V. R. Supradeepa, C. M. Long, R. Wu, F. Ferdous, E. Hamidi, D. E. Leaird, and A. M. Weiner, "Comb-based radiofrequency photonic filters with rapid tunability and high selectivity," *Nature Photonics*, vol. 6, 2012.

[4] D. Grodensky, D. Kravitz, and A. Zadok, "Ultra-Wideband Microwave-Photonic Noise Radar Based on Optical Waveform Generation," *Photonics technology letters*, vol. 24, no. 10, pp. 839–841, 2012.

[5] D. Marpaung, J. Yao, and J. Capmany, "Integrated microwave photonics," *Nature Photonics*, vol. 13, pp. 80–90, 2019.

[6] C. Haffner, W. Heni, Y. Fedoryshyn, J. Niegemann, A. Melikyan, D. L. Elder, B. Baeuerle, Y. Salamin, A. Josten, U. Koch, C. Hoessbacher, F. Ducry, L. Juchli, A. Emboras, D. Hillerkuss, M. Kohl, L. R. Dalton, C. Hafner, and J. Leuthold, "All-plasmonic Mach-Zehnder modulator enabling optical high-speed communication at the microscale," *Nature Photonics*, vol. 9, no. 8, pp. 525–528, 2015.

[7] D. Marpaung, B. Morrison, M. Pagani, R. Pant, D.-Y. Choi, B. Luther-Davies, S. J. Madden, and B. J. Eggleton, "Low-power , chip-based stimulated Brillouin scattering microwave photonic filter with ultrahigh selectivity," *Optica*, vol. 2, no. 2, pp. 76–83, 2015.

[8] T. J. Kippenberg, R. Holzwarth, and S. A. Diddams, "Microresonator-Based Optical Frequency Combs," *Science*, vol. 332, no. April, pp. 555–560, 2011.

[9] C.-Y. Y. Jin and O. Wada, "Photonic switching devices based on semiconductor nano-structures," *Journal of Physics D: Applied Physics*, vol. 47, no. 13, p. 133001, 2014.

[10] K. Nozaki, T. Tanabe, A. Shinya, S. Matsuo, T. Sato, H. Taniyama, and M. Notomi, "Sub-femtojoule all-optical switching using a photonic-crystal nanocavity," *Nature Photonics*, vol. 4, no. 7, pp. 477–483, 2010.

[11] K. Nozaki, S. Matsuo, T. Fujii, K. Takeda, A. Shinya, E. Kuramochi, and M. Notomi, "Femtofarad optoelectronic integration demonstrating energy-saving signal conversion and nonlinear functions," *Nature Photonics*, vol. 13, pp. 454–459, 2019.

[12] Y. Ota, R. Katsumi, K. Watanabe, S. Iwamoto, and Y. Arakawa, "Topological photonic crystal nanocavity laser," *Communications Physics*, vol. 86, pp. 4–6, 2018.

[13] T. Udem, R. Holzwarth, and T. W. Hansch, "Optical frequency metrology," *Nature*, vol. 416, pp. 233–237, 2002.

[14] T. Fortier and E. Baumann, "20 years of developments in optical frequency comb technology and applications," *Communications Physics*, vol. 153, pp. 1–16, 2019.

[15] J. L. Hall, "Nobel Lecture: Defining and measuring optical frequencies," *Reviews of Modern Physics*, vol. 78, pp. 1279–1295, 2006.

[16] T. W. Hänsch, "Nobel Lecture: Passion for precision," *Reviews of Modern Physics*, vol. 78, pp. 1297–1309, 2006.

[17] R. Paschotta, "https://www.rp-photonics.com/mode_locking.html,"

[18] T. Udem, J. Reichert, R. Holzwarth, and T. W. Hansch, "Accurate measurement of large optical frequency differences with a mode-locked laser," *Optics Letters*, vol. 24, no. 13, pp. 881–883, 1999.

[19] H. R. Telle, G. Steinmeyer, A. E. Dunlop, J. Stenger, D. H. Sutter, and U. Keller, "Carrier-envelope offset phase control : A novel concept for absolute optical frequency measurement and ultrashort pulse generation," *Applied Physics B*, vol. 332, pp. 327–332, 1999.

[20] Y. K. Chembo, "Kerr optical frequency combs: Theory, applications and perspectives," *Nanophotonics*, vol. 5, no. 2, pp. 214–230, 2016.

[21] T. J. Kippenberg, S. M. Spillane, and K. J. Vahala, "Kerr-Nonlinearity Optical Parametric Oscillation in an Ultrahigh- Q Toroid Microcavity," *Physical Review Letters*, vol. 98, no. 8, pp. 18–21, 2004.

[22] A. A. Savchenkov, A. B. Matsko, D. Strekalov, M. Mohageg, V. S. Ilchenko, and L. Maleki, "Low Threshold Optical Oscillations in a Whispering Gallery Mode CaF 2 Resonator," *Physical Review Letters*, vol. 93, no. 243905, pp. 2–5, 2004.

[23] P. Del'Haye, A. Schliesser, O. Arcizet, T. Wilken, R. Holzwarth, and T. J. Kippenberg, "Optical frequency comb generation from a monolithic microresonator," *Nature*, vol. 450, no. 7173, pp. 1214–1217, 2007.

[24] T. Ohara, H. Takara, and T. Yamamoto, "Over-1000-Channel Ultradense WDM Transmission," *Journal of Lightwave Technology*, vol. 24, no. 6, pp. 2311–2317, 2006.

[25] A. Pasquazi, M. Peccianti, L. Razzari, D. J. Moss, S. Coen, M. Erkintalo, Y. K. Chembo, T. Hansson, S. Wabnitz, P. Del'Haye, X. Xue, A. M. Weiner, and R. Morandotti, "Micro-combs: A novel generation of optical sources," *Physics Reports*, vol. 729, pp. 1–81, 2017.

[26] W. Liang, A. A. Savchenkov, A. B. Matsko, V. S. Ilchenko, D. Seidel, and L. Maleki, "Generation of near-infrared frequency combs from a MgF 2 whispering gallery mode resonator," *Optics Letters*, vol. 36, no. 12, pp. 2290–2292, 2011.

[27] R. Henriet, G. Lin, A. Coillet, M. Jacquot, L. Furfaro, L. Larger, and Y. K. Chembo, "Kerr optical frequency comb generation in strontium fluoride whispering-gallery mode resonators with billion quality factor," *Optics Letters*, vol. 40, no. 7, pp. 1567–1570, 2015.

[28] S. B. Papp and S. A. Diddams, "Spectral and temporal characterization of a fused-quartz-microresonator optical frequency comb," *Physical Review A*, vol. 84, no. 053833, pp. 1–7, 2011.

[29] A. A. Savchenkov, A. B. Matsko, and V. S. Ilchenko, "Optical resonators with ten million finesse," *Optics Express*, vol. 15, no. 11, pp. 300–305, 2007.

[30] I. S. Grudinin, N. Yu, and L. Maleki, "Generation of optical frequency combs with a CaF 2 resonator," *Optics Letters*, vol. 34, no. 7, pp. 878–880, 2009.

[31] F. Ferdous, H. Miao, D. E. Leaird, K. Srinivasan, J. Wang, L. Chen, L. T. Varghese, and A. M. Weiner, "Spectral line-by-line pulse shaping of on-chip microresonator frequency combs," *Nature Photonics*, vol. 5, pp. 770–776, 2011.

[32] A. L. Gaeta, M. Lipson, and T. J. Kippenberg, "Photonic-chip-based frequency combs," *Nature Photonics*, vol. 13, no. 3, pp. 158–169, 2019.

[33] Y. Okawachi, K. Saha, J. S. Levy, Y. H. Wen, M. Lipson, and A. L. Gaeta, "Octave-spanning frequency comb generation in a silicon nitride chip," *Optics Letters*, vol. 36, no. 17, pp. 3398–3400, 2011.

[34] K. Saha, Y. Okawachi, B. Shim, J. S. Levy, R. Salem, A. R. Johnson, M. A. Foster, M. R. E. Lamont, M. Lipson, and A. L. Gaeta, "Modelocking and femtosecond pulse generation in chip-based frequency combs," *Optics Express*, vol. 21, no. 1, pp. 97–100, 2013.

[35] X. Ji, F. Barbosa, S. Roberts, A. Dutt, J. Cardenas, Y. Okawachi, A. Bryant, A. Gaeta, and M. Lipson, "Ultra-low-loss on-chip resonators with sub-milliwatt parametric oscillation threshold," *Optica*, vol. 4, no. 6, 2017.

[36] B. Stern, X. Ji, Y. Okawachi, A. L. Gaeta, and M. Lipson, "Battery-operated integrated frequency comb generator," *Nature*, vol. 562, pp. 401–406, 2018.

[37] J. Faist, F. Capasso, D. L. Sivco, C. Sirtori, A. L. Hutchinson, and A. Y. Cho, "Quantum Cascade Laser," *Science*, vol. 264, no. 4, pp. 553–558, 1994.

[38] C. Gmachl, D. L. Sivco, R. Colombelli, and F. Capasso, "Ultra-broadband semiconductor laser," *Nature Letters*, vol. 415, no. 2, pp. 883–887, 2002.

[39] M. G. Thompson, A. R. Rae, M. Xia, R. V. Penty, and I. H. White, "InGaAs Quantum-Dot Mode-Locked Laser Diodes," *IEEE Journal of Selected Topics in Quantum Electronics*, vol. 15, no. 3, pp. 661–672, 2009.

[40] V. Torres-Company and A. M. Weiner, "Optical frequency comb technology for ultra-broadband radio-frequency photonics," *Laser and Photonics Reviews*, vol. 8, no. 3, pp. 368–393, 2014.

[41] A. Bartels, D. Heinecke, and S. A. Diddams, "10-GHz Self-Referenced Optical Frequency Comb," *Science*, vol. 326, no. 681, pp. 325–326, 2009.

[42] J. Capmany and D. Novak, "Microwave photonics combines two worlds," *Nature Photonics*, vol. 1, no. 6, pp. 319–330, 2007.

[43] T. Ikegami and Y. Suematsu, "Resonance-Like Characteristics of the Direct Modulation of a Junction Laser," *Proceeding of the IEEE*, vol. 55, no. 1, pp. 122–123, 1967.

[44] H. Murata, A. Morimoto, T. Kobayashi, and S. Yamamoto, "Optical pulse generation by electrooptic-modulation method and its application to integrated ultrashort pulse generators," *IEEE Journal of Selected Topics in Quantum Electronics*, vol. 6, no. 6, pp. 1325–1331, 2000.

[45] M. Fujiwara, J. Kani, H. Suzuki, K. Araya, and M. Teshima, "Flattened optical multicarrier generation of 12.5 GHz spaced 256 channels based on sinusoidal amplitude and phase hybrid modulation," *Electronic Letters*, vol. 37, no. 15, pp. 967–968, 2001.

[46] T. Healy, F. C. G. Gunning, A. D. Ellis, and J. D. Bull, "Multi-wavelength source using low drive-voltage amplitude modulators for optical communications," *Optics Express*, vol. 15, no. 6, pp. 2981–2986, 2007.

[47] L. Shang, A. Wen, G. Lin, and Y. Gao, "A fl at and broadband optical frequency comb with tunable bandwidth and frequency spacing," *Optics Communications*, vol. 331, pp. 262–266, 2014.

[48] C. He, S. Pan, R. Guo, Y. Zhao, and M. Pan, "Ultraflat optical frequency comb generated based on cascaded polarization modulators," *Optics Letters*, vol. 37, no. 18, pp. 3834–3836, 2012.

[49] S. Ozharar, F. Quinlan, I. Ozdur, S. Gee, and P. J. Delfyett, "Ultraflat Optical Comb Generation by Phase-Only Modulation of Continuous-Wave Light," *Photonics Technology Letters*, vol. 20, no. 1, pp. 36–38, 2008.

[50] V. Torres-Company, J. Lancis, and P. Andres, "Lossless equalization of frequency combs," *Optics Letters*, vol. 33, no. 16, pp. 1822–1824, 2008.

[51] B. H. Kolner and M. Nazarathy, "Temporal imaging with a time lens," *Optics Letters*, vol. 14, no. 12, p. 630, 1989.

[52] M. T. Kauffman, W. C. Banyai, A. A. Gidl, and D. M. Bloom, "Time-to-frequency converter for measuring picosecond optical pulses Time-to-frequency," *Applied Physics Lettersd*, vol. 64, no. 270, 1994.

[53] J. Azaña, N. K. Berger, B. Levit, and B. Fischer, "Spectro-Temporal Imaging of Optical Pulses With a Single Time Lens," *IEEE Photonics Technology Letters*, vol. 16, no. 3, pp. 882–884, 2004.

[54] Y. Dou, H. Zhang, and M. Yao, "Improvement of flatness of optical frequency comb based on nonlinear effect of intensity modulator," *Optics Letters*, vol. 36, no. 14, p. 2749, 2011.

[55] J. V. Howe, J. Hansryd, and C. Xu, "Multiwavelength pulse generator using time-lens compression," *Optics Letters*, vol. 29, no. 13, pp. 1470–1472, 2004.

[56] R. Wu, V. R. Supradeepa, C. M. Long, D. E. Leaird, and A. M. Weiner, "Generation of very flat optical frequency combs from continuous-wave lasers using cascaded intensity and phase modulators driven by tailored radio frequency waveforms," *Optics Letters*, vol. 35, no. 19, p. 3234, 2010.

[57] Y. Dou, H. Zhang, and M. Yao, "Generation of Flat Optical-Frequency Comb Using Cascaded Intensity and Phase Modulators," *Photonics Technology Letters*, vol. 24, no. 9, pp. 727–729, 2012.

[58] C. Chen, C. He, D. Zhu, R. Guo, F. Zhang, and S. Pan, "Generation of a flat optical frequency comb based on a cascaded polarization modulator and phase modulator," *Optics Letters*, vol. 38, no. 16, p. 3137, 2013.

[59] T. Sakamoto, T. Kawanishi, and M. Izutsu, "Asymptotic formalism for ultraflat optical frequency comb generation using a Mach–Zehnder modulator," *Optics Letters*, vol. 32, no. 11, pp. 1515–1517, 2007.

[60] T. Yamamoto, K. Hitomi, and W. Kobayashi, "Optical Frequency Comb Block Generation by Using Semiconductor Mach – Zehnder Modulator," *Photonics Technology Letters*, vol. 25, no. 1, pp. 40–42, 2013.

[61] N. Yokota, K. Abe, S. Mieda, and H. Yasaka, "Harmonic superposition for tailored optical frequency comb generation by a Mach – Zehnder modulator," *Optics Letters*, vol. 41, no. 5, pp. 1026–1029, 2016.

[62] T. Sakamoto, T. Kawanishi, and M. Izutsu, "Widely wavelength-tunable ultra-flat frequency comb generation using conventional dual-drive Mach-Zehnder modulator," *Electronic Letters*, vol. 43, no. 19, pp. 3–4, 2007.

[63] A. Apolonski, A. Poppe, G. Tempea, C. Spielmann, T. Udem, R. Holzwarth, T. W. Hänsch, and F. Krausz, "Controlling the Phase Evolution of Few-Cycle Light Pulses," *Physical Review Letters*, vol. 85, no. 4, pp. 740–745, 2000.

[64] J. M. Dudley and J. R. Taylor, "Ten years of nonlinear optics in photonic crystal fibre," *Nature Photonics*, vol. 3, no. 2, pp. 85–90, 2009.

[65] J. K. Ranka, R. S. Windeler, and A. J. Stentz, "Visible continuum generation in air – silica microstructure optical fibers with anomalous dispersion at 800 nm," *Optics Letters*, vol. 25, no. 1, pp. 796–798, 2000.

[66] T. A. Birks, W. J. Wadsworth, and P. S. J. Russell, "Supercontinuum generation in tapered fibres," *Optics Letters*, vol. 25, no. 19, 2000.

[67] H. Hu, F. D. Ros, M. Pu, F. Ye, K. Ingerslev, E. Porto, Y. Amma, Y. Sasaki, T. Mizuno, Y. Miyamoto, L. Ottaviano, E. Semenova, P. Guan, D. Zibar, M. Galili, K. Yvind, T. Morioka, and L. K. Oxenløwe, "Single-source chip-based frequency comb enabling extreme parallel data transmission," *Nature Photonics*, vol. 12, no. August, pp. 469–474, 2018.

[68] K. R. Tamura, H. Kubota, and M. Nakazawa, "Fundamentals of Stable Continuum Generation at High Repetition Rates," *IEEE Journal of Quantum Electronics*, vol. 36, no. 7, pp. 773–779, 2000.

[69] R. Wu, V. Torres-company, D. E. Leaird, and A. M. Weiner, "Supercontinuum-based 10-GHz flat-topped optical frequency comb generation Rui," *Optics Express*, vol. 21, no. 5, pp. 6045–6052, 2013.

[70] Y. Liu, H. Tu, and S. A. Boppart, "Wave-breaking-extended fiber supercontinuum generation for high compression ratio transform-limited pulse compression," *Optics Letters*, vol. 37, no. 12, pp. 2172–2174, 2012.

[71] D. Y. Oh, K. Y. Yang, C. Fredrick, G. Ycas, S. A. Diddams, and K. J. Vahala, "Coherent ultra-violet to near-infrared generation in silica ridge waveguides," *Nature Communications*, vol. 82, pp. 1–7, 2017.

[72] M. Porcel, F. Schepers, J. Epping, T. Hellwig, M. Hoekman, R. Heideman, P. van der Slot, C. Lee, R. Schmidt, R. Bratschitsch, C. Fallnich, and K. Boller, "Two-octave spanning supercontinuum generation in stoichiometric silicon nitride waveguides pumped at telecom wavelengths," *Optics Express*, vol. 25, no. 2, pp. 1596–1603, 2017.

[73] R. Halir, Y. Okawachi, J. S. Levy, M. A. Foster, M. Lipson, and A. L. Gaeta, "Ultrabroadband supercontinuum generation in a CMOS-compatible platform," *Optics Letters*, vol. 37, no. 10, pp. 1685–1687, 2012.

[74] B. Kuyken, X. Liu, R. M. O. Jr, R. Baets, G. Roelkens, and W. M. J. Green, "Mid-infrared to telecom-band supercontinuum generation in highly nonlinear silicon-on- insulator wire waveguides," *Optics Express*, vol. 19, no. 21, pp. 20172–20181, 2011.

[75] H. Francis, S. Chen, C.-h. Ho, K.-j. Che, Y.-r. Wang, M. Hopkinson, and C.-Y. Jin, "Generation of optical frequency combs using a photonic crystal cavity," *IET Optoelectronics*, vol. 13, no. 1, pp. 1–4, 2018.

[76] J. Kim and Y. Song, "Ultralow-noise mode-locked fiber lasers and frequency combs : principles , status and applications," *Advances in Optics and Photonics*, vol. 8, no. 3, pp. 1–70, 2016.

[77] V. Brasch, M. Geiselmann, T. Herr, G. Lihachev, M. H. P. Pfeiffer, M. L. Gorodetsky, and T. J. Kippenberg, "Photonic chip – based optical frequency comb using soliton Cherenkov radiation," *Science*, vol. 351, no. 6271, 2016.

[78] H. Francis, S. Chen, K.-j. Che, M. Hopkinson, and C.-Y. Jin, "Photonic Crystal Cavity-Based Intensity Modulation for Integrated Optical Frequency Comb Generation," *Crystals*, vol. 493, pp. 1–10, 2019.

[79] A. J. Seeds and K. J. Williams, "Microwave Photonics," *Journal of Lightwave Technology*, vol. 24, no. 12, pp. 4628–4641, 2006.

[80] J. Wu, X. Xu, T. G. Nguyen, S. T. Chu, B. E. Little, R. Morandotti, A. Mitchell, and D. J. Moss, "RF Photonics: An Optical Microcombs' Perspective," *IEEE Journal of Selected Topics in Quantum Electronics*, vol. 24, no. 4, 2018.

[81] J. Sancho, J. Bourderionnet, J. Lloret, S. Combrié, I. Gasulla, S. Xavier, S. Sales, P. Colman, G. Lehoucq, D. Dolfi, J. Capmany, and A. D. Rossi, "Integrable microwave filter based on a photonic crystal delay line," *Nature Communications*, vol. 3, no. 1075, 2012.

[82] V. Torres-company, D. E. Leaird, and A. M. Weiner, "Simultaneous broadband microwave downconversion and programmable complex filtering by optical frequency comb shaping," *Optics Letters*, vol. 37, no. 19, pp. 3993–3995, 2012.

[83] J. Capmany, S. Member, and B. Ortega, "A Tutorial on Microwave Photonic Filters," *Journal of Lightwave Technology*, no. February, pp. 201–228, 2006.

[84] L. Lundberg, K. Magnus, A. Lorences-riesgo, M. Mazur, V. Torres-Company, J. Schroder, and P. Andrekson, "Frequency Comb-Based WDM Transmission Systems Enabling Joint Signal Processing," *Applied Science*, vol. 8, no. 5, p. 718, 2018.

[85] J.-x. Cai, H. G. Batshon, M. V. Mazurczyk, O. V. Sinkin, S. Member, D. Wang, M. Paskov, W. W. Patterson, C. R. Davidson, S. Member, P. C. Corbett, G. M. Wolter, T. E. Hammon, M. A. Bolshtyansky, D. G. Foursa, S. Member, A. N. Pilipetskii, and S. Member, "70.46 Tb/s Over 7,600 km and 71.65 Tb/s Over 6,970 km Transmission in C + L Band Using Coded Modulation With Hybrid Constellation Shaping and Nonlinearity Compensation," *Journal of Lightwave Technology*, vol. 36, no. 1, pp. 114–121, 2018.

[86] E. Yablonovitch, "Inhibited Spontaneous Emission in Solid-State Physics and Electronics," *Physical Review Letters*, vol. 58, no. 20, pp. 2059–2062, 1987.

[87] S. John, "Strong Localization of Photons in Certain Disordered Dielectric Superlattices," *Physical Review Letters*, vol. 58, no. 23, 1987.

[88] J. J. J. D. Joannopoulos, S. Johnson, J. N. J. Winn, and R. R. R. D. Meade, *Photonic Crystals: Molding the Flow of Light*. Princeton University Press, second ed., 2008.

[89] E. Yablonovitch and T. J. Gmitter, "Photonic Band Structure: The Face-Centered-Cubic Case," *Physical Review Letters*, vol. 63, no. 18, pp. 1950–1953, 1989.

[90] S. Noda, K. Tomoda, and N. Yamamoto, "Full Three-Dimensional Photonic Bandgap Crystals at Near-Infrared Wavelengths," *Science*, vol. 289, no. July, pp. 604–607, 2000.

[91] B. C. López, "Materials Aspects of Photonic Crystals," *Advanced Materials*, no. 20, pp. 1679–1704, 2003.

[92] E. Kuramochi, K. Nozaki, A. Shinya, K. Takeda, T. Sato, S. Matsuo, H. Taniyama, H. Sumikura, and M. Notomi, "Large-scale integration of wavelength-addressable all-optical memories on a photonic crystal chip," *Nature Photonics*, vol. 8, no. May, pp. 2–9, 2014.

[93] C. Husko, A. De Rossi, S. Combrí, Q. V. Tran, F. Raineri, and C. W. Wong, "Ultrafast all-optical modulation in GaAs photonic crystal cavities," *Applied Physics Letters*, vol. 94, no. 2, pp. 2007–2010, 2009.

[94] Y. Akahane, T. Asano, and B.-s. Song, "High- Q photonic nanocavity in a two-dimensional photonic crystal," *Nature Letters*, vol. 425, no. 10, pp. 4–7, 2003.

[95] E. Kuramochi, M. Notomi, S. Mitsugi, A. Shinya, T. Tanabe, and T. Watanabe, "Ultrahigh- photonic crystal nanocavities realized by the local width modulation of a line defect," *Applied Physics Letters*, vol. 041112, pp. 6–9, 2006.

[96] K. Nozaki, S. Kita, and T. Baba, "Room temperature continuous wave operation and controlled spontaneous emission in ultrasmall photonic crystal nanolaser," *Optics Express*, vol. 15, no. 12, pp. 1340–1346, 2007.

[97] J. Vuckovic, D. Englund, D. Fattal, E. Waks, and Y. Yamamoto, "Generation and manipulation of nonclassical light using photonic crystals," *Physica E*, vol. 32, pp. 466–470, 2006.

[98] Q. V. Tran, S. Combrí, P. Colman, and A. De Rossi, "Photonic crystal membrane waveguides with low insertion losses," *Applied Physics Letters*, vol. 95, no. 6, pp. 1–4, 2009.

[99] M. Notomi, A. Shinya, S. Mitsugi, G. Kira, E. Kuramochi, and T. Tanabe, "Optical bistable switching action of Si high-Q photonic-crystal nanocavities," *Optics Express*, vol. 13, no. 7, p. 2678, 2005.

[100] T. Tanabe, K. Nishiguchi, E. Kuramochi, and M. Notomi, "Low power and fast electro-optic silicon modulator with lateral p - i - n embedded photonic crystal nanocavity," *Optics Express*, vol. 17, no. 25, pp. 22505–22513, 2009.

[101] B. R. Bennett, R. A. Soref, and J. A. Del Alamo, "Carrier-Induced Change in Refractive Index of InP, GaAs, and InGaAsP," *IEEE Journal of Quantum Electronics*, vol. 26, no. 1, pp. 113–122, 1990.

[102] A. De Rossi, M. Lauritano, S. Combrié, Q. V. Tran, and C. Husko, "Interplay of plasma-induced and fast thermal nonlinearities in a GaAs-based photonic crystal nanocavity," *Physical Review A - Atomic, Molecular, and Optical Physics*, vol. 79, no. 4, pp. 1–9, 2009.

[103] T. Tanabe, M. Notomi, S. Mitsugi, A. Shinya, and E. Kuramochi, "All-optical switches on a silicon chip realized using photonic crystal nanocavities," *Applied Physics Letters*, vol. 87, no. 15, pp. 1–3, 2005.

[104] K. Nozaki, A. Shinya, M. Notomi, S. Matsuo, T. Sato, Y. Suzaki, T. Segawa, and R. Takahashi, "First demonstration of 4-bit, 40-Gb/s optical RAM chip using integrated photonic crystal nanocavities," *Photonics in Switching (PS), 2012 International Conference on*, vol. 1, pp. 1–3, 2012.

[105] R. Boyd, *Nonlinear Optics*. Elsevier, third edit ed., 1992.

[106] T. Tanabe, K. Nishiguchi, A. Shinya, K. Eiichi, H. Inokawa, and M. Notomi, "Fast all-optical switching using ion- implanted silicon photonic crystal nanocavities," *Applied Physics Letters*, vol. 90, no. 031115, 2007.

[107] K. Nozaki, T. Tanabe, A. Shinya, S. Matsuo, T. Sato, H. Taniyama, and M. Notomi, "All-optical switching with extremely-small control energy in InGaAsP-based photonic crystal nanocavity," *2009 IEEE LEOS Annual Meeting Conference Proceedings*, vol. 1, pp. 34–35, 2009.

[108] Y. Yu, E. Palushani, M. Heuck, N. Kuznetsova, P. T. T. Kristensen, S. Ek, D. Vukovic, C. Peucheret, L. K. Oxenløwe, S. Combrié, A. de Rossi, K. Yvind, J. Mørk, L. K. Oxenlowe, S. Combrié, A. de Rossi, K. Yvind, and J. Mork, "Switching characteristics of an InP photonic crystal nanocavity: Experiment and theory," *Optics Express*, vol. 21, no. 25, p. 31047, 2013.

[109] Y. Yu, E. Palushani, M. Heuck, D. Vukovic, and C. Peucheret, "Nonlinear switching dynamics in a photonic-crystal nanocavity," *Applied Physics Letters*, vol. 071112, no. 2014, pp. 1–13, 2015.

[110] M. Heuck, S. Combrie, G. Lehoucq, S. Malaguti, G. Bellanca, S. Trillo, P. T. Kristensen, J. Mork, J. P. Reithmaier, and A. de Rossi, "Heterodyne pump probe measurements of nonlinear dynamics in an indium phosphide photonic crystal cavity," *Applied Physics Letters*, vol. 103, no. 18, p. 181120, 2013.

[111] G. Moille, S. Combri, and A. D. Rossi, "Modeling of the carrier dynamics in nonlinear semiconductor nanoscale resonators," *Physical Review A*, vol. 023814, 2016.

[112] G. Moille, S. Combrié, K. Fuchs, M. Yacob, J. P. Reithmaier, and A. D. Rossi, "Acceleration of the nonlinear dynamics in p-doped indium phosphide nanoscale resonators," *Optics Letters*, vol. 42, no. 4, pp. 794–799, 2017.

[113] Y. Shen, N. C. Harris, S. Skirlo, M. Prabhu, T. Baehr-jones, M. Hochberg, X. Sun, S. Zhao, H. Larochelle, D. Englund, and M. Solja, "Deep learning with coherent nanophotonic circuits," *Nature Photonics*, vol. 11, no. June, pp. 441–445, 2017.

[114] M. Soljačić, J. D. Joannopoulos, M. Soljac, and J. D. Joannopoulos, "Enhancement of nonlinear effects using photonic crystals," *Nature Materials*, vol. 3, no. 4, pp. 211–219, 2004.

[115] K. Nozaki, E. Kuramochi, A. Shinya, and M. Notomi, "25-channel all-optical gate switches realized by integrating silicon photonic crystal nanocavities," *Optics Express*, vol. 22, no. 12, pp. 3491–3496, 2014.

[116] A. Geravand, M. Danaie, and S. Mohammadi, "All-optical photonic crystal memory cells based on cavities with a dual-argument hysteresis feature," *Optics Communications*, vol. 430, no. 7, pp. 323–335, 2018.

[117] A. Tavousi, "Optik Wavelength-division demultiplexer based on hetero-structure octagonal-shape photonic crystal ring resonators," *Optik - International Journal for Light and Electron Optics*, vol. 179, no. 2018, pp. 1169–1179, 2019.

[118] A. Farmani, A. Mir, and M. Irannejad, "2D-FDTD simulation of ultra-compact multifunctional logic gates with nonlinear photonic crystal," *Journal of the Optical Society of America B*, vol. 36, no. 4, pp. 811–818, 2019.

[119] Y. Long, Y. Zhang, X. Zhang, J. Xia, J. Dong, and J. Wang, "Linear and nonlinear microwave responses of a microwave photonic filter based on a photonic crystal microcavity," *Journal of Applied Physics*, vol. 121, no. 23, 2017.

[120] Y. Long, J. Xia, Y. Zhang, J. Dong, and J. Wang, "Photonic crystal nanocavity assisted rejection ratio tunable notch microwave photonic filter," *Nature Publishing Group*, no. January, 2017.

[121] T. Baba, "Slow light in photonic crystals," *Nature Photonics*, vol. 2, no. 8, pp. 465–473, 2008.

[122] M. Gay, L. Bramerie, L. A. Neto, S. D. Le, J.-c. Simon, C. Peucheret, Z. Han, X. Checoury, G. Moille, J. Bourderionnet, A. D. Rossi, and S. Combrié, "Silicon-on-Insulator RF Filter Based on Photonic Crystal Functions for Channel Equalization," *Photonics Technology Letters*, vol. 28, no. 23, pp. 2756–2759, 2016.

[123] Y. Yu, W. Xue, E. Semenova, K. Yvind, and J. Mork, "Demonstration of a self-pulsing photonic crystal Fano laser," *Nature Photonics*, vol. 11, no. 2, pp. 81–84, 2017.

[124] A. Tartakovskii, *Quantum Dots*. Cambridge University Press, first ed., 2012.

[125] K. Takeda, T. Sato, A. Shinya, K. Nozaki, W. Kobayashi, H. Taniyama, M. Notomi, K. Hasebe, T. Kakitsuka, and S. Matsuo, "Few-fJ/bit data transmissions using directly modulated lambda-scale embedded active region photonic-crystal lasers," *Nature Photonics*, vol. 7, no. 7, pp. 569–575, 2013.

[126] M. Loncar, T. Yoshie, A. Scherer, P. Gogna, and Y. Qiu, "Low-threshold photonic crystal laser," *Applied Physics Letters*, vol. 2680, no. 2002, pp. 140–144, 2002.

[127] Y. Li, A. Bhattacharyya, C. Thomidis, T. D. Moustakas, and R. Paiella, "Ultrafast all-optical switching with low saturation energy via intersubband transitions in GaN/AlN quantum-well waveguides," *Optics Express*, vol. 15, no. 26, p. 17922, 2007.

[128] C. Reese, C. Becher, A. Imamoğlu, E. Hu, B. D. Gerardot, and P. M. Petroff, "Photonic crystal microcavities with self-assembled inAs quantum dots as active emitters," *Applied Physics Letters*, vol. 78, no. 16, pp. 2279–2281, 2001.

[129] T. Yoshie, O. Shchekin, H. Chen, D. Deppe, and A. Scherer, "Quantum dot photonic crystal lasers," *Electronic Letters*, vol. 38, no. 17, pp. 967–968, 2002.

[130] C. Smith, H. Benisty, D. Labilloy, U. Oesterle, R. Houdre, T. F. Krauss, R. De la Rue, and C. Weisbuch, "Near-infrared microcavities confined by two- dimensional photonic bandgap crystals," *Electronic Letters*, vol. 35, no. 3, pp. 228–230, 1999.

[131] M. Nomura, S. Iwamoto, K. Watanabe, N. Kumagai, Y. Nakata, S. Ishida, and Y. Arakawa, "Room temperature continuous-wave lasing in photonic crystal nanocavity," *Optics Express*, vol. 14, no. 13, pp. 1067–1069, 2006.

[132] S. Strauf, K. Hennessy, M. T. Rakher, Y. Choi, A. Badolato, L. C. Andreani, E. L. Hu, P. M. Petroff, and D. Bouwmeester, "Self-Tuned Quantum Dot Gain in Photonic Crystal Lasers," *Physical Review Letters*, vol. 127404, no. 3, pp. 25–28, 2006.

[133] V. Loo, C. Arnold, O. Gazzano, A. Lemaı, I. Sagnes, O. Krebs, P. Voisin, P. Senellart, and L. Lanco, "Optical Nonlinearity for Few-Photon Pulses on a Quantum Dot-Pillar Cavity Device," *Physical Review Letters*, vol. 166806, no. 10, pp. 1–5, 2012.

[134] D. Englund, A. Majumdar, M. Bajcsy, A. Faraon, P. Petroff, and J. Vuc, "Ultrafast Photon-Photon Interaction in a Strongly Coupled Quantum Dot-Cavity System," *Physical Review Letters*, vol. 093604, no. 3, pp. 2–5, 2012.

[135] H. Nakamura, Y. Sugimoto, K. Kanamoto, N. Ikeda, Y. Tanaka, Y. Nakamura, S. Ohkouchi, Y. Watanabe, K. Inoue, H. Ishikawa,

and K. Asakawa, "Ultra-fast photonic crystal/quantum dot all- optical switch for future photonic networks," *Optics Express*, vol. 12, no. 26, pp. 6606–6614, 2004.

[136] H. Nakamura, K. Kanamoto, Y. Nakamura, S. Ohkouchi, H. Ishikawa, and K. Asakawa, "Nonlinear optical phase shift in InAs quantum dots measured by a unique two-color pump/probe ellipsometric polarization analysis," *Journal of Applied Physics*, vol. 96, no. 3, pp. 1425–1434, 2004.

[137] C. Y. Jin, O. Kojima, T. Kita, O. Wada, and M. Hopkinson, "Observation of phase shifts in a vertical cavity quantum dot switch," *Applied Physics Letters*, vol. 98, no. 23, pp. 2009–2012, 2011.

[138] D. M. Lukin, A. D. White, M. A. Guidry, R. Trivedi, N. Morioka, C. Babin, J. Ul-hassan, N. T. Son, T. Ohshima, P. K. Vasireddy, M. H. Nasr, J.-p. W. Maclean, C. Dory, E. A. Nanni, J. Wrachtrup, and F. Kaiser, "Spectrally reconfigurable quantum emitters enabled by optimized fast modulation," *arXiv*, no. 1, pp. 0–8, 2020.

[139] J. Li, R. Yu, and Y. Wu, "Dipole-induced high-order sideband comb employing a quantum dot strongly coupled to a photonic crystal cavity via a waveguide," *Physical Review B - Condensed Matter and Materials Physics*, vol. 89, no. 035311, pp. 1–6, 2014.

[140] J. Li, R. Yu, C. Ding, W. Wang, and Y. Wu, "Optical-frequency-comb generation and entanglement with low-power optical input in a photonic molecule," *Physical Review A - Atomic, Molecular, and Optical Physics*, vol. 90, no. 3, pp. 1–8, 2014.

[141] J. Li, Y. Qu, R. Yu, and Y. Wu, "Generation and control of optical frequency combs using cavity electromagnetically," *Physical Review A*, vol. 97, no. 023826, pp. 1–8, 2018.

[142] G. Calajo, L. Rizzuto, R. Passante, G. Calajò, L. Rizzuto, and R. Passante, "Control of spontaneous emission of a single quantum emitter through a time-modulated photonic-band-gap environment," *Physical Review A*, vol. 96, no. 2, pp. 1–8, 2017.

[143] M. Metcalfe, S. M. Carr, A. Muller, G. S. Solomon, and J. Lawall, "Resolved Sideband Emission of InAs = GaAs Quantum Dots Strained by Surface Acoustic Waves," *Physical Review Letters*, vol. 037401, no. July, 2010.

[144] T. Uesugi, B.-s. Song, T. Asano, and S. Noda, "Investigation of optical nonlinearities in an ultra-high-Q Si nanocavity in a two-dimensional photonic crystal slab," *Optics Express*, vol. 14, no. 1, pp. 377–386, 2006.

[145] W. Suh, S. Member, Z. Wang, S. Member, and S. Fan, "Temporal Coupled-Mode Theory and the Presence of Non-Orthogonal Modes in Lossless Multimode Cavities," *IEEE Journal of Quantum Electronics*, vol. 40, no. 10, pp. 1511–1518, 2004.

[146] A. E. Miroshnichenko, S. F. Mingaleev, S. Flach, and Y. S. Kivshar, "Nonlinear Fano resonance and bistable wave transmission," *Physical Review E - Statistical, Nonlinear, and Soft Matter Physics*, vol. 71, no. 3, pp. 1–8, 2005.

[147] B. E. Little, S. T. Chu, H. A. Haus, J. Foresi, and J. Laine, "Microring Resonator Channel Dropping Filters," *Journal of Lightwave Technology*, vol. 15, no. 6, pp. 998–1005, 1997.

[148] M. Soljačić, M. Ibanescu, S. G. Johnson, Y. Fink, and J. D. Joannopoulos, "Optimal bistable switching in nonlinear photonic crystals," *Physical Review E - Statistical Physics, Plasmas, Fluids, and Related Interdisciplinary Topics*, vol. 66, no. 5, p. 4, 2002.

[149] S. Thoms and D. S. Macintyre, "Investigation of CSAR 62, a new resist for electron beam lithography," *Journal of Vacuum Science & Technology B, Nanotechnology and Microelectronics: Materials, Processing, Measurement, and Phenomena*, vol. 32, no. 6, pp. 1–5, 2014.

[150] P. Marin-Palomo, J. Kemal, M. Karpov, A. Kordts, M. Pfeiffer, P. Trocha, S. Wolf, V. Brasch, M. H. Anderson, R. Rosenberger, K. Vijayan, W. Freude, T. J. Kippenberg, and C. Koos, "Microresonator-based solitons for massively parallel coherent optical communications," *Nature Publishing Group*, vol. 546, pp. 274–279, 2017.

[151] M. Notomi, "Manipulating light with strongly modulated photonic crystals," *Reports on Progress in Physics*, vol. 73, no. 9, 2010.

[152] R. Prasanth, J. E. Haverkort, A. Deepthy, E. W. Bogaart, J. J. Van Der Tol, E. A. Patent, G. Zhao, Q. Gong, P. J. Van Veldhoven, R. Nötzel, and J. H. Wolter, "All-optical switching due to state filling in quantum dots," *Applied Physics Letters*, vol. 84, no. 20, pp. 4059–4061, 2004.

[153] H. Nakamura, S. Nishikawa, S. Kohmoto, K. Kanamoto, and K. Asakawa, "Optical nonlinear properties of InAs quantum dots by means of transient absorption measurements," *Journal of Applied Physics*, vol. 94, no. 2, pp. 1184–1189, 2003.

[154] C.-Y. Jin, R. Johne, M. Y. Swinkels, T. B. Hoang, L. Midolo, P. J. Van Veldhoven, and A. Fiore, "Ultrafast non-local control of spontaneous emission," *Nature Nanotechnology*, vol. 9, no. 11, pp. 886–890, 2014.

[155] T. Kitada, T. Kanbara, K. Morita, and T. Isu, "A GaAs/AlAs Multilayer Cavity with Self-Assembled InAs Quantum Dots Embedded in Strain-Relaxed Barriers for Ultrafast All-Optical Switching Applications," *Applied Physics express*, vol. 1, no. 092302, pp. 1–4, 2008.

[156] I. Fushman, E. Waks, D. Englund, N. Stoltz, P. Petroff, and J. Vučković, "Ultrafast nonlinear optical tuning of photonic crystal cavities," *Applied Physics Letters*, vol. 90, no. 9, pp. 2005–2008, 2007.

[157] C. Y. Jin, O. Kojima, T. Kita, O. Wada, M. Hopkinson, and K. Akahane, "Vertical-geometry all-optical switches based on InAs/GaAs quantum dots in a cavity," *Applied Physics Letters*, vol. 95, no. 2, pp. 2–5, 2009.

[158] H. Oda, K. Inoue, Y. Tanaka, N. Ikeda, Y. Sugimoto, and K. A. Hiroshi Ishikawa, "Self-phase modulation in photonic-crystal- slab line-defect waveguides," *Applied physics letters*, vol. 231102, no. January 2007, pp. 2005–2008, 2007.

[159] K. Inoue, H. Oda, N. Ikeda, and K. Asakawa, "Enhanced third-order nonlinear effects in slow- light photonic-crystal slab waveguides of line-defect," *Optics Express*, vol. 17, no. 9, pp. 7206–7216, 2009.

[160] S. Boscolo and M. Midrio, "Y junctions in photonic crystal channel waveguides : high transmission and impedance matching," *Optics Letters*, vol. 27, no. 12, pp. 1001–1003, 2002.

[161] J. S. Turner, J.-m. Lourtioz, V. Berger, J.-m. Gérard, and A. Tchelnokov, *Photonic Crystals*. Springer, second ed., 2008.

[162] A. Martinez, P. Sanchis, and J. Marti, "Mach – Zehnder interferometers in photonic crystals," *Optical and Quantum Electronics*, vol. 37, pp. 77–93, 2005.

[163] A. R. Chalcraft, S. Lam, D. O'Brien, T. F. Krauss, M. Sahin, D. Szymanski, D. Sanvitto, R. Oulton, M. S. Skolnick, A. M. Fox, D. M. Whittaker, H. Y. Liu, and M. Hopkinson, "Mode structure of the L3 photonic crystal cavity," *Applied Physics Letters*, vol. 90, no. 24, pp. 1–4, 2007.

[164] K. P. Nagarjun, Jeyaselvan Vadivukarassi, S. Shankar Kumar, and V. R. Supradeepa, "Generation of tunable, high repetition rate frequency combs with equalized spectra using carrier injection based silicon modulators," *Optics Express*, vol. 26, no. 8, p. 975218, 2018.

[165] D. T. Spencer, T. Drake, T. C. Briles, J. Stone, L. C. Sinclair, C. Fredrick, Q. Li, D. Westly, B. R. Ilic, A. Bluestone, N. Volet, T. Komljenovic, L. Chang, S. H. Lee, D. Y. Oh, T. J. Kippenberg, E. Norberg, L. Theogarajan, M.-g. G. Suh, K. Y. Yang, H. P. Martin, K. Vahala, N. R. Newbury, K. Srinivasan, J. E. Bowers, S. A. Diddams, S. B. Papp, M. H. Pfeiffer, T. J. Kippenberg, E. Norberg, L. Theogarajan, K. Vahala, N. R. Newbury, K. Srinivasan, J. E. Bowers, S. A. Diddams, and S. B. Papp, "An optical-frequency synthesizer using integrated photonics," *Nature*, vol. 557, no. 7703, pp. 81–85, 2018.

[166] M. V. Kotlyar, T. Karle, M. D. Settle, L. O'Faolain, and T. F. Krauss, "Low-loss photonic crystal defect waveguides in InP," *Applied Physics Letters*, vol. 3588, no. March, pp. 1–4, 2004.

[167] R. Welty, C. Reinhardt, I. Han, Y. Du, and S. Yoo, "Chlorine-Hydrogen ECR Etching of InGaAsPDnP," in *International Semiconductor Device Research Symposium*, pp. 422–423, 2003.

[168] P. Strasser, R. Wuest, F. Robin, D. Erni, and H. Jackel, "Detailed analysis of the influence of an inductively coupled plasma reactive-ion etching process on the hole depth and shape of photonic crystals in InP-InGaAsP," *Journal of Vacuum Science & Technology B: Microelectronics and Nanometer Structures*, vol. 25, no. 2, p. 387, 2007.

[169] P. Strasser, R. Wüest, F. Robin, D. Erni, and H. Jäckel, "Deep dry etching of InP with a Cl 2 /CH 4 /H 2 mixture on an ICP-RIE for photonic crystals.," in *Proc. 27th Workshop Compound Semicond. Dev. & Integrated Circuits*, pp. 81–82, 2003.

[170] E. Pommereau, L. Legouezigou, S. Hubert, A. Sainson, J.-P. Chandouineau, S. Fabre, G.-H. Duan, B. Lombardet, R. Ferrini, and

R. Houdre, "Fabrication of low loss two-dimensional InP photonic crystals by inductively coupled plasma etching," *Journal of Applied Physics*, vol. 2242, pp. 1–5, 2004.

[171] S. Guilet, S. Bouchoule, C. Jany, C. S. Corr, and P. Chabert, "Optimization of a inductively coupled plasma etching process adapted to nonthermalized InP wafers for the realization of deep ridge heterostructures," *Journal of Vacuum Science & Technology B*, vol. 24, no. 5, pp. 2381–2385, 2006.

[172] C. Cojocaru, F. Raineri, R. Raj, P. Monnier, O. Drisse, and L. Legoue, "Room-temperature simultaneous in-plane and vertical laser operation in a deep-etched InP-based two-dimensional photonic crystal," *IEE Proceedings - Optoelectronics*, vol. 152, no. 2, pp. 4–7, 2005.

[173] K. H. Lee, S. Guilet, G. Patriarche, I. Sagnes, A. Talneau, K. H. Lee, S. Guilet, G. Patriarche, I. Sagnes, and A. Talneau, "Smooth sidewall in InP-based photonic crystal membrane etched by inductively coupled plasma Smooth sidewall in InP-based photonic crystal membrane etched by N 2 -based inductively coupled plasma," *Journal of Vacuum Science & Technology B*, vol. 1327, pp. 1326–1339, 2008.

[174] R. Dylewicz, R. M. D. L. Rue, R. Wasielewski, P. Mazur, G. Mezosi, and A. C. Bryce, "Fabrication of submicron-sized features in InP / InGaAsP / AlGaInAs quantum well heterostructures by optimized inductively coupled plasma etching with chemistry," *Journal of Vacuum Science & Technology B*, vol. 1327, no. 2002, 2010.

[175] P. Strasser, R. Wiiest, F. Robin, D. Erni, and H. Jackel, "Process optimization for dry etching of InP/InGaAsP-based photonic crystals with a Cl2/CH4/H2 mixture on an ICP-RIE," *International Conference on Indium Phoshide and Related Materials*, vol. Conference, pp. 6–9, 2004.

[176] L. Gatilova, S. Bouchoule, S. Guilet, and P. Chabert, "Investigation of InP etching mechanisms in a inductively coupled plasma by optical emission spectroscopy," *Journal of Vacuum Science & Technology A*, vol. 262, no. 12, pp. 262–266, 2009.

[177] K. Kennedy, K. Groom, and R. Hogg, "Fabrication of v-groove gratings in InP by inductively coupled plasma etching with," *Semiconductor Science and Technology*, vol. 21, 2005.

[178] A. Matsutani, H. Ohtsuki, A. Matsutani, H. Ohtsuki, F. Koyama, A. Matsutani, H. Ohtsuki, E. Process, A. Matsutani, A. Takada, A. Matsutani, and A. Takada, "Vertical and Smooth Etching of InP by Cl 2 / Xe Inductively Coupled Plasma," *Japanese journal of applied physics*, pp. 2–4, 1999.

[179] S. L. Rommel, J.-h. Jang, W. Lu, G. Cueva, L. Zhou, I. Adesida, G. Pajer, A. Lepore, Z. Schellanbarger, J. H. Abeles, S. L. Rommel, J.-h. Jang, W. Lu, G. Cueva, and L. Zhou, "Effect of H2 on the etch profile of InP / InGaAsP alloys in inductively coupled plasma reactive ion etching chemistries for photonic device fabrication," *Journal of Vacuum Science & Technology B*, vol. 1130, no. 1989, pp. 1–5, 2011.

[180] J. Etrillard, P. Ossart, G. Patriarche, M. Juhel, J. F. Bresse, and C. Daguet, "Anisotropic etching of InP with low sidewall and surface induced damage in inductively coupled plasma etching using," *Journal of Vacuum Science & Technology A*, vol. 626, no. June 1998, 1998.

[181] E. Kuramochi, K. Nozaki, A. Shinya, H. Taniyama, K. Takeda, T. Sato, S. Matsuo, and M. Notomi, "Ultralow bias power all-optical photonic crystal memory realized with systematically tuned L3 nanocavity," *Applied Physics Letters*, vol. 221101, 2015.

[182] B. Wang, *Light control by nanostructured metal surfaces and photonic crystals in nanobeams and freestanding membranes*. PhD thesis, Eindhoven University of Technology, 2011.

[183] K. Kounoike, M. Yamaguchi, M. Fujita, T. Asano, J. Nakanishi, and S. Noda, "Investigation of spontaneous emission from quantum dots embedded in two-dimensional photonic-crystal slab," *Electronic Letters*, vol. 41, no. 25, pp. 8–9, 2005.

[184] S. Noda, M. Fujita, and T. Asano, "Spontaneous-emission control by photonic crystals and nanocavities," *Nature Photonics*, vol. 1, no. 8, pp. 449–458, 2007.

[185] E. Purcell, "Spontaneous emission probabilities at radio frequencies," *Physical Review*, vol. 69, no. 681, 1946.

[186] J. Vuckovic, "Quantum optics and cavity QED with quantum dots in photonic crystals," in *Quantum Optics and Nanophotonics*, no. 8, ch. 5, 2017.

[187] T. Tanabe, H. Taniyama, and M. Notomi, "Carrier Diffusion and Recombination in Photonic Crystal Nanocavity Optical Switches," *Conference on Lasers and Electro-Optics and 2008 Conference on Quantum Electronics and Laser Science*, vol. 26, no. July 2008, pp. 1396–1403, 2008.

[188] T. Baba, D. Sano, K. Nozaki, K. Inoshita, Y. Kuroki, and F. Koyama, "Observation of fast spontaneous emission decay in GaInAsP photonic crystal point defect nanocavity at room temperature," *Applied Physics Letters*, vol. 3989, 2004.

[189] M. Takiguchi, H. Sumikura, M. Birowosuto, E. Kuramochi, T. Sato, K. Takeda, S. Matsuo, and M. Notomi, "Enhanced and suppressed spontaneous emission from a buried heterostructure photonic crystal cavity," *Applied Physics Letters*, vol. 091113, no. 8, pp. 1–5, 2013.

[190] B. Wild, R. Ferrini, R. Houdre, M. Mulot, S. Anand, and C. J. M. Smith, "Temperature tuning of the optical properties of planar photonic crystal microcavities," *Applied Physics Letters*, vol. 84, no. 7, pp. 4–7, 2003.

[191] M. Nomura, S. Iwamoto, N. Kumagai, and Y. Arakawa, "Temporal coherence of a photonic crystal nanocavity laser with high spontaneous emission," *Physical Review B - Condensed Matter and Materials Physics*, vol. 75, no. 195313, pp. 4–6, 2007.

[192] A. J. Seeds, "Microwave photonics," *Ieee Transactions on Microwave Theory and Techniques*, vol. 50, no. 3, pp. 877–887, 2002.

[193] X. Xu, J. Wu, T. G. Nguyen, T. Moein, S. T. Chu, B. E. Little, R. Morandotti, A. Mitchell, and D. J. Moss, "Photonic microwave true time delays for phased array antennas using a 49 GHz FSR integrated optical micro-comb source," *Photonics Research*, vol. 6, no. 5, p. B30, 2018.

[194] J. Yao, "Photonics to the Rescue," *IEEE Microwave Magazine*, no. September, pp. 46–60, 2015.

[195] A. Haboucha, W. Zhang, T. Li, M. Lours, A. N. Luiten, Y. L. Coq, and G. Santarelli, "Optical-fiber pulse rate multiplier for ultralow phase-noise signal generation," *Optics Letters*, vol. 36, no. 18, pp. 3654–3656, 2011.

[196] H. Jiang, J. Taylor, F. Quinlan, T. Fortier, and S. A. Diddams, "Noise Floor Reduction of an Er : Fiber Laser-Based Photonic Microwave Generator," vol. 3, no. 6, 2011.

[197] T. M. Fortier, F. Quinlan, A. Hati, C. Nelson, J. A. Taylor, Y. Fu, J. Campbell, and S. A. Diddams, "Photonic microwave generation with high-power photodiodes," *Optics Letters*, vol. 38, no. 10, pp. 1712–1714, 2013.

[198] F. Quinlan, F. N. Baynes, T. M. Fortier, Q. Zhou, A. Cross, J. C. Campbell, and S. A. Diddams, "Optical amplification and pulse interleaving for low-noise photonic microwave generation," *Optics Letters*, vol. 39, no. 6, pp. 1581–1584, 2014.